MODELLING THE COMMINUTION PROCESS IN THE ROTARY OFFSET CRUSHER

Titus Nghipulile

A thesis submitted to the School of Chemical and Metallurgical Engineering, Faculty of Engineering and the Built Environment, University of the Witwatersrand, Johannesburg, South Africa, in fulfilment of the requirements for the Doctor of Philosophy in Engineering

May 2024

DECLARATION

I declare that this thesis is my own unaided work. It is being submitted for the Degree of Doctor of Philosophy in Engineering to the University of the Witwatersrand, Johannesburg. It has not been submitted before for any degree or examination to any other University.

Titus Nghipulile

02/05/2024
Date

ACKNOWLEDGEMENTS

First and foremost, the Almighty GOD has been there to provide strength and wisdom in the last four years. I would like to extend my gratitude to my supervisors (Prof. M. Bwalya, Prof. H. Simonsen, and Prof. I. Govender) for the guidance along the journey which started at the beginning of 2020. I am grateful to Prof. Indresan Govender for providing access to the DEM software through the University of KwaZulu Natal. I am equally grateful to Professor Michael Moys who has contributed some ideas during initiation of my project.

The University of the Witwatersrand has supported me through the Postgraduate Merit Awards (PMA) from 2020 to 2023. The PMA offered some relief as it catered for my tuition fees. I am equally grateful to Mintek for the support through the science vote funding during the period I was working there. I also acknowledge the former colleagues in the Minerals Processing Division at Mintek for the support and encouragement while I was studying. Jonathan Desebrook from Mineralogy Division at Mintek is highly appreciated for his tireless efforts in ensuring the mineralogical analyses and image processing are completed.

I express my profound gratitude to my family, brethren, and friends for the encouragement, love, and prayers over the years. Justina Shikongo, many thanks for your understanding, love and prayers during the periods when I had to spend many hours analysing the data and writing the thesis. To everyone else who have been with me along the journey, thank you very much and God bless you.

ABSTRACT

There is always a search for size reduction solutions due to the inherent energy inefficiency associated with comminution devices. The rotary offset crusher (ROC) is a new comminution device with a promising performance potential in terms of throughput due to enhanced speed of transportation induced by the centrifugal force of the discs and high frequencies of closure and opening of crushing chamber. The lack of fundamental understanding of the micro-processes that are facilitating both comminution and material transport in this new crusher necessitated a thorough investigation of key factors that drive comminution in this equipment. A combination of experimental and numerical modelling techniques was used to study the effect of key operating variables such as speed of the discs, offset between the vertical axes of the discs, feed size distribution and feed rate.

The offset provides some flexibility in the system, but it does not significantly improve the crushing efficiency or the throughput. The speeds of the discs proved to be the key determinants of the degree of breakage achieved in the crusher. Both compressive and shear energies are active, with compressive energy dominating at lower speeds and decreasing with gradual increase in speed while the shear force increases with the increasing speed. Those trends render the device operating at higher speeds to be analogous to a laboratory pulveriser. Feed rates of at least 10 tph and feeds with wide size distributions (including near-vertical exit gap particles) are recommended for future studies in the quest to optimize the throughput of the crusher.

Further work is recommended to investigate the effect of crusher profiles on the product quality (size and shape), power draw and throughput. It is anticipated that modifying the crusher profile can further intensify the crushing forces imposed on the particles. Consideration should also be given to increase the opening of the comminution cavity in order to be able to choke feed the crusher and thereby promoting rock-on-rock crushing. It is also recommended that the vibratory motion for the top disc be considered in order to intensify the compressive loads experienced by the particles. Overall, the redesign of this engineering device is necessary to reduce comminution by attrition due to disc-particle contacts and intensify the compressive forces.

TABLE OF CONTENTS

LIST OF TABLES

LIST OF FIGURES

LIST OF ABBREVIATIONS AND SYMBOLS

Ai	Bond abrasion index
ROC	Rotary offset crusher
HPGR	High Pressure Grinding Roll
VRM	Vertical roller mill
ROM	Run-of-mine
DEM	Discrete element method
PRM	Particle replacement method
BPM	Bonded particle model
VSD	Variable speed drive
PGMs	Platinum Group Metals
UG2	Upper Group 2 PGM ore
M_i	Initial steel plate mass
M_f	Final steel plate mass
CWi	Crushability work index
C	Impact strength per unit thickness
C_{50}	Median of C
SEM	Scanning electron microscope
BSE	Back-scattered secondary electrons
g	Acceleration due to gravity (m/s^2)
h	Net drop height of the steel disc
τ	Residence time of particles in a comminution machine
DWT	Drop weight test
E_i	Input energy in the DWT
m_d	Mass of drop weight in Eq. (2.9)
E_{cs}	Specific comminution energy (in kWh/t)
t_{10}	Percent passing the tenth of the feed size given by Eq. (2.1)

A and b	ore breakage parameters as defined in Eq. (2.1)
L	Original particle size in Eq. (2.12)
M	Maximum t_{10} for the material in Eq. (2.12)
t_n	percent passing the $1/n^{th}$ of the feed size class
B_{ij}	Cumulative breakage function
β	Material-dependent breakage parameter
ϕ	Fraction of fine particles resulting from single breakage event
γ	Related to relative number of fines produced in a breakage event
R	Relative particle size
F	Force
F_n	Normal force acting on particles (as defined by Eq. (2.10))
F_t	Tangential force acting on particles (as defined by Eq. (2.11))
v_n	Normal relative velocity of the particles (in Eq. (2.10))
v_t	Tangential relative velocity of the particles (in Eq. (2.11))
K_n	Stiffness of the spring in normal direction (in Eq. (2.10))
K_t	Stiffness of the spring in tangential direction (in Eq. (2.11))
C_n	Normal damping coefficient in Eq. (2.10)
C_t	Tangential damping coefficient in Eq. (2.11)
ε	Coefficient of restitution
Δx	Amount of overlap of particles (in mm) in Eq. (2.10) and (2.11)
Δt	Integration time step
F^g	Gravitational force actin on the particle
F^c	Contact forces between the particles and surrounding particles or walls
F^{nc}	Non-contact forces acting on the particle
Mij	Resultant contact torque acting on the particle
P	Power (in Watt)
N	Rotational speed in revolution per minutes (rpm)
N_c	Critical speed (in rpm)

T	Torque (in Nm)
ω	Angular velocity in radians per seconds (rad/s)
E_k	Stored kinetic energy in Joules
I	Moment of inertia
N_p	Number of particles during DEM simulation
m_t	Total mass of particles (balls) fed to the ROC during DEM simulation
m_s	Mass of a single particle (ball) fed to the ROC during the DEM simulation
d_i	Diameter of a ball (particle) for DEM simulation
ρ	Density of the balls (particles) fed to the ROC in kg/m^3
SG	Specific gravity
Q	Throughput in tonne per hour (tph) or kilogram per hour (kg/h)
F	Feed rate in tph or kg/h
V	Volumetric throughput of the crusher
w	width of jaws in the jaw crusher
S	Closed side setting
T	Throw of the crusher
D	Vertical depth between the jaws in the jaw crusher
G	Crusher gape
G_{exit}	Vertical exit gap
CSS	Closed site setting
OSS	Open side settings
RMSE	Root mean square error
R^2	Coefficient of correlation
d_{80}	80 % passing size
R_{80}	Reduction ratio calculated using the d_{80} of the feed and product
d_{50}	50 % passing size
R_{50}	Reduction ratio calculated using the d_{50} of the feed and product
F80	80% passing size of the feed

P80	80% passing size of the product
φ (r/r′,t	Breakage function
a (r,t)	Selection function
$P_0(r)$	Particle number distribution density at the inlet of the grinder
P(r)	Particle number distribution density at the outlet
$\underline{f}$	Feed size distribution vector
$\underline{p}$	Product size distribution vector
$\underline{\underline{C}}$	Classification function
$\underline{\underline{B}}$	Breakage distribution function in matrix form
$\underline{\underline{I}}$	Identity matrix
$(\cdot)^{-1}$	Inverse of a square matrix
N_e	Number of crushing events in Evertsson model
π	Mathematical symbol for Pi (22/7)
P-P	Particle-Particle contacts
P-BD	Particles-bottom disc contact
P-TD	Particles-top disc contact
E_{impact}	Impact energy
E_{shear}	Shear energy
$E_{dissipated}$	Dissipated energy
E_u	Energy utilization
N_{diff}	Speed difference
C_{diff}	Type of profile on the crushing surface
X_f	Feed aperture size
X_{offset}	Horizontal offset between the discs
Y_{gap}	Exit gap
e*	Relative specific energy in Eq. (2.13)
e_{50}	Median particle specific fracture energy in Eq. (2.13)
e_{50}	Specific impact energy in Eq. (2.13)
σ^2	Variance
F_x	Force in x –direction
F_y	Force in y-direction

v_x	Translational velocity in the x –direction
v_y	Translational velocity in the y-direction

CHAPTER 1: INTRODUCTION

1.1 Rationale of the study

Comminution is employed as the first stage of processing in the mining industry where the run-of-mine (ROM) is crushed and milled to ensure the liberation of the valuable minerals from the gangue. It is well-known that comminution devices are characterized by low energy efficiencies due to the random nature of force transmission to the particles in some comminution devices such as the tumbling mills (Legendre & Zevenhoven, 2014). The inefficiency results in the utilization of a small fraction of the available energy for comminution while the rest is dissipated as noise, heat, and mechanical losses, as well as used for elastic particle deformation (Jeswiet & Szekeres, 2016; Legendre & Zevenhoven, 2014; Radziszewski, 2013; Sadrai et al., 2011; Tavares & King, 1998). For example, the efficiency of the ball mills, in terms of energy utilization for breakage, is less than 5% (Wills & Finch, 2016). Innovation in comminution is thus expected to continue unabated to address the inefficiencies that are inherent to comminution devices and circuits. For many decades, comminution research has focused on the design and optimization of milling devices, with little attention given to the crushing devices, and thus possibly missing out on the possible gains that can be achieved by improving the performance of crushers (Cleary & Sinnott, 2015). This study investigated the processes underpinning the performance of the rotary offset crusher (ROC), which is a new comminution device with a promising performance potential in terms of throughput due to the enhanced rate of impact impartation and the speed of transportation induced by the centrifugal force of the discs (Nghipulile, 2019).

The laboratory-scale ROC employs a simple design with two parallel 500 mm diameter discs that are not mechanically linked and there is a provision to offset the axis of the upper disc. The discs are made of mild steel. The shifting of the axis relative to the lower disc is a key factor behind the breakage mechanism of this crusher. Thus, in rotation, there is a geometrical expansion and contraction of the conical space between the two discs in each revolution[1]. The effect of the

[1] The volume expansion and contraction can only happen when the crusher is operated with an offset greater than the flattened edge (10 mm) of the top disc.

horizontal offset between the axes of the discs on the crusher performance is not fully understood (Nghipulile, 2019). The frequency of the cyclic expansion and contraction of this space depends on the rotational speed of the discs (another important operating variable). The effect of the rotational speed on both material comminution and transport is not fully established beyond 830 rpm (Nghipulile, 2019). In this design, only the lower disc is driven by the motor via the V-belt drive. The transfer of the rotational motion to the upper disc is via the particles that are trapped between the faces of the upper and lower discs. The particles in the crushing zone are crushed as the high-speed discs spin and their inter-spatial geometry is changed. The particles move centrifugally from the center of the bottom disc to the periphery where they are discharged being smaller than the vertical interval between the edges of the discs.

Table 1. 1: Description of parts for ROC

Part number	**Description**
1	Feed material
2	Conveyor belt
3	Feed chute
4	Top disc (weighing 69 kg)
5	Bottom disc (weighing 104 kg)
6	Vertical exit gap
7	Horizontal offset
8	Crusher product
9	Belt drive
10	Motor

In the previous study, it was found that the ROC can potentially have a performance advantage, in terms of capacity, compared to the cone crusher (Nghipulile, 2019). However, there were some limitations in understanding the full potential of this equipment because it was suspected that the laboratory prototype that was used to conduct the experiments had structural weakness(es) that could limit the energy transfer to the particles. Instead of building a new equipment to conduct more experiments and also to develop a deeper understanding of the processes underpinning the performance of the ROC, it was recommended to use numerical simulation tools such as the discrete element method (DEM) to answer some of the research questions that remained outstanding. The main advantage of the DEM is that it can provide the micro-dynamic data to assess the performance of the equipment before further modifications can be made to the original design (Li, 2013). The main objective of the research on the ROC is to evaluate whether the centrifugal force, accompanied by rapid expansion and contraction of the crushing chamber associated with this crusher, gives it a performance advantage over the existing crushing devices. Using the DEM simulation, the study sought to answer the following research questions.

- Using the DEM, can it can be shown that the capacity is enhanced in the ROC due to rapid centrifugal transportation resulting from the rotating discs?
- Are the resultant stressing forces due to accompanying contraction and expansion of the ROC crushing chamber sufficient to provide matching breaking force as particles are transported through the crusher?
- What are the dominant breakage mechanisms in this equipment and how are they affected by the key operating variables?
- Can the DEM assist in showing the force profile that would fully explain the performance and limitation of this equipment?

The main difference between the centrifugal-force driven ROC and gravity-driven conventional crushers (e.g., cone crushers) is the orientation of the crushing chamber as shown in Figure 1.1. The description of various parts of the ROC is provided in Table 1.1. The implementation of the ROC in the mineral industry or any other industry would depend on the potential performance advantages that it could offer in terms of throughput, energy consumption and product quality (size distribution and shape). It is also acknowledged that the full potential of the ROC can only be established when there is an adequate fundamental understanding of transportation and comminution processes in its crushing zone. It has been argued that in order to develop a deeper understanding of performance potential of a specific equipment, it is critical to investigate how the variations in equipment geometry, shaft velocities, particle sizes, and material properties, among other variables, affect its performance (Legendre & Zevenhoven, 2014). To develop that fundamental understanding of the micro-processes that are contributing to the overall transportation and comminution behaviours of particles in the ROC, the DEM simulation study, coupled with experimental work, was considered.

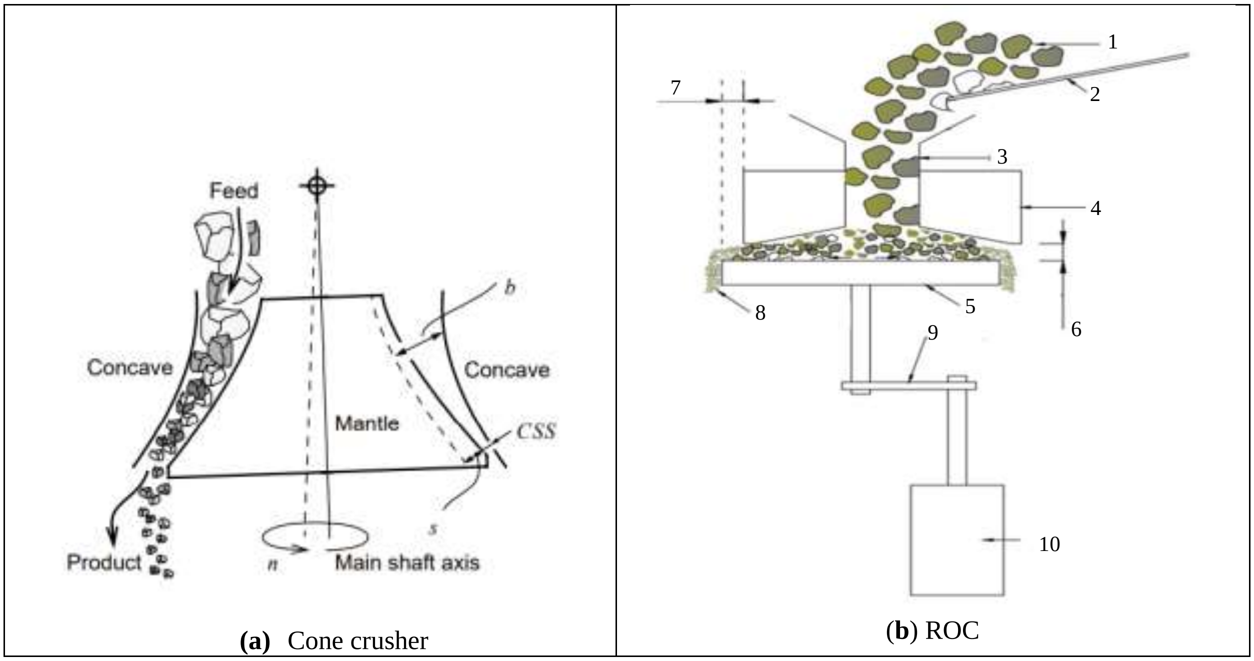

*Figure 1.1: (**a**) Functional diagram for cone crusher* (Evertsson, 1999) *and (**b**) Functional diagram of rotary offset crusher* (Nghipulile et al., 2021). *CSS stands for Close Side Setting, n is the rotational speed, b is the gape and s is the throw (difference between Open Side Setting (OSS) and CSS).*

The DEM, based on the work of Cundall & Strack (1979), proved to be the most viable approach for this kind of study because it is widely used to study the rheological and breakage behaviour in comminution devices and other engineering devices (Weerasekara et al., 2013). For crushers, Sinnott & Cleary (2015) used the DEM to study the particle flow and breakage in the jaw, gyratory, cone and roll crushers while Johansson et al. (2017), Li, McDowell, & Lowndes (2012), Quist & Evertsson (2010) focused on cone crushers to investigate the particle flow and breakage. Quist (2017) compared the performance of cone crusher and HPGR using the DEM simulations. Djordjevic et al. (2003) used the DEM to understand the load behaviour in horizontal and vertical impact crushers. The micro-properties and dynamic information of the material being processed by the comminution equipment provided by the DEM make it possible to have a better understanding of the particle flow and breakage (Quist & Evertsson, 2016). The DEM thus makes it possible to investigate the micromechanics which combine to produce complex macroscopic behaviours (Potyondy & Cundall, 2004). Such enormous information cannot easily be obtained from physical experiments.

1.2 Scope of the study

It is possible to study the effect of various ROC operating variables (e.g., speed, offset, vertical exit gap) and feed material characteristics (e.g., top size, strength, shape, and mineralogical composition) on crusher performance in terms of size reduction ratio, power draw, and throughput using the laboratory ROC. The laboratory prototype was thus used to conduct experiments to investigate the effect of rotational speed (330, 550, 830, 1000 rpm) while the other operating variables (feed rate of 1 tph, horizontal offset of 10 mm, and vertical exit gap of 4 mm) were kept constant. The four operating speeds were tested with two different mono-size feeds (−19+13.2 and −13.2+9.5 mm) for both silica (a single component material) and UG2-platinum bearing ore (a multi-component material). The mono-size feeds of silica were also used to investigate the effect of the horizontal offset (10, 16 and 23 mm) while the other operating variables (feed rate of 1 tph, speed of 830 rpm, vertical exit gap of 1.5 mm) were fixed. The effect of feed size distribution was also investigated using silica of feeds with different proportions of four mono-size fractions (−19+13.2, −13.2+9.5, −9.5+6.7 and −6.7+4.75 mm) while other variables (speed of 830 rpm, vertical exit gap of 3 mm and horizontal offset of 10 mm) were fixed. Furthermore, single particle comminution behaviour was investigated by feeding individual particles to the ROC with the vertical exit gap and horizontal offset of 4 and 10 mm respectively. Same mono-size feeds of silica and UG2 ore were tested at 550 and 1000 rpm during single particle crushing tests.

It is difficult to obtain the measurements of the internal dynamic information on granular behaviour with respect to rheology and breakage from physical experimentation with crushers (Cleary & Sinnott, 2015). Discrete element modelling of comminution devices has proven to be a viable approach which can provide micro-properties and dynamic information of the material flow and fracture in the crushers (e.g.,(Barrios & Tavares, 2016; Bwalya & Chimwani, 2022; Chen et al., 2021; Cleary & Sinnott, 2015; Guo et al., 2024; Johansson et al., 2017; Manocada et al., 2021; Refahi et al., 2010). To gain a better insight into the micro-processes facilitating the comminution in this device, a discrete element method (DEM) simulation study was conducted to study the effect of the operating rotational speed of the discs and horizontal offset on the size reduction ratio, ratio of shear energy to impact energy (inferring the degree of dominance of the different breakage mechanisms), specific comminution energy, and throughput. The ROC was simulated when it was fed with single particle as well as when it was fed with many particles. The Ab-t_{10} breakage model, that is based on the work of Vogel & Peukert (2004) and further developed by Shi & Kojovic (2007), was used to study the crushing behaviour of the polyhedrons. This model can predict the breakage behaviour of particles, including non-spherical particles as demonstrated in previous studies (André & Tavares, 2020; Guo et al., 2024; Jiménez-Herrera et al., 2018; Tavares et al., 2020).

Discrete element modelling of the crushing device was performed using the polyhedral particles to study the effect of the rotational speed (550, 1000, 1450, 1900 and 2350 rpm) on single particle crushing when the crusher is operated under different dynamics, viz., (1) stationary top disc, and (2) both discs rotating at the same speed. DEM simulations with many polyhedral particles, to study the effect of speed and horizontal offset, were based on conditions used in the experimental work as well as extrapolated parameters. The results generated from both physical and computational experiments provided the insights into performance potential of the current design of the ROC for hard rocks application.

1.3 Structure of the thesis

The thesis is organised in the following nine chapters.

- In Chapter 1, the background and scope of the study are discussed. The scope of the study guided the development of the methodology discussed in Chapter 3.
- Chapter 2 reviews the relevant literature on the subject being investigated. This includes fracture mechanics, modelling of comminution and particle flow in crushers, and DEM as a tool for studying transportation and breakage. It is acknowledged that the ROC is a new technology which is still not very well-documented in the literature. However, the principles underpinning its performance can be described by those documented for other engineering devices with similar design features or those designed/operated for the same purpose (i.e. crushing or milling).
- Chapter 3 describes the suite of experimental and simulation work that was conducted. This entails the discussion of the breakage characterization tests to understand the fracture behaviour of the materials (silica and UG2 platinum-bearing ore ore) used in the test work, ROC crushing test work, DEM calibration tests, and DEM simulation setup.

- The results of the breakage characterization test work which were conducted using silica and UG2 ore are presented and discussed in Chapter 4.
- The experimental results on single particle and many particles (at the feed rate of 1 tph) are discussed in Chapter 5. The results guided the parameterization of DEM simulation of the ROC.
- The ROC experimental results were compared to those of cone crusher (in terms of product size distribution and particle shape) in Chapter 6.
- The DEM results of the single polyhedral particle breakage are discussed in Chapter 7 for a variety of operating speeds while changing the crusher dynamics (stationary top disc and both discs rotating).
- Chapter 8 is on the presentation and analysis of the DEM simulation results which are based on conditions used in the experimental work as well as extrapolated range.
- In Chapter 9, the main research findings are summarized. Based on the results, the perceived way forward on the ROC research is also presented.

CHAPTER 2: LITERATURE REVIEW

2.1. Crushers in comminution circuits

Comminution is the head operation in the minerals industry which involves the particle size reduction in order to liberate the valuable mineral(s) from the gangue. The run-of-mine (ROM) ore, with the top size which can be as high as 1.5 m, is fed to the jaw or gyratory crushers for primary crushing to have the ore with the top size between 10 and 20 cm. The primary crusher product is further reduced in the secondary crusher (and sometimes also to a subsequent tertiary crusher) to the top size between 0.3 and 2 cm, which is often advanced to the milling circuit for further mineral liberation prior to the downstream separation and recovery processes. The cone crusher is used for secondary and tertiary crushing. Alternatively, the impact crushers may also be used for secondary and tertiary crushing. The high-pressure grinding rolls (HPGR) technology which has been associated with the cement industry for many decades (Altun et al., 2011; Farzanegan et al., 2016), and introduced in the minerals industry since the 1970s, is said to be relatively energy efficient when compared to conventional crushers and tumbling mills due to efficient energy utilization when particles are compressed in bed between parallel plates (Schönert, 1988, 1996). That efficient breakage mechanism in the HPGR is referred to as inter-particle breakage mechanism (Charikinya et al., 2015; Djordjevic, 2010; Knecht & Patzelt, 2004; Rosario et al., 2011; Saramak, 2011). The summary of crushers in the minerals industry is provided in Table 2.1. The design and operational features of the different crushers are discussed elsewhere (Chimwani, 2024; P. W. Cleary & Sinnott, 2015; Gupta & Yan, 2016; Wills & Finch, 2016).

Table 2. 1: Comparison of different crushers in the mineral industry (Chimwani, 2024)

Type of crusher	**Top feed size (m)**	**Type of force**	**Stage**	**Product size determining parameter**
Jaw crusher	1.5	Compressive	Primary	CSS
Gyratory crusher	1.37	Compressive	Primary	Set
Impact crusher	0.6	Impact	Secondary/Tertiary	Rotor liner clearance
Cone crusher	0.432	Compressive	Secondary/Tertiary	CSS
HPGR	0.15	Compressive	Secondary/Tertiary	Roller gap

The application of the ROC in the minerals industry can be expected to be secondary or tertiary crushing. However, its implementation will depend on the potential performance benefits in terms of energy consumption, capacity and product size. Once the full potential of the ROC is established, it has to be benchmarked against the existing devices including the cone crusher, HPGR, and impact crusher.

2.2. Fracture mechanics of rocks

The pioneering work of Griffith (1920) on the concept of "surface energy" provides the foundation of fracture mechanics of brittle materials such as rocks. Griffith postulated that for any extension of a crack dimension (usually measured in terms of length) in a material (e.g. rocks), there is a corresponding increase in the area of the new surface. Mathematical description of Griffith theory is discussed elsewhere (King, 2012; Tan, 2011). It is a well-known phenomenon that nucleation and propagation of cracks within materials start from the place (s) with structural weakness (e.g. joints and voids) which are often prevalent in the ore particles. This is because rocks are characterised by inhomogeneities such as joints, voids and a variety of minerals dispersed as grains of various size distributions (Estay & Chiang, 2013; Park et al., 2018; Sima, Jiang, & Zhou, 2014; Ündül, Amann, & Plötze, 2015; Xu & Li, 2017; Zhao & Zhang, 2020; Zhou et al., 2018; Zhou, Gu, & Wang, 2015). The non-uniform stress distribution within different particles of the same ore/material presents a challenge when studying the fracture process of rocks in comminution devices, with the validity of the deduced inferences highly dependent on the statistical measures (e.g., variance (Tavares & King, 1998)).

2.2.1 Breakage modes in brittle materials

One important aspect that should be understood for the ROC is the failure process of the particles in the crushing zone. Numerical simulations were performed in this study, as discussed in Chapters 3, 7 and 8, to enhance the understanding of the failure process of the particles nipped between the discs. Depending on the loading type (tensile, compressive or shear), the failure modes of rocks can generally be classed into three types: (1) mode I (tension, opening), mode II (shear, sliding) and mode III (shear, tearing) (Al-shayea, 2005; Alneasan et al., 2018, 2019). One of these modes or a combination of them, with a combination of modes I and II being common in rocks (Al-shayea, 2005), facilitates the nucleation and propagation of cracks in the rocks whose intensities are aided by the presence of the inhomogeneities and the magnitude of the applied stress (tensile, compressive or shear). Since the tensile strength of rock is very much smaller compared to its compressive and shear strengths (Aadnøy & Looyeh, 2019; You, 2015), a rock material is more likely to fail in tension than in compression. It can be argued that efficiency in comminution can only be improved significantly if tensile stress is intensified in the device. Efficient conversion of compressive and shear stresses to tensile stress is not currently achieved in many comminution devices (Sadrai et al., 2006, 2011), and this contributes to the inherent low efficiency which comminution process has come to be known for.

During a failure process, a variety of cracks can be observed in rocks. For example, when the particles are under the uniaxial compressive stress, types of cracks which can be observed are shown in Figure 2.1. The wing cracks, also called tensile cracks, are initiated at the tip of the flaw and propagate smoothly towards the direction of maximum compression (Park & Bobet, 2009). The secondary cracks, commonly referred to as shear cracks (Yunteng et al., 2017) also initiate at the flaws' tips, but these are co-planar with the flaw. Furthermore, the coalescence cracks initiate with the progression of the tensile cracks or shear cracks or a combination of tensile and shear cracks (Bobet & Einstein, 1998; Jiang et al., 2019; Vásárhelyi & Bobet, 2000; Yunteng et al., 2017; Zhao et al., 2016). The spacing between the pre-existing flaws determines the length of the coalescence cracks.

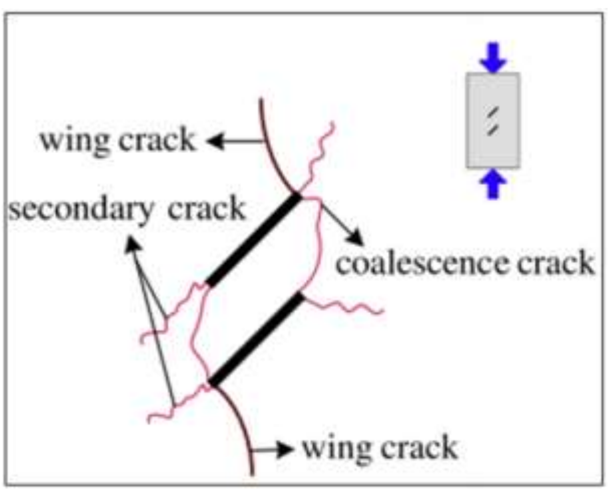

Figure 2. 1: Three types of cracks observed in gypsum specimens under uniaxial compressive loading in the top diagram (Bobet & Einstein, 1998; Xu & Li, 2017)

2.2.2 Breakage mechanisms in comminution devices

In comminution machines, there are various breakage mechanisms (impact, compression and abrasion) whose degree of dominance is dependent on the type of loading force (tensile, compressive or shear) which is applied to the particles. Some of the key questions which this study attempted to answer in Chapters 5 to 8 include;

- What are key breakage mechanisms in the ROC?
- How are the breakage mechanisms affected by key operating variables?

It is acknowledged that the performance of any comminution machine does not only depend on its operating conditions, but it is equally affected by the mechanical properties (e.g. toughness and brittleness) of the material (Parapari et al., 2020; Zuo & Shi, 2016). In Chapter 4, the breakage characteristics obtained from experiments that were conducted on the materials used in the ROC test work (silica and UG2 platinum-bearing ore) are discussed.

2.2.2.1 Impact breakage and t_{10} - E_{cs} model

Impact breakage which happens when large compressive stress (e.g., the sharp "blows" applied to the particles in the impact crushers) is applied, causes the parent particles to shatter and thus produces daughter particles of the wider size distribution (King, 2012). The t_{10} index is usually used to describe the breakage characteristics of a particular ore (Narayanan et al., 1987) which is subjected to impact breakage. This index, given by Eq. (2.1), basically represents the cumulative mass passing the 1/10th of the feed size and thus essentially describing the rate at which fines are generated (Napier-Munn et al., 2005). Fitting the experimental results to Eq. (2.1) allows the computation of breakage parameters *A* and *b*, with parameter *A* representing the maximum value of t_{10} while parameter *b* is the slope of the linear part of the typical plot of t_{10} as a function of specific energy (E_{cs}). The product of the model parameters (*A* and *b*) has been accepted as the best indicator for the ore resistance to impact breakage (Kojovic & Shi, 2008; Shi et al., 2015). A smaller *A* x *b* value shows that the ore has a higher resistance to impact breakage and vice versa. The standard classification for material hardness based on the product of the impact breakage parameters is given in Table 2.2.

$$t_{10} = A \times (1 - e^{-bE_{cs}}) \quad (2.1)$$

Where E_{cs} is the specific comminution energy, A and b are material specific impact breakage parameters.

*Table 2. 2: Classification of A*b parameter (Napier-Munn et al., 2005)*

A*b range	Classification
0 to 30	Very hard
~30 to 39	Hard
~39 to 43	Moderately hard
~43 to 56	Medium
~56 to 67	Moderately soft
~67 to 127	Soft
~127 to 956	Very soft

2.2.2.2 Inter-particle comminution

Inter-particles comminution is dominant in the high pressure grinding rolls (HPGR) and vertical roller mills (VRM) (Altun et al., 2015; Reichert et al., 2015; Rosario & Hall, 2010; Saramak et al., 2017; Wang et al., 2009)). The very high compressive stresses associated with the environment result in microcracks being induced in the particles (Ozcan & Benzer, 2013) which can be advantageous in some downstream processes such as leaching because the lixiviant can percolate through the cracks and dissolve the target metal(s) (Ghorbani et al., 2011, 2013; Y. Tang et al., 2020). Higher energy efficiencies in machines with inter-particle comminution as a dominant mechanism can be explained using the fundamental work of Professor Klaus Schönert and his colleagues in Germany (Schönert, 1996; Schönert, 1988) on energy utilization of various breakage mechanisms shown in Figure 2.2. They established that the confined particle bed breakage is highly efficient, in terms of energy utilization, compared to the random impact and abrasion breakage encountered in the tumbling mills.

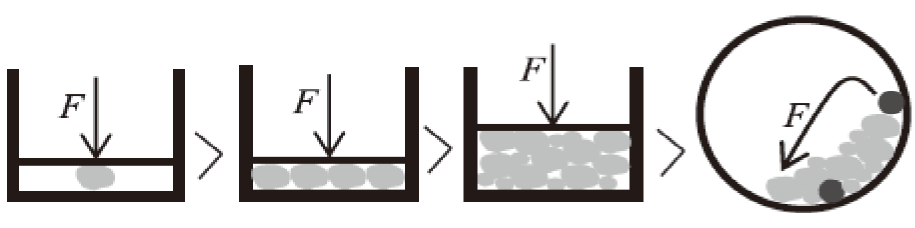

Figure 2. 2: The order of energy utilisation for various breakage mechanisms (Schönert, 1988)

Energy savings ranging between 10 and 30 % have been reported for the circuits incorporating HPGR and VRM (Altun et al., 2015; Reichert et al., 2015; Rosario & Hall, 2010; Saramak et al., 2017; Wang et al., 2009). The benefits characterizing the HPGR and VRM place an expectation on the new crushing technologies to have a similar breakage mechanism in order to leverage on high energy efficiency.

The amenability of the ore to bed comminution (inter-particle breakage) can be investigated using a piston-die apparatus and the relationship between the compression pressure and bed porosity is given by the following equation (Heckel, 1961).

$$\ln\left(\frac{1}{\varepsilon}\right) = cP + a \tag{2.2}$$

Where ε is bed porosity, P is compression pressure, c and a are parameters related to the properties of the materials being compressed (Liu and Powell, 2016). Parameters c relates to the porosity reduction rate caused by particle rearrangement during the compaction stage or particle breakage in the compression stage. Parameter a is related to the initial particle bed porosity when the compression pressure is zero.

The porosity of the bed is calculated using the following equation.

$$\varphi = \left(1 - \left(\frac{\text{Bulk density}}{\text{Particle density}}\right)\right) \times 100 \tag{2.3}$$

The ratio of the bed height reduction (initial height h_0 minus final bed height h_f) to the initial bed height is referred to as the bed compaction ratio (C) and this is calculated using Eq. (2.4).

$$C = \frac{h_0 - h_f}{h_0} \tag{2.4}$$

If the initial bed porosity is denoted as ε_0 and the final bed porosity as ε (i.e., when compression stops), the relative bed porosity reduction ε_r is calculated using the following equation.

$$\varepsilon_r = \frac{\varepsilon_0 - \varepsilon}{\varepsilon_0} \tag{2.5}$$

Acknowledging that the particle bed height reduction is directly related to the bed porosity reduction in the bed compression test (Liu and Powell, 2016), Eq. (2.6) relating the bed relative porosity reduction with the bed compaction ration can be written and this makes it possible to calculate the relative bed porosity reduction from the initial porosity and bed height reduction.

$$\varepsilon_r = \frac{C(1-\varepsilon_0)}{\varepsilon_0(1-C))} \qquad (2.6)$$

In Chapter 4, the relative bed porosity reduction for different size fractions of silica and UG2 ore were calculated from experimental data generated using the piston and die apparatus.

2.2.2.3 Abrasion and its likelihood in the ROC

The last mode of breakage, abrasion, is regarded as a surface phenomenon that occurs when applied forces are parallel to their plane of contact (Napier-Munn et al., 2005). Abrasion, as a surface process, does not result in a wide product size distribution because it simply entails the smoothing off of initial surface angularity on the particles which are generally under shear stress (Weerasekara et al., 2013). In the ROC, abrasion is expected due to the comminuted particles sliding along the discs' surfaces. In this study, the effects of the rotational speed (in Chapters 7 and 8) and offset (in Chapter 8) on the degree of shearing breakage mechanism due to particles-surfaces contacts were investigated using discrete element modelling. It must also be noted that a gouging abrasion, a severe form of abrasion wear can occur when particles can cause a deep scratch or indentation to the equipment (Jiang et al., 2018) and this should be minimized during operation. However, wear was not a subject of focus for the current study and thus gouging abrasion could not be observed during DEM simulations since the wear model in the simulator was 'disabled" to allow the simulator to study material comminution and transport. It is suggested that future studies should also consider the wear of the crushing surfaces. Process material of various characteristics (e.g., size, strength, etc.) can be created in the simulator with a crushing surface of ideal mechanical properties for liners in the crushers.

2.3 Modelling size reduction and particle flow in crushers

The performance of the ROC can be described fully using the models which consider both the breakage and transportation of particles. However, the interactions between the flow and comminution models can be complex because the overall size reduction in the ROC is a result of successive comminution events as particles move radially (along the comminution cavity) between the discs. The calculation process shown in Figure 2.3, suggested by Evertsson (1999), can be applied to all crushers including the ROC. The comminution and flow models that were developed for conventional crushers are reviewed in the following subsections to serve as the basis for studying the material comminution and transport in the ROC.

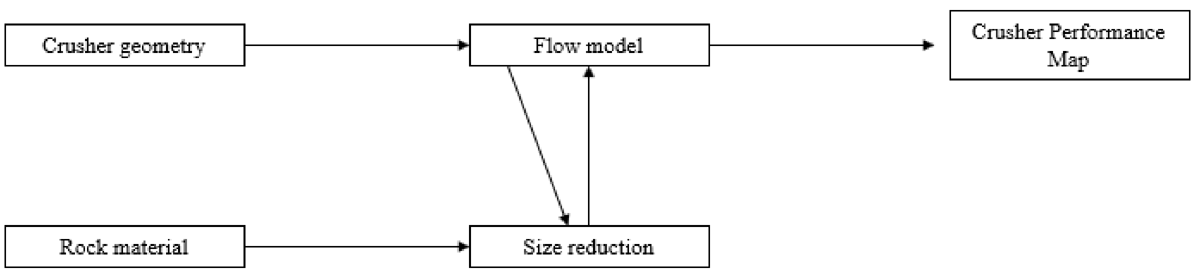

Figure 2. 3: Modular structure for calculation process of the modelling the performance of a cone crusher (Evertsson, 1999)

2.3.1 Comminution models for crushers

Fragmentation of rocks is a probabilistic (stochastic) process because particles of the same ore and size distribution are characterized by distinct inhomogeneities (e.g., mineral distribution, type and intensity of cracks, etc.). Mathematical models are used to describe the breakage process, with all those stochastic integrodifferential equations premised on the non-linear integral Kolmogorov-Chapman-Smoluchovski equation (Padokhin & Zueva, 2009; Solsvik & Jakobsen, 2015). The Kolmogorov-Chapman-Smoluchovski equation accounts for the probabilistic nature of the fragmentation process through the selection $a(r, t)$ (usually denoted as S) and breakage distribution $\varphi\ (r/r',t)$ (usually denoted as B) functions as shown in Eq. (2.7) for the batch perfect-mixing apparatus. The selection function describes the disappearance rate of a specific size class r per unit time (Dundar, Benzer, & Aydogan, 2013). The breakage function defines the average size distribution of the progeny particles resulting from the fracture of the parent size fraction (Kelly & Spottiswood, 1990).

$$\frac{\partial P(r,t)}{\partial t} = -a(r,t)P(r,t) + \int_{r}^{r_{max}} a(r',t)\varphi(r/r',t')P(r',t)dr' \qquad (2.7)$$

Where *P(r, t)* is probability density of the particle size distribution, *a(r, t)* is the selection function, *φ (r/r´, t)* is the breakage distribution (probability density of the transition of particles from class of sizes *r´* to the class of sizes *r)*, *r* is fixed particle size, r_{max} is the maximum particle size, *r´* is particle size at the time point *t´*.

Assuming perfect-mixing and hydrodynamic flow pattern of the carrier and solid phases in the comminution equipment, Eq. (2.7) can be modified, to describe the fragmentation process of continuous apparatuses, as follows (Padokhin & Zueva, 2009).

$$\frac{\partial P(r,t)}{\partial t} = -a(r,t)P(r,t) + \int_{r}^{r_{max}} a(r',t)\varphi(r|r',t)dr' + \frac{Q}{V}[P_0(r) - P(r)] \qquad (2.8)$$

Where *P(r) = p(r)V* is the particle number distribution density in the working volume of the grinder (at the outlet), $P_0(r)$ is the particle number distribution density at the inlet of the grinder, *Q* is the volumetric flow rate of a material through the apparatus, *V* is the working volume.

The two models, incorporating the selection and breakage functions, which are mainly applied to the crushers are discussed in the following subsections.

2.3.1.1 Whiten model

In 1972, Whiten proposed a simple model describing size reduction in cone crushers, which has since been applied to other comminution devices such as the jaw crushers (Johansson et al., 2017) and impact crushers (Nikolov, 2004; Nikolov, 2002; Segura-salazar et al., 2017). Whiten (1972) schematically represented his model with a flow sheet in Figure 2.4. The model reasonably assumes that the particles fed to the crusher can either be broken or dropped through the crusher unbroken. The broken particles then have the same chance of dropping through the crusher and, in the process, they may be broken further. This process successively happens until the particles leave the crushing chamber.

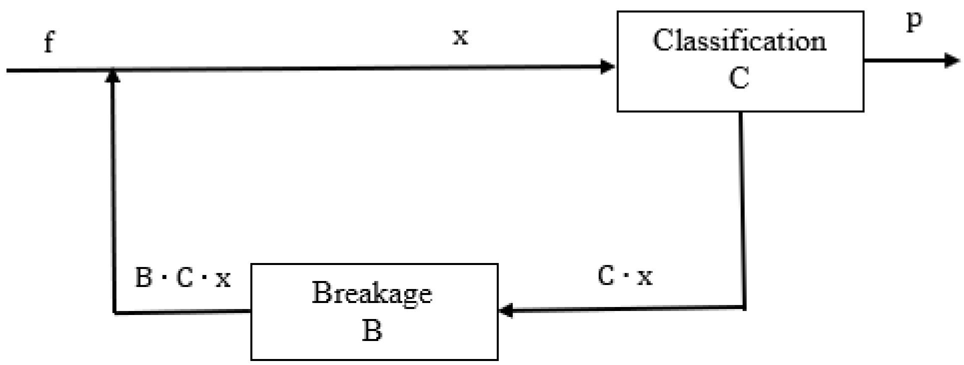

Figure 2. 4: Symbolic model for crushers (Whiten, 1972)

In Figure 2.4, the crusher is simplified into a single breakage zone and a mass balance around the circuit results in the following Whiten model which can be used to predict the product size distribution for crushers (Gupta & Yan, 2006).

$$\underline{p} = (\underline{\underline{I}} - \underline{\underline{C}}) \cdot (\underline{\underline{I}} - \underline{\underline{B}} \cdot \underline{\underline{C}})^{-1} \cdot \underline{f} \qquad (2.9)$$

Where $\underline{f}$ is the feed size distribution vector, $\underline{p}$ is the product size distribution vector, $\underline{\underline{C}}$ is the classification function (a diagonal matrix describing the proportion of particles in each size fraction selected to enter the crushing zone, $\underline{\underline{B}}$ is the breakage distribution function (a lower triangular matrix giving the relative distribution of each size fraction after breakage), $\underline{\underline{I}}$ is the identity matrix and $(\cdot)^{-1}$ represents the inverse of a square matrix.

2.3.1.2 Evertsson model

Further to Whiten's work, in the late 1990s, Evertsson and his colleagues developed the model describing the comminution process in cone crushers (Evertsson, 1998, 1999; Evertsson & Bearman, 1997). They conceptualised the crushing process by assuming that there is no internal particle size classification occurring within a crusher chamber. This is a reasonable assumption for the case when the crusher is choking. Unlike the Whiten model which considers a single crushing zone, here the breakage zone is subdivided into several size reduction cycles. The product of a breakage zone becomes the feed for the next breakage zone as shown in Figure 2.5. In each compression stroke of the cone, some particles are selected for breakage and depending on whether the particles reach the critical stress, they may fracture. When the strength of a particle is larger than the applied stress, the particle does not break, but it weakens and can easily fracture when the subsequent load is applied (Brosh et al., 2014). In addition, these unbroken particles can contribute to the generation of fines due to attrition at the contact points (Evertsson & Bearman, 1997). The size distribution of the daughter fragments is influenced by the specific breakage appearance function of the material. For the sequential process, the product size distribution can be computed using this equation:

$$\underline{p} = [\prod_{i=1}^{N_e}[\underline{\underline{B_i}} \cdot \underline{\underline{S_i}} + (\underline{I} - \underline{\underline{S_i}})]] \cdot \underline{f} \qquad (2.10)$$

Where $\underline{f}$ and $\underline{p}$ represents feed and product mass flow rates, $\underline{\underline{B_i}}$ and $\underline{\underline{S_i}}$ are breakage and selection functions respectively, while N_e is the total number of crushing events that occur within the modelled crusher.

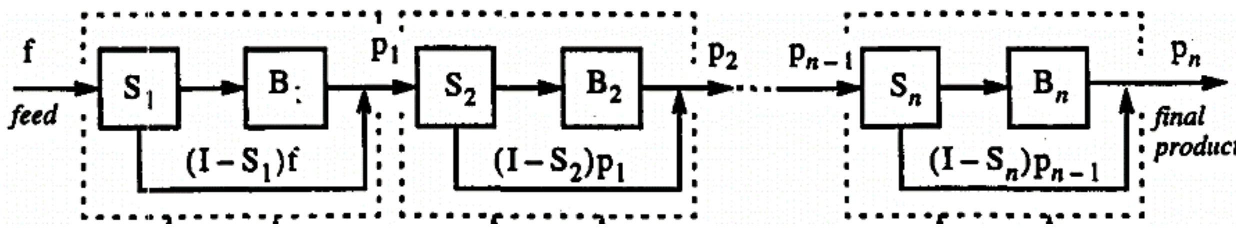

Figure 2. 5: A model for the cone crusher with N crushing events (Evertsson & Bearman, 1997)

2.3.2 Modelling particle flow in crushers

Evertsson (1999) developed the analytical model for the particle flow in the cone crusher. Mathematical equations are left out considering that transportation mechanisms in conventional crushers and ROC are different, i.e. in the conventional crushers; the material transport is governed by gravity while centrifugal motion facilitates the transportation of particles in the ROC.

2.3.2.1 Evertsson flow model for cone crusher

The operating principle for the cone crusher is shown in Figure 2.6. The chamber geometry of the cone crusher is made up of the concave bowl which is housing a mantle that is supported by the shaft which rests off-centre on the lever gear causing an eccentric motion when the gear rotates. Thus causes the mantle to cyclically move forward and backward relative to the concave (crushing surface), i.e. there is squeezing motion (forward movement of the mantle) and releasing motion (backward movement of the mantle). For squeezing motion, the particles are compressed and, depending on the level of applied stress (relative to the critical stress of the processed material) they are comminuted or simply weakened. On the other hand, during the releasing motion, the material flows through the chamber. This type of flow is governed by gravity as well as the motion of the mantle. The importance of squeezing and releasing motions (vibratory motion) in the ROC has been investigated using the DEM, and as discussed in Chapters 7, the lack of vibratory motion suggests shear as a dominant breakage mechanism in the ROC. This is an important aspect that should be considered in future design modifications of the crusher.

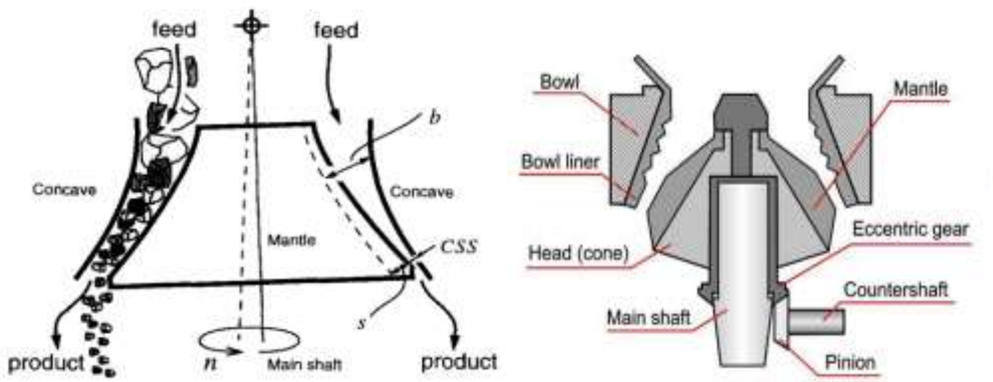

Figure 2. 6: Functional diagram for cone crusher(Evertsson, 1999; Wills & Finch, 2016)

Evertsson proposed that material transportation in the cone crusher is achieved through either one or a combination (depending on the speed of the eccentricity) of three mechanisms, viz. sliding, free fall and squeezing.

- Sliding occurs when the particle is in contact with the mantle and thus slides downwards. During sliding the material is affected by gravity as well as normal and frictional forces. In the ROC, depending on the shape and orientation of the centrifugally accelerated particles, sliding along the crushing discs can be expected.
- If the mantle accelerates away rapidly enough, the corresponding particle will fall freely. The particle is only affected by gravity until it comes into contact with the mantle again. In the ROC, free fall is only occurring in the feeding chute while in the crushing zone, the particles are centrifugally accelerated.
- When the particle comes into contact with both the mantle and concave, squeezing occurs. During squeezing, the particles are compressed and thus comminuted. The velocity of the

particle is affected by the motion of the mantle. Depending on the geometry of the crushing chamber, there is a likelihood of the occurrence of the shear stress which can make the velocity of the particle relative to the mantle surface to be zero. In the ROC, squeezing is expected when the particles get trapped between discs. Until they are comminuted to allow their release along the comminution cavity, the particles will move with the discs with a substantial amount of shear stress expected to act on the nipped particles.

2.3.2.2 Conceptualisation of particle flow in the ROC

Material transport in the crushing zone of the ROC is facilitated by both rotational and translation motions. Some scenarios, reported by various researchers, involving both translational and rotational motions, which could serve as the basis for modelling the particle flow in the ROC include (1) a ball rolling on a freely spinning turntable (Agha et al., 2015; Burns, 1981; Ehrlich & Tuszynski, 1995; Romer, 1981; Tiersten, 2015; Weckesser, 1997) and (2) the physics of game of "curling" (Maeno, 2014; Nyberg, Alfredson, Hogmark, & Jacobson, 2013; Nyberg, Alfredsson, & Hogmark, 2013; Penner, 2016, 2018, 2019; Shegelski & Lozowski, 2019; Shegelski & Lozowski, 2016). For the ball or sphere rotating on the spinning turntable, this is analogous to the particle sliding on the spinning bottom disc of the ROC (assuming that fracture does not happen). The game of curling involves propelling the 18 kg disk-shaped granite rock down a sheet of ice towards a target that is approximately 28 m away. The curler gives the rock some initial angular velocity which results in the rock undergoing between 1 and 4 rotations as it travels down the ice. The initial angular velocity causes the rock to deflect or curl away from the straight-line path. For both the scenarios above, the translational and rotational motions are described by the following equations:

$$m\frac{dv_x}{dt} = \sum F_x \qquad (2.11)$$

$$m\frac{dv_y}{dt} = \sum F_z \qquad (2.12)$$

$$\mathrm{I}\frac{d\omega}{dt} = \sum(r \times F) \qquad (2.13)$$

Where m and I are the mass and moment of inertia of the stone respectively, v_x and v_z are translational velocities in x and z directions respectively, ω is the angular velocity (positive in a counterclockwise direction), F_x and F_z are the frictional forces in x and y directions respectively, and r is the radius of the running band.

Eq. (2.11) to (2.13) can be numerically integrated to obtain the accelerations, velocities and positions of the particle in the crushing zone. This can make it possible to describe the motion of particles in the crushing zone of the ROC assuming that fragmentation does not take place. Nonetheless, a realistic modelling approach should incorporate breakage. Considering comminution, every time a particle is broken, the produced progeny particles would have their own motions. The numerical computation method discussed in section 2.3 can be useful in that regard as it can provide information on the breakage of particles in the ROC crushing zone.

2.3.3 Limitations of mathematical models

The models discussed in sections 2.2.1 and 2.2.2 can predict the product size distribution and the flow patterns respectively. However, the valuable information on micro-dynamics that are contributing to macroscopic material behaviour in the crusher are not captured. Additionally, such mathematical models are unable to investigate the changes in the performance of the crusher (such as the ROC) as a result of changes to the crusher design geometry and/or operating variables (Li, 2013). Consequently, without an alternative modelling approach to provide micro-dynamic data, the machines can only be developed realistically through iterative modifications to the original design, i.e., having a series of prototypes of a particular machine to enable physical experiments. However, physical experiments can be expensive and time consuming. Other approaches had to be considered since this project aimed at improving the fundamental understanding of the micro-processes that are contributing to the overall transportation, and comminution behaviour of particles in the ROC. The application of numerical methods, specifically the DEM discussed in the next section, proved to be the most viable approach for this kind of study.

2.4 DEM as a simulation tool to study material breakage and material in the ROC

Computer simulations are useful to researchers and designers as they can be used to improve the understanding of the processes, such as particle flow and fragmentation, occurring in equipment before they are fabricated or further developed and thus saving on costs and risks associated with physical prototyping and experimentation. Continuum and discrete modelling approaches are used to study the bulk behaviour. For the continuum approach, the substance is assumed to be continuous and that it fills the space it occupies. This suggests that the behaviour of individual particles, such as in the ROC, is ignored. The finite element method (FEM) is a common example of continuum modelling approaches. For the discrete approach, as the name suggests, the individual particles are considered distinct entities and thus the granular material can be represented as an assembly of particles. The discrete element method (DEM) is a popular example of discrete modelling approaches used to study particle behaviour in comminution devices. This is discussed in detail in the following subsections.

2.4.1 Introduction to DEM

The DEM, based on the work of Cundall & Strack (1979), is an effective method of addressing engineering problems in granular and discontinuous materials, especially in granular flows, powder mechanics, rock mechanics, and comminution (Weerasekara et al., 2013). The DEM software uses Newton's laws of motion to calculate the forces acting on individual particles in the system (e.g., ROC) and thereby calculating the instantaneous kinematics of those particles. The total force acting on the particle accounts for the body forces (e.g., gravity) and the forces resulting from interaction among the particles or between the particles and the boundary walls (or any other surface interacting with the particles in the simulated device).

There are both open-source and commercial DEM codes. The open-source codes include LIGGGHTS, YADE-OPEN, ESys-Particle and LMGC90 while the commercial software include Rocky-ESSS, PCF3D, EDEM, Chute Maven, Chute Analyst and PASSAGE (Bharadwaj, 2014). The main advantages of the open-source codes include (1) no licence cost, (2) the users have full control of source, and (3) cost effective for larger organizations with multiple users. The main drawback is that the users are required to have good programming background. For the commercial software, they can be expensive in terms of licence cost but the users are not required to have programming experience. The commercial ROCKY software was used in this study to improve the simulate the particles breakage and flow in the ROC and thereby improving the understanding of the processes underpinning the performance of this new crushing device.

2.4.2 Governing motion equations

In DEM, Newton's second law is applied to determine the rotational and translational motions of individual particles after every contact event (Cundall and Strack, 1979) using the simplest geometry of sphere. The governing equations for the translational and rotational motions of particle *i* with mass m_i and moment of inertia I_i can be written as (the variables used here are shown in Figure 2.7, which shows the forces and torques acting on particle *i* that is in contact with particle *j*):

$$m_i \frac{dv_i}{dt} = F_i^g + \sum_j F_{ij}^c + \sum_k F_{ik}^{nc} \qquad (2.9)$$

$$I_i \frac{d\omega_i}{dt} = \sum_j M_{ij} \qquad (2.10)$$

Where m_i is the mass of a particle, v_i is the translational velocity of the particle, t is time, F^g is the gravitational force acting on the particle, F^c represents the contact forces between the particle and surrounding particles or walls (as discussed in the next section, this is the summation of normal and tangential forces), F^{nc} represents the non-contact forces acting on the particle (such as electrostatic and magnetic forces), I_i is the moment of inertia acting on particle i, ω_i is the angular velocity for the particle, and M_{ij} is the resultant contact torque acting on the particle.

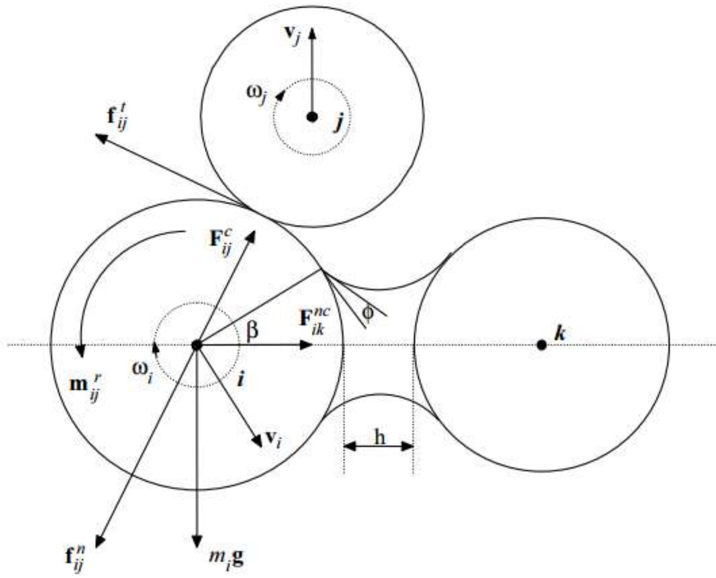

Figure 2. 7: Schematic illustration of the forces acting on particle i from contacting particle j and non-contacting particle k (drawn after (Zhu et al., 2007)

2.4.3 Contact detection and contact models

Contacts exist only when the distance between the centres of the two particles is less than the sum of their radii and the difference between these is the particle overlap (Lin. & Ng,1997). Therefore, the contact detection process just involves checking the distance between particles in the system. Once the contact has been detected, the force-displacement laws (contact models) are used to update the magnitude of contact forces arising from relative motion at each contact (Cundall & Strack, 1979; Naik et al., 2013; Ting, et al., 1989). The contact models relate the amount of overlap between two objects (particles) to determine the magnitudes of forces (tangential and normal). The material and interaction properties (e.g. shear modulus, restitution, coefficients of friction, etc.) defined by the user are also used in the calculations.

A comprehensive review of all known contact models used in DEM simulations is reported by various researchers such as those for Horabik & Molenda (2016), Luding (2008), Thornton, et al. (2013). Of these contact models, the most widely used is the linear spring-dashpot (Hertz-Mindlin (no-slip)) model, shown in Figure 2.8. The rest of the contact models are included in Appendix A.

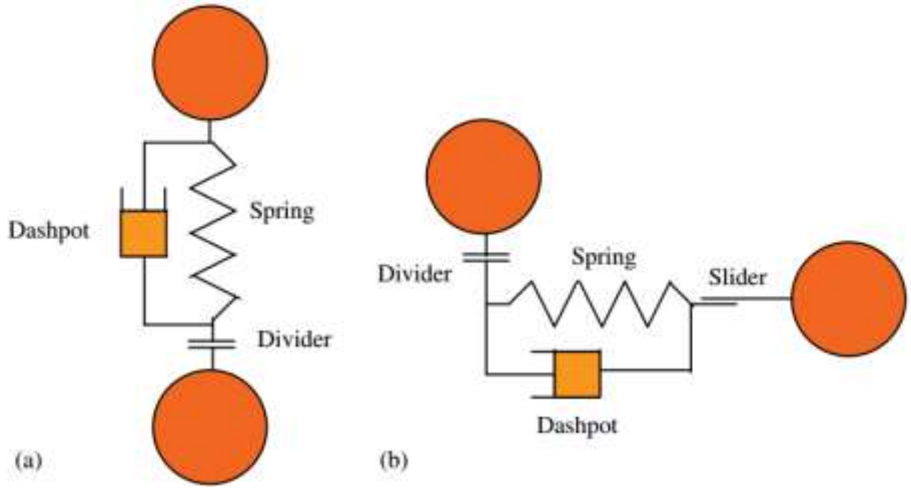

Figure 2. 8: The spring-dashpot model, (a) in the normal direction and (b) tangential direction (Jiang, Yu, & Harris, 2006)

The model in Figure 2.8 is the default model in many DEM software applications due to its acceptable accuracy and efficiency (Mateo-Ortiz & Mendez, 2016). The model uses a spring-dashpot response to normal contact between particles and/or geometry, a Coulomb friction coefficient (μ) for shear interactions and a second spring-dashpot response to tangential or rolling friction interaction (Ye et al., 2019). With this model, particles are allowed to overlap and the amount of overlap (Δx) is proportional to the forces between the interacting entities, i.e. normal and tangential forces of the overlapping entities which are calculated using the following equations.

$$\mathrm{F_n = -K_n \Delta x + C_n v_n} \tag{2.10}$$

$$\mathrm{F_t = \min\{\mu F_n, \sum K_t v_t \Delta t + C_t v_t\}} \tag{2.11}$$

Where Δt is the integration time step, F_n and F_t are normal and tangential forces to the contact plane, μ is the coefficient of static friction, K_n and K_t are stiffness of the spring in the normal and tangential directions respectively and they determine the maximum overlap between the particles, C_n and C_t are normal and tangential damping coefficients respectively which are related to the coefficient of restitution ε. The coefficient of restitution is defined as the ratio of the post-collisional (rebound) to pre-collisional (impact) normal component of the relative velocity (Sinnott & Cleary, 2015; Wang et al., 2018). Thornton et al. (2013) and Wang et al. (2018) described in detail how the value of ε can be calculated. The equations for calculating the spring stiffness constants and damping coefficients are included in Appendix A. The integral term in Eq. (2.11) represents an incremental spring that stores energy from the relative motion and models the elastic tangential deformation of the contacting surfaces (Cleary & Morrison, 2016; Cleary & Sinnott, 2015).

2.4.4 Application of DEM to the science of comminution

Application of DEM to comminution equipment includes the following: among many studies, studying breakage in tumbling mills (Bruchmüller et al., 2011; Cleary, 2001; Cleary & Morrison, 2011; Khanal & Morrison, 2008; Kime, 2016; Morrison, Cleary, & Sinnott, 2009; Pedrayes et al., 2018; Rajamani, Rashidi, & Dhawan, 2014; Weerasekara, Liu, & Powell, 2016; Mishra & Rajamani, 1992). For crushers, Sinnott & Cleary (2015) used the DEM to study the particle flow and breakage in the jaw, gyratory, cone and roll crushers while Johansson et al. (2017), Li, McDowell, & Lowndes (2012), Quist & Evertsson (2010) focused on cone crushers to investigate the particle flow and breakage. Quist (2017) compared the performance of cone crusher and HPGR using the DEM simulations. Djordjevic et al. (2003) used the DEM to understand the load behaviour in horizontal and vertical impact crushers.

The information that can be generated using the DEM includes the distribution of collision energies, types of collisions, rate of collisions, residence time of particles, discharge rate from the device and damage response of the rocks (Weerasekara et al., 2013), which can be used to predict the key quantities in comminution machines such as flow patterns and load behaviour (Gutierrez & Guichou, 2014; Khanal & Morrison, 2008; Kime, 2016; Mateo-Ortiz & Méndez, 2016), power draw (Gutierrez & Guichou, 2014; Khanal & Morrison, 2008; Kime, 2016; Morrison et al., 2009; Rajamani et al., 2014), forces acting on particles and equipment (Khanal & Morrison, 2008; Kime, 2016; Mateo-Ortiz & Méndez, 2016; Obermayr et al., 2011), wear and stress patterns on surfaces (Rajamani et al., 2014; Quist, Evertsson, & Franke, 2011), breakage rates (Gutierrez & Guichou, 2014; Lee et al., 2010), particle orientation (Mateo-Ortiz & Méndez, 2016; Weerasekara et al., 2013), crack branching and extension (D. André et al., 2019; Cil et al., 2013; Koyama & Jing, 2007), number of impacts (Gutierrez & Guichou, 2014), lifter design (Rajamani et al., 2014), and liberation (Herbst et al., 2008).

The micro-properties and dynamic information of the material being processed by the comminution equipment provided by the DEM make it possible to have a better understanding of the particle flow and breakage (Quist & Evertsson, 2016). The DEM thus makes it possible to investigate the micromechanics which combine to produce complex macroscopic behaviours (Potyondy & Cundall, 2004). Such enormous information cannot easily be obtained from physical experiments. The dynamic behaviour of the particles in the ROC can be qualitatively and/or quantitatively studied using the DEM. In the keynote address King (1993) postulated that an advanced understanding of the micro-processes in individual comminution equipment is key to developing efficient comminution equipment (Powell & Morrison, 2007). In this study, the DEM was used to study the dynamic behaviour of particles within the ROC as a way of deepening the understanding of the processes facilitating the flow and breakage of particles in the crusher. The simulation results were validated using the data obtained from the experiments conducted with the laboratory prototype of the crusher.

2.4.4.1 Modelling breakage in DEM

A comprehensive review of approaches that are considered to model particle breakage in comminution machines is provided by Jiménez-Herrera, Barrios, & Tavares (2018) and Lisjak & Grasselli (2014). The two common methods are the particle replacement method (PRM) and the bonded particle model (BPM). The PRM approach involves the instantaneous replacement of a parent particle with small fragments (progeny particles) every time a critical stress condition for fracture is met (Jiménez-Herrera et al., 2018; Quist & Evertsson, 2016). In Figure 2.9, the breakage process based on PRM in the DEM is illustrated. This involves the removal of each parent particle after fracture and replacing them with a set of progeny particles. After the replacement of the parent particles, the progeny particles are created, and these are subjected to another load resulting in further breakage and then the replacement process is repeated until the minimum size is reached. For the ROC, this minimum size is dependent on the vertical exit gap; for as long as the progeny particles that are generated are less than the vertical exit gap, the process stops.

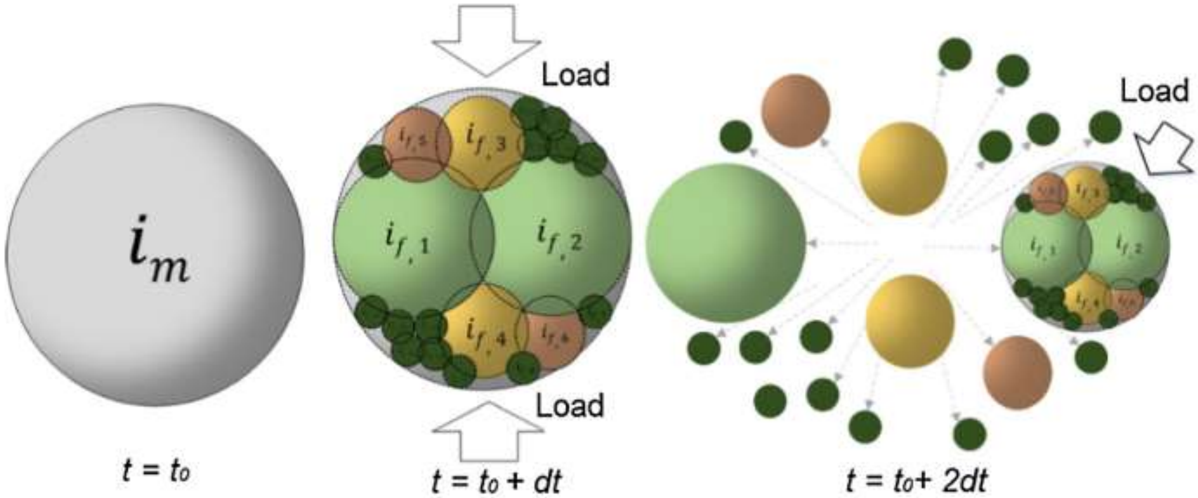

Figure 2. 9: Illustration of a PRM in DEM (Jiménez-Herrera et al., 2018)

The BPM, proposed by Potyondy and Cundall (2004) and further developed and applied by Cho et al. (2007), is based on bonding a cluster of sub-particles (also called primary or fraction particles) together using imaginary beams between individual particles to form agglomerates. The smallest size of the daughter particles produced from a comminution device is thus dependent on the chosen primary particle size in the agglomerate.

Advantages and drawbacks of PRM and BPM are discussed in detail in Jiménez-Herrera et al. (2018), Lisjak & Grasselli (2014), and Quist & Evertsson (2016). The most notable benefits of the PRM include: (1) it is less computationally expensive than BPM since it requires fewer particles in total and (2) it is also relatively easy to calibrate as experimentally derived breakage can be applied directly. However, its main drawback is that it is difficult to implement breakage sensitivity to the loading conditions on the particles when using the PRM. For the BPM, some of its advantages include (1) the meta-particles conform to any loads acting on it and thus break whenever the loading constraint is reached, and (2) the meta-particles may also be sequentially broken down in several steps. The drawbacks for the BPM include (1) all sub-particles need to be included from the beginning of the simulation when creating meta-particles and thus can limit the total number of meta-particles being modelled, (2) the mass conservation problem as a result of the poor packing factor used when clustering the primary particles together.

Once the parent particles are created in the simulation, fracture can be studied using existing models, with the two common models discussed below.

a) Ab - t_{10} model

The original work of Vogel and Peukert (2004), and the subsequent work by Shi & Kojovic (2007), resulted in the development of the *Ab* - t_{10} model shown in Eq. (2.12) which is currently used in DEM software. This breakage model treats every particle as an individual entity that can be instantly broken into fragments whose size distribution is dependent on the magnitude of the impact energy.

$$t_{10} = M\left(1 - \exp(-Se_{cum}\frac{L}{L_{ref}})\right) \qquad (2.12)$$

Where t_{10} is the percentage of fragments passing a screen size of $1/10^{th}$ of the original particle size L and M is the maximum t_{10} for a material subject to breakage, e_{cum} is total specific contact energy (computed by summing the work done by the contact forces at all contacts points in a particle during the loading period). The contact energy computed includes both the elastic and the dissipated energy in the normal direction.

b) Tavares breakage model

The breakage model based on the work of Tavares & King (1998) was also recently incorporated in the DEM software. For impact breakage, they described the breakage probability using the upper-truncated log-normal distribution of the specific fracture energy (e) as shown in Eq. (2.13).

$$\mathrm{P_0(e)} = \frac{1}{2}\left[1 + \mathrm{erf}\left(\frac{\ln \mathrm{e}^* - \ln \mathrm{e}_{50}}{\sqrt{2\sigma^2}}\right)\right] \qquad (2.13)$$

Where e^* is the relative specific fracture energy (defined by Eq. (2.14)), e_{50} is the median particle specific fracture energy, and σ^2 is the variance of the log-normal distribution of fracture energies.

$$\mathrm{e}^* = \frac{\mathrm{e_{max}\,e}}{\mathrm{e_{max} - e}} \qquad (2.14)$$

Where e_{max} corresponds to the specific impact energy above which all particles would break in a single impact.

The median of fracture energy log-normal distribution (e_{50}) is calculated using the following equation:

$$e_{50} = e_{\infty}\left[1 + \left({}^{d_{p,0}}\!/_{d_p}\right)^{\emptyset}\right] \tag{2.15}$$

Where e_{∞}, $d_{p,0}$ and $\emptyset$ are the estimated model's constants. Typical values for some materials including silica and some ores are listed in Tavares (2004) and Tavares & King (1998).

2.4.4.2 Representation of irregular particles

Prior to a particle simulation, the unknown material properties and parameters of the numerical simulation should be determined directly (experimentally) or iteratively (by reproducing an experiment within a particle simulation) (Boikov et al., 2018; Chen et al., 2018; Coetzee, 2016; Pachón-morales et al., 2019). The particle irregularity must be considered when modelling the bulk material behaviour in order to enhance the reliability of the simulation results. The common shapes that are considered in various DEM packages to model the real particle shape include polyhedron, super-quadratic and multi-spheres (Cho et al., 2007; Cleary & Morrison, 2016; Coetzee, 2016; Khazeni & Mansourpour, 2018; Latham, Munjiza, Garcia, Xiang, & Guises, 2008; Ting, Khwaja, Meachum, & Rowell, 1993; Yang, Guo, Buettner, & Curtis, 2019; Lu & McDowell, 2007). The multi-sphere method entails the creation of particle shape using many overlapping spheres. For the polyhedron which was used in this current study, the particle shape is defined in terms of corners, edges and faces, making it possible for the bulk behaviour of complex flat-faced particles to be modelled. The super quadratic particle shape representation is defined with the following equation.

$$\left(\frac{x}{a}\right)^m + \left(\frac{y}{b}\right)^m + \left(\frac{z}{c}\right)^m = 1$$

Where exponent *m* is a constant that controls the sharpness of corners and edges of particles while *a*, *b* and *c* are constants whose ratios determine the aspect ratios ($A_{xy} = {}^{b}/_{a}$ and $A_{xz} = {}^{c}/_{a}$).

2.4.5 Material calibration

Calibration is the process of finding an adequate parameter set that results in nearly the same simulation bulk behaviour as observed in the real-world experiments (Richter et al., 2020). For reliable simulation results to be obtained, there is a need for material calibration to create a link between characteristics in the simulation and the physical experiments. What happens is that, a suitable experiment (e.g. angle of repose, uniaxial compression) considering the mechanisms happening in the equipment to be modelled is set up, with a series of experiments conducted to find the characteristics of bulk material. A simple representative simulation of the physical experimental set-up is then created in DEM software. Through an iteration process, and using optimization techniques, a set of parameters that minimise the deviation between the measurements for the simulation and experiments is established.

For any physical system being modelled with DEM software, the input parameters can be classified into four groups (Boikov et al., 2018). These four groups are related to (1) boundary (wall), (2) particle (an individual entity of the processed material), (3) Paired (can be interactions amongst particles, or between particles and the boundary), and (4) common.

- The boundary parameters are the properties of the material of construction for the wall or boundary, and this includes its density, Poisson's ratio and Young's modulus (ESSS, 2020).
- The particle parameters are properties of the material being processed in the system including Poisson's ratio, Young's modulus, bulk density, particle shape, particle size distribution, and rolling resistance (for spherical particles).
- The paired parameters include paired particle-particle ($SF_{p\text{-}p}$) and particle-boundary ($SF_{p\text{-}b}$) static friction coefficients, particle-particle ($DF_{p\text{-}p}$) and particle-boundary ($DF_{p\text{-}b}$) dynamic friction coefficients as well as the coefficients of restitution for particle-particle ($COR_{p\text{-}p}$) and particle-boundary ($COR_{p\text{-}b}$) interactions.
- The common parameters include the acceleration due to gravity and the type of contact model for interaction (linear or non-linear).

Boikov et al. (2018) further proposed the classification in Table 2.3 of the method (experimentally or iteratively) of obtaining the DEM input parameters. The relevant tests were adopted to calibrate the DEM input parameters as discussed in the next chapter.

Table 2. 3: Division of input parameters (Boikov et al., 2018)

Measured directly	**Obtained iteratively**
• Poisson' ratio (boundary/particle) • Young modulus (boundary/particle) • Bulk and solid densities • Shape • Particle size distribution	• $SF_{p\text{-}p}$ • $SF_{p\text{-}b}$ • $DF_{p\text{-}p}$ • $DF_{p\text{-}b}$ • $COR_{p\text{-}p}$ • $COR_{p\text{-}b}$ • Rolling resistance

2.5 Pi Theorem for Dimensional Analysis

The ROC represents a dynamic system whose behaviour is complex. Dimensionless numbers can be used to normalise characteristics curves of various materials (and operating conditions) and thus adopting a philosophical approach to study the behaviour of materials in this novel crusher. The theoretical foundation of dimensional analysis (DA) which is now widely used in many fields of study is the Pi theorem which was formulated by Buckingham in 1914 (Tan, 2011). The Pi theorem is mathematically described in Appendix B. The Pi theorem shows that the physical law for a problem can be expressed as a causal relationship in dimensionless form. The application of the theorem was demonstrated in Chapter 5.

2.6 Summary of research gaps

It is common knowledge that prior to this study there was not so much documented scholarly information on the principles underpinning the performance of the ROC. The study's scope in Chapter 1 and methodology in Chapter 3 were framed in a way that they could contribute to improved understanding of both material transport and comminution. The main knowledge gap was broken into the following sub-gaps;

a) Breakage mechanisms in the ROC at various operating conditions (especially speed), was not fully understood for the current ROC prototype. Additionally, the failure process of particles nipped between the discs in the ROC was not fully understood. A combination of experimental and simulation results generated in the study contributed to improved understanding of the failure modes and mechanisms for a variety of operating conditions.

b) There was no substantial information about the effect of the operating variables (rotational speed, offset, directions of the rotation of the two discs and speed differentials between the speeds of the crusher discs) on ROC performance in terms of throughput and specific comminution energy. A combination of experimental and simulation results provided performance trends which can be used to optimize the crusher performance.

This study developed the methodology (in Chapter 3) which aimed at addressing the above research gaps and the results are discussed in Chapters 4 to 8.

CHAPTER 3: METHODOLOGY

3.1 Introduction

The study comprised laboratory experimental work and DEM simulations to generate the data which helped to understand the comminution and transportation mechanisms in the ROC. Silica and UG2-platinum bearing ore were used to conduct the test work. Sample preparation was done on the bulk sample with the top size of 75 mm in order to obtain sub-samples for mineralogical characterization, breakage characterization using comminution-scale tests (Bond crushability tests, Bond abrasion tests, drop weight tests and compression breakage tests) and crushing tests using the laboratory ROC and cone crusher. After calibration of the breakage model in the DEM simulation software using experimental data generated with the laboratory prototype, the ROC was simulated to derive data which provided deeper insights of the principles driving its performance. A more detailed discussion of the physical experiments and simulations is done in the subsequent sections.

3.2 Experimental procedures

3.2.1 Sample Preparation

Figure 3.1 presents the process followed to prepare the samples of silica and platinum group metals (PGMs) ore, classified as upper group (UG2), which were used to conduct various tests and analyses. For the Bond crushability work index (C_{Wi}) determination tests, 30 rocks (roughly cubical in shape – no slabs or slivers) in the size range of -75+50 mm were sampled from the feed materials as per standard procedures (Bond, 1947)). The same rocks were used to determine the specific gravity (SG) of the materials. For each material, the remaining sample after sub-sampling for the C_{Wi} test work were crushed to -19 mm using the jaw crusher, and thereafter representative subsamples for the Bond abrasion test, chemical analysis and mineralogical characterization were removed. The sample for the Bond abrasion test was screened over a 12 mm sieve to remove the fines because the standard procedures (Gupta and Yan, 2016) require the feed material in the -20+12 mm size range. The rest of size fractions of -19+13.2 mm, -13.2+9.5 mm, -9.5+6.7 mm and -6.7+4.75 mm were prepared for drop weight tests, compression tests and comminution experiments in the ROC and cone crusher as shown in Figure 3.1. The drop weight test, compression test and cone crusher only used the two mono-size feeds of -19+13.2 and -13.2+9.5 mm while the ROC used feeds of different size distribution to investigate the effect of operating variables. The effect of speed was investigated using the two mono-sized feeds used in the cone crusher for comparative purposes. The -19+13.2 mm and -6.7+4.75 mm was used to study the effect of the horizontal offset. The effect of feed size distribution was assessed using the feeds constituting the different proportions of the four size classes (-19+13.2, -13.2+9.5, -9.5+6.7 and -6.7+4.75 mm).

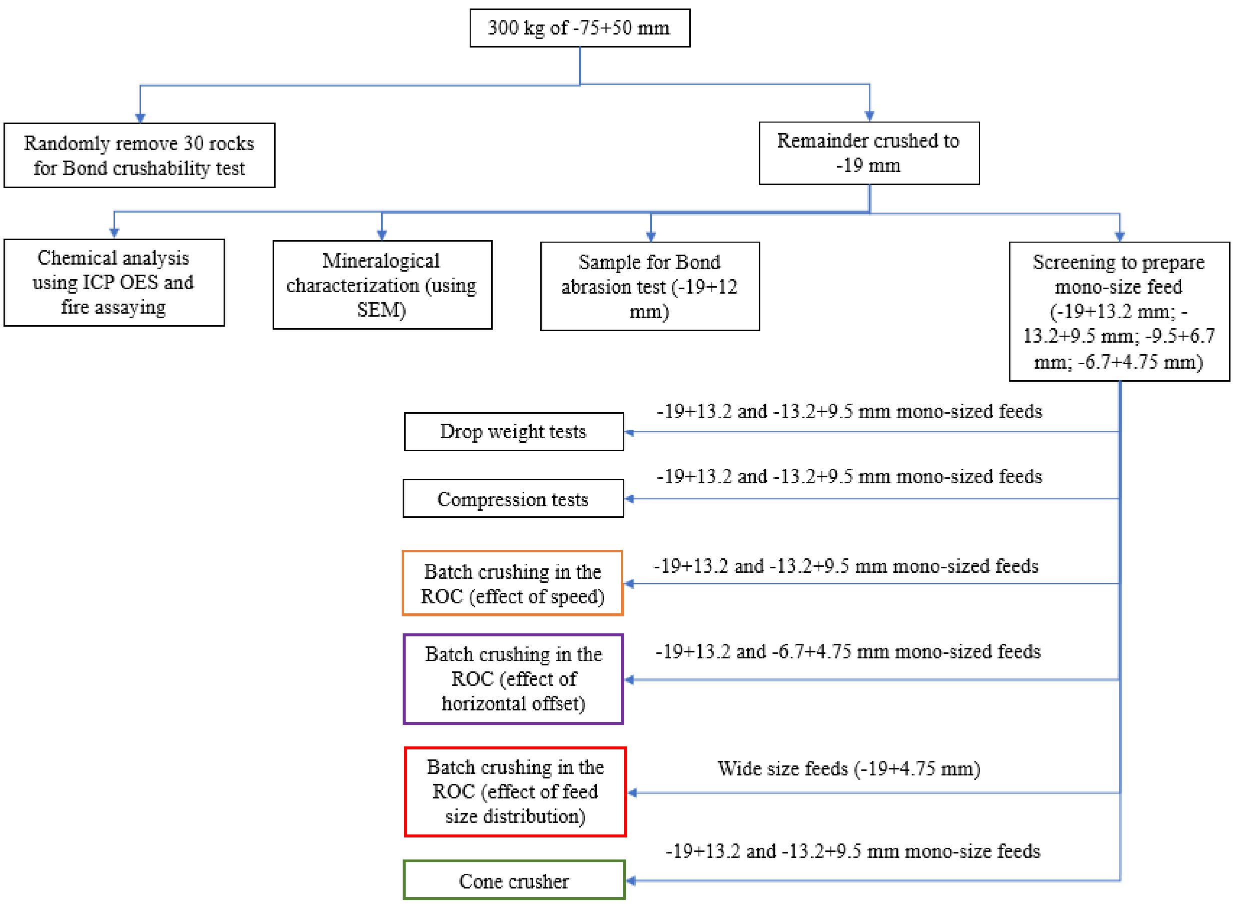

Figure 3. 1: Sample preparation of the silica and UG2 ore

3.2.2 Chemical and mineralogical characterization

From the bulk test samples, 1 kg sub-samples of −19 mm of UG2 ore were obtained using the rotary splitter. The sub-sample of the UG2 ore was pulverised to 90% passing 20 µm and chemically assayed for base metals and other metallic gangue elements using inductively coupled plasma optical emission spectroscopy (ICP OES) after the sample is dissolved.

The representative samples of silica and UG2 ore were also mineralogically characterized using a Carl Zeiss Evo MA15 scanning electron microscope (SEM) equipped with a Bruker energy dispersive X-ray analyser. A voltage of 20 kV wit abeam current of 3.3 nA was used. The detection limit of the SEM EDS is in the range of 0.1 – 0.5 wt%. The purpose of the SEM analyses was to identify the mineral phases in the two materials.

3.2.3 Breakage characterization of silica and UG2 ore

The capacity and power consumption of the crusher when it is in operation are significantly dependent on both the material characteristics (Gupta & Yan, 2016; King, 2001; Tavares, 2008) and operating parameters (e.g., setting). It is thus critical that the feed materials are well characterized in terms of their breakage behaviour because ore characteristics have a significant effect on equipment performance. For the conventional crushers (e.g., cone crusher), the breakage characterization tests provide the data which can be useful when selecting the crusher or predicting the performance of the crushers (e.g. using JKSimMet software). For the ROC, which is still being developed, the applicability of the existing models derived from those breakage tests will require further validation. The following sub-sections discuss various tests which were conducted to study the breakage characteristics of silica and UG2 ore.

3.2.3.1 Determination of crushability (impact) work indices

Bond's standard procedures for crushability measurement were followed using the impact pendulum to obtain the crushing work indices of the materials. The test consists of dropping two pendulum-mounted hammers simultaneously against the individual irregularly shaped −75+50 mm particles. From a starting angle of 10º, the angles used in positioning the hammers are raised 5º each time until fracture of the particle occurs (i.e., mass reduction of 33% (w/w)). For each material, the same procedures were repeated on 30 rocks to account for inherent variations in the strength of particles of the same material. One important parameter calculated is the impact energy per unit of thickness (denoted by C). This is calculated using the following equation which divides the impact energy with the thickness (d) of the individual particles (Bond, 1947).

$$C = \frac{117(1-\cos\phi)}{d} \qquad (3.1)$$

Where ϕ is the angle in radians, d is given in mm and C in J/mm.

The median of C, i.e. C_{50}, and particle solid density (ρ) are then used to calculate the crushing work index using the following Bond equation.

$$C_{Wi} = \frac{53.49C_{50}}{\rho} \qquad (3.2)$$

Where C_{Wi} is given in kWh/t.

The experimentally determined C_{Wi} is used to estimate the net power required to cause the required size reduction in the conventional crushers.

3.2.3.2 Measuring the abrasiveness of the materials

In the ROC, the particle (s) sliding in the crushing zone is in direct contact with crushing surfaces (discs) and neighbouring particles. It is thus expected that a significant proportion of fines in the product will be generated as the results of these contacts. Wear of the crushing surfaces will be encountered, with its extent dependent on the abrasiveness of the process material. The abrasion index (*Ai*) is used as a measure of the relative abrasiveness of different rock materials (e.g., silica and UG2 ore) which is being processed in comminution machine. Hence, it is used to calculate the wear rates in crushers and the ball consumption rate in the ball mills (Gupta & Yan, 2016). The abrasiveness of silica and UG2 ore were measured using the standard Bond abrasion mill following the standard procedures discussed elsewhere (Gupta and Yan, 2016). The paddle was also weighed and the loss in mass (in grams) of the paddle, same as *Ai*, was calculated using Eq. (3.3). For each material, the test was done in triplicate and the average was taken as the abrasive index.

$$\mathrm{Ai} = \mathrm{M_i} - \mathrm{M_f} \qquad (3.3)$$

Where *Ai* is the Bond abrasion index (in grams), M_i is the initial steel plate mass and M_f is the final steel plate mass.

Since the crushing surfaces of the ROC are not yet lined with hardened steel or any other appropriate hard alloy, the results of the Bond abrasion test cannot be directly related to the experimental crushing data. A comprehensive study on the wear of the ROC crushing surfaces lined with the suitable liners should be undertaken in future because the implementation of the ROC will depend not only on the performance potential in terms of capacity, energy consumption and size reduction, but also on the maintenance costs due to replacing of liners.

3.2.3.3 Single-particle impact breakage tests using the drop weight tester

Single-particle breakage tests gained popularity, not only because of the minimum sample preparation which is required, but most importantly due to the fact that the loading conditions closely resemble those present in several industrial crushers where the rock particles are mainly stressed and crushed individually (Tavares, 2008). Silica and UG2 ore particles were individually subjected to the impact loads using the simple drop-weight testing (DWT) apparatus which is discussed elsewhere (Bwalya & Chimwani, 2020). The main objective was to assess the amenability of the two size fractions to impact crushing. It is noted that standard procedures and equipment as recommended by JKTech was not used in this study and therefore the obtained results should not be assumed to represent the standard impact parameters which are obtained using the JKTech Drop weight tester.

For each experiment (i.e. energy level), 20 particles were used to account for the inherent variation in terms of product size distributions of various particles for the same material with the same impact energy. The standard deviation of the mass of individual particles has been maintained to ±0.01 g. The single particles were individually impacted once at five input energies (0.25, 2.22, 4.43, 6.16 and 8.13 J). For each input energy, the progeny particles from the 20 impacted particles were combined and dry screened using the sieves which were stacked in a root two series. Genç et al. (2004) used the same methodology to study the breakage characteristics of various materials including quartz and some ores. The solid cylindrical weight made of mild steel weighing 2.5 kg was dropped from a predetermined height to impact the particle placed on the anvil. Table 3.3 lists the impact energies used which are basically the potential energies of the drop weight just before it is released to allow it to accelerate and impact the particle. The specific input energies corresponding to the five energies are also listed in Table 3.1. The specific input energy was calculated using the following equation.

$$E_{cs} = \frac{Mgh}{3.6 \times \dot{m}_p} \quad (3.4)$$

Where E_{cs} is the specific input energy (in kWh/t), M is the mass of the drop weight (in kg), g is the acceleration due to gravity (m/s^2), h is the net drop height (in m), $\dot{m}_p$ is the mean mass of particles (in grams) and 3.6 is a conversion factor of specific energy from J/g to kWh/t.

Table 3. 1: Specific energies of drop weight tests

Impact energy (J)	E_{cs} **(kWh/t)**			
	Silica		UG2 ore	
	-19+13.2 mm	-13.2+9.5 mm	-19+13.2 mm	-13.2+9.5 mm
0.246	0.011	0.028	0.007	0.012
2.216	0.103	0.253	0.066	0.112
4.432	0.205	0.505	0.132	0.224
6.156	0.285	0.702	0.183	0.311
8.126	0.377	0.926	0.242	0.411

The dimensions (in terms of length, width and thickness – see illustration in Figure 3.2) of the progeny particles which are coarser than 2 mm (based on the sieve diameter) were measured using the digital Vernier calliper to develop the shape characteristics of the progeny particles.

Figure 3. 2: Measurement of length, width and thickness of -9.5+6.7 mm UG2 particle

3.2.3.4 Investigating compression breakage characteristics

The mono-sized particles (−19+13.2 and −13.2+9.5 mm) of silica and UG2 ore were used to investigate the compression breakage behaviour for various maximum loads ranging between 20 and 160 kN as listed in Table 3.2. Amsler compressive strength testing machine shown in Figure 3.3 was used to hydraulically apply the load to the 40 mm bed of particles in the 50 mm diameter cylinder through the bottom plate which is driven at a constant loading rate. A requirement for the piston-die breakage tests is to ensure homogeneity throughout the bed by avoiding the unfilled spaces between particles (Leon et al., 2020). The piston chamber was shaken prior to loading to ensure a good reorganization of the particles. The dial gauge was installed to measure the final particle bed heights. The specific input energy was estimated from the maximum load and maximum displacement (post compaction and compression) using the following equation. The values of mass of the bed of particles, total displacement targeting various maximum loads and specific input energies (estimated using Eq. (3.5)) are also listed in Table 3.2. As for the DWT, the dimensions of the coarser progeny particles were also measured. The tests were for the 160 kN load were done in duplicate.

$$E_{cs} = \frac{1}{2} x \frac{F_{max} \times \Delta H}{3.6 \times m_{bed}} \qquad (3.5)$$

Where E_{cs} is the specific input energy (in kWh/t), F_{max} is the maximum force (in N), ΔH is the displacement (in m), m_{bed} is the mean mass of particles (in g) and 3.6 is a conversion factor of specific energy from J/g to kWh/t.

Table 3. 2: Specific energies for compression breakage characterization tests

Maximum load (kN)	***E_{cs}* (kWh/t)**			
	Silica		UG2 ore	
	-19+13.2 mm	-13.2+9.5 mm	-19+13.2 mm	-13.2+9.5 mm
20	0.17	0.31	0.05	0.30
40	0.51	0.71	0.19	0.66
80	1.64	1.61	0.74	1.63
120	2.80	2.37	1.65	1.81
160	3.76	4.08	2.86	3.04

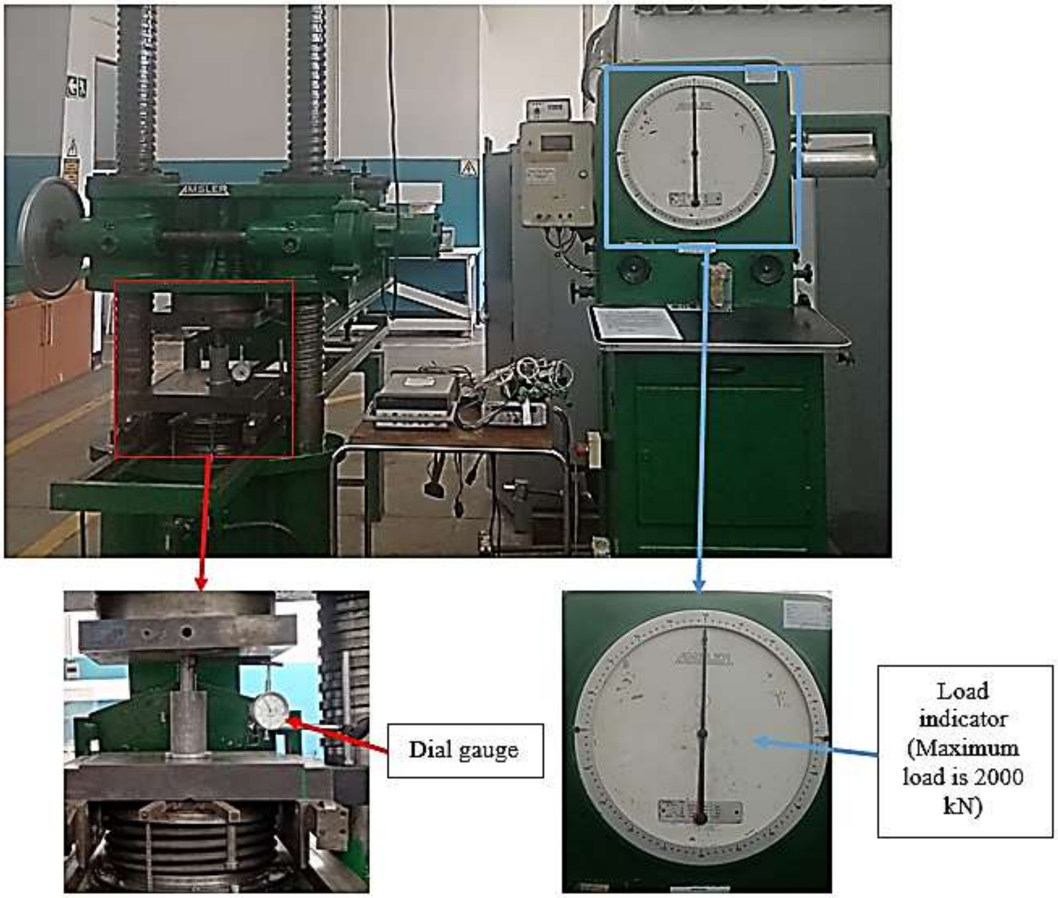

Figure 3. 3: Experimental set-up for compression breakage

3.2.4 Crushing test work with the Rotary Offset Crusher

The crushing tests were conducted using the laboratory ROC (in Figure 3.4) whose design and operating characteristics are listed in Table 3.3. The machine is located in Professor Peter King (Minerals Processing) laboratory in the School of Chemical and Metallurgical Engineering at University of the Witwatersrand. The crusher is powered using a 3 kW three-phase induction motor. This motor has a full-load speed of 1420 rpm. The variable speed drive (VSD) was installed to allow the adjustment of the speed of the bottom disc. A photograph showing the installed VSD is shown in Figure 3.5. The mechanical tachometer type 2200 (Nghipulile, 2019) was used to measure the rotational speed of the bottom disc for a variety of frequencies to allow the generation of the calibration curve in Figure 3.6.

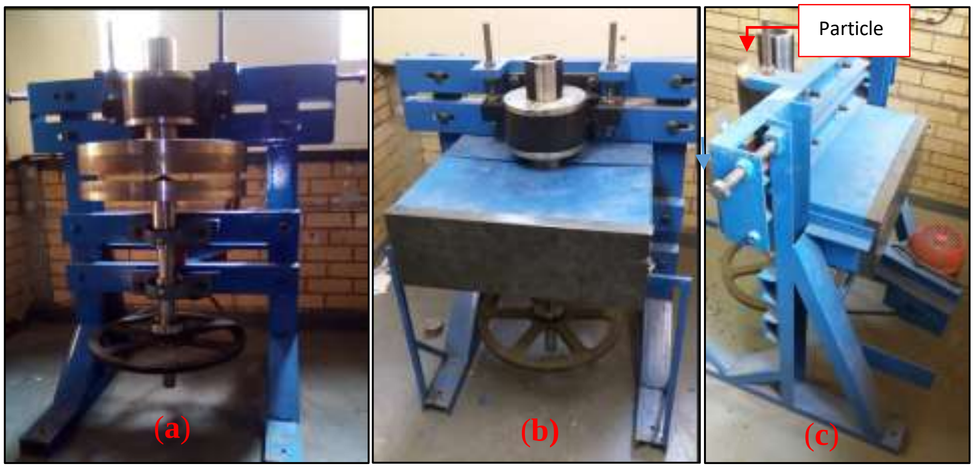

*Figure 3. 4: Laboratory prototype of the rotary offset crusher, (**a**) illustration of the discs (during operation to disc horizontally shifted to the right to provide the offset), (**b**) Front-end of the crusher fitted with the sample collection box, (**c**) Back-end of the crusher fitted with the sample collection box.*

Table 3. 3: Design and operating parameters of ROC

Parameter	Unit	Value
Diameter of top disc	mm	500
Diameter of bottom disc	mm	500
Total footprint (L x W)	m	1.1 x 1.1
Motor power	kW	3
Motor full-load speed	rpm	1420
Speed drive type	-	Variable speed drive

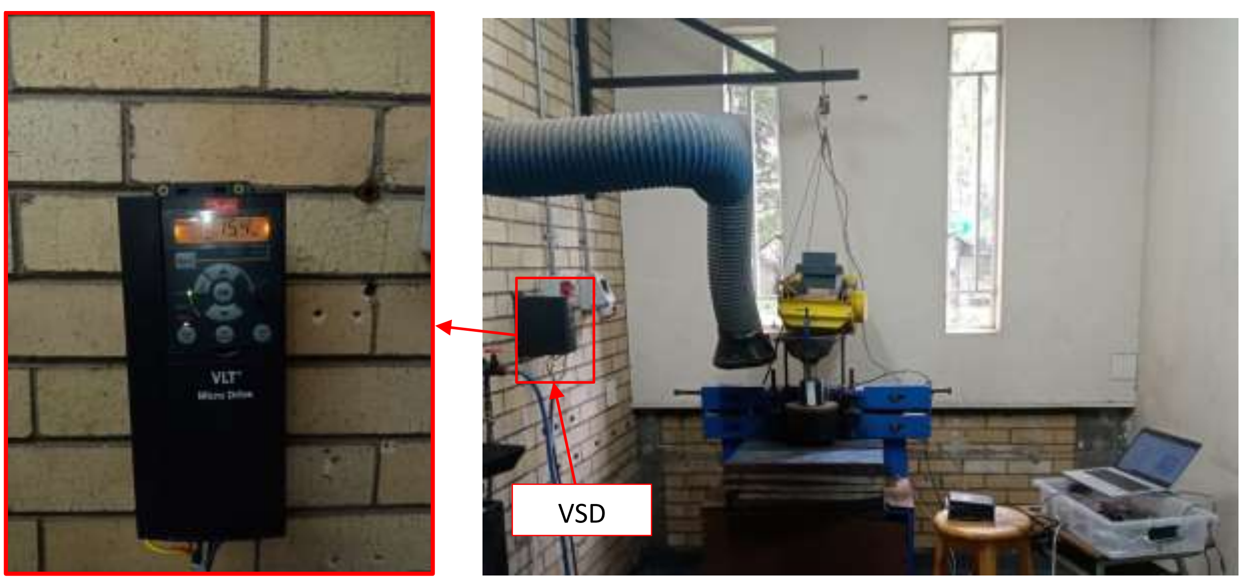

Figure 3. 5: Installed variable speed drive with a potentiometer to allow the adjustment of the frequency

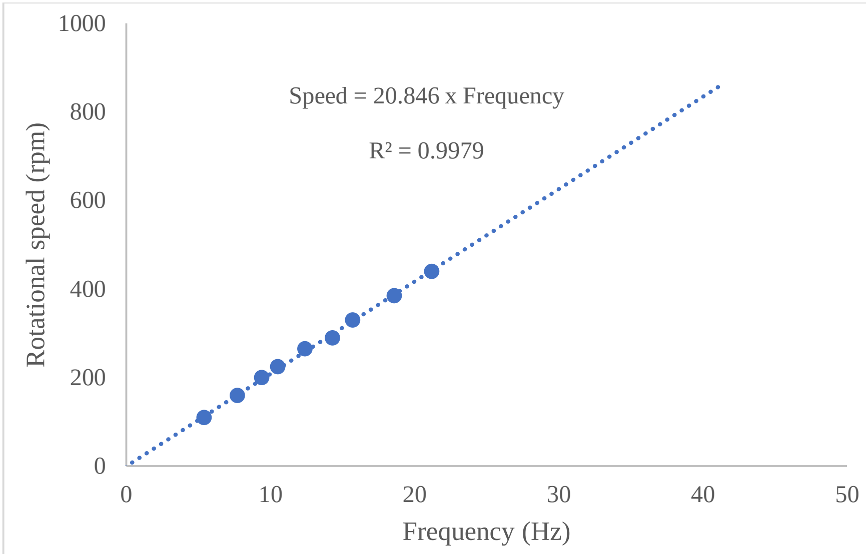

Figure 3. 6: Speed calibration curve

Various crushing tests that were conducted to investigate the effect of rotational speed, offset, vertical exit gap and feed size distribution are discussed below.

3.2.4.1 Effect of rotational speed

To investigate the fracture of single particles in the ROC, the following experiments were designed whereby the crusher was fed with individual silica and UG2 particles. This was done for −19+13.2 mm and −13.2+9.5 mm particles of both silica and UG2 ore. Two speeds (550 and 1000 rpm) of the 500-mm-diameter cylindrical discs were tested. The variable speed drive allows the speed adjustments. The vertical exit gap and horizontal offset were fixed at 4 and 10 mm, respectively. To account for inherent variation among individual particles of the same material and generate enough samples for particle size analysis, each test was repeated ten times. The standard deviation of the mass for the ten particles individually fed to the crusher was maintained at ±0.01 g as a way of using the particles with comparable densities that can infer comparable mineralogical composition (especially in the case of a multi-component UG2 ore). The experimental results for single particle breakage were used to calibrate the Ab-t_{10} breakage model in the DEM simulator.

The 2 kg mono-sized feeds (−19+13.2 mm and −13.2+9.5 mm) of silica and UG2 ore were crushed at 330, 550, 830 and 1000 rpm speeds while the horizontal offset and vertical exit gap were fixed at 10 and 4 mm respectively. The feed rate was approximately 1 tph.

The crusher products were dry screened using the screens arranged in the root two series, ranging between feed screen size and 38 µm. The dimensions (in terms of length, width and thickness) of the progeny particles which are coarser than 3.35 mm (based on the sieve diameter) were also measured using the digital Vernier calliper to develop the shape characteristics.

3.2.4.2 Effect of horizontal offset

The −19+13.2 and −6.7+4.75 mm silica particles were used to study the effect of horizontal offset (0, 10, 16 and 23 mm) while the rotational speed and vertical exit gaps were fixed at 830 rpm and 1.5 mm respectively. The 23 mm offset is the maximum offset that can be achieved with the current laboratory prototype as shown in Figure 3.7.

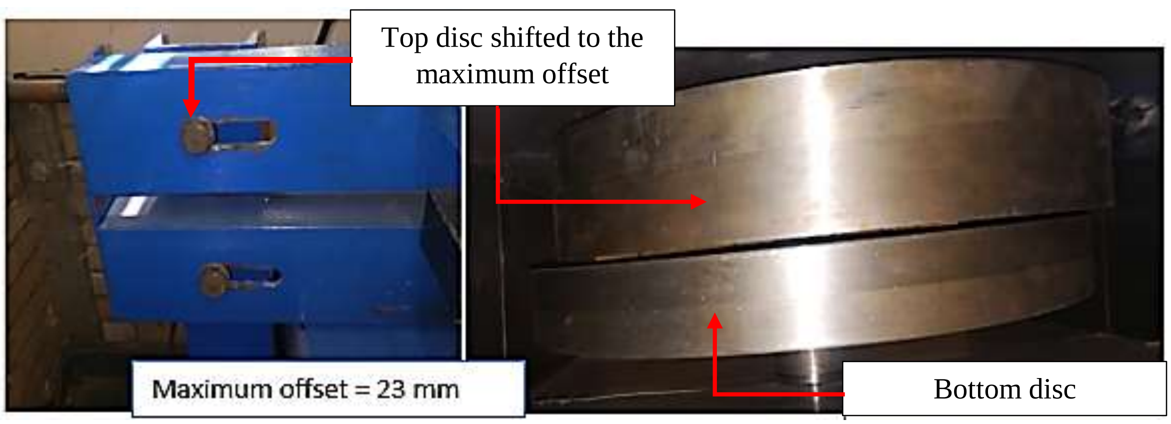

Figure 3. 7: Illustration of the maximum offset of 23 mm achievable for the current laboratory ROC

3.2.4.3 Crusher feeds with wide size distributions

Two feed samples were made up using the silica particles in these size ranges: −19+13.2 mm, −13.2+9.5 mm, −9.5+6.7 mm, −6.7+4.75 mm. The tests were conducted with the ROC operating at the speed of 830 rpm while the feed rate and exit gap were fixed at 1 tph and 3 mm respectively. The feed size distributions of the two tests, which were done in duplicate, are shown in Table 3.4. The first feed sample has the same proportions (by mass) of the four size classes while the second feed sample constitutes 33 % of the −19+9.5 mm, with the rest being −9.5+4.75 mm particles.

Table 3. 4: Mass distributions (by size) for the ROC feed samples with wide size distributions

Screen size (µm)	**Feed sample 1**		**Feed sample 2**	
	Mass fraction (%)	Cumulative mass passing (%)	Mass fraction (%)	Cumulative mass passing (%)
13200	26.8	73.2	16.3	83.7
9500	25.1	48.1	16.7	66.9
6700	26.0	22.1	34.9	32.1
4750	22.1	0.0	32.1	0.0
Total	100.0		100.0	

3.2.5 Crushing test work with the cone crusher

The WESCONE W300 cone crusher at Mintek was used to crush the same mono-size feeds of silica and UG2 ore and have products with PSD comparable to those of ROC by carefully adjusting the close side setting (CSS). The design and operating characteristics are listed in Table 3.5.

Table 3. 5: Design and operating parameters of cone crusher

Parameter	**Unit**	**Value**
Motor power	kW	9.2
Minimum design CSS	mm	2
Operating CSS	mm	4

The crusher products for the -19+13.2 mm feeds with comparable PSDs for the -19+13.2 mm crushed in the ROC were classified as -1 mm and +1 mm for mineralogical characterization using the Carl Zeiss Evo MA15 scanning electron microscope (SEM) equipped with a Bruker energy dispersive X-ray analyser (Bruker AXS GmbH, Karlsruhe, Germany). The purpose of SEM analyses was (1) to identify phases in the sample using energy dispersive spectrometry (EDS) and (2) capture the backscattered electron (BSE) images, which were processed using Stream Essentials® software version 1.5.1 to estimate the particle morphology in terms of sphericity and aspect ratio.

3.3 DEM simulations

Discrete element method simulations of UG2 ore particle breakage were carried out using commercial Rocky DEM® software version 2023 R2. The breakage of silica was not simulation. The geometries of the various components of the ROC (lower disc, upper disc, and hopper) were imported into the DEM software using the widely exchangeable STereoLithographic (STL) format. Polyhedron particles were generated using the particle generator within the DEM software. Figure 3.8a illustrates the shape of real particles. It is evident from Figure 3.8a that the UG2 ore particles are non-spherical. Figure 3.8b shows the simulated polyhedral particles. The particle shape was not calibrated. The use of non-spherical particle to study breakage makes it possible to have realistic granular behaviour with DEM simulations (André & Tavares, 2020; Eliáš, 2014; Govender et al., 2018; Moncada et al., 2022; Tavares et al., 2020). The hysteretic linear spring-dashpot model was used to model normal contact force while the linear spring Coulomb limit law was chosen to model the tangential contact force. Mathematical description of the models is included in Appendix A. The hysteretic linear spring-dashpot model is a normal elastoplastic contact model which accounts for plastic deformation behaviour during loading and unloading. The two models are discussed in details elsewhere (Tavares et al., 2020) where they were used to simulate the breakage behaviour of polyhedral particles and the results were satisfactory.

(**a**) Real particle for UG2 ore

(**b**) Simulated polyhedral particles (with equivalent diameter of 15.8 mm)

*Figure 3. 8: UG2 ore particles **(a)** and polyhedral particles generated in the simulator (**b**)*

The specific gravity of the UG2 ore was measured on 30 individual rocks using the Archimedes method in Eq. (3.6). The average particle *SG* was determined as 3.32. The bulk density was measured by filling a known volume with material and simply finding the weight of the material.

The measurements were repeated ten times using the −19+13.2 mm particles and the average bulk density was found to be 1753 kg/m^3. The average porosity, estimated using Eq. (3.7), was found to be 48% (v/v).

$$\mathrm{SG} = \frac{\mathrm{W_a}}{\mathrm{W_a} - \mathrm{W_w}} \tag{3.6}$$

Where W_a and W_w is the mass of the rock specimen in air and mass of rock specimen in water.

$$\text{Porosity} = \left(1 - \left(\frac{\text{Bulk density}}{\text{Particle density}}\right)\right) \times 1000 \tag{3.7}$$

3.3.1 Calibration

The calibrated parameters are given in Table 3.6. Except for the material density, particle density and breakage model parameters, it is acknowledged that the other material properties (Young Modulus and Poisson ratio) as well as the contact parameters such as friction coefficients were not experimentally determined. The default parameters in the DEM software were used. It is recommended that future studies on DEM simulation of the device should improve on this limitation. However, it is the candidate's view that the indicative results are adequate to provide general performance trends of the device which was the main objective of the study.

The parameters for the Ab-t_{10} breakage model were calibrated through the particle fracture response data in terms of fragment distribution, which were generated using the single particle experiments conducted with the laboratory ROC. The breakage function in the DEM software was changed to ensure the simulated size distribution is similar to the experimental size distribution in terms of P_{80} sizes. The breakage function that yielded similar $\mathrm{P_{80}}$ sizes was adopted in all simulations. The selection function coefficient of 0.002 kg/J compares to what was calibrated for the copper ore when the same breakage model was also used (Jiménez-Herrera et al., 2018). The minimum fragment size in the DEM was set at 300 µm to cut down on the computational cost.

Table 3. 6: DEM input parameters (P⁻P is ore particle and ore particle interaction and P⁻B is ore particle and boundary interaction)

Parameter	Unit	Description/Value
Material (ore and boundary) properties		
Material	-	UG2 platinum-bearing ore
Ore SG	-	3.32
Mean feed size	mm	15.8
Breakage model	-	$Ab - t_{10}$ model
Selection function coefficient	kg/J	0.002
Minimum size of fragments	mm	0.3
Poisson ratio	-	0.3
Young modulus of ore	N/m^2	1×10^8
Young modulus for boundary	N/m^2	1×10^{11}
Density of boundary	kg/m^3	7850
Contact parameters		
Static and dynamic friction (P⁻B)	-	0.3
Static and dynamic friction (P⁻P)	-	0.7
Coefficient of restitution (P⁻B)	-	0.3
Coefficient of restitution (P⁻P)	-	0.3

Table 3.7 summarizes the percent errors between experimental and simulated P_{80} sizes and throughputs. Figure 3.9 shows the experimental and simulated PSDs. The simulated product size distribution is truncated due to the restricted minimum particle size. Lichter et al. (2009) made the same observation for the cone crusher simulation. There is a slight overestimation of the fineness of the progeny size distribution. The errors between experimental and simulated P_{80} sizes were less than 10%. The errors between average experimental and simulated throughputs were 3% and 10.3% for 550 and 1000 rpm respectively. The analysis and interpretation of the simulation results were done cognizant of the discrepancies in Table 3.6.

Table 3. 7: Experimental and simulated P_{80} sizes and throughputs

Speed (rpm)	**P_{80}**			**Q (kg/h)**		
	Experimental (mm)	Simulated (mm)	Error (%)	Experimental (mm)	Simulated (mm)	Error (%)
550	2.14	1.99	6.71	35.3	36.4	3.0
1000	2.09	1.92	7.85	39.5	43.6	10.3

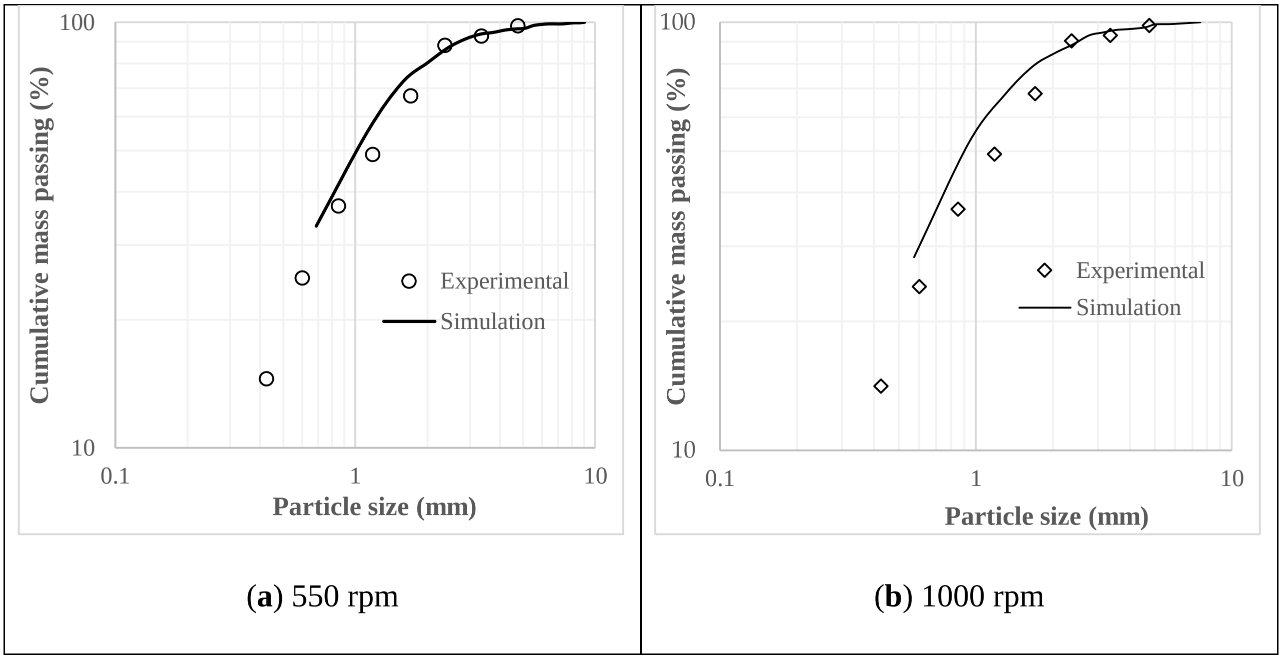

Figure 3. 9: Experimental and simulated product size distribution for single UG2 ore and polyhedral particles at 550 and 1000 rpm

3.3.4 Simulating material breakage and transport

After the calibration of the DEM parameters was completed, the following simulations were conducted to study particle breakage and transport in the ROC.

3.3.4.1 Single particle breakage

Simulations of single particle breakage were performed for a variety of speeds (550, 1000, 1450, 1900 and 2350 rpm) while the offset and vertical exit gap were fixed at 10 and 4 mm respectively. This was done for two following scenarios; (1) stationary top disc (this closely represents the experimental setup with the top disc not rotating when a single particle is fed to the crusher), and (2) both discs rotating at the same speed, i.e., the top disc was not friction driven as it was the case with the laboratory prototype.

3.3.4.2 Simulation breakage and transportation of many particles

A variety of simulations of breakage and transport of many particles were performed for the following operating conditions in order to investigate the effect of the horizontal offset, operating speed, speed differential, feed rate, feed size distribution on the crusher performance in terms of size distribution, power draw and throughput.

- Effect of offset (0, 10, 20 and 30 mm) was investigated with mono-size feeds (particle diameter of 15.8 mm) while fixing the feed rate, rotational speed and vertical exit gap at 1 tph, 1000 rpm and 4 mm respectively. Both discs were rotated at the same speed, i.e., the top disc was not friction driven as it was the case with the laboratory prototype.
- Effect of rotational speed (330, 550, 1000, 1450, 1900, and 2350 rpm) was investigated with mono-size feeds (particle diameter of 15.8 mm) while fixing the feed rate, offset and vertical exit gap at 1 tph, 10 mm and 4 mm respectively. Both discs were rotated at the same speed, i.e., the top disc was not friction driven as it was the case with the laboratory prototype.
- Effect of speed differential (in the range of 0 and 20%, top disc slower than the bottom disc which was rotated at the speed of 330 rpm) was investigated while fixing the feed rate, offset and vertical exit gap at 1 tph, 10 mm and 4 mm respectively.
- Effect of co-current and counter-current rotation was studied considering 330, 1000 and 2350 rpm speeds. Both discs were rotated at the same speed, i.e., the top disc was not friction driven as it was the case with the laboratory prototype.
- Effect of rotational speed (330, 1000 mm and 2350 rpm) was also investigated with a feed with a mono-sized feed (particle diameter of 15.8 mm) with an increased feed rate of 10 tph while the offset and exit gap were fixed at 10 mm and 4 mm respectively. Both discs were rotated at the same speed, i.e., the top disc was not friction driven as it was the case with the laboratory prototype.
- Effect of rotational speed (330, 1000 mm and 2350 rpm) was also investigated with a feed with wide size distribution (-19+4.75 mm) shown in Table 3.8 while fixing the feed rate, offset and exit gap at 10 tph, 10 mm and 4 mm respectively. Both discs were rotated at the same speed, i.e., the top disc was not friction driven as it was the case with the laboratory prototype.

Table 3. 8: Feed size distributions simulated for a feed rate of 10 tph

Screen size (mm)	Mass fractions (%)
19.0	0
13.2	26.8
9.5	25.1
6.7	26.1
4.75	22.1
Total	**100.0**

3.4 Summary of the methodology

The methodology was developed to contribute to improved understanding of the comminution processes in the ROC. The chemical composition and mineralogical characteristics of the materials (silica and UG2 ore) were determined. Secondly, the materials were characterized using the standard bench-scale comminution tests including the Bond crushability test (to get crushability indices) and Bond abrasion test (to get the abrasion indices). Thirdly, the breakage characterization tests were conducted using the DWT and piston-die tester for impact and compression breakage respectively. Crushing experiments with the laboratory ROC and cone crusher were also conducted. Finally, the ROC was simulated using the DEM software to derive data which provided deeper insights of the principles underpinning its performance. Experimental data and simulations outputs are discussed in Chapters 4 to 8 to make inferences on the processes which are facilitating the breakage and flow of particles in the crusher.

CHAPTER 4: MINERALOGICAL AND BREAKAGE CHARACTERISTICS OF SILICA AND UG2 PLATINUM ORE

4.1 Introduction

In this chapter, the characteristics of materials which were used for crushing test work using the ROC and cone crusher are discussed. Chemical composition and mineralogical characteristics are presented before discussing the breakage characteristics - crushability index, abrasion index, and impact breakage and compression fracture responses.

4.2 Chemical and mineralogical characterization

The silica sand (single component material) that was used in the test work has a purity of >99% SiO_2 (XRF assay) while the chemical composition of the UG2 ore (a multi-component material) is given in Table 4.1.

Table 4. 1: Chemical composition of the UG2 ore

Element	Al	Ca	Co	Cr	Cu	Fe	Mg	Mn	Ni	Pb	Si	Ti	V	Zn	Au	Pd	Pt	As
Concentration	6.05	2.27	<0.05	9.6	<0.05	11.2	9.67	0.15	0.095	<0.05	16.3	0.3	<0.05	<0.05	0.03	0.91	1.28	<0.01
Unit	%														ppm			

Silica feed sample (-13.2+9.5 mm) was also mineralogically examined using the SEM, the BSE images are shown in Figure 4.1. The sample predominantly consists of quartz. It can be observed that the sample was coarse grained and had a granoblastic interlobate texture. Contacts between most of quartz grains are sutured and well interlocked, indicating intense pressure dissolution (Javed et al., 2023). Natural micro-cracks (some indicated by the red line on the micrographs), which are formed under pressure and temperature during geological events, were also apparent throughout the sample. The interlocking crystalline texture should contribute to its strength. However, natural micro-cracks may contribute to its weakening, and largely control its overall stress response (Askaripour et al., 2022).

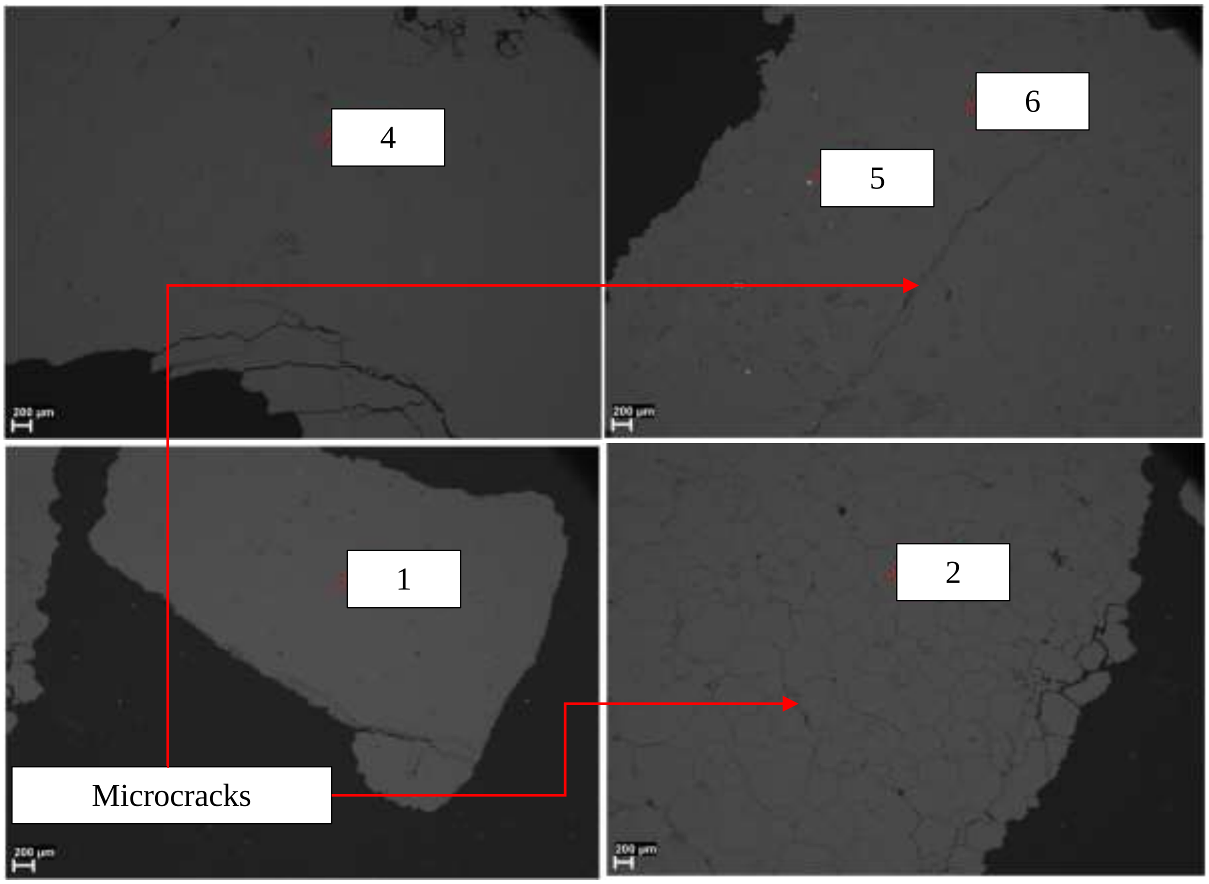

Figure 4. 1: BSE SEM micrographs of the feed; identified phases: quartz (1, 2, 3, 4, and 6) and zircon (5)

The BSE images for the feed sample of UG2 (-19 mm) are shown in Figure 4.2. Mineral phases were identified based on the SEM EDS chemical composition. It was observed that the sample predominantly consists of chromite, pyroxene, and plagioclase. The sulphide mineralization includes chalcopyrite and pentlandite. Iron sulphide minerals including pyrite and pyrrhotite were also reported for same ore (Nghipulile et al., 2023). Chromite occurs as rounded grains, both liberated and within the silicate phases.

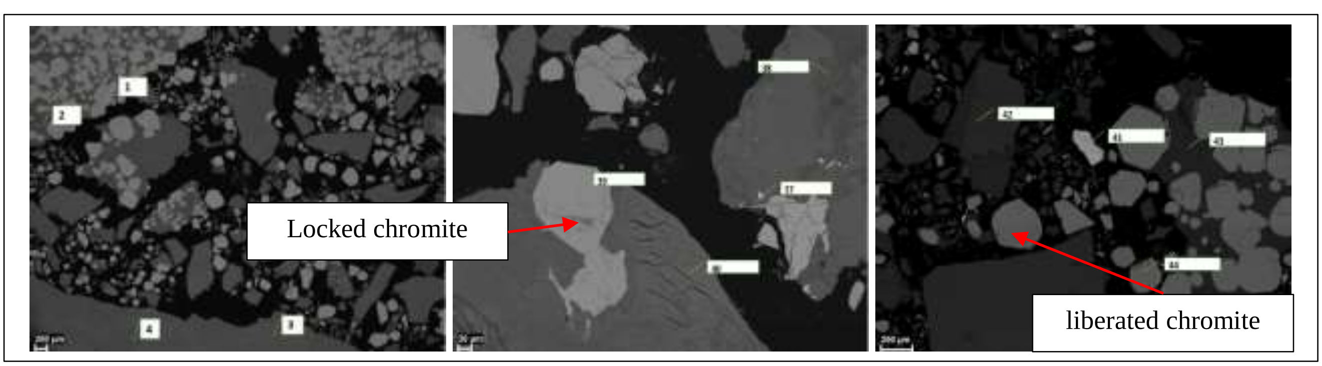

Figure 4. 2: BSE SEM micrographs of the feed; identified phases: chromite (1, 39 and 44), plagioclase (2, 4, 38 and 43), pyroxene (3, 40 and 42), pentlandite (37) and chalcopyrite (41)

4.3 Crushability and abrasiveness

The raw data from the Bond crushability tests are listed in Tables C1 to C4 in Appendix C. The C_{Wi} and *Ai* values for silica and UG2 ore are listed in Table 4.2. Comparable size distributions of silica and UG2 ore fragments produced during the crushability tests are shown in Figure 4.3. Based on the classification of crushability indices in Table 4.3, both materials have a 'soft' crushability index, with silica being slightly harder than the UG2 ore. The slight difference in the crushability indices can be attributed to the distinct mineralogical characteristics of the two materials. Silica sample has interlocking crystalline structure amongst quartz grains and can thus be expected to have a higher strength. Results from the drop weight and compression tests (discussed later in this Chapter) as well as the ROC and cone crusher tests (discussed in Chapters 5 and 6) were used to compare the comminution behaviour of the two materials.

Table 4. 2: CWi values for silica and UG2 ore

Material	**Solid density (kg/m^3)**	**C_{Wi} (kWh/t)**	***Ai***
Silica	2.67	13.8	0.45
UG2 ore	3.37	10.4	0.12

Table 4. 3: Classification of crushability (Napier-Munn et al., 2005)

C_{Wi} (kWh/t)	**Description of crushability**
<10	Very soft
10 – 14	Soft
14 – 18	Medium
18 – 22	Hard
22 – 26	Very hard
>26	Extremely hard

A higher *Ai* value obtained for silica confirms its relatively high abrasiveness, i.e. high wear rate of the ROC can be expected when processing silica. Silica is highly abrasive, e.g., it was reported that it can potentially wear the material of construction 100 times faster than limestone

(Bhattacharyya & Bock, 1978). Since the crushing surfaces of the ROC are not yet lined with hardened steel or any other appropriate hard alloy as it is the case for the jaw and cone crushers, the results of the Bond abrasion test could not be related to the experimental crushing data in this thesis. It is recommended that a comprehensive study on the wear of the ROC crushing surfaces, with the removable liners, be undertaken in the future when the crusher is operated for extended duration (e.g. several hours).

4.4 Breakage probabilities as a function of input energy

The product size distributions for the impact and compression breakage characterization tests are listed in Appendix D. The breakage probabilities (*BPs*) are shown in Figures 4.3 and 4.4 for the impact and compression breakage respectively. The *BP* represents the proportion passing the original narrow size range (Campos et al., 2020). It can be observed that the breakage probabilities increase at low specific energies until the maximum specific input energy is reached. Beyond that maximum point, the BPs become nearly constant with increasing energy. This was also observed with iron concentrate by Campos et al. (2020). A constant *BP* does not suggest that no damage or fragmentation has occurred to the particles. There was size reduction happening to the progeny particles in size classes below the parent size class as shown in progressive shift of cumulative distributions shown in Figures D1 to D4 in Appendix D. Assuming the size distribution does not change, the increase in the input energy still causes the internal damage to the particles (L. M. Tavares, 2005).

From Figure 4.3, it can be observed that the -19+13.2 mm UG2 ore is very weak in strength (particles simply shatter) when subjected to impact loading because the probability of breakage was about 95% even for the lowest specific input energy. The comparable BP for this size class for different energies does not imply comparable product size distributions. As can be observed in Figure D1 in Appendix D, the product size distribution increases with the input energy for the -19+13.2 mm of UG2 ore. A contrary trend was observed when the same material was compressed using the piston-die apparatus (see Figure 4.3). It is evident from Figure 4.3 that the *BPs* are comparable for the same size range and seem to be independent of the material type. This suggests that silica and UG2 ore have similar breakage response when they are compressed in bed (e.g., in HPGR). Comparable breakage response has also been observed in Chapter 6 when they were crushed using the ROC, which basically confirmed that compression breakage (rather than impact breakage) entailing slow application of stress facilitates breakage, together with shear action, in the ROC.

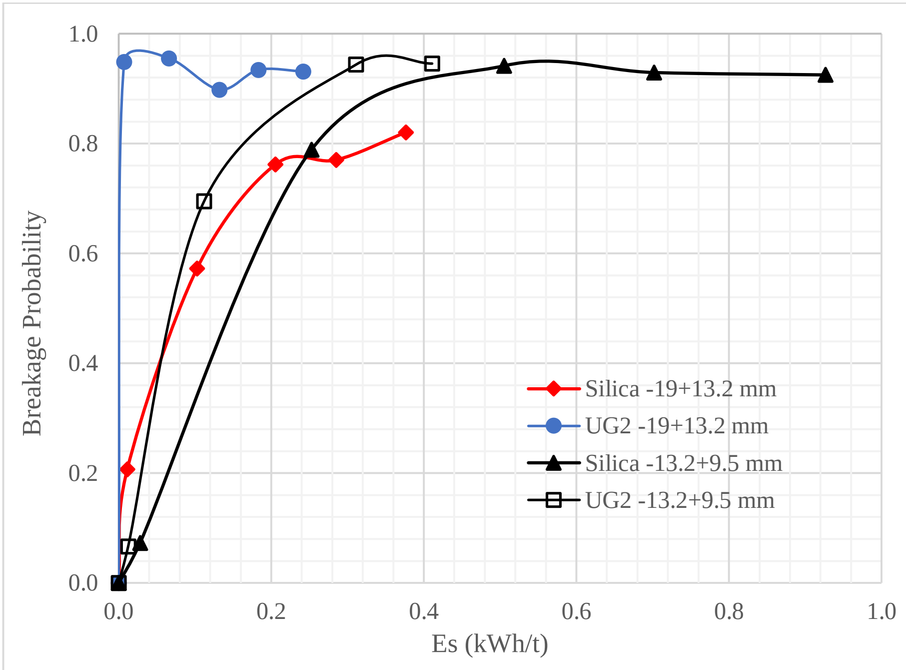

Figure 4. 3: Breakage probabilities for impact breakage tests

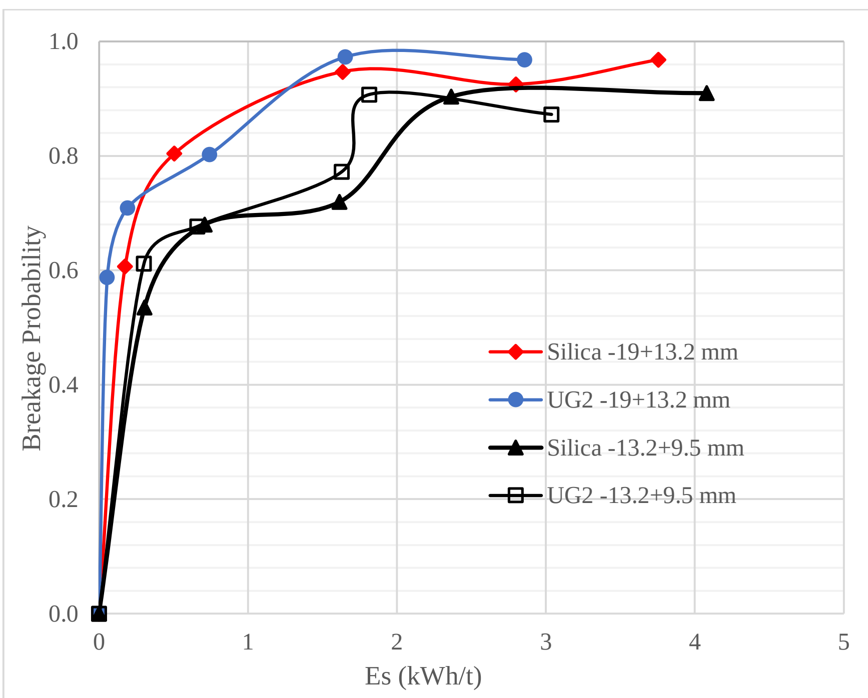

Figure 4. 4: Breakage probabilities for compression breakage tests

4.5 Relationships between input energy and product size reduction

4.5.1 t_{10} - E_{cs} relationship

The product size distributions generated from both impact and compression breakage tests were fitted to the t_{10} breakage model (Eq. 2.1) to allow the determination of parameters A and b using the iteration method with the objective of minimizing the residual error between the experimental and model t_{10} values. The *solver* function in Microsoft Excel® was used with a constraint of $A \leq 100$. A fair degree of fitness of the experimental and model t_{10} can be observed in Figure 4.5 while the values of A and b as well as their product ($A \times b$) are listed in Table 4.4. Resistance to impact and compression loadings of the size fractions are indicated in Table 4.4 based on the standard classification in Table 2.1. The $A \times b$ values listed in Table 4.4 should not be assumed to be for the materials used, but rather just for the size fractions tested. To obtain the $A \times b$ for silica and UG2 ore, the standard procedures using the JK drop weight tester with a variety of size fractions and energy inputs (Napier-Munn et al., 2005) are recommended.

Table 4. 4: Summary of DWT and compression results

Type of test	Material	Size class (mm)	A	b	A x b	R^2 value (%)	Classification
DWT	Silica	-19+13.2	43.98	3.56	156.63	87	Very soft
	UG2 ore		50.65	3.62	183.20	98	Very soft
	Silica	-13.2+9.5	96.71	0.43	41.76	96	Moderately hard
	UG2 ore		97.88	0.76	74.38	98	Soft
Compression	Silica	-19+13.2	28.07	1.77	49.59	85	Medium hard
	UG2 ore		42.64	2.00	85.28	88	Soft
	Silica	-13.2+9.5	27.31	1.14	31.27	92	Hard
	UG2 ore		37.21	1.13	42.08	98	Moderately hard

The DWT results in Table 4.4 show that the A x b indices for UG2 ore are slightly higher than those for silica, which infers that UG2 ore (with reference to tested size fractions) has a slightly lower resistance to impact breakage compared to silica. Overall, the amenability to impact breakage can be classified in the following order: -19+13.2 mm of UG2 ore, -19+13.2 mm of silica, -13.2+9.5 mm of UG2 ore and -13.2+9.5 mm of silica. The same trend was also observed for the compression breakage results. Since for the particle bed, the bed porosity reduction caused by compression is a critical factor affecting particle breakage (Liu & Powell, 2016), the t_{10}–E_{cs} relationship discussed in this thesis is only applicable for the bed configuration that was used in testing the breakage behaviour of the two size fractions of silica and UG2 ore.

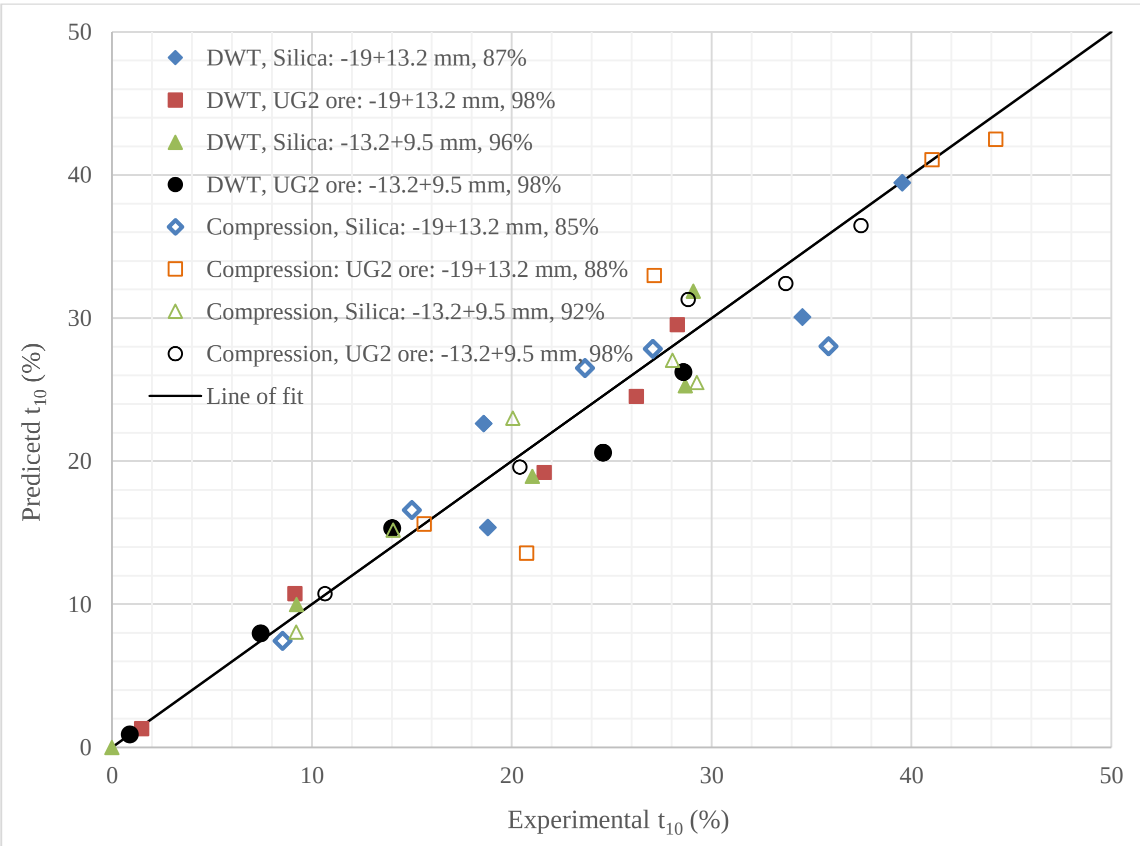

Figure 4. 5: Experimental versus predicted t_{10} for drop weight and compression test; R^2 values are included in the legend

The relative bed porosity reduction (ε_r) is plotted against the specific energy in Figure 4.6. It can be observed that ε_r generally increases with the input energy. The bed porosity reduction ratios for the -19+13.2 mm of silica and UG2 ore were comparable for specific energy until 2.5 kWh/t. Such a trend can possibly be attributed to comparable initial bed porosities of 49.3% and 48% for the -19+13.2 mm size fraction of silica and UG2 ore. The results for the -13.2+9.5 mm are not comparable for the two materials. The UG2 ore (for this size class) had higher bed porosity reduction ratios than silica. The results could be attributed to the difference in the response to compressive stress for the two materials as can suggested by the *A* x *b* in Table 4.4. The t_{10} values are plotted against the bed porosity reduction in Figure 4.7.

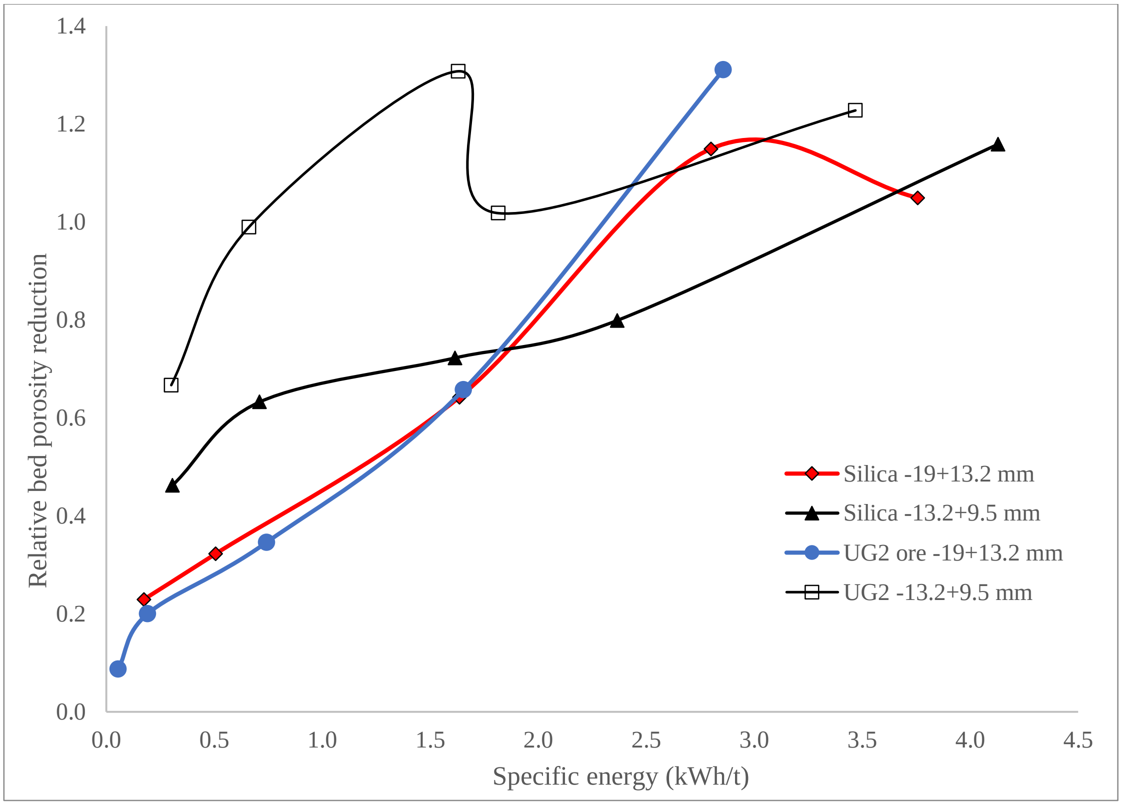

Figure 4. 6: Relative bed porosity reduction versus specific input energy

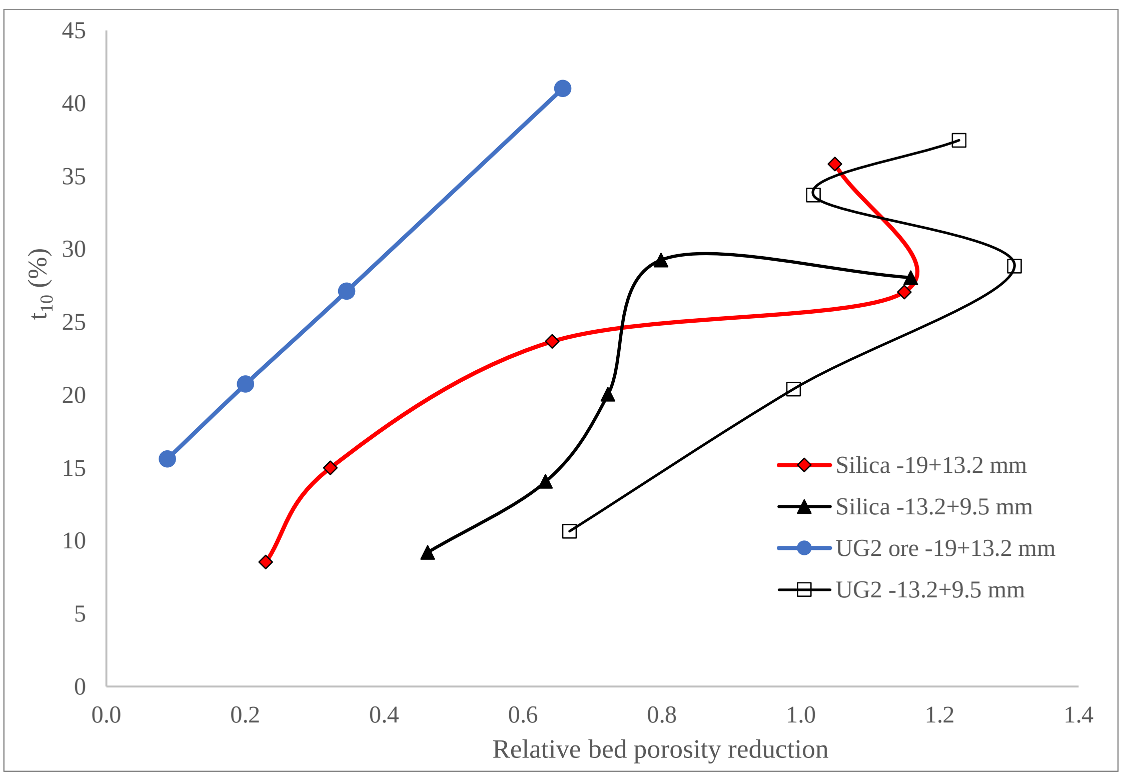

Figure 4. 7: t_{10} versus relative bed porosity reduction

It can be observed from Figure 4.7 that the -19+13.2 mm of UG2 ore, which was classified as 'soft' in Table 4.4 has high t_{10} values for any of the relative bed porosity reduction compared to the -19+13.2 mm of silica and -13.2+9.5 mm of both silica and UG2 ore. Despite similar reduction in the bed porosity which was observed for the -19+13.2 mm of the two materials, the actual size reduction in terms of the fineness index t_{10} is different, i.e., the softer material (UG2 ore) produced more fines (in terms of t_{10}) than silica (relatively harder). Comparing the results in Figure 4.7 for the -13.2+9.5 mm size fractions, it is evident that more fines were produced with silica than UG2 ore for the same bed porosity reduction. The results could be attributed to a higher initial bed porosity of 52.6% for -13.2+9.5 mm particles of silica (compared to the initial bed porosity of 45.8% for -13.2+9.5 mm of UG2 ore). The results highlight that the generation of the fines during confined bed comminution is influenced by both the initial bed porosity and relative hardness of the ore.

4.5.3 The t_n - t_{10} relationships

The t_n parameters (t_2, t_4, t_{10}, t_{25}, t_{50}, and t_{75}), calculated from product size distributions of both the DWT and compression breakage tests, were fitted to the equation 4.1 (King, 2012) in order to estimate material-specific parameter α.

$$t_n = 1 - (1 - t_{10})^{\left(\frac{10-1}{n-1}\right)^{\alpha}} \qquad (4.3)$$

Where t_n is cumulative % passing where $1/n^{th}$ of the parent size, α is the material specific parameter, n is X/x, X is the feed size and x is the sieve size.

Figures 4.8 to 4.12 show the predicted versus experimental t_n parameters while the α values are listed in Table 4.5.

Table 4. 5: Model parameter α

Type of test	Material	α
Compression	Silica	0.514
	UG2 ore	0.432
DWT	Silica	0.650
	UG2 ore	0.520

A fair degree of fitness can be observed in Figures 4.8 to 4.12. Parameter α values are relatively higher for silica than UG2 ore for both DWT and compression. The differences in the α values can be attributed to distinct mineralogical characteristics. As discussed in Chapter 6, parameter α values from the DWT and compression tests were used to estimate the ROC product size distribution for any arbitrary speed in the range of 300 and 1000 rpm.

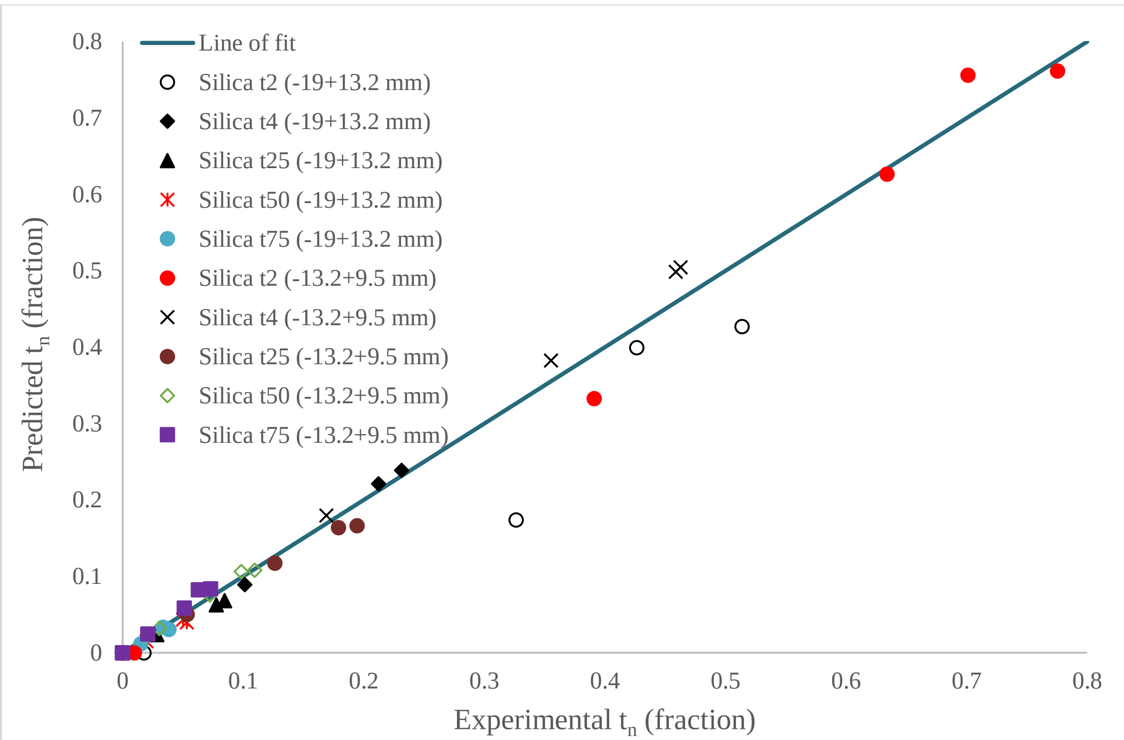

Figure 4. 8: Experimental versus predicted t_n for the drop weight tests conducted with silica

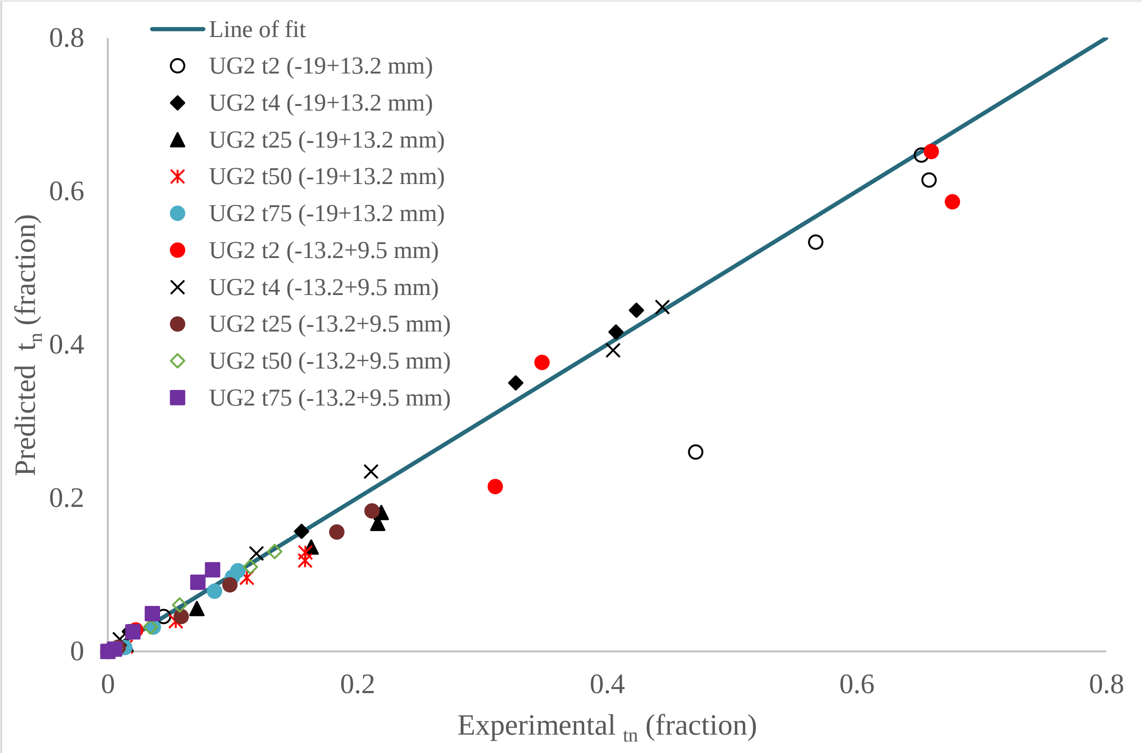

Figure 4. 9: Experimental versus predicted t_n for the drop weight tests conducted with UG2 ore

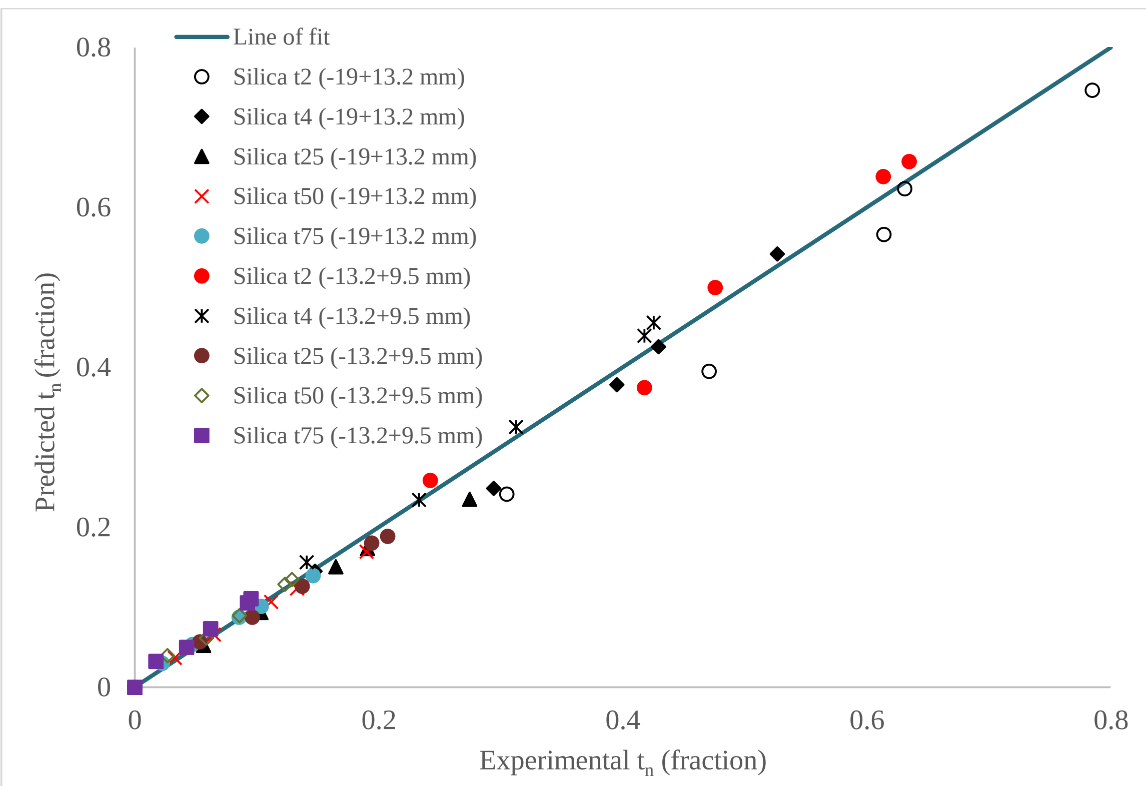

Figure 4. 10: Experimental versus predicted t_n for the compression breakage tests conducted with silica

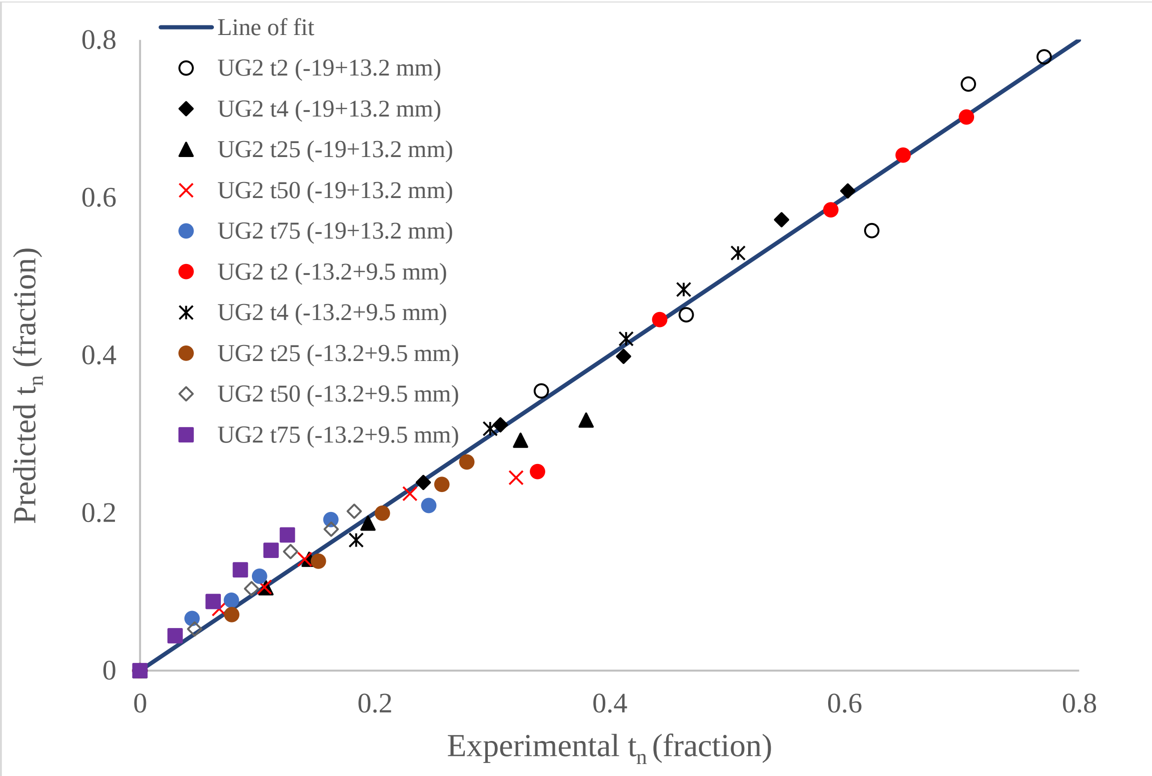

Figure 4. 11: Experimental versus predicted t_n for the compression breakage tests conducted with UG2 ore

4.6 Shape characterization

Figures 4.12 to 4.15 show the average dimensions of coarse particles produced with the -19+13.2 mm and -13.2+9.5 mm feeds for the drop weight and compression tests with comparable specific input energies. It can be observed that coarse progeny particles (+3.35 mm) for the two types of breakage tests have comparable dimensions (length, width and height). This is true for both feed size classes and two materials. It can be concluded that while the product size distribution of coarser particles can be different for impact and compression tests, the particle shapes are comparable. The reason could be the similar dominant compressive stress that is applied on the particles during impact loading and bed comminution (the difference being in the dynamic of application of the load).

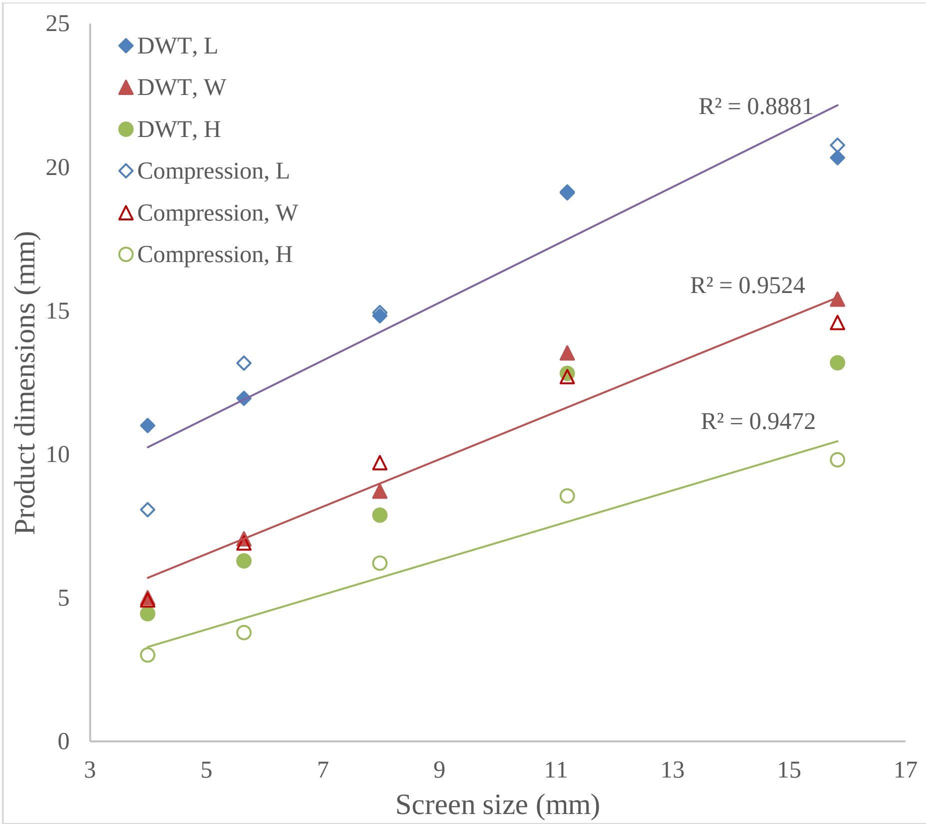

Figure 4. 12: Product dimensions of -19+13.2 mm silica (~0.2 kWh/t)

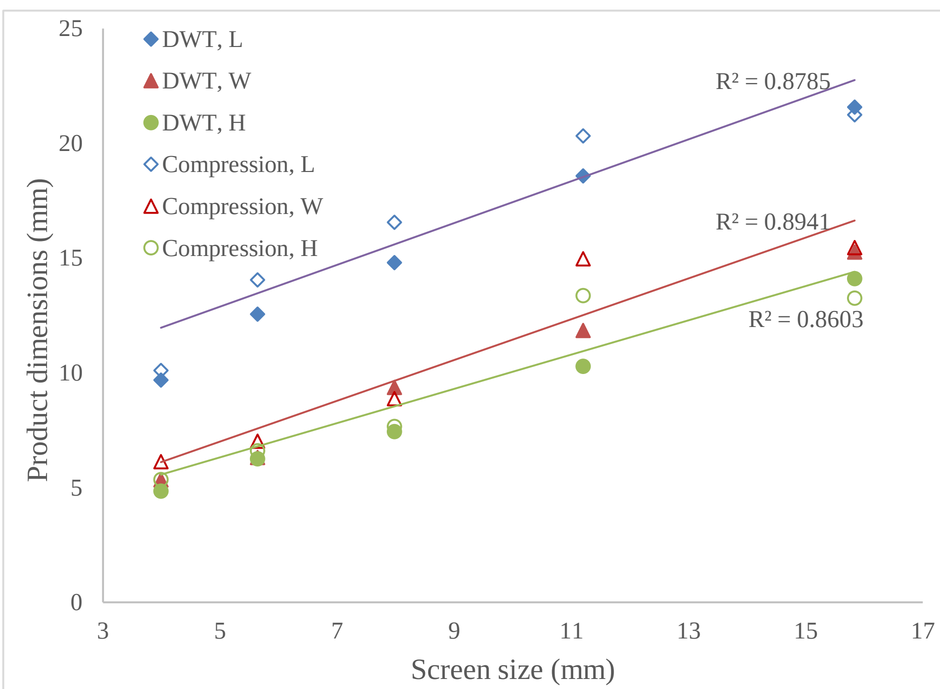

Figure 4. 13: Product dimensions of -19+13.2 mm UG2 ore (~0.2 kWh/t)

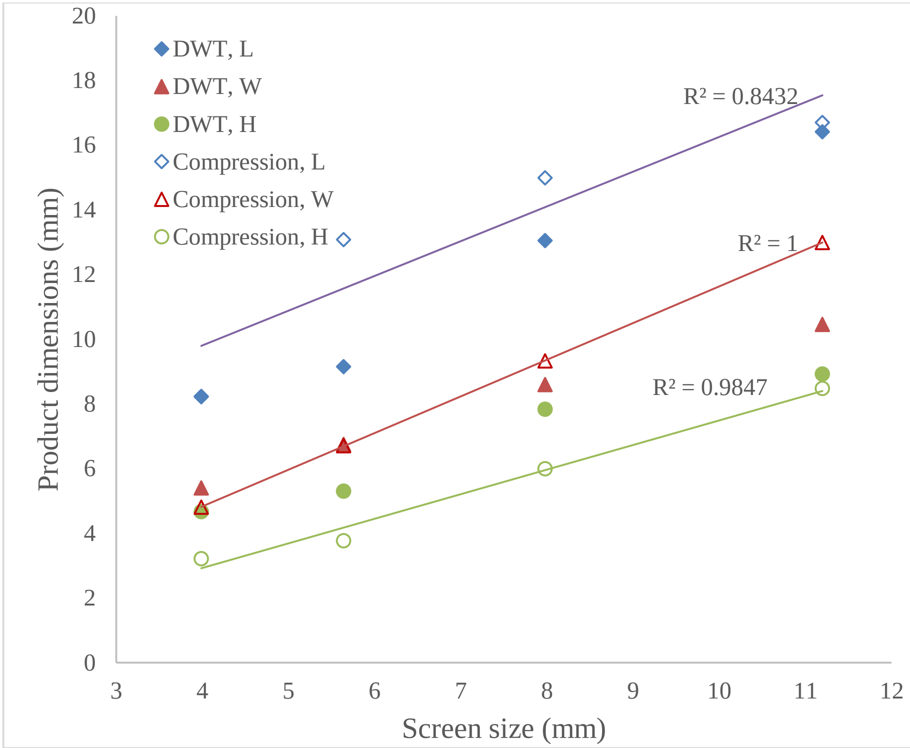

Figure 4. 14: Product dimensions of -13.2+9.5 mm silica (~0.7 kWh/t)

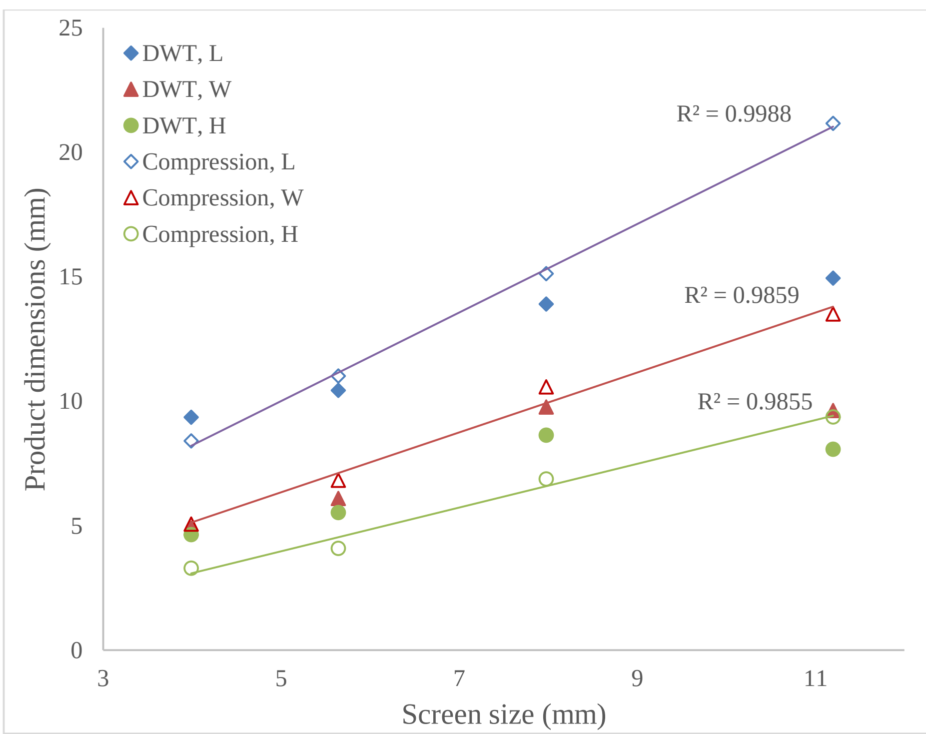

Figure 4. 15: Product dimensions of -13.2+9.5 mm UG2 ore (~0.3 kWh/t)

4.7 Conclusions

Silica and UG2 ore which were used to conduct comparative crushing test work with the ROC and cone crusher, as discussed in Chapters 5 and 6, were characterized in terms of their chemical composition, mineralogical characteristics, Bond crushability index (silica is relatively harder than the UG2 ore), abrasiveness (silica is more abrasive than the UG2 ore), impact breakage (silica has higher resistance to impact breakage than the UG2 ore) and compression breakage (UG2 ore is relatively less resistant to compression stress than silica). The shapes of the coarse progeny particles (+3.35 mm) generated from the impact and compression tests are comparable. The breakage model parameters derived in this chapter were used in section 5.3.3 in Chapter 5 to model the breakage process in the ROC.

CHAPTER 5: PERFORMANCE EVALUATION OF THE LABORATORY PROTOTYE OF ROTARY OFFSET CRUSHER

5.1 Introduction

In this chapter, dimensional analysis was applied on the key variables (feed rate, angular velocity, particle size and vertical exit gap)) that are affecting material comminution and transport in the ROC. Furthermore, experimental results of silica and UG2 ore comminution are presented. Silica and UG2 ore were used to investigate the effect of rotational speed, offset, vertical exit gap and feed size distribution on crusher performance. Single particle comminution was investigated by feeding individual particles to the crusher operated at the speeds of 550 and 1000 rpm. The effect of speed was also investigated using the rotational speeds ranging between 300 and 1000 rpm while the feed rate, offset and exit gaps were fixed at 1 tph, 10 mm and 4 mm respectively. Experimental data were fitted to the existing models to assess whether the product size distributions can be predicted using the empirical mathematical models. The effect of the horizontal offset on size reduction and throughput was investigated using offsets of 10, 16 and 23 mm while the feed rate and speed were fixed at 1 tph and 830 rpm respectively. The vertical exit gap of 1.5 mm was used. The effect of feed size distribution on size reduction was investigated with mono-size feed (-19+13.2 mm) and feed with a wide size distribution (-19+4.75 mm).

5.2 Derivation of the dimensionless number(s) relating the key operating variables

5.2.1 Key operating variables

The following variables affecting transportation and/or breakage mechanisms in the ROC were identified for the dimensional analysis.

i. Feed rate (*f*): Obviously, there is a direct relationship between the feed rate and crusher throughput. The material in the feeding zone is free falling. Depending on the volumetric capacity of the crushing zone (and material properties affecting rate of breakage and thus residence time of the process material in the crushing zone), the feed rate can be increased to achieve high crusher capacities.

ii. Angular velocity (ω): Angular velocity is directly proportional to the centrifugal acceleration of the particles nipped radially moving between in the space between the discs. Studying the effect of angular velocity in the ROC can be complex because the particles get sequentially crushed (once they are arrested as they go along the comminution cavity) and flow radially (once they are released following a compression event). After a series of arrest-release events, the progeny particles are then discharged. Angular velocity of the speed of the discs is a key operating variable affecting the performance of the crusher (Nghipulile, 2019).

iii. Particle size ($\bar{d}$): Kinematic parameters (e.g., velocity, acceleration, etc.) of the particles are dependent on the feed particle size. The particle size will affect the size reduction ratio. The particle strength generally decreases with particle mean size (Tavares & King, 1998). The feed size distribution, feed rate and feeding condition (choke feeding) can determine the occurrence of inter-particle comminution within the compression zone of the crusher.

iv. Vertical exit gap(z_{gap}): The residence time and largest size of the fragments produced following a series of crushing events in the ROC is also dependent on the vertical interval between the edges of the discs. This implies that the vertical exit gap affects both the throughput and size reduction ratio. It can be argued that decreasing the exit gap results in high reduction ratios, but throughput may be negatively affected due to higher residence time (also suggesting increase in specific energy). A trade-off should be made to reduce the feed particle size to the target product size with less power draw while the throughput is maximized.

The offset between the vertical axes of the discs was not considered in the dimensional analysis at this stage because previous results did not show that it has no significant influence on both size reduction and throughput (Nghipulile, 2019). However, that still needs to be investigated further in future studies. If it is established that it affects the dynamics of the ROC, albeit an improved design which may be developed in future, the dimensional analysis could be revised.

The other variables that could potentially affect the particle flow in the ROC crushing zone include the following (these are not considered for the dimensionless analysis because their effects are already accounted for in the five key operating variables).

- The porosity of the particles in the crushing zone can affect the packing of the particles when they are nipped between the discs. Theoretically, this can only be expected when there is a bed of particles in the crushing zone under choke feeding condition or due to slow crushing kinetics and thus slow transportation of particles to the periphery of the crushing zone.
- Stress (or pressure) distribution in radial axis of the disc. Compressive stress along the concave disc/plate (top disc) is impacted into the particles as they progressively move along the comminution cavity.

5.2.2 Dimensional analysis

Dimensionless analysis was done considering the four key variables (*n*) listed below.

$$\begin{cases} [f] = \frac{kg}{s} = \left[\frac{M}{T}\right] \\ [\omega] = s^{-1} = \left[\frac{1}{T}\right] \\ [d] = m = [L] \\ \left[z_{gap}\right] = m = [L] \end{cases} \tag{5.1}$$

The reference dimensions (denoted as *r*) used to express the key variables affecting particle transportation are *M*, *L* and *T*.

The number of dimensionless numbers (π-groups) can be calculated using the following equation.

$$\pi - groups = n - r \tag{5.2}$$

From Eq. (5.2), the total number of π-groups is 1. These can be represented as π_1.

The repeating variables, a set of variables which by themselves cannot form a dimensionless group, were identified among the four variables. Using that criterion, the feed rate, angular velocity and vertical exit gap are repeating variables and the remainder particle size is non-repeating variable.

$$\pi_1 = df^e\omega^f z^g \qquad (5.3)$$

The magnitude of π_1 can be expressed as follows.

$$[\pi_1] = [d][f]^e[\omega]^f[z]^g \qquad (5.4)$$

The rest of the calculations are included in Appendix E, with the final dimensionless number given by the following equation.

$$\pi_1 = \frac{d}{z} \qquad (5.5)$$

5.2.3 Demonstrating dependence of specific energy on exit gap and feed size

Considering exit gaps of 1 and 2 mm, the effect of feed size and exit gap on the specific comminution energy was evaluated using the Bond equation shown below.

$$E = 10W_i\left(\frac{1}{\sqrt{P_{80}}} - \frac{1}{\sqrt{F_{80}}}\right) \qquad (5.6)$$

Where E is specific energy in kWh/t, W_i is the work index of the material (this was done for UG2 ore whose W_i is 10.4 kWh/t as discussed in Chapter 4), F_{80} and P_{80} are 80% passing sizes of the feed and product respectively.

Specific energies are plotted against the feed size in Figure 5.1. It is evident that as long as the product size distribution is constant (assumed to be equal to the exit gap), energy increases with the parent particle size. The crusher operating at a smaller exit gap will draw more power. Reduction ratios (R_{80}) were also calculated using Eq. (5.7) to illustrate the significance of Eq. (5.5) on the size reduction. It is acknowledged that Eq. (5.5) is analogous to the reduction ratio of the crusher (if d is replaced by F_{80} and z by P_{80}).

$$R_{80} = \frac{F_{80}}{P_{80}} \qquad (5.7)$$

The reduction ratios are plotted against the feed particle size in Figure 5.2. Obviously, the reduction ratio increases linearly with the feed size (assuming a constant product size). Based on the slopes of the graphs representing the 1 and 2 mm exit gaps, it is evident that the reduction ratio is inversely proportional to the exit gap.

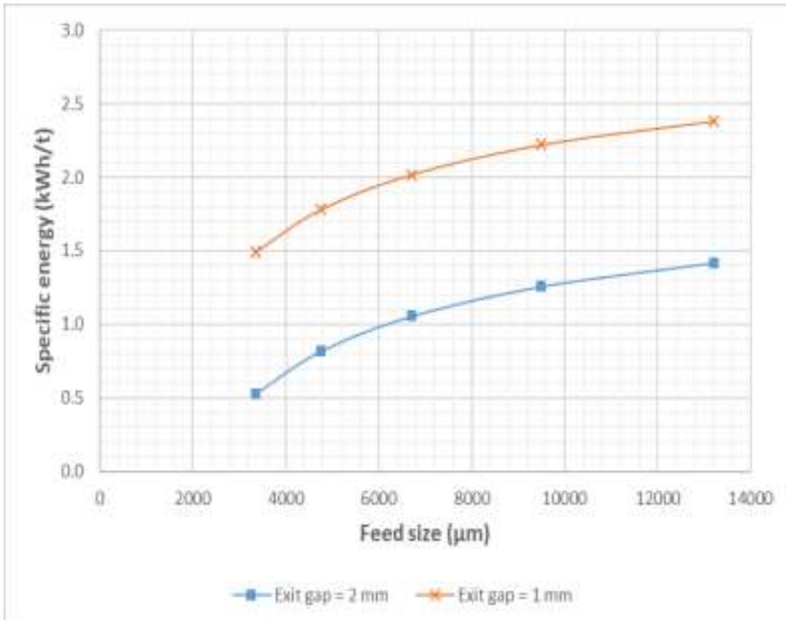

Figure 5. 1: Specific energy as a function of feed size and vertical exit gap

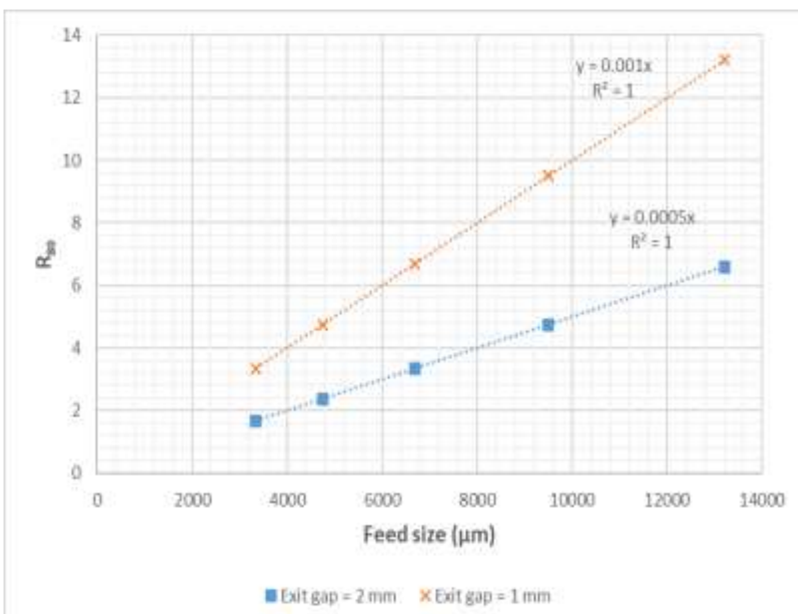

Figure 5. 2: Reduction ratio as a function of feed size and vertical exit gap

5.2.4 Theoretical throughput

The theoretical mass throughput of the particles in the ROC can be calculated using the following equation.

$$Q_{m,f} = m_p \frac{N_p}{t} \qquad (5.8)$$

Where m_p is the mass of a particle (assuming a spherical particle) and it is given by Eq. (7.9)), N_p is the number of particles and t is the residence time of the particles (in hours).

$$m_p = \frac{\pi \rho d^3}{6} \qquad (5.9)$$

Overall, the theoretical mass throughput (in tph) can be calculated using the following equation.

$$Q_m = \frac{\pi \rho d^3 N_p}{6t} \qquad (5.10)$$

The above production model can be modified to incorporate the production factors in order to allow the estimation of the crusher throughput per month as shown in the following equation.

$$Q_m = \frac{\pi \rho d^3 N_p}{6t} sfw \qquad (5.11)$$

Where s is the hours per shift, f is the number of shifts per day and w is the working days per month.

It is evident from Eq. (5.11) that the feed size (d) is directly proportional to the crusher throughput. Since exit gap is inversely proportional to the residence time (Nghipulile, 2019), the crusher throughput is directly proportional to the exit gap. It is acknowledged that the exit gap was fixed at 4 mm during the DEM simulations discussed in Chapters 7 and 8. Future studies should look into changing the exit gap and feed size to relate the dimensionless number in Eq. (5.5) to the key operating variables. This will allow a philosophical relationship to be derived to explain the mechanism underpinning the crusher performance.

5.3 Breakage of single particles in the laboratory ROC

The mono-sized feeds (-19+13.2 and -13.2+9.5 mm) were crushed in the ROC at various speeds (550 and 1000 rpm) while the vertical exit gap and offset were fixed at 4 and 10 mm respectively. Experimental product size distributions of UG2 ore (multi-component material) are compared to those of silica (single-component material) in Figure 5.3.

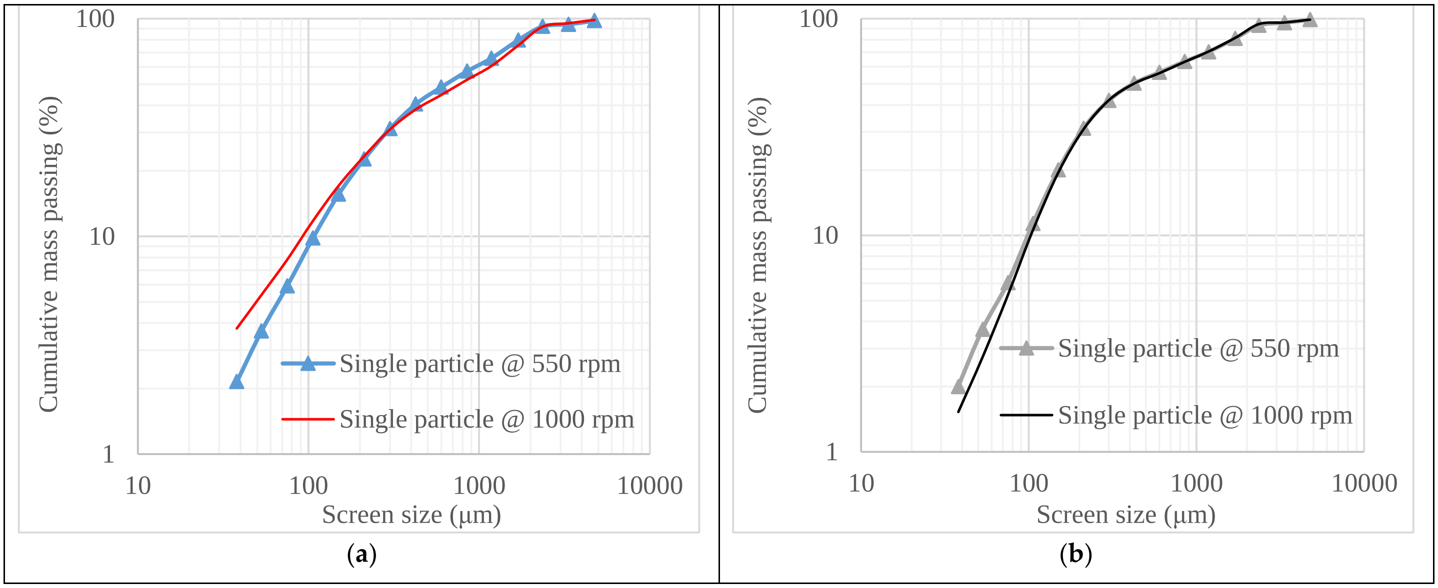

*Figure 5. 3: Product size distributions after crushing -19+13.2 mm particles, (**a**) silica and (**b**) UG2 ore*

It can be observed in Figure 5.3 that for each material, the size distributions for 550 and 1000 rpm speeds are comparable for the particle sizes above 100 µm. The product P_{80} sizes are below 2 mm, suggesting the reduction ratios of at least 8 (calculated assuming the feed size of 15.8 mm, i.e., the geometric mean of the feed size class (-19+13.2 mm)). Feeding one particle to the ROC does not accelerate the top disc. This suggests that the parent particle and subsequent fragments in the crushing zone were forced against a stationary body (top disc) while radially moving to the periphery. It is worth mentioning that crusher design with a stationary top disc (assuming the disc is not a free wheel) is not suitable for the hard rocks as two problems are likely to happens, viz. frequent jamming and high wear rate (due to the expected higher degree of dominance of the abrasion mechanism). The free wheel ensures some degree of flexibility which can facilitate the release of the arrested particles along the comminution cavity and thus preventing jamming. The torque values during operation can provide some insights in the crusher dynamics. The typical signal is presented in Figure 5.4 (for the test with UG2 ore at 1000 rpm).

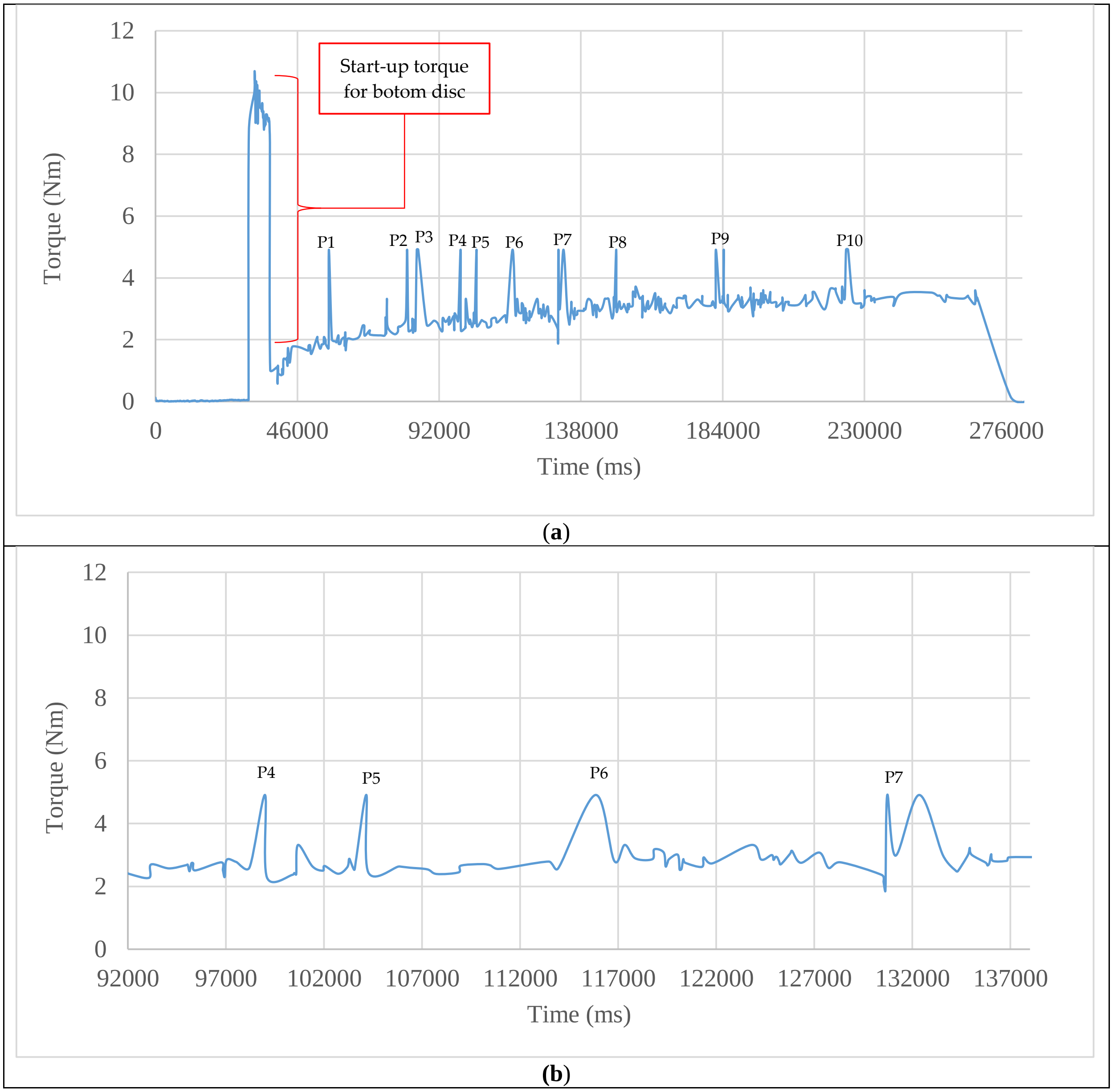

*Figure 5. 4: Torque signals for the ROC in operation (speed was 1000 rpm, vertical exit gap of 4 mm gap, horizontal offset of 10 mm), successively fed with single particle of UG2 ore, (**a**) full signal and (**b**) signals for time ranging between 92 000 and 138 000 milliseconds (particles 4 to 7). P stands for particle.*

It is evident that there is slight increase in the torque when a single particle is fed to the crusher. From Figure 5.4, it is clear that the peaks in the torque signal for the different particles are corresponding to a common value of approximately 5 Nm (suggesting comparable breakage energy for the individual particles). Breakage of a single particle is instantaneous, with no successive peaks in the torque signal during the processing of each particle. The progeny particles produced move radially along the comminution cavity until they are nipped again between the two discs. Any subsequent nipping is followed by further breakage (abrasion due to the rotation of disc and compression as the particle(s) is forced against the stationary top disc). The simulation results discussed in Chapters 7 and 8 provided insights into the intensities of compressive and shear stresses for a variety of operating speeds when the crusher.

5.3 Operating the crusher with 1 tph to investigate the effect of rotational speed

5.3.1 Reduction ratios

The reduction ratios (R_{50}), calculated from the P_{50} sizes, are shown in Figure 5.5. Product size distributions are included in Appendix F. The product fineness increases with rotational speed for as long as the crusher is operating above 550 rpm. For the speed regime where the reduction ratio is increasing with the rotational speed, it can be speculated that increasing speed is accompanied by more crushing actions. Increasing speed suggests that the particles nipped between the discs are subjected to many crushing actions, which can be classified as compressive and shearing actions. The compressive action can be subdivided into "hammering" and "squeezing" types, depending on the rate of rotation and other types of motion imposed on the disc, e.g., the vibratory motion of a top disc could intensify hammering actions, while its absence implies that only squeezing action is prevalent in the crusher. The current laboratory version does not have vibratory motion. For the UG2 ore, reduction ratios are comparable for the two mono-size feeds, and they are not changing when the speed was increase from 830 to 1000 rpm. This is contrary to silica, whose graphs show a steady increase in the reduction ratio with speeds above 550 rpm. Reduction ratios for the coarser and finer feeds of silica are not comparable for speeds below 830 rpm. The trend is what is expected with the coarser feed (-19+13.2 mm) having high reduction ratios than the finer feed (-13.2+9.5 mm). The little improvement in the reduction ratio could suggest a limitation of breakage force with the current design. From Figure 5.5, a little improvement in the reduction ratio for -19+13.2 mm of silica could suggest a limitation of breakage force with the current design. Overall, with the -19 mm materials, it can be argued that abnormal breakage region is being approached. This suggests that the ROC may perform better for fine crushing for as long as the vertical exit gap is well controlled.

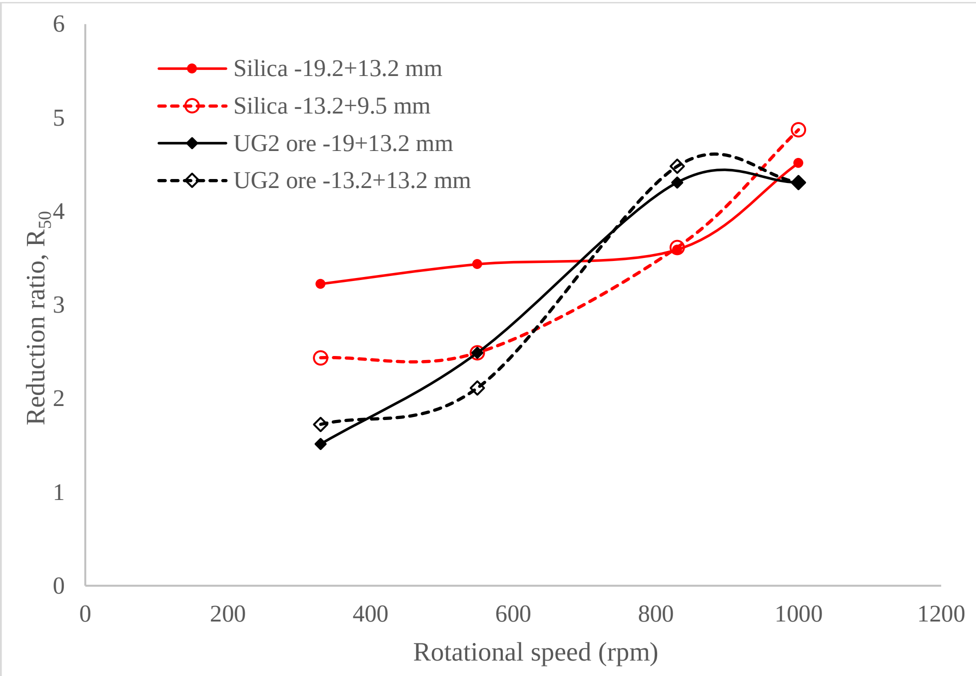

Figure 5. 5: Reduction ratios of silica and UG2 ore crushed in the ROC

5.3.2 Fitting experimental data to empirical model of cumulative breakage function

The product size distributions in Appendix F were plotted on a normalized horizontal axis as shown in Figure 5.6. The overlapping of curves suggests that the breakage behaviour of the two materials is comparable. Self-similar breakage behaviour is well discussed in the literature (Camalan, 2020; Fuerstenau et al., 1990; Klichowicz et al., 2014). Similar normalized product size distributions in Figure 5.6 suggest that the breakage distribution functions for the two materials are normalizable and thus the experimental data could be fitted to the following Austin empirical model (Austin et al., 1984).

$$B_{ij} = \Phi\left(R_{ij}\right)^{\gamma} + (1 - \Phi)\left(R_{ij}\right)^{\beta} \qquad (5.12)$$

Where R is a relative particle size given by $\frac{x_{i-1}}{x_j}$ (j>i, where i and j represent size classes), β is a material-dependent parameter (whose values usually range between 2.5 and 5 according to Austin et al. (1984), but as reported in some studies β can be greater than 5, for example, Ozkan et al. (2003) reported the β value of 6.4 for the lignite coal and Petrakis & Komnitsas (2017) reported a β value of 5.8 for quartz), γ is also a material-dependent parameter with values between 0.5 and 1.5 according to Austin et al. (1984), and finally Φ_j is a fraction of fine particles resulting from a single breakage event and it is also dependent on the material. The value of γ is related to the relative number of fines produced and thus related to the milling efficiency (Petrakis & Komnitsas, 2017) while Φ and β are related to the coarser end of the breakage distribution function and show how fast parent particles migrate to the smaller size classes.

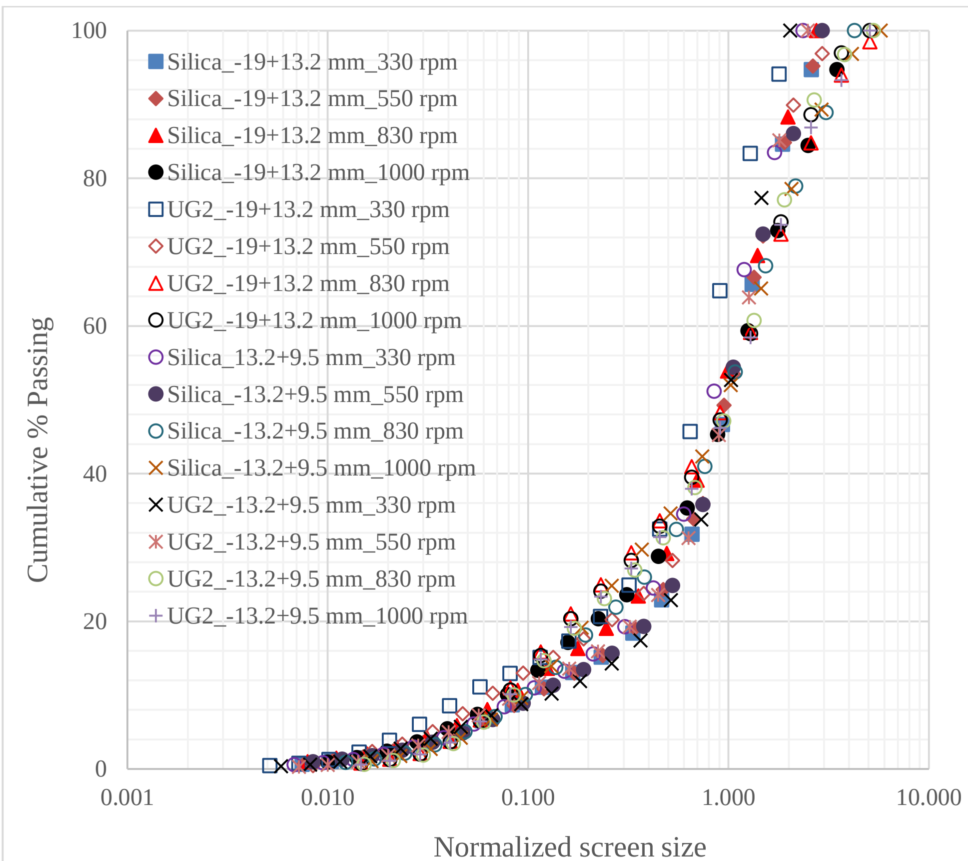

Figure 5. 6: Normalized size distributions for effect of speeds

The truncated product size distributions (considering the size distribution of progeny particles in the size classes below the feed size class) were calculated from PSDs included in Appendix F. The breakage probabilities were at least 80% in all tests. In the effort to estimate the breakage distribution parameters, the experimental data were fitted to Eq. (5.12) to get the breakage parameters using the iteration method with the set objective function that minimises the *RMSE* between the experimental and model data. This was done using Microsoft Excel® *Solver* add-in tool. To allow the analysis of the sensitivities of parameters Φ (related to coarser-end of the size distribution) and γ (related to the fine-end of the size distribution) on the change in the rotational speed of the discs, the β parameter (generally accepted to be a constant as a material specific parameter (Austin et al., 1984)) was fixed for both silica and UG2 ore using literature values of 5.8 (Petrakis et al., 2017) and 6.3 (Makgoale, 2019) respectively. A fair degree of fitness can be observed in Figure 5.7 showing the experimental and model cumulative breakage parameters.

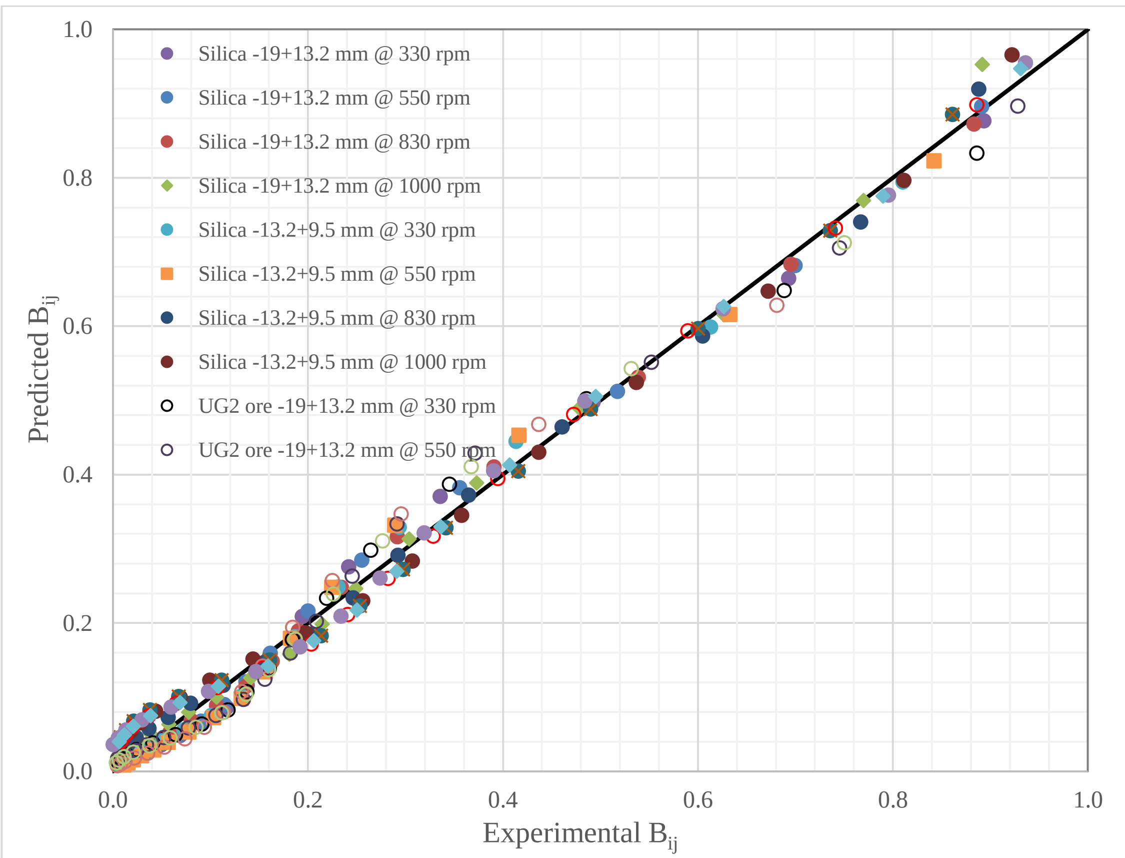

Figure 5. 7: Experimental versus predicted B_{ij}

The breakage parameters are plotted against the crusher speed in Figures 5.8 and 5.9. It can be observed in Figure 5.8 that Φ values are increasing with speed while the γ values in Figure 5.9 are decreasing with speed. It can be inferred that the two trends of the two parameters suggest the trends in the dominance of the different breakage mechanism as the speed increases.

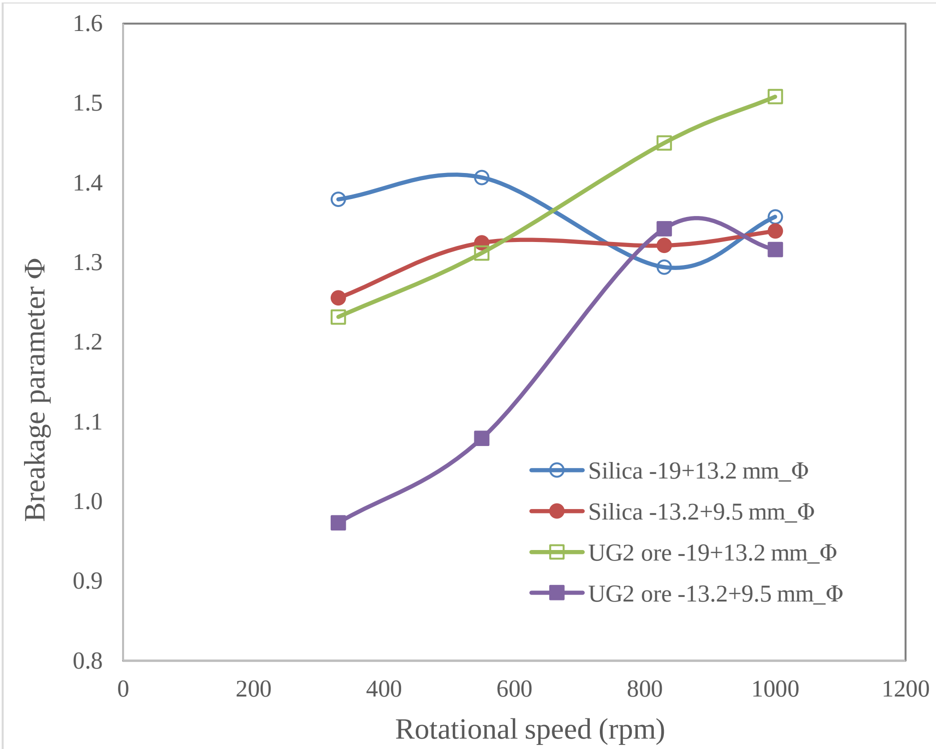

Figure 5. 8: Breakage distribution parameter Φ as function of rotational speed

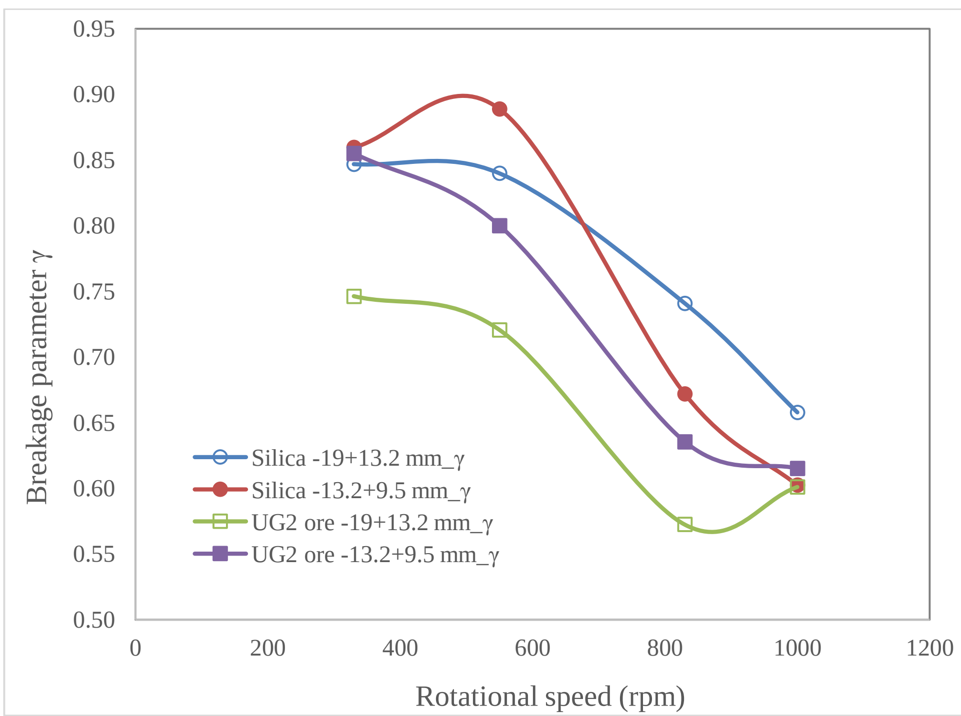

Figure 5. 9: Breakage distribution parameter γ as function of rotational speed

In Chapters 7 and 8, the DEM results provided insights into the breakage mechanism when the operating variables are changed. The effect of speed has shown that compressive breakage decreases with the rotational speed while the strength of the shear breakage mechanism increases steadily with the crusher speed. It can, therefore, be concluded that Φ is related to shear mechanism while γ relates to compressive breakage mechanism. This interpretation should just be limited to the ROC for now, because the application of Eq. (5.12) is limited to getting the breakage parameters in the current literature.

5.3.3 Fitting experimental data to t_n model

The experimental t_{10} values are plotted against the rotational speed in Figure 5.10. Like the reduction ratios, the t_{10} increases with the rotational speed, with shapes of the graphs for the two materials being distinct. For any speed, the t_{10} value can be estimated using Eq. (5.13) whose fair degree of fitness can be observed in Figure 5.11.

$$t_{10,N} = a \times (1 - e^{-mN^n}) \qquad (5.13)$$

Where $t_{10,N}$ is the t_{10} corresponding speed N (in revolutions per second) while a, m and n are model parameters.

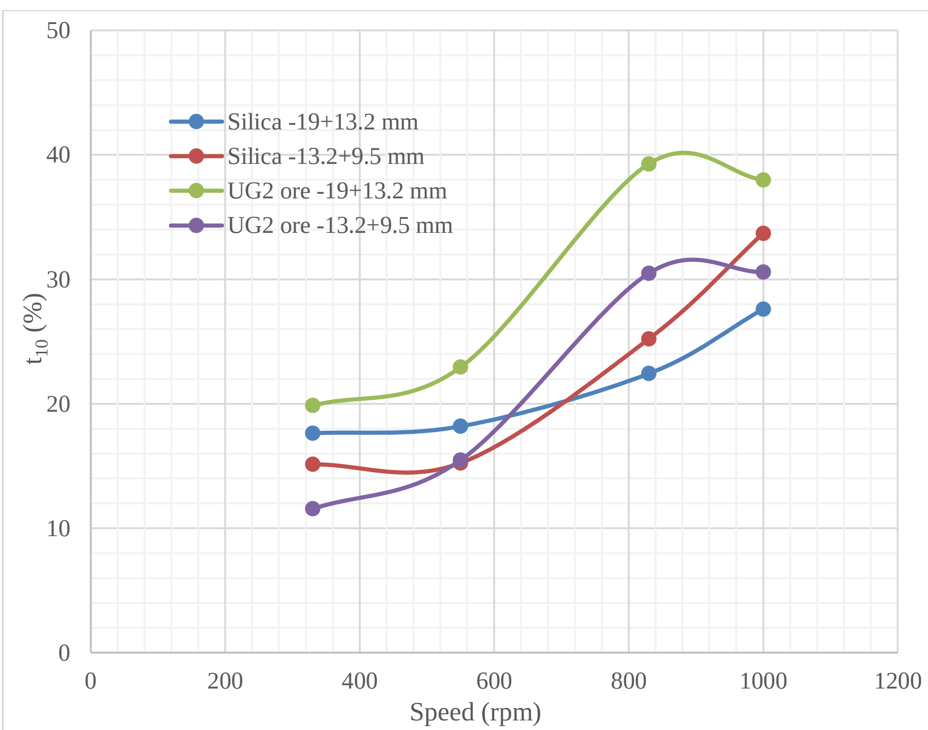

Figure 5. 10: Experimental t_{10} values as function of speed

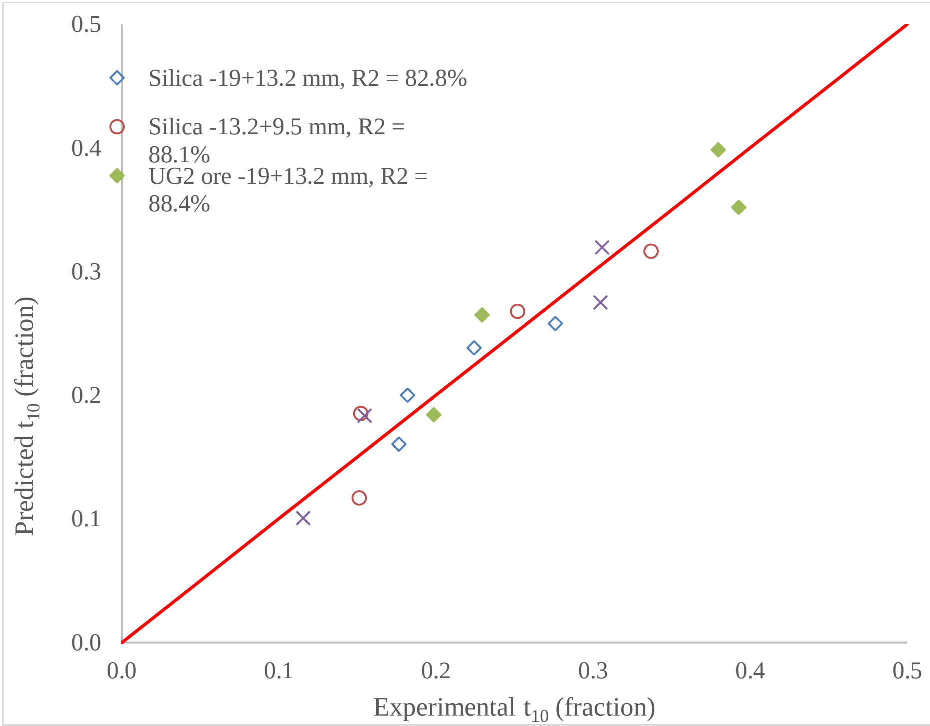

Figure 5. 11:: Experimental t_{10} versus model t_{10} (function of speed)

Table 5.1 lists the model parameters in Eq. (5.13). Parameters *m* and *n* are decreasing with feed particle size. They can thus be attributed to material properties at this stage. As the database expands, this conclusion should be revisited.

Table 5. 1: Summary of model parameters for Eq. (5.13)

Model Parameters	**Silica**		**UG2 ore**	
	-19+13.2 mm	-13.2+9.5 mm	-19+13.2 mm	-13.2+9.5 mm
a	2.438	22.540	1.576	0.462
m	0.032	0.001	0.034	0.022
n	0.447	0.902	0.769	1.414

Substituting Eq. (5.13) into Eq. (4.3), results in Eq. (5.14) which can be used to estimate the product size distribution for any rotational speed in the range of 330 and 1000 rpm (speed range which is currently tested with the laboratory prototype). It should also be noted that the current model is only validated for the ROC operated with the feed rate of 1 tph.

$$t_n = 1 - \left(1 - (a \times (1 - e^{-mN^n}))\right)^{\left(\frac{10-1}{n-1}\right)^{\alpha k}} \qquad (5.14)$$

Where α is material-specific breakage parameter.

The t_n were calculated using Eq. (5.14) with the α values for silica and UG2 ore obtained from the DWT and compression data (discussed in Chapter 4) used in the calculations. Figures 5.12 and 5.13 show the results for the experimental versus predicted t_n values obtained using the α values of drop weight and compression breakage tests respectively. A higher dispersion can be observed at higher experimental values (>0.4) in both Figures 5.12 and 5.13, with the slightly better degree of correlation obtained from the drop weight tests which used single particles (see Figure 5.12). This is assumed to be an indication of the dominance of the single particle breakage in the ROC when the crusher is operated with the feed rate of 1 tph. The results in Chapter 7 provide evidence of single particle comminution along the comminution cavity. However, it is acknowledged that the robustness of the Eq. (5.14) should still be tested in future when more experimental data are available at various operating conditions.

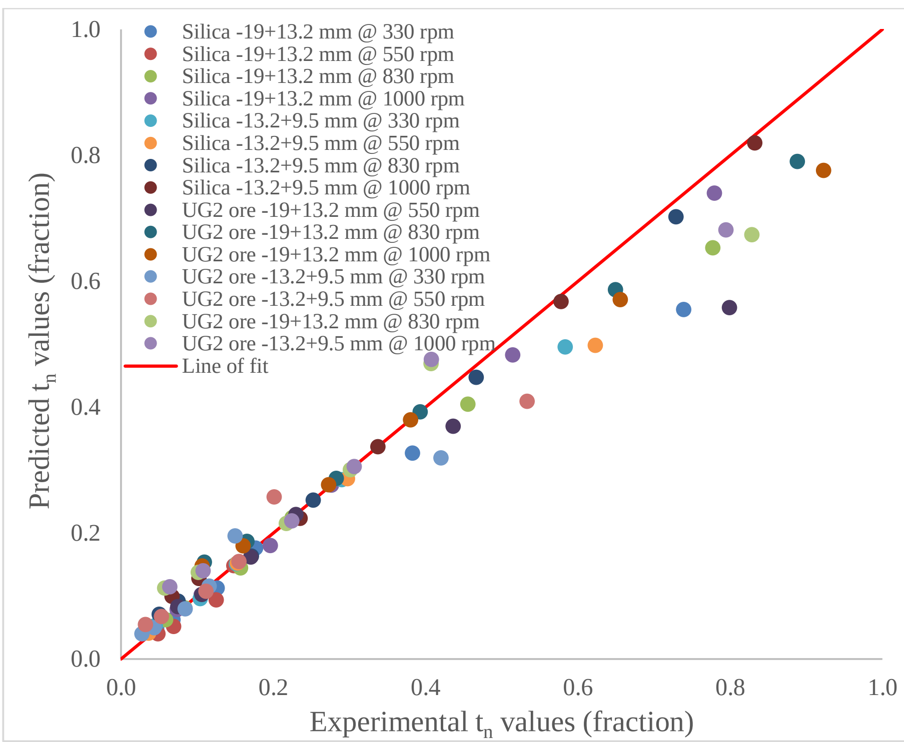

Figure 5. 12: Experimental versus model t_n values using the α from drop weight tests

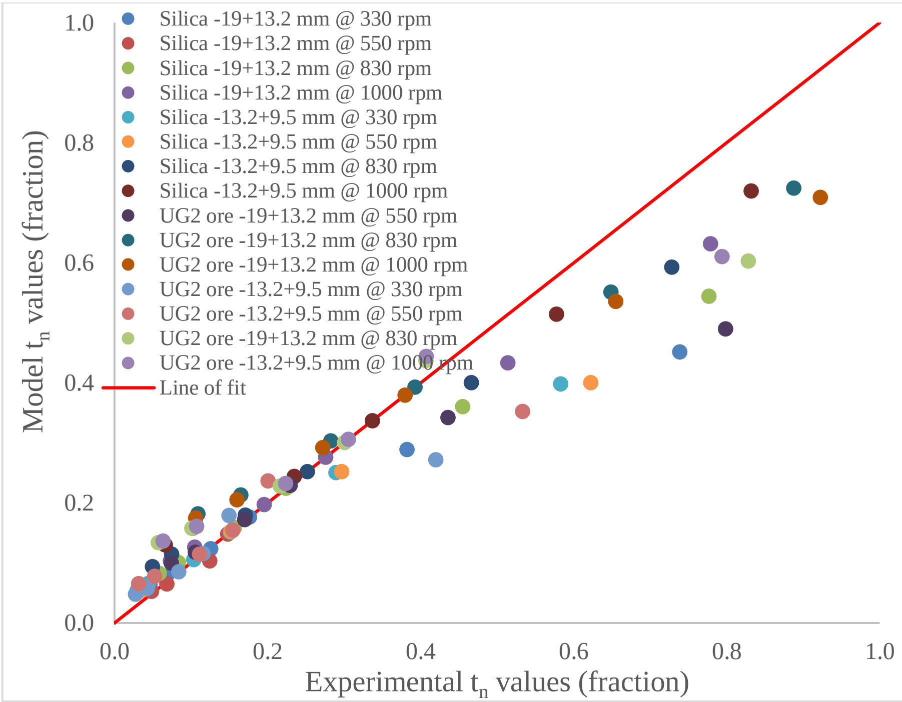

Figure 5. 13: Experimental versus model t_n values using the α from compression tests

5.3.4 Slab formation

As an attempt to characterize the coarse silica particles (those larger than 3 mm) discharged from the crusher, the dimensions (width, height and length) of those particles were measured using a Vernier calliper. The average values for the products discharged from the crusher operating at 330, 550 and 830 rpm are shown in Figure 6.11. Similar shape characteristics were observed for the UG2 ore. It is clear that slab particles were produced. This suggests that the particles in the crushing chamber get discharged for as long their thickness is less than the exit gap. Surface breakage (abrasion), which is one of the dominating mechanisms due to the rotational nature of the discs makes it possible for that to happen. From Figure 5.14, it was observed that the maximum heights for 330, 550 and 830 rpm were 6.74 mm, 6.15 mm and 4.35 mm respectively. It can thus be concluded that the thickness of the slab particles produced by the ROC decreases with the rotational speed. But the widths and lengths at all speeds are relatively the same.

The production of slab particles by the ROC is a result of the crusher discs failing to deliver the force required to shatter the silica particles. In the crushing zone, the particles need to be exposed to the highest crushing pressure to ensure efficient body (catastrophic) breakage. A more robust hydraulic system for the ROC to ensure maximum delivery of available energy to the particles nipped between the discs is one area of improvement that could be looked at in the future. One way that could be implemented to eliminate the coarse and slab particles is to change the profile of the discs. In general, the crushing surfaces in crushers are corrugated, toothed, or ribbed. For the toothed profiles, the shape of the teeth is generally pyramidal. The toothed surfaces offer additional complex penetrating and compressive forces that help to bring about breakage (by shattering mechanism) of hard ores (Gupta & Yan, 2006). It has been reported that corrugated profiles offer compound crushing by compression, tension, and shear (Wills & Napier-Munn, 2006). Some common profiles and their applications in the jaw crushers are summarized in Table G1 in Appendix G. It is argued that the slab shaped particles can only be "eliminated" if the particles are subjected to a single pressure point such as that provided by a ball.

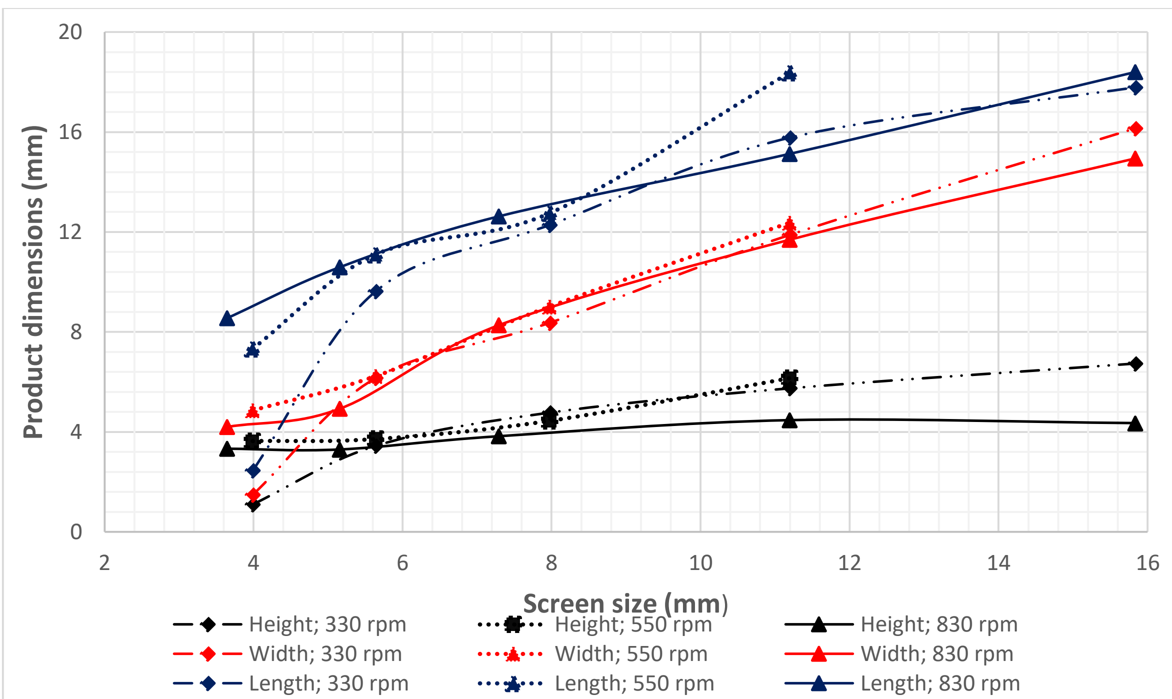

Figure 5. 14: Trend in particle dimensions (measured using a Vernier calliper) increasing with product size (as given b size analysis)

It is acknowledged that the simulations in Chapters 7 and 8 used the conical profile that is currently on the crusher because the focus of the study was to understand the mechanism driving the performance of the current prototype. In future studies, it is recommended that the DEM should also be used to investigate the various corrugation designs that can be fitted on the ROC. At this point, it worthy pointing out that with the spinning nature of the flywheels (discs), and as discussed in Chapters 7 and 8 that shearing action increases with the rotating speed, the corrugation added to the discs may wear off faster (suggesting high operating costs) as the speeds of the disc increases. It is further postulated that a corrugated surface is most likely going to increase the residence time and thus reduce the throughput compared to the flat surface. The product size distribution could also be much wider because the particles will experience more differential forces in the crushing zone. Once the crusher profiles and motion of discs have been optimized, the discs can be fitted with replaceable liners, made from manganese steel, or "Ni-hard," a Ni-Cr alloyed cast iron (Wills & Finch, 2016). Hard liners are essential, not only to reduce wear, but also to minimize the crushing energy consumption by reducing the deformation of the surface at each contact point.

Elimination of slab particles can possibly also be tackled using solutions such as (1) choke feeding the crusher with a feed with a wider size distribution (some particles should be less than the vertical exit gap) to promote rock-on-rock crushing (Evertsson & Bearman, 1997), (2) imposition of vibratory motion to intensify the delivery of the impact forces to the particles (comparable to the nutating motion in cone crushers (Evertsson, 1999)).

5.3.5 Relative abrasiveness of silica and UG2 ore during crushing tests

The abrasive indices for silica and UG2 ore, discussed in Chapter 4, showed that silica is very abrasive than the UG2 ore. The Bond abrasion test results have been useful in estimating the wear rates of the liners in conventional crushers as well as the media consumption rate in tumbling mills. Some correlations between *Ai* and wear rate are shown in Figure H1 in Appendix H. Using the relationship for jaw and cone crushers in Figure H (Gupta & Yan, 2016), the liner wear rates when processing silica and UG2 ore in the ROC can be expected to be approximately 0.028 and 0.014 kg/kWh respectively. This is when it is assumed that the same material of construction is used in both conventional crushers and ROC. Figure 5.15 shows a fire spark captured on the video taken when processing silica in the ROC with the rotational speed of 1000 rpm. There were no sparks during the UG2 ore processing.

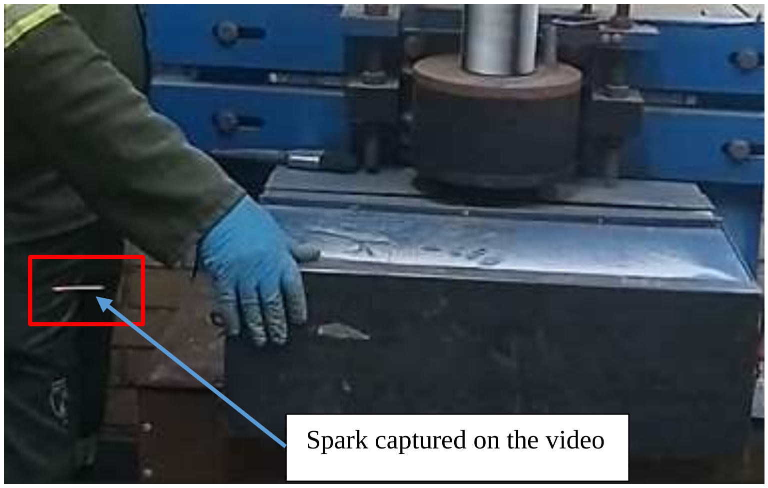

Figure 5. 15: Illustration of spark when processing silica in the ROC

5.4 Effect of horizontal disc offset on crusher performance

The product size distributions for the -19+13.2 mm and -6.7+4.75 mm size fractions of silica that were used to investigate the effect of horizontal offset on crusher performance are shown in Figures 5.16 and 5.17 for -19+13.2 mm and -6.7+4.75 mm mono-size feeds respectively. The 10 mm offset seems to yield finer size distribution on the coarse end of the size scale for the -19+13.2 mm feed and a finer size distribution at the finer end of the size scale for the -6.7+4.75 mm feed. The 16 mm offset product size distribution is generally coarser for both feeds. Reduction ratios and total specific energies are plotted against the offset in Figure 5.18. It can be observed that for both feeds the reduction ratio did not change significantly with speed. Since high reduction ratios were recorded with a reduced gap (1.5 mm) compared to the 4 mm gap reduction ratios in Figure 5.5, it is clear that the exit gap is the main determinant of the reduction ratio that can be achieved, i.e., . Crusher dynamics in terms of speed of the discs also plays a significant role in the reduction ratio as discussed in section 5.3 of this Chapter as well as in Chapters 7 and 8. In Figure 5.19, the throughput is also plotted against the offset. For the –6.7+4.75 mm feed particles, the throughput did not change with the increasing offset. This is contrary to the results for the -19+13.2 mm which show throughput increasing slightly with offset.

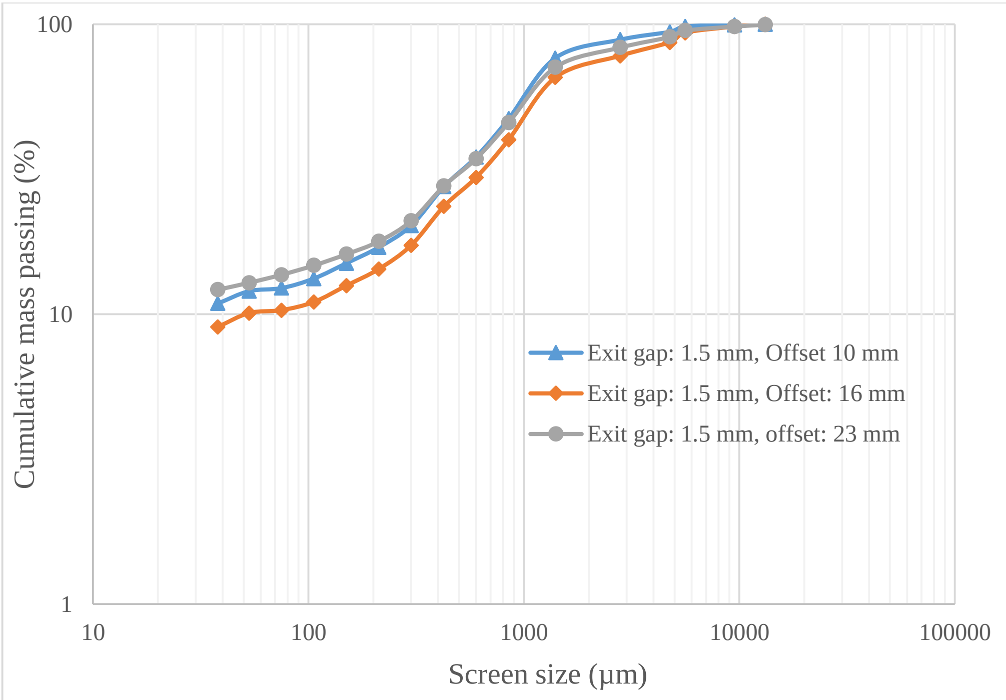

Figure 5. 16: Product size distributions for various offset with -19+13.2 mm feed, exit gap of 1.5 mm

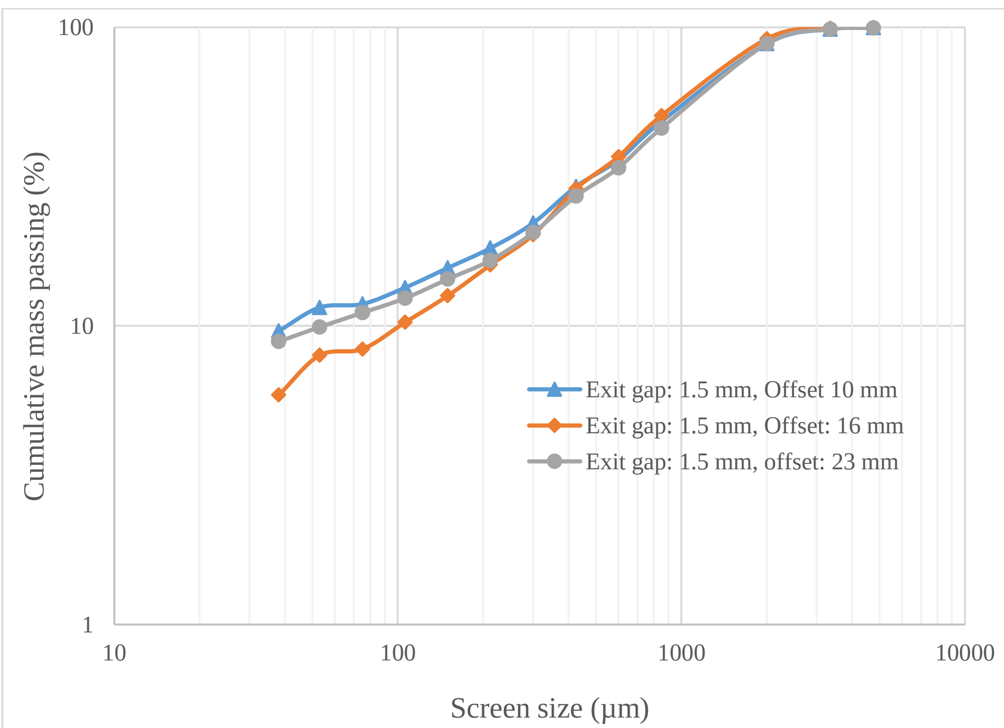

Figure 5. 17: Product size distributions for various offset with -6.7+4.75 mm feed, exit gap of 1.5 mm

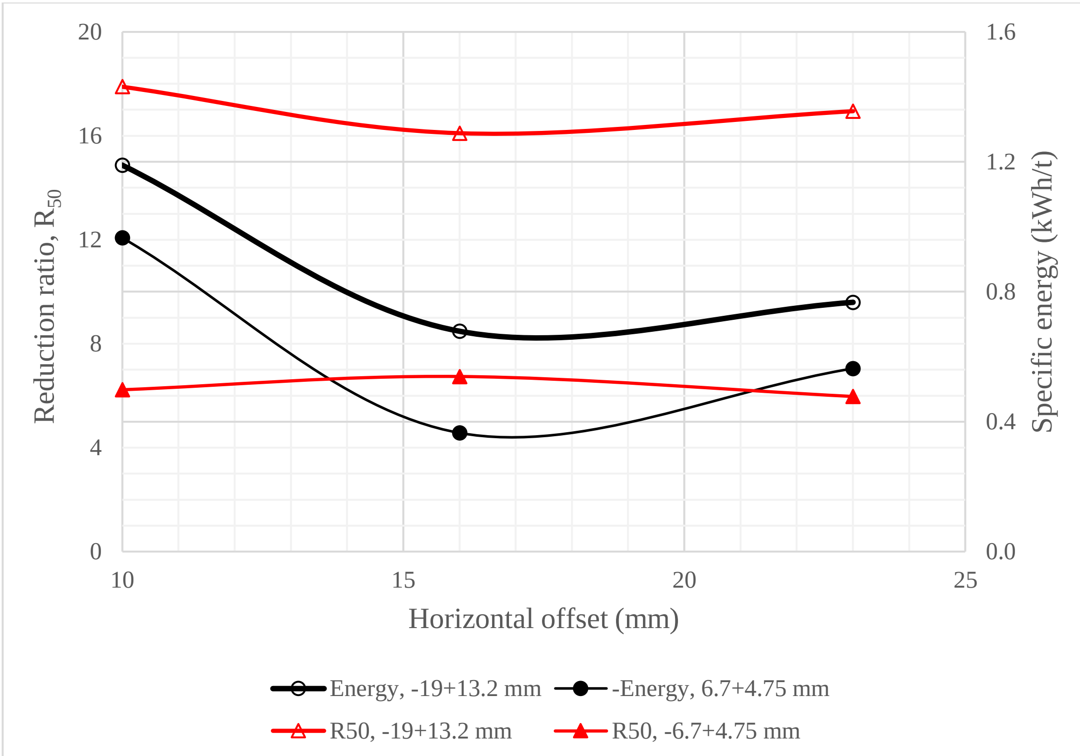

Figure 5. 18: The relationship between reduction ratios, specific energy and offset for various feed size and exit gaps; speed was 830 rpm

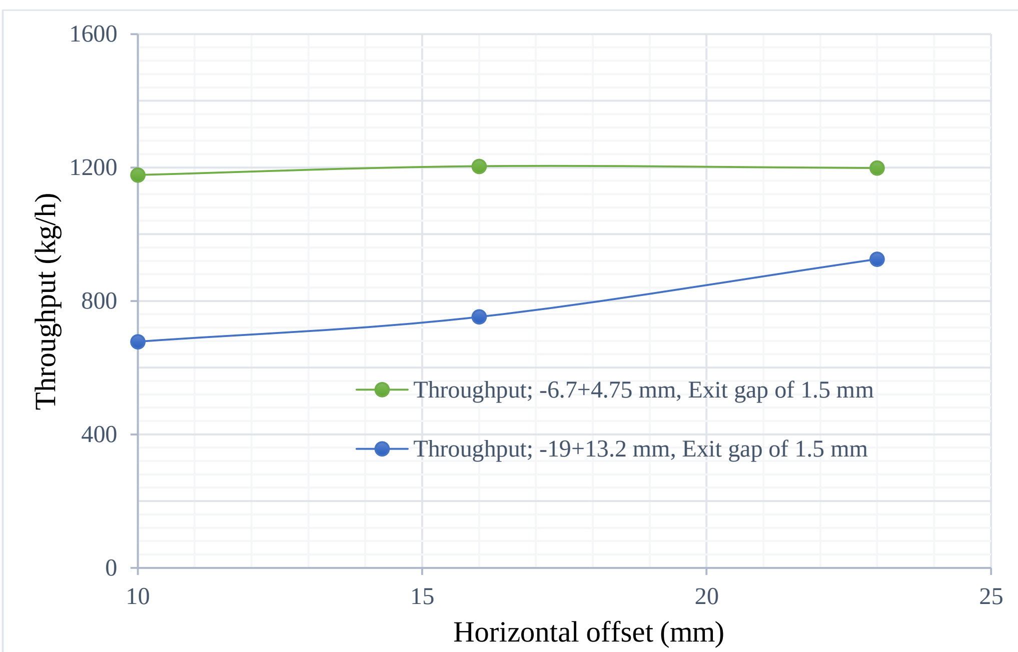

Figure 5. 19: The relationship between throughput and offset for various feed size and exit gaps; speed was 830 rpm

5.6 Effect of feed with wide size distribution

To investigate the effect of feed size distribution, a limited scope of work was conducted with the crusher operated with the horizontal offset and rotational speed of 23 mm and 830 rpm respectively. The feed rate and vertical exit gap were 1 tph and 3 mm respectively. It is known that materials get weaker with the increasing particle size due to the increase in the internal flaws (Rozenblat et al., 2011; L. . Tavares & King, 1998). Though that is a general trend for most materials, it has also been reported in the literature (Bwalya & Chimwani, 2020) that silica particles with different sizes can have the same threshold (minimum) energy.

With a wide size distribution, the feed particles can be assumed to be transported along the comminution cavity and get nipped between the two discs. This implies that the transportation of the daughter particles produced from the size classes on the right is delayed as they get "blocked" by the particles of lower size classes and thereby promoting inter-particle comminution. This can potentially promote inter-particle breakage due increased particle-particle contacts. It is also acknowledged that the feed rate will play a significant role in the promotion of inter-particle comminution in the device. The size distributions for the feeds and products are plotted in Figure 5.20. For comparison purposes, the product size distribution for the case when only the -19+13.2 mm particles were fed to the crusher operated under the same conditions is also included in Figure 5.20. The results are summarised in Table 5.2. The reduction ratios (based on 50 % passing sizes of the feeds and products) are at least 7.5. The ratio of the R_{50} for the two tests (T1 and T2) is equal to the inverse of the ratio of their F_{50}.

Table 5. 2: Reduction ratios

Description	**F_{50} (mm)**	**P_{50} (mm)**	**R_{50}**
T1 (wide PSD)	9.8	1.3	7.5
T2 (wide PSD)	8.1	0.92	8.8
Mono-sized feed (-19+13.2 mm)	15.8	1.8	8.8

Though the -19+13.2 mm (mono-size feed) has the same reduction ratio as T2 (feed with a wide size distribution), it had a high proportion of coarser particles. This can be observed in Figure 5.20 for the screen sizes above 1 mm that the cumulative mass passing for -19+13.2 mm are less than for tests with the feeds that have wide size distributions (T1 and T2). However, for the screen sizes below 200 µm, the test with -19+13.2 mm had more fines (high cumulative mass passing) than test T1 product. The -19+13.2 mm particles fed to the ROC are subjected to primary crushing when they just get nipped between the discs which can result in the production of fragments of a wider size distribution. These progeny particles are transported along the surface of the discs until when they get arrested (nipped) again. It was observed that the 'slab' particles, with dimensions as those shown in Figure 5.14, were also produced with the wide feed size distribution.

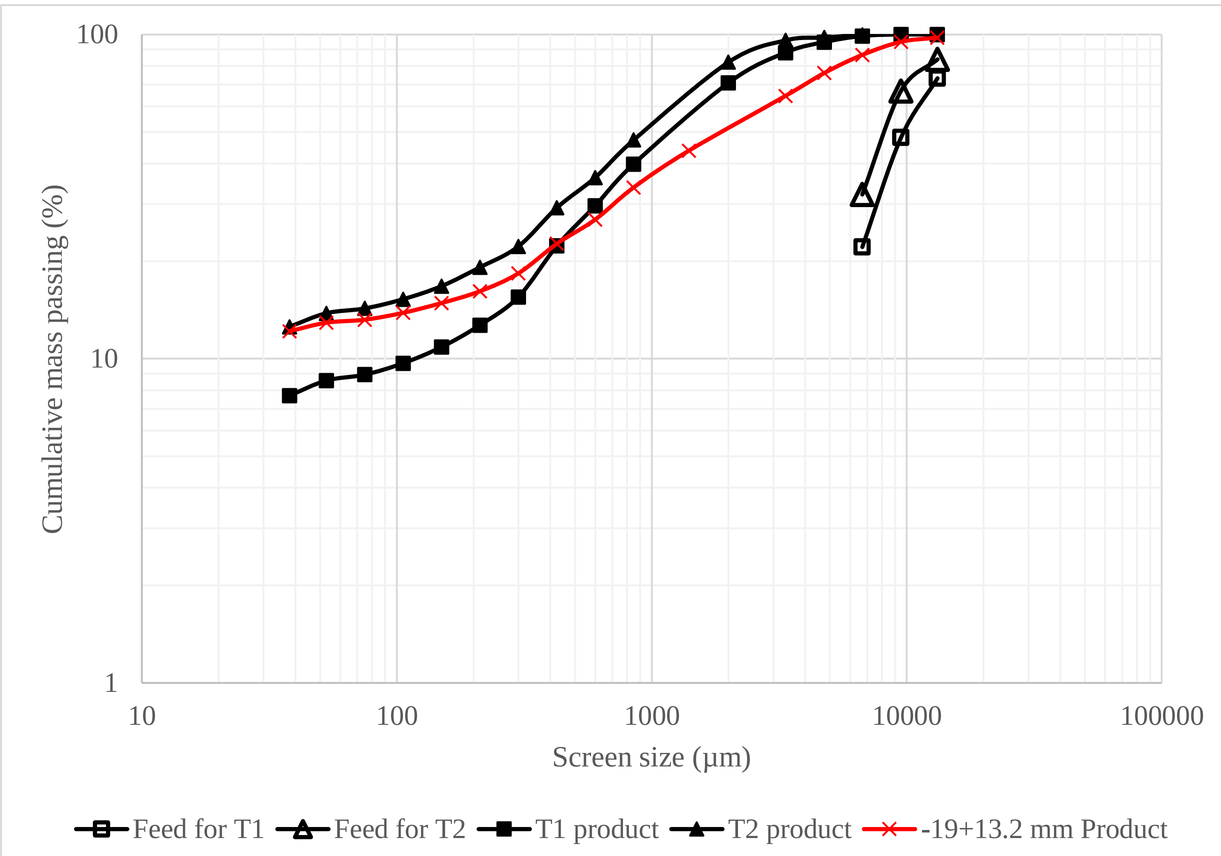

Figure 5. 20: Effect of feed size distribution on the product size distributions

6.6 Conclusions

Dimensional analysis was applied to the key operating variables and the dimensionless number relating feed size and vertical exit gap was derived. Apart from the dimensionless number in Eq.

(5.5), the ratio of shear energy and impact energy, discussed in Chapters 7 and 8, is another dimensionless number which proved to be highly dependent on the rotational speed of the discs. Experimental results for single particle crushing showed the reduction ratio are indifferent for 550 and 1000 rpm as shown by self-similar size distributions. This is contrary to previous results reported for the ROC (with both discs rotating) fed with many particles, which showed consistent increase of reduction ratio with the rotational speed (Nghipulile et al., 2021). Since the single particle nipped between the discs cannot provide enough friction to drive the top disc, it means that single particle in the crushing zone is forced against the stationary surface and once the applied stress is beyond the breakage energy threshold, breakage takes place. It is acknowledged that the crusher dynamics for the current and previous studies are different since with many particles, the freewheeling top disc is also accelerated to the speed closer or equal to that of the bottom disc.

The indications, so far, have highlighted that the disc speed is a key factor affecting the performance. Chapters 7 and 8 will discuss how speed affects the dominance of the breakage mechanisms in the crusher. From the experimental results, there is a slight increase in crusher throughput with the offset between the vertical axes of the discs. The reduction ratio seems to be indifferent for the three offsets that were tested which suggests that there are no benefits which can be derived from operating the ROC with offset greater than 10 mm (equivalent to 2% of the disc diameter). Effect of feed size distribution suggests that the feed with a wide size distribution of -19+4.75 mm (compared to mono-size feed of -19+13.2 mm) tends to produce a fine product, but not necessarily a high proportion of very fine particles (<212 μm). Slab particles were produced from the ROC. This could be attributed to insufficient crushing energy (suggesting a need to increase the compressive/tensile stress in the crusher) and shape of the profiles on the crushing surfaces. Choke feeding conditions were not investigated in this study. This could be one way to promote inter-particle comminution which can possibly make contribution to the elimination of the slab particles as well as energy efficiency. Another way to promote inter-particle crushing could be a crusher feed with a wide size distribution (with some near-vertical exit gap particles. This will allow the small particles in the feed to fill the voids between the larger particles which increase the density and promote attrition crushing and thereby breaking the flaky elongated particles. It is important that the crusher feed is evenly distributed to minimize segregation due to differences in the particle size. It is well known that segregation can negatively affect the performance of the crushers. With coarser feed on one end of the crushing chamber and the finer feed in the other end, this would reduce the probability of rock-on-rock crushing (Gröndahl et al., 2018; Nematollahi et al., 2021) and can also contribute to uneven wear of crusher liners around the crushing chamber.

The crusher should also be operated at an optimal speed and profiles should be added to maximize delivery of crushing forces to the particles. As already mentioned, the imposition of vibratory motion, as a way of increasing the compressive stress that is delivered to the particles, should be considered in the future designs. Optimizing the crusher exit gap, in relation to the feed size, to ensure that the ROC is used for the correct application (crushing stage) should also be looked at in future studies. It is recommended that a locked-cycle be conducted to establish the full potential of the device when it operated in closed circuits with the screens and allow the near size particles to fill the voids between the larger particles in the fresh feed to intensify rock-on-rock attrition crushing (choke feeding condition will be required). It is anticipated that recycling the near size particles with the fresh feed could also contribute to the reduction/elimination of the flaky elongated particles.

CHAPTER 6: COMPARATIVE STUDY OF CONE CRUSHER AND ROC: EFFECT ON PRODUCT SIZE DISTRIBUTION AND PARTICLE SHAPE

6.1 Introduction

In this chapter, the cone crusher and ROC are compared in terms of product size distribution and shape. Particle morphology such as shape can have a significant impact on the efficiency of mineral separation processes such as flotation (Burat et al., 2023; Dehghani et al., 2013; Guven, 2022) and gravity separation (Chikerema, 2011; Z. Tang et al., 2018) as well as mechanical (Rong et al., 2013) and rheological behaviours (Åkerstedt, 2019; Bhambhani, 2019; Desriviers Lehyt et al., 2019; Hafez et al., 2021; Shimoska et al., 2013) of granular materials. It is acknowledged that there are many indices used to describe the shape of the granular materials, including circularity, sphericity, angularity, elongation, aspect ratio, flatness, and compactness. Sphericity and aspect ratio were used to provide shape characteristics for ROC and cone crusher products with comparable size distributions.

6.2 Product size distribution

The cone crusher product size distributions are shown in Figure 6.1 together with the ROC product size distributions. The CSS and vertical exit gap of the cone crusher and ROC were bot equal to 4 mm. It is evident from Figure 6.1 that comparable product PSDs can be achieved for the two crushing devices, when the ROC is operated at 550 rpm for UG2 ore and coarser feed (-19+13.2 mm) of silica. For the finer feed (-13.2+9.5 mm) of silica, the cone crusher product PSDs compared fairly with the product PSD of ROC operated at 330 rpm. It is noted that the crushers were not choke fed during experimentation and their feed rate was approximately 1 tph. Choke feeding conditions could have generated different results and most likely relatively high proportions of fines in the products. The objective of the scope of the work that was conducted, as part of this study, was to get comparable PSDs for the products discharged from the two crushers and compare their shape characteristics as discussed in section 6.2.

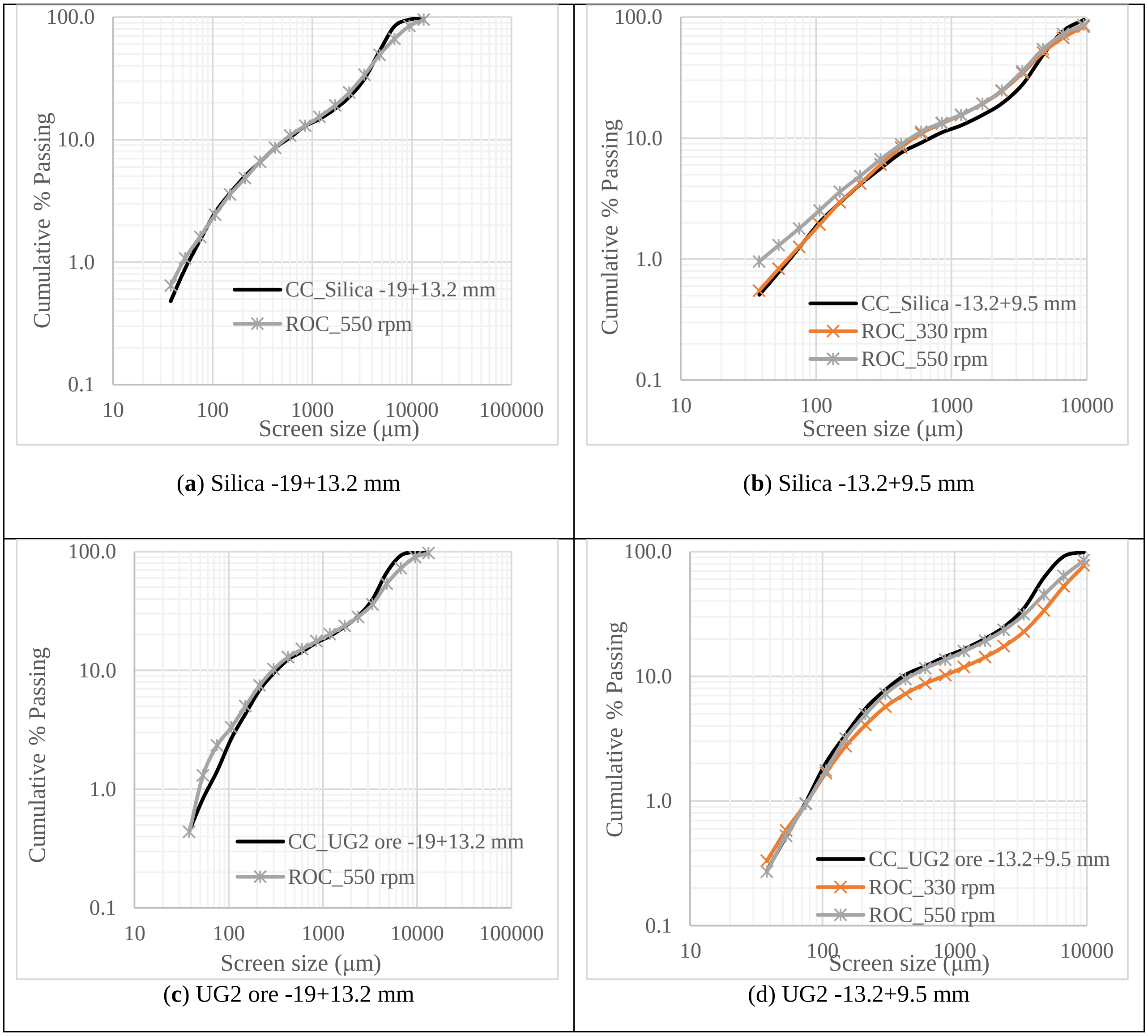

(**a**) Silica -19+13.2 mm

(**b**) Silica -13.2+9.5 mm

(**c**) UG2 ore -19+13.2 mm

(d) UG2 -13.2+9.5 mm

Figure 6. 1: Size distribution of ROC and cone crusher, (a) -19+13.2 mm of silica, (b) -13.2+9.5 mm of silica, (c) -19+13.2 mm of UG2 ore, and (d) -13.2+9.5 mm of silica

6.3 Shape factors for cone crusher and ROC products

Figures 6.2 and 6.3 show the ROC and cone crusher products for some of the tests with the -19+13.2 mm feeds and comparable product size distributions. It can be observed that both crushers discharged the slab particles. The particles only slip through based on whether their thicknesses are smaller than the CSS/OSS. Evidently, coarser slabby (flattened) particles were discharged from the ROC than the cone crusher as shown in Figure 6.2.

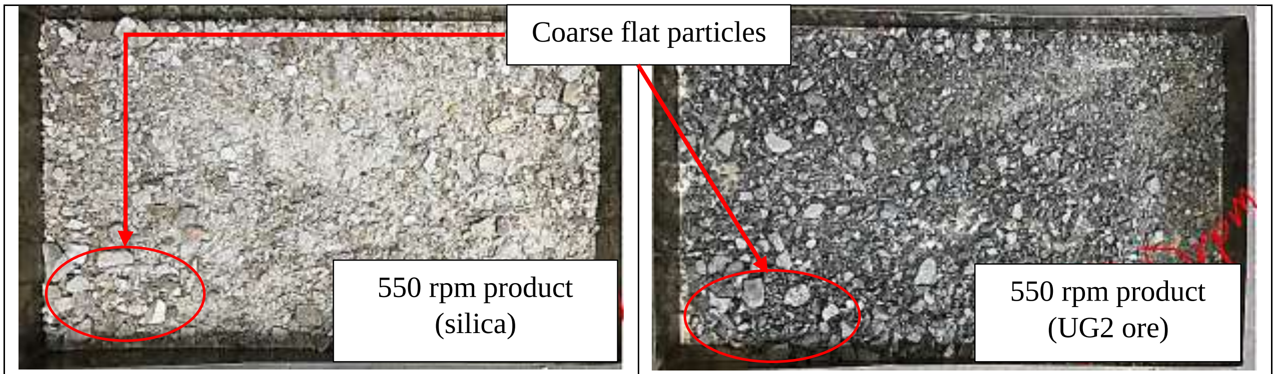

(a) (b)

*Figure 6. 2: Photographs of ROC products for -19+13.2 mm feeds crushed at 550 rpm; silica (**a**) and UG2 ore (**b**)*

(a) (b)

Figure 6. 3: Cone crusher products for the (a) silica and (b) UG2 ore (comparable PSDs to those shown in Figure 6.2)

Sphericity and aspect ratio were used to provide shape characteristics for ROC and cone crusher products for the -19+13.2 mm mono-size feed. The aspect ratio (*L*/*W*) of an object is the ratio of its longest dimension to its shortest dimension. Sphericity (ψ) is calculated using the following equation.

$$\psi = \frac{S_n}{S} \tag{6.1}$$

Where S_n is the nominal surface area (surface area of a sphere having the same volume as the object) and S is the surface area of the particle.

The sphericity and aspect ratios of individual grains in the progeny particles, classified as -1 mm and +1 mm, are shown in Tables 6.1 and 6.2 for silica and UG2 ore respectively. Measurements were done on at least 1000 grains for each size fraction. Since the individual grains in the +1 mm are mostly unliberated, as shown in Figures 6.4a and 6.4c for UG2 and in Figures 6.5a and 6.5c for silica, the shape characteristics are expected to be comparable for the two crushers. This can be inferred from both sphericity and aspect ratios in Tables 6.1 and 6.2. The -1 mm samples had more liberated grains (e.g., in Figures 6.4b and 6.4d and Figures 6.5b and 6.5d) and thus provided reliable shape characteristics of the individual particles. Table 6.1 shows that the sphericity and aspect ratios of the -1 mm progeny particles from tests conducted with silica are comparable. Table 6.2 also shows comparable average sphericity for -1 mm grains of silicates and chromite in the products of the two crushers. It is concluded that the shapes of the products of the two crushers are comparable under the operating conditions tested. One important morphological characteristic that may be worth investigating in the future is the surface roughness of the particles discharged from the crushers.

Table 6. 1: Shape characteristics of -19+13.2 mm silica progeny particles from the cone crusher and ROC

Characteristics	**Calculated statistics**	**Cone crusher**		**ROC**	
		-1 mm	+1 mm	-1 mm	+1 mm
Sphericity	Average	0.510	0.584	0.499	0.676
	Minimum	0.000	0.000	0.000	0.000
	Maximum	1.000	1.000	1.000	1.000
	σ	0.409	0.437	0.408	0.441
Aspect ratio	Average	-	1.489	-	1.366
	Minimum	-	1.000	-	1.000
	Maximum	-	9.000	-	4.000
	σ	-	0.720	-	0.578

Table 6. 2: Shape characteristics of -19+13.2 mm UG2 ore progeny particles from the cone crusher and ROC

Factor	Calculated statistics	Cone crusher				ROC			
		Silicates		Chromite		Silicates		Chromite	
		-1 mm	+1 mm	-1 mm	+1 mm	-1 mm	+1 mm	-1 mm	+1 mm
Sphericity	Average	0.552	0.499	0.685	0.552	0.523	0.612	0.810	0.767
	Minimum	0.000	0.000	0.000	0.000	0.000	0.000	0.000	0.000
	Maximum	0.960	1.000	0.000	0.000	1.000	1.000	1.000	1.000
	σ	0.467	0.460	0.436	0.454	0.187	0.445	0.340	0.436
Aspect ratio	Average	-	1.850	-	1.825	-	1.536	-	1.396
	Minimum	-	1.000	-	1.000	-	1.000	-	1.000
	Maximum	-	17.000	-	6.000	-	14.000	-	10.000
	σ	-	1.485	-	1.544	-	0.934	-	0.949

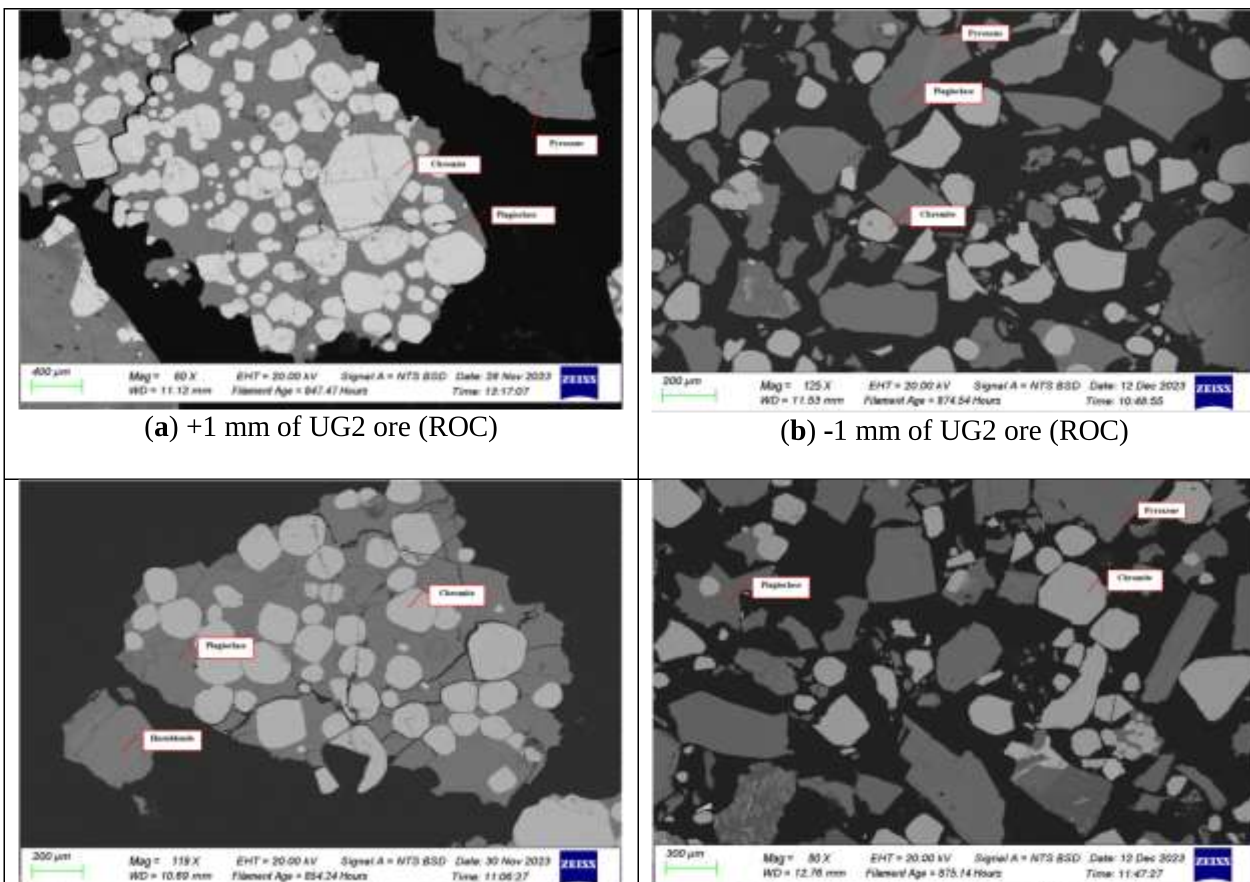

(**a**) +1 mm of UG2 ore (ROC)

(**b**) -1 mm of UG2 ore (ROC)

(**c**) +1 mm of UG2 ore (cone crusher)

(**d**) -1 mm of UG2 ore (cone crusher)

Figure 6. 4: SEM BSE images of UG2 progeny particles (-1 mm and +1 mm) of ROC and cone crusher

(**a**) +1 mm of silica (ROC)

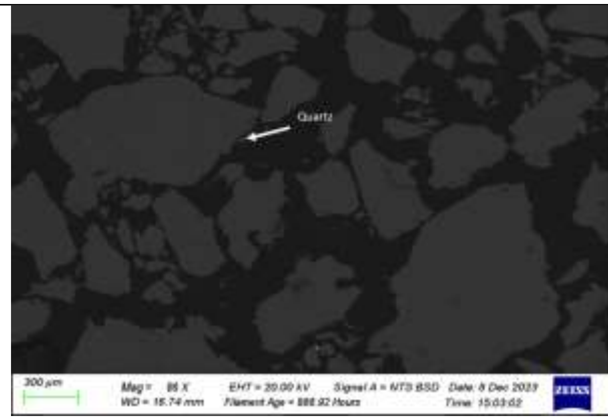

(b) -1 mm of silica (ROC)

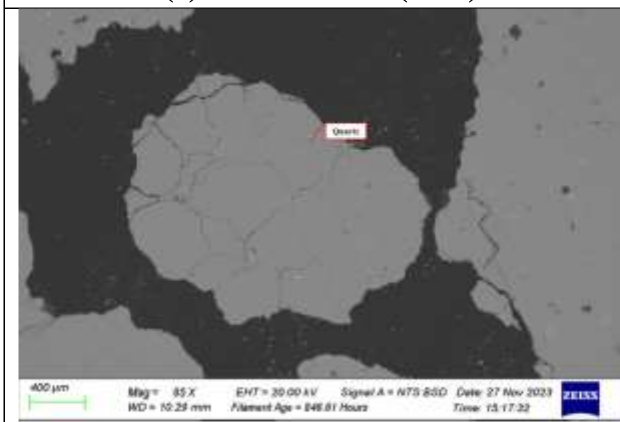

(**c**) +1 mm of silica (cone crusher)

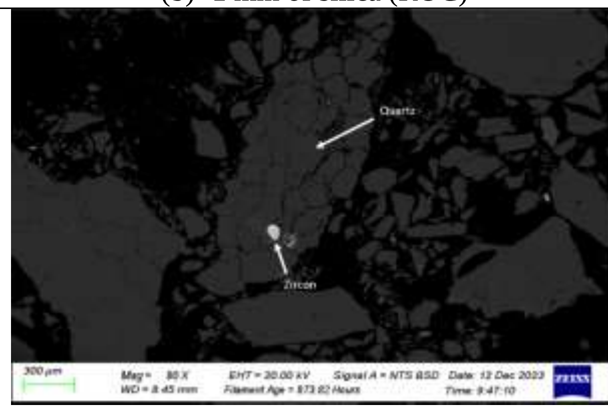

(**d**) -1 mm of silica (cone crusher)

Figure 6. 5: SEM BSE images of silica progeny particles (-1 mm and +1 mm) of ROC and cone crusher

6.4 Conclusions

The limited crushing tests conducted with the cone crusher and ROC suggest that under comparable feeding condition, the products of the two crushers can have comparable size distributions. Furthermore, the shape characteristics in terms of sphericity and aspect ratio are also comparable for the two crushers. It is recommended that more experiments should be conducted choke feeding condition and a variety of other operating variables (feed size distribution, feed material (strength), vertical exit gap for the ROC, CSS for cone crusher, rotational speed, horizontal offset for ROC) in order to generate more comparative data for performance evaluation in terms of product size distribution, power draw and throughput. It is recommended that the structure hosting the discs should be reinforced to allow the delivery of maximum force to the particles.

CHAPTER 7: DICRETE ELEMENT MODELLING OF THE BREAKAGE OF SINGLE POLYHEDRON PARTICLES IN THE ROC

7.1 Introduction

The fragmentation process can be modelled using existing mathematical modelling approaches which account for the stochastic nature of comminution by using the selection and breakage functions. The shortcoming of such approaches is the inability to capture the micro-dynamic information which are contributing to overall particle breakage and flow in comminution equipment (Li, 2013). Numerical simulation tools such as discrete element method (DEM) make it possible to mechanistically model engineering devices such as the ROC whose principles underpinning its performance are not yet fully understood. To gain a better insight into the comminution process in this device, a discrete element modelling of the crushing device was performed using the simulated single polyhedral ore particles to study the effect of the rotational speed (550, 1000, 1450, 1900 and 2350 rpm) on single particle crushing when the crusher is operated under different dynamics, viz., (1) stationary top disc, and (2) both discs rotating at the same speed.

The Ab-t_{10} breakage model (Vogel & Peukert, 2004;Shi & Kojovic, 2007) was used to study the crushing behaviour of the single polyhedral particle. Experimental data for the single UG2 ore particle (-19+13.2 mm) crushed in the laboratory ROC (discussed in Chapter 5) were used to calibrate the breakage parameters of the Ab-t_{10} breakage model. This model can predict the breakage behaviour of particles, including non-spherical particles (André & Tavares, 2020; Guo et al., 2024; Jiménez-Herrera et al., 2018a; Tavares et al., 2020) and thus realistic particles such as polyhedrons can be used. The results generated from the computational experiments provided the preliminary insights into performance potential of the current design of the ROC for hard rocks application.

7.2 Effect of crusher dynamics on normal and tangential forces

7.2.1 Both discs rotating at same speed

The fragmentation process of a single particle along the comminution cavity is simple to describe, with the size of the particles progressively reduced. Sequential arresting (nipping) and release (moving further along the comminution cavity of the crusher until they get arrested between the discs again) happens until the progeny particles are small enough to escape from the crushing zone. Figure 7.1 illustrates the progressive comminution when the two discs are both rotating at 1450 rpm. Similar diagrams could be shown for the other simulated speeds.

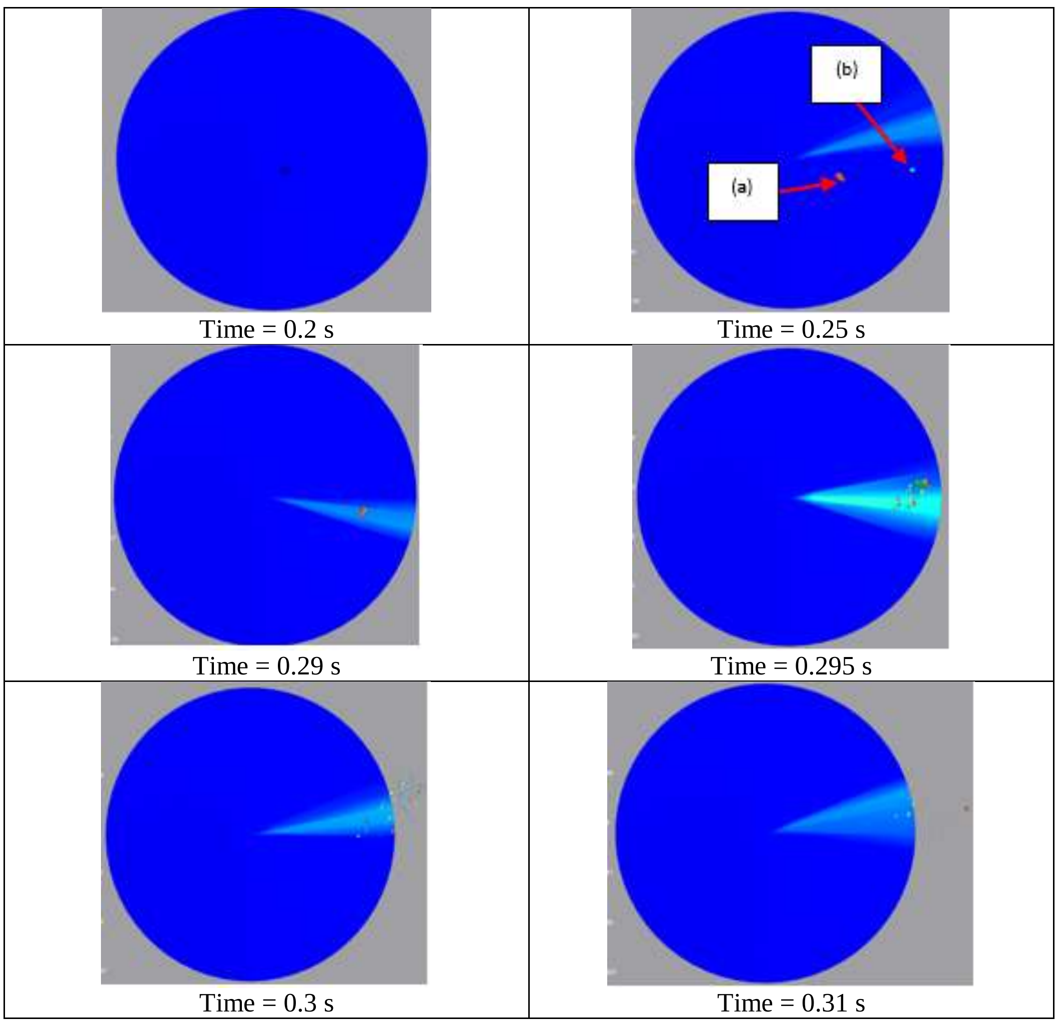

Figure 7. 1:. Spatial images of progressive particle breakage along the comminution cavity when ROC is operated with both discs rotating at same speed (1450 rpm), (a) parent particle (most of it) and (b) chipped fragment from the parent particle.

Figure 7.2 shows the normal and tangential forces acting on the particle(s) because of bottom disc-particle interactions for various speeds. Similar trends could be shown for the forces due to upper disc and particle interactions. It is evident that fracture events of the particle(s) correspond to the higher normal and tangential forces. For the speed of 1450 rpm in Figure 7.1, it can be observed that a body breakage of the particle happens when the simulation time is 0.295 s. This time, in turn, corresponds to the highest normal and tangential forces of 4.6 and 1.4 N respectively as shown in Figure 7.2. Prior to 0.295 s, as evident for simulation time of 0.25 s in Figure 7.1, chipping of small fragments from the parent particle was happening.

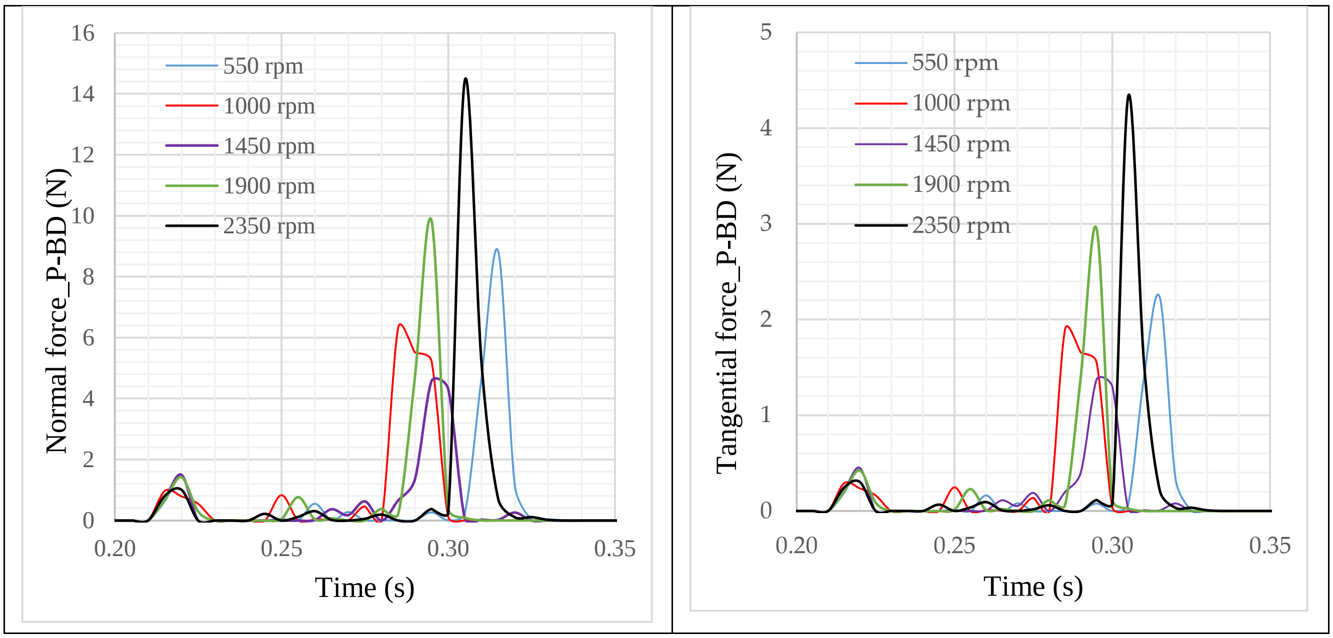

Figure 7. 2:. Normal and tangential forces due to bottom disc and particles interactions for various speeds for the simulated ROC with both discs rotating at same speeds

7.2.2 Stationary top disc

The normal and tangential forces acting on the particle(s) as a result of bottom disc-particle interactions are shown in Figure 7.3 for various speeds. Similar trends could be shown for forces due to the upper disc and particle interactions. Compared to Figure 7.2, it is evident that with the stationary top disc, the residence time is relatively longer (e.g., approximately 0.73 s for 1900 rpm speed). It is also evident that both normal and tangential forces are relatively higher when the crusher is operated with a stationary top disc. Since these forces can be used to infer the wearing characteristics due to the geometry-particle contacts, the results suggest that the wear of the crushing surfaces can be reduced by manipulating the crusher dynamics, with a stationary disc crusher expected to be associated with higher wear rates. Optimization of the operating speed can be conducted to reduce the shear stress due to discs-particles contacts while promoting interparticle comminution within the device.

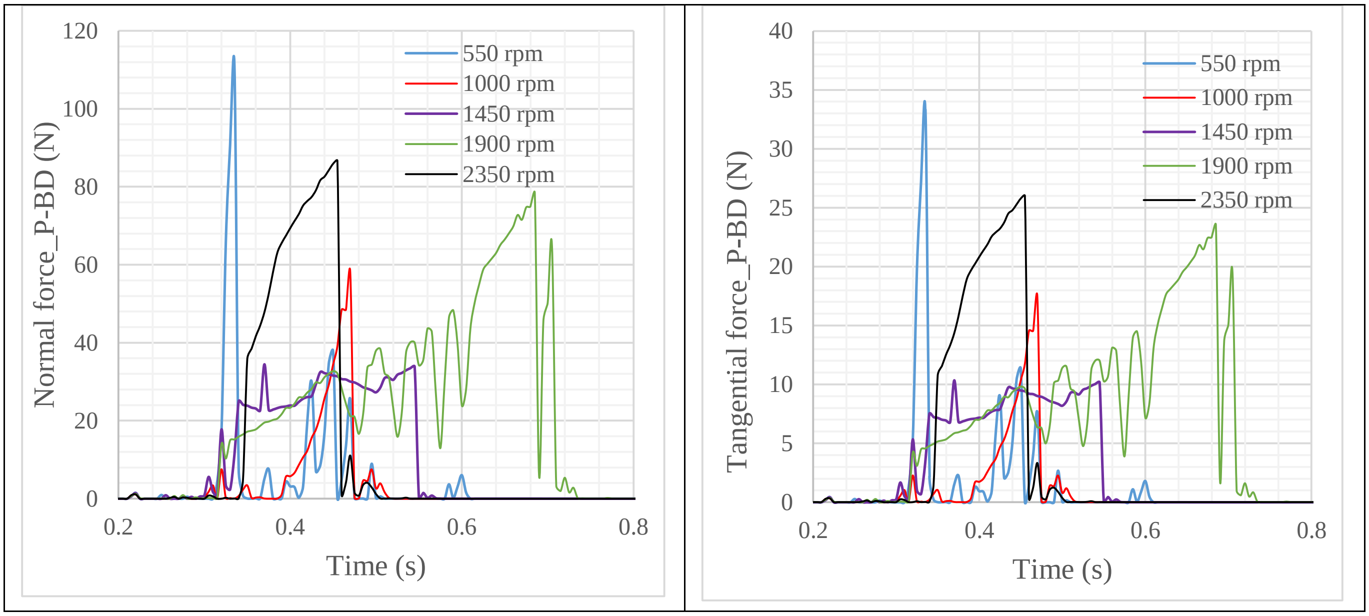

Figure 7. 3:. Normal and tangential forces due to bottom disc and particles interactions for various speeds for the simulated ROC with stationary top disc

7.3 Effect of crusher dynamics on size reduction ratio and specific comminution energy

7.3.1 Size reduction ratio

Figure 7.4 shows the reduction ratios, in terms of 80% passing sizes, for the two scenarios, i.e., (1) stationary top disc and (2) both discs rotating at the same speeds. As already observed from experimental data (see Figure 5.3 in Chapter 5), when the top disc is stationary, the crusher reduction ratios tend to be comparable for various speeds. This is also evident for simulated reduction ratio (shown by black line) in Figure 7.4. A similar trend could not be observed for the simulated ROC operated with both discs rotating at the same speed. For this crusher dynamic, the reduction ratio increases with the speed until 1000 rpm, beyond which it consistently decreases with the speed. For this limited simulation dataset, the results suggest the 1000 rpm speed to be the optimal speed for maximizing the reduction ratio when the two discs are rotated at the same speed. The reduction ratios of at least 8 for both scenarios compare well to those observed from experimental data in Figure 5.3.

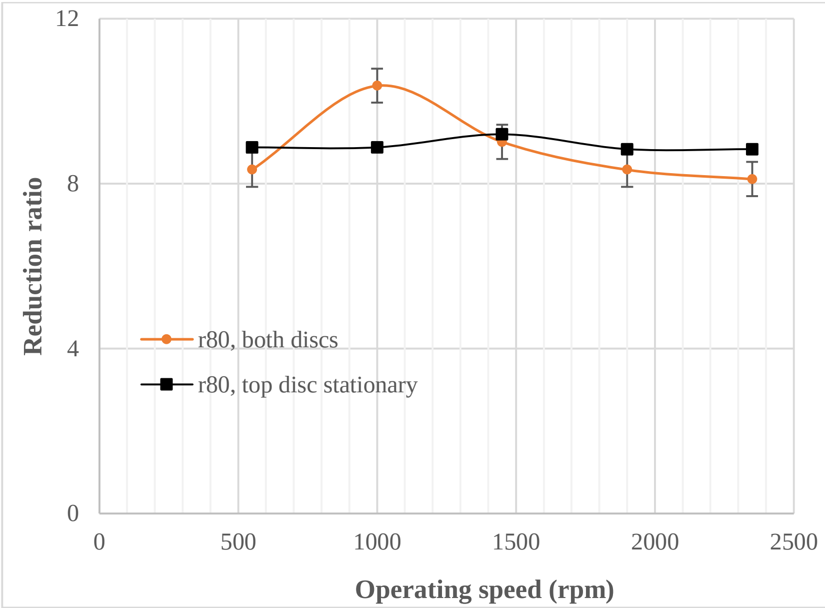

Figure 7. 4:. Reduction ratio against crusher speed

7.3.2 Energy consumption

The impact (compressive), shear and dissipated energies due to particle-particle, particle-bottom disc and particle-top disc interactions are presented in Figures 7.5 and 7.6 for case 1 (stationary top disc) and case 2 (both discs rotating at same speed) respectively. From Figure 7.5, it is evident that shear energies due to particle-bottom disc (P–BD) and particle-top disc (P–TD) interactions are higher than the corresponding impact energies. This highlights that the ROC with a stationary disc is characterized by high shear actions which, in turn, could contribute to high operating costs (due to frequent replacement of crusher liners). The impact energies due to particle-discs interactions are highest at 1450 rpm. This is also the speed at which the shear energy due to particle-top disc is highest. A slightly higher reduction ratio at this speed (see Figure 7.4) can be attributed to the increased compressive and shearing actions.

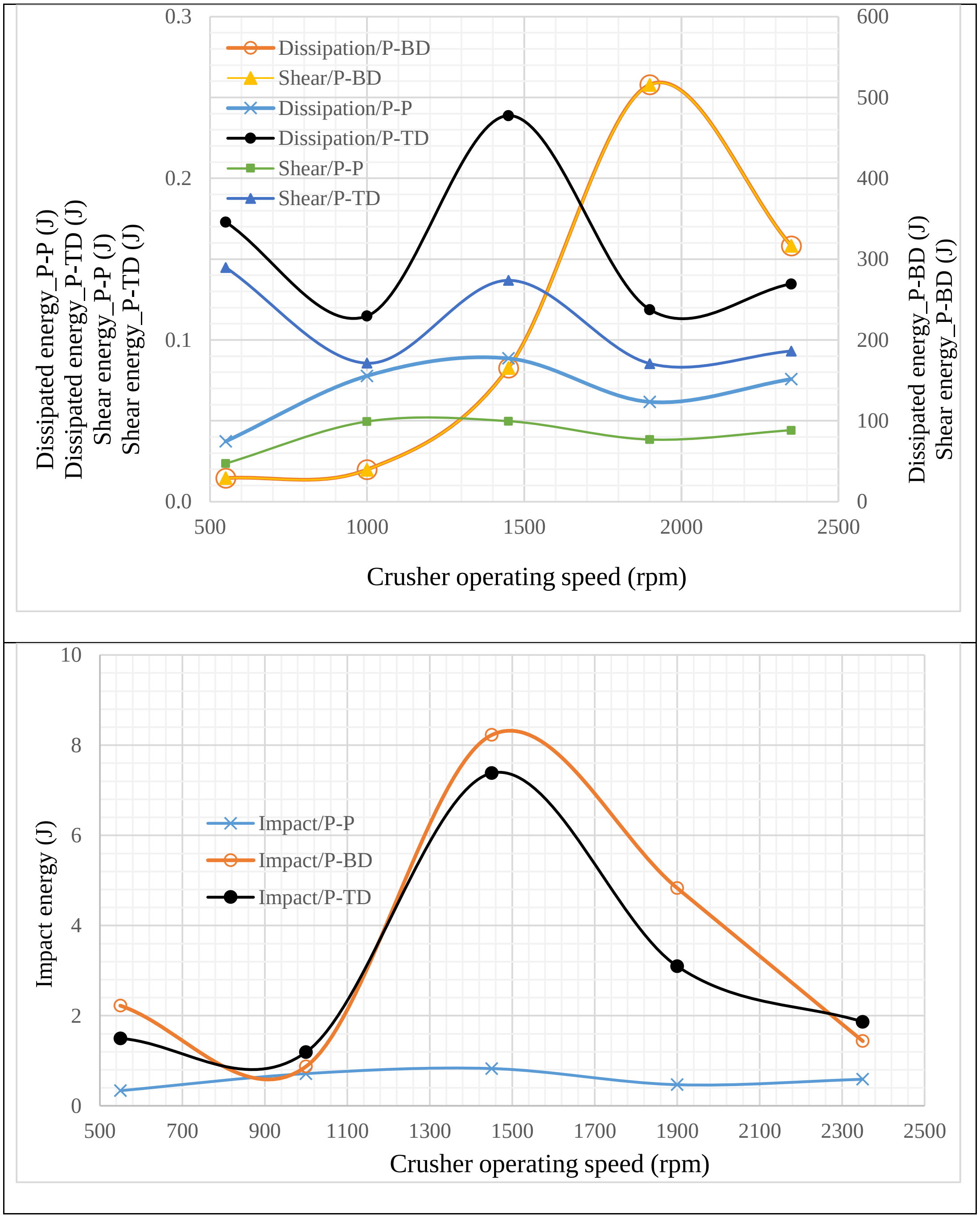

Figure 7. 5:. Impact, shear and dissipated energies due to interactions when the ROC is operated with a stationary top disc. P-P, P-BD and P-BD denotes particle-particle, particle-bottom disc and particle-top disc interactions respectively.

From Figure 7.6, it is evident that the shear energy due to geometry-particle contacts increases with the speed which suggests that the degree of shear breakage mechanism increases with the speed. Compared to the crusher design with the stationary top disc (see Figure 7.5), the shear and dissipated energies are significantly lower when both discs are rotating at the same speed. The impact energy due to P-BD interaction decreases with gradual increase in the rotational speed of the discs until 1000 rpm, beyond which it is relatively constant.

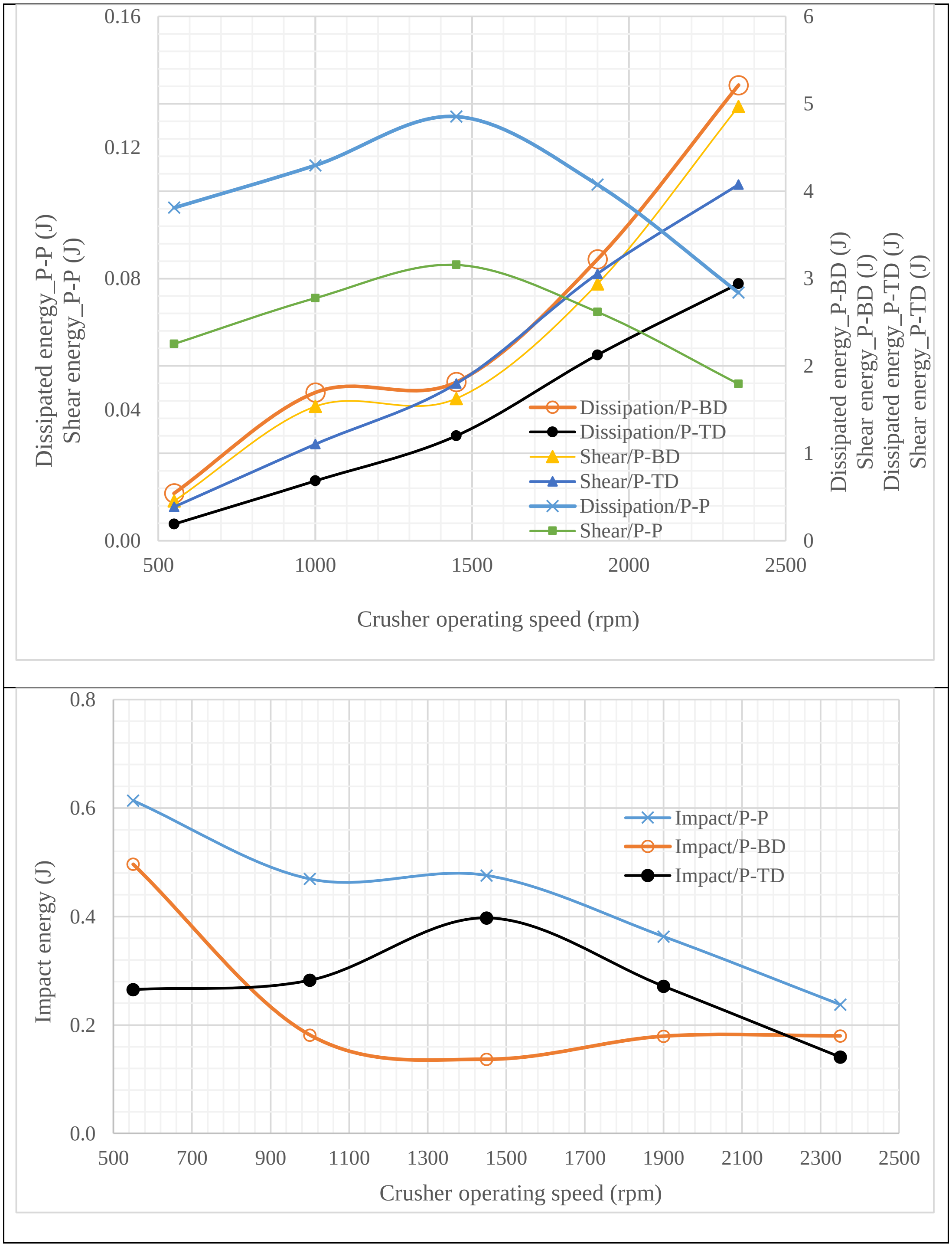

Figure 7. 6:. Impact, shear and dissipated energies due to interactions when the ROC is operated with both discs rotating at the same speed. P-P, P-BD and P-BD denotes particle-particle, particle-bottom disc and particle-top disc interactions respectively.

From Figure 7.6, the impact energy due to P-TD is showing a different trend, with it increasing with speed until 1450 rpm, beyond which it decreases with increasing speed. The shear energy due to particle-particle interactions is also highest at 1450 rpm. For optimization purposes, it is desirable that the crusher is associated with many particle-particle (P-P) events (interparticle comminution) and minimal shearing actions due to discs-particles interactions.

The specific comminution energy was calculated from the sum of impact and shear energies using the following equation.

$$E_{cs} = \frac{(E_{impact} + E_{shear})}{3.6 \times M_p} \tag{7.1}$$

Where 3.6 is a conversion factor, E_{impact} is the sum of impact energy due to particle-particle, particle-bottom disc and particle-top disc interactions, E_{shear} is the sum of shear energy due to particle-particle, particle-bottom disc and particle-top disc interactions and M_p is the mass of the particle.

Eq. (7.1) was modified to include the dissipated energy (i.e., the energy that is not recovered and is absorbed in the dashpots) in order to calculate the total specific energy as follows.

$$E_{s,total} = \frac{(E_{impact} + E_{shear} + E_{dissipated})}{3.6 \times M_p} \tag{7.2}$$

Where $E_{dissipated}$ is the sum of dissipated energy due to particle-particle, particle-bottom disc and particle-top disc interactions.

The ratio of specific comminution energy to total specific energy was defined as energy utilization (E_u) as shown in the following equation to evaluate the efficient utilization of the available energy for breakage.

$$E_u = \frac{E_{cs}}{E_{s,total}} \times 100 \tag{7.3}$$

Comminution energy, total specific energy and energy utilization are summarized in Table 7.1. As expected, the ROC with a stationary top disc is characterised by higher specific energies which is attributed to high shear energy of that stationary disc. For the ROC with a stationary top disc, the energy utilization is approximately 50% for all speeds. This implies that half of the input energy of the system was utilized to effect breakage. Changing the system dynamics (e.g., allowing both discs to rotate) can be said to provide some performance advantages since the specific energies reduced significantly to below 1 kWh/t and energy utilization (especially at low speeds) also increased. The reduction in the specific energy is attributed to the reduced shear energy due to discs-particles interactions as a result of increased flexibility in the crusher.

Table 7. 1: Summary of net comminution and total energies

Speed (rpm)	**Comminution energy**				**Total specific energy (kWh/t)**	**Energy utilization (%)**
	Impact (J)	**Shear (J)**	**TOTAL (J)**	**Specific (kWh/t)**		
Case 2 – stationary top disc						
550	4.058	29.145	33.203	1.844	3.471	53.133
1000	2.778	39.659	42.437	2.357	4.571	51.568
1450	16.434	165.466	181.899	10.103	19.313	52.315
1900	8.401	515.661	524.062	29.109	57.768	50.389
2350	3.891	316.420	320.311	17.792	35.388	50.276
Case 2 – both discs rotating at the same speed						
550	1.375	0.902	2.277	0.126	0.173	73.162
1000	0.933	2.714	3.647	0.203	0.341	59.378
1450	1.010	3.508	4.518	0.251	0.426	58.951
1900	0.814	6.062	6.876	0.382	0.685	55.766
2350	0.558	9.090	9.648	0.536	0.993	53.966

Shear/impact ratios, calculated from the shear and impact energies, are plotted against the energy utilization in Figure 7.7. It is evident that the shear/impact ratio increases with the rotating speed and it is inversely proportional to the energy utilization. To maximize the energy utilization, it is recommended that the ROC is operated at low speeds. At higher speeds, the ROC is comparable to a laboratory pulverizing device, with abrasion comminution being dominant over compressive comminution. Thus, to advance the ROC from the status of a laboratory pulveriser to an innovative comminution device requires further design innovations. Apart from the importance of disc profiling discussed in Chapter 5, the device could have vertical vibratory motion to the top disc to increase the compressive stress and thereby shattering the particles which could partly reduce the slabby particles discharged from the crusher. Furthermore, interparticle comminution has to be promoted when the crusher is fed, under choking condition, with the feed that has a suitable size distribution. Increasing the height of the feed opening/gape of the crusher's comminution cavity to promote interparticle comminution, as shown in Figure 7.8, is recommended in future studies.

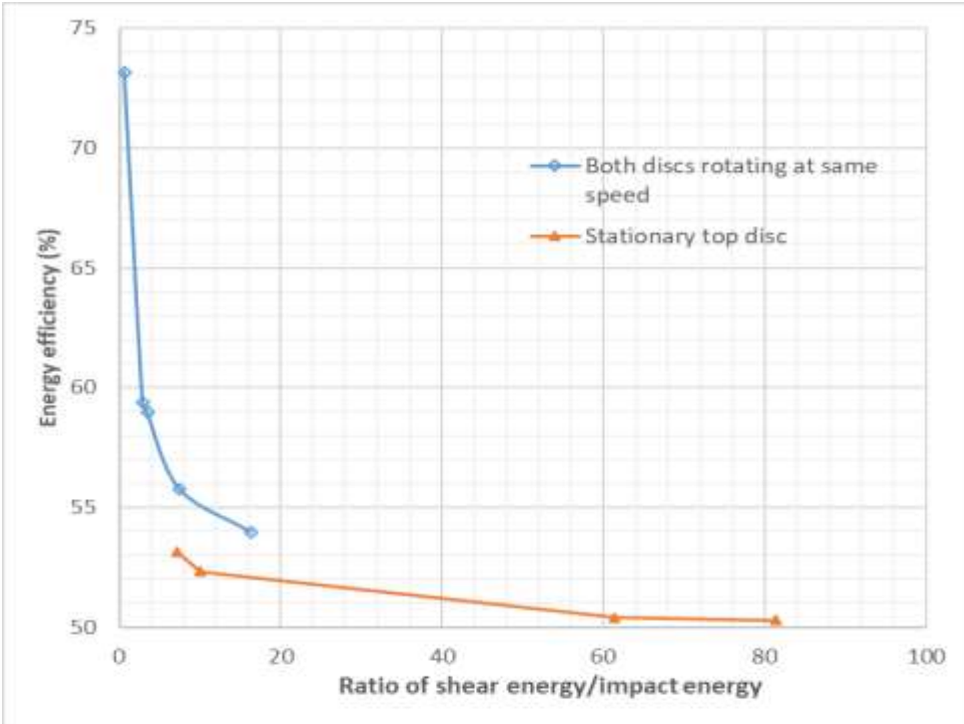

Figure 7. 7:. Relationship between discharge rate (throughput), reduction ratio and crusher operating speed

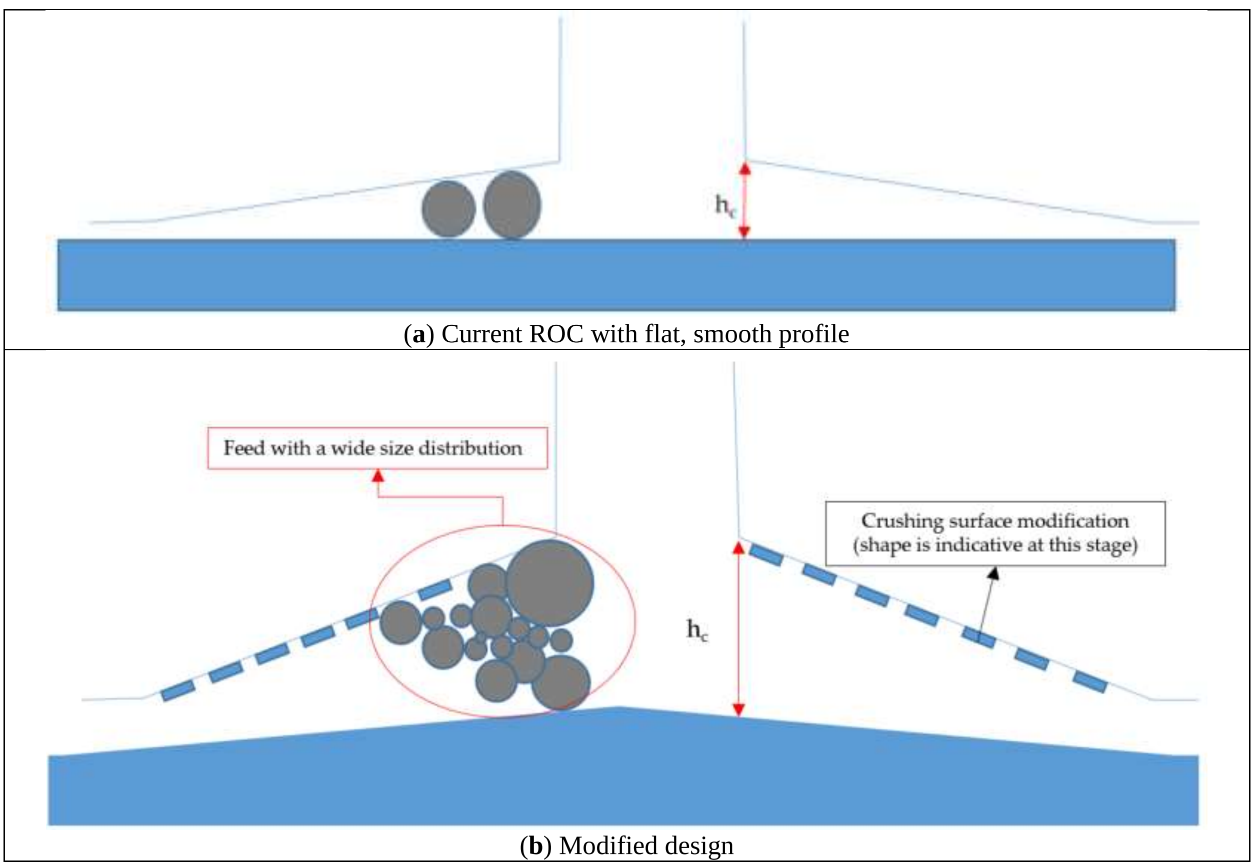

*Figure 7. 8:. ROC crushing chamber, (**a**) current design and (**b**) modified design for consideration in future studies*

7.4. Effect of crusher dynamics on throughput

The throughput of the crusher was evaluated using the following equation.

$$Q = \frac{M_f}{t} \qquad (7.4)$$

Where Q is the throughput in kg/h, M_f is the feed mass and t is the residence time in the crushing zone.

Figure 7.9 plots the throughput (and the reduction ratio) against crusher operating speed. The difference in the crusher's dynamic due to the speed differential, affects the rate at which the progeny particles are discharged from the crushing zone. While comparable reduction ratios were achieved for the two crusher designs, the difference in dynamics allows fast transmission of compressive and shear stresses on the particles (hence faster throughput) when both discs are spinning at the same rate.

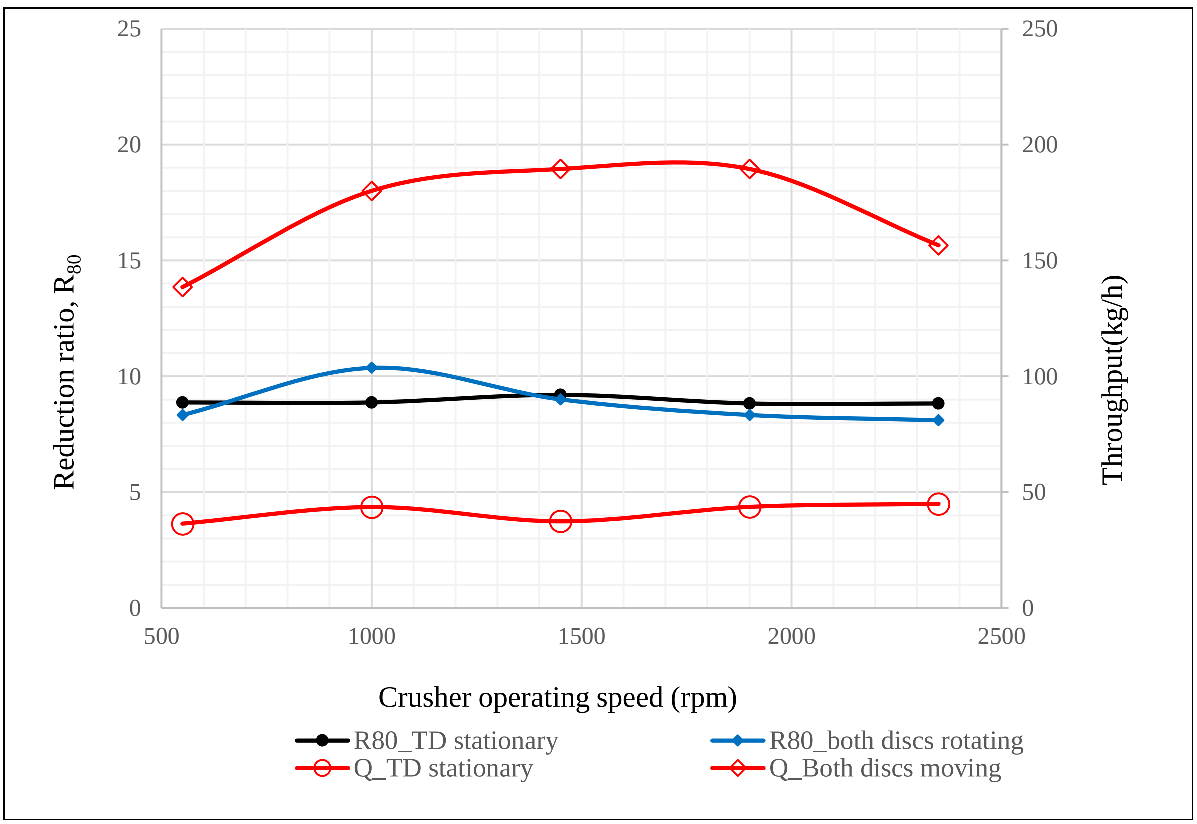

Figure 7. 9:. Relationship between throughput, reduction ratios and crusher operating speed

From Figure 7.9, it is evident that the stationary top disc negatively affects the crusher throughput, with throughputs less than 50 kg/h and seem insensitive to the rotational speed. When the crusher is simulated with both discs rotating at the same speed, the progeny particles tend to be discharged faster, with throughputs greater than 130 kg/h. It is acknowledged that further simulation studies involving calibration of geometry-particle interaction parameters and particle shape could provide more insights into the performance potential of the crusher in terms of throughput. It is thus recommended that once the crushing chamber is redesigned to promote interparticle comminution, material transport should be thoroughly investigated in order to benchmark the ROC to other crushing devices. Decoupling material transport during the simulation is also recommended as it can provide more insights on the flow behaviour of particles (of different shapes) in the ROC with a variety of profile. The optimized profile can then be adopted for the crusher to maximize the throughput and also investigate the opportunities to improve product quality (in terms of shape and size).

7.5 Discussions

Dynamic information about the crusher was provided by the DEM simulations. This includes the normal and tangential forces acting on the particles (e.g., in Figures 7.2 and 7.3). It is evident from Figures 7.2 and 7.3 that when the crusher is operated with a stationary top disc, the residence times are relatively longer. This suggests low throughputs, as depicted in Figure 7.9. Optimization of the ROC throughput is highly dependent on the rate of rotation of the discs, with the difference in the speeds of discs proving to be an important variable which should be considered in future studies. It is evident that the stationary disc crusher has high normal and tangential forces compared to the ROC with both discs, which are rotated at the same speed. Since higher forces suggest a higher wear rate (higher operating costs), it is recommended that the crusher not be operated with the stationary disc. The crusher with both discs rotating should rather be optimized further in the quest to increase inter-particle comminution and reduce crushing surface wear while not compromising on the throughput.

While Figure 7.4 suggests comparable reduction ratios for the two crusher designs, the impact and shear energies due to the geometry-particle contacts are relatively higher (see Figures 7.5 and 7.6) when the ROC is operated with a stationary top disc. This translates into high specific energies, which is another motivation to disqualify the implementation of such a design. On the other hand, the specific energies for the ROC with both discs rotating are less than 1 kWh/t, as shown in Table 7.1. Realistic energy consumption of the device can only be quantified in future work when the crusher is operated under choke feeding conditions to promote interparticle comminution and the opening of the comminution cavity has been increased as suggested in the modified design shown in Figure 7.8.

The ratio of shear energy and impact energy against the energy utilization in Figure 7.7 has shown that high energy utilization (>53%) can only be achieved with the ROC operating with both discs rotating. However, the crusher should not be operated at speeds above 1000 rpm if an energy utilization of >60% is desired (as shown in Table 7.1). Operating the crusher at higher speeds, as recommended in a previous study (Nghipulile, 2019), may not be the best option since this can be associated with high wear rate, but not necessary an improved crushing efficiency.

7.5. Conclusions

Discrete element modelling of single particle breakage in the ROC was conducted. Experimental test work with the laboratory ROC generated data that were used to validate the breakage function in the Ab-t_{10} breakage model. With a single particle, throughput above 130 kg/h can be achieved when both discs are rotating at the same speed. This is contrary to the ROC with a stationary top disc, which has throughputs below 50 kg/h. Specific energies are above 1 kWh/h due to higher normal and tangential forces when the crusher has a stationary disc. On the other hand, to have specific energies below 1 kWh/t, the crusher should be operated with both discs rotating at the same speed. It is acknowledged that the magnitude of specific energies would be higher when the ROC is fed with many particles, but the deduced trend is still expected. The results are discussed in Chapter 8.

Based on the available information, it is not recommended to operate the ROC with a stationary disc, as such an operation will be associated with higher operating costs. Both discs should be allowed to rotate, but the speed differential between the discs can be optimized to reduce wear while not compromising on throughput. For easy control during operation, it is recommended that both discs have separate drivers, rather than relying on friction to drive the freewheeling top disc.

CHAPTER 8: USING DISCRETE ELEMENT METHOD TO STUDY THE EFFECT OF OPERATING VARIABLES ON ROC PERFORMANCE

8.1 Introduction

The results of the DEM simulations for the crusher fed with many particles are presented. The breakage and transportation of many particles in the ROC was simulated to try to gain a deeper insight into the mechanisms underpinning the performance of this novel crushing device. The ROC was simulated to understand the effect of the offset between the vertical axes, speeds of the discs, differential between the speeds of the discs and direction (co-current or counter-current) of rotation of the discs as well as the feed rate. Simulations generated data which provided insights into the effect of operating variables on the degree of dominance for different breakage mechanisms and failure modes.

8.2 Effect of horizontal offset

One unique design feature of the ROC is the horizontal offset between the vertical axes of the two discs. The feed rate, speed and exit gap were fixed at 1 tph, 1000 rpm and 4 mm respectively while the offset was varied (base (no offset), 10, 20 and 30 mm). The effect of the offset can only be pronounced for offset values greater than 10 mm due to the flattened edge of the top disc which is on the current design.

8.2.1 Effect of horizontal offset on impact and shear energies

The different energies due to contacts are plotted against the offset in Figures 8.1 and 8.2. While the impact and shear energies due to particles-particles (P-P) contacts seem to be indifferent for all the offsets, they are slightly higher for the 10 mm offset. This suggests that a 10 mm offset (representing 2% of the disc diameter) may be optimal for the promotion of inter-particle comminution. At this offset, the impact and shear energies (due to P-P interactions) are 27.8 J and 4.59 J. This suggests that particle fracture due to P-P interaction is highly driven by compressive stress (6 × shear stress). Energies due to particles-bottom disc (P-BD) interactions are also not significantly changing with the offset, but the shear stress is dominant (shear energy is ~60 J) compared to the compressive stress (impact energy is ~15 J). Energies due to particles-top disc (P-TD) contacts are very high when the crusher is operated with no offset between the vertical axes of the discs. However, when there is an offset, P-TD contact energies are fairly constant for all simulated offsets. The same trends can be deduced for the dissipated energy. Figure 8.2 also shows the dissipated energy at 1 s for the four offsets. Similar images for impact and shear energies are included in Appendix I. It can thus be concluded that shear breakage mechanism is dominant in the ROC over impact breakage and the degree of dominance is not very sensitive to the change in the offset (assuming crusher is operated with offsets in the range of 10 to 30 mm, feed rate of 1 tph, speed of 1000 rpm and exit gap of 4 mm). As argued in Chapter 5, the offset provides necessary flexibility. However, as the results in Figure 8.1 show, there is no benefit in increasing the offset beyond 10 mm. It is for this reason that the effect of speed, feed size distribution and feed rate were studied with the crusher offset of 10 mm.

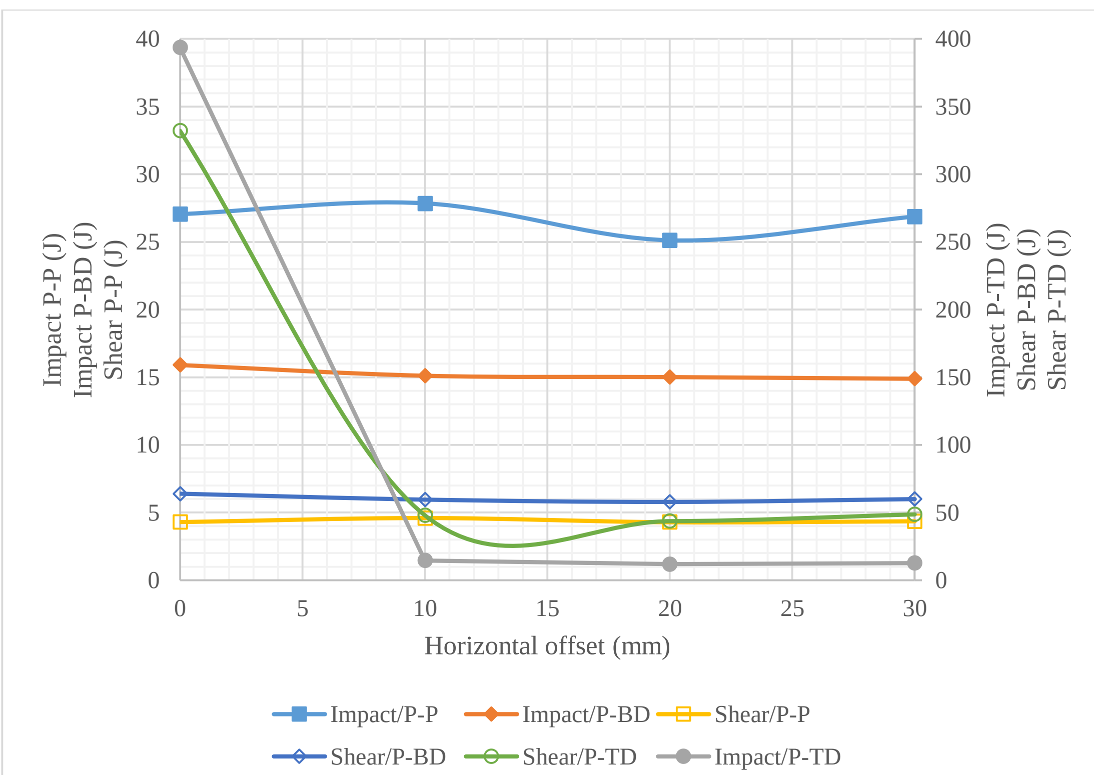

Figure 8. 1: Impact and shear energies as function of horizontal offset

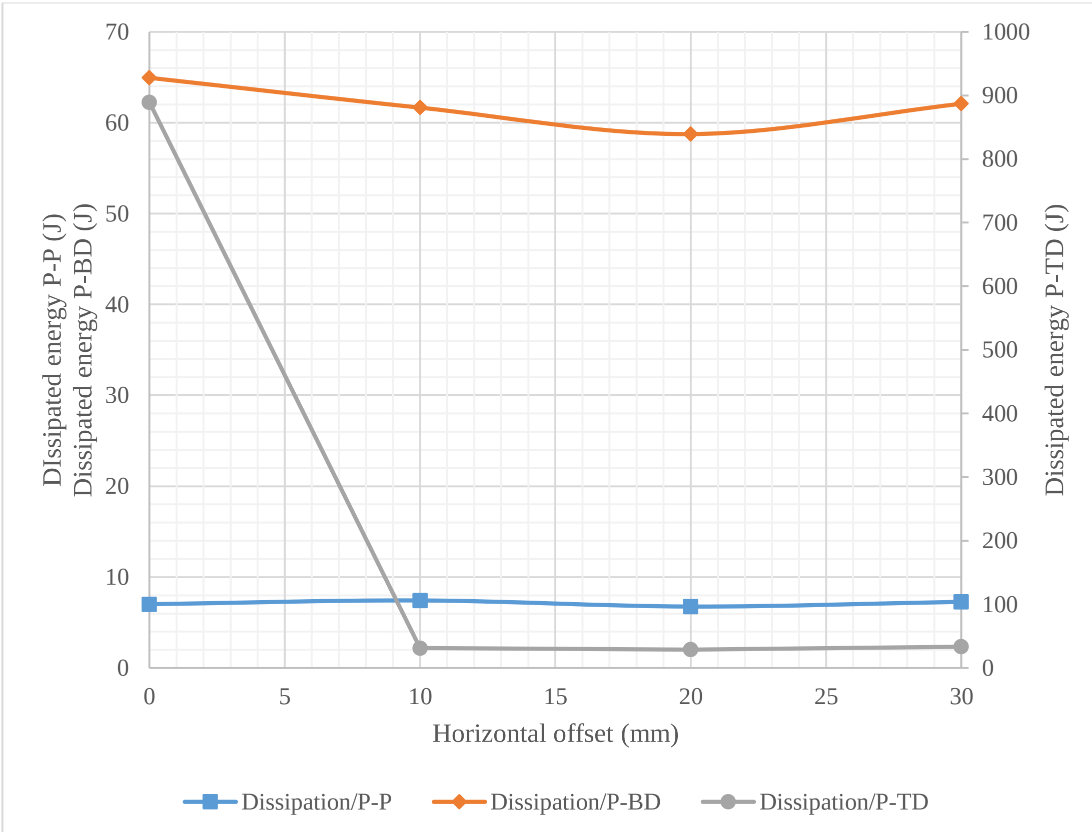

Figure 8. 2: Impact and shear energies as function of horizontal offset

8.2.2 Crushing efficiency and throughput

Table 8.1 summarizes the comminution energy and energy utilization using the equations that were discussed in Chapter 5. Specific energy is highest for 0 mm offset. With no offset, the energy dissipated is highest (Figure 8.2) and this results in low energy efficiency (only ~48% of the available energy was used to effect comminution). Energy utilization is about 63% when there is an offset between the vertical axes of the discs. Comparable specific input energies can be observed for the horizontal offsets of 10-, 20-, and 30-mm. Similar input energies produced crusher products with comparable size distributions as shown in Figure 8.3. It can be concluded that the offset does not significantly affect the product size distribution. However, it is undesirable to operate the crusher with no offset between the vertical axes of the discs because that is associated with power draw, it is over 50% less efficient. A slightly high shearing action with a 30 mm offset (see Table 8.1) seems to have contributed to a significant production of the progeny particles. This can be attributed to Mode III (shearing, tearing) as qualitatively shown in Figure 8.4 that after 0.5 s, more fines were produced for the 30 mm offset.

Table 8. 1: Summary of energy utilization for effect of offset

Offset (mm)	**Comminution energy**		**Total energy (kWh/t)**	**Energy utilization (%)**	**Shear to Impact ratio**
	J	kWh/t			
0	836.9	0.83	1.73	47.9	0.92
10	169.6	0.17	0.27	63.0	1.95
20	157.8	0.16	0.25	62.8	2.03
30	167.4	0.17	0.26	63.5	2.07

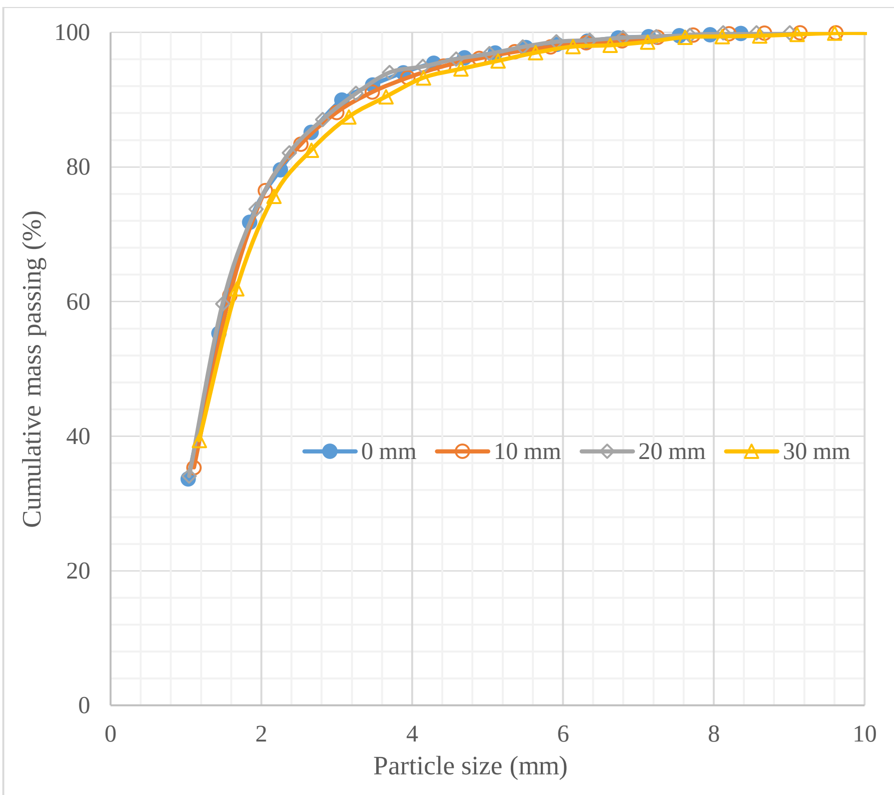

Figure 8. 3: Product size distributions for different offsets

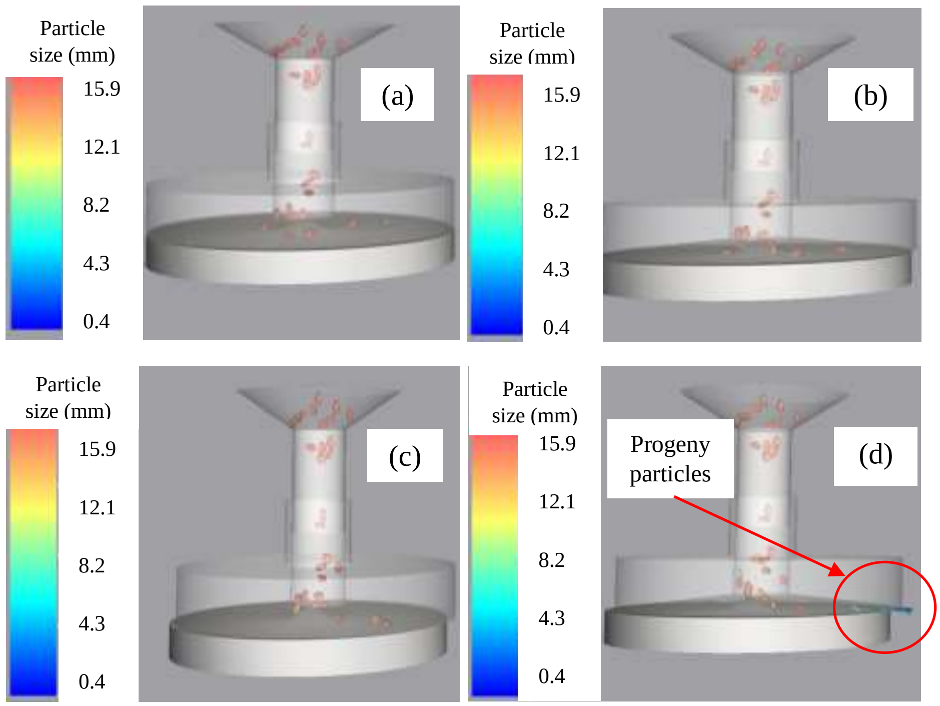

Figure 8. 4: Particle size at 0.5 seconds, (a) 0 mm offset, (b) 10 mm offset, (c) 20 mm offset, and (d) 30 mm offset

Reduction ratios (R_{80}) were calculated using the following equation.

$$R_{80} = \frac{F}{P_{80}} \qquad (8.1)$$

Where *F* is the mean feed size (15.8 mm).

As a way of deducing the trend for reduction ratios from physical experiments and DEM simulation, Figure 8.5 compares the R_{80} for the physical experiments conducted at 830 rpm and 3 mm gap to the R_{80} for simulated ROC operating at 1000 rpm and 4 mm gap. It is evident that the reduction ratio decreases at higher offsets (23 and 30 mm). Though the trends were not generated at the exactly similar operating conditions, the general trend provides a confidence in the DEM's ability to provide a realistic prediction of the real system. The throughput is plotted in Figure 8.6 together with the reduction ratio. While the throughput increased slightly when the offset was increased beyond 10 mm, this is just a 2% increase. It is note that a slight increase in throughput was also observed from physical experiments (see Figure 5.19 in Chapter 5). It can thus be argued that the ROC throughput is not sensitive to the change in the offset between the vertical axes. This is true with the current design that has a flattened edge of 10 mm on the top disc. The change in the profiles on the discs could change the system dynamics which could yield different trends on the effect of offset.

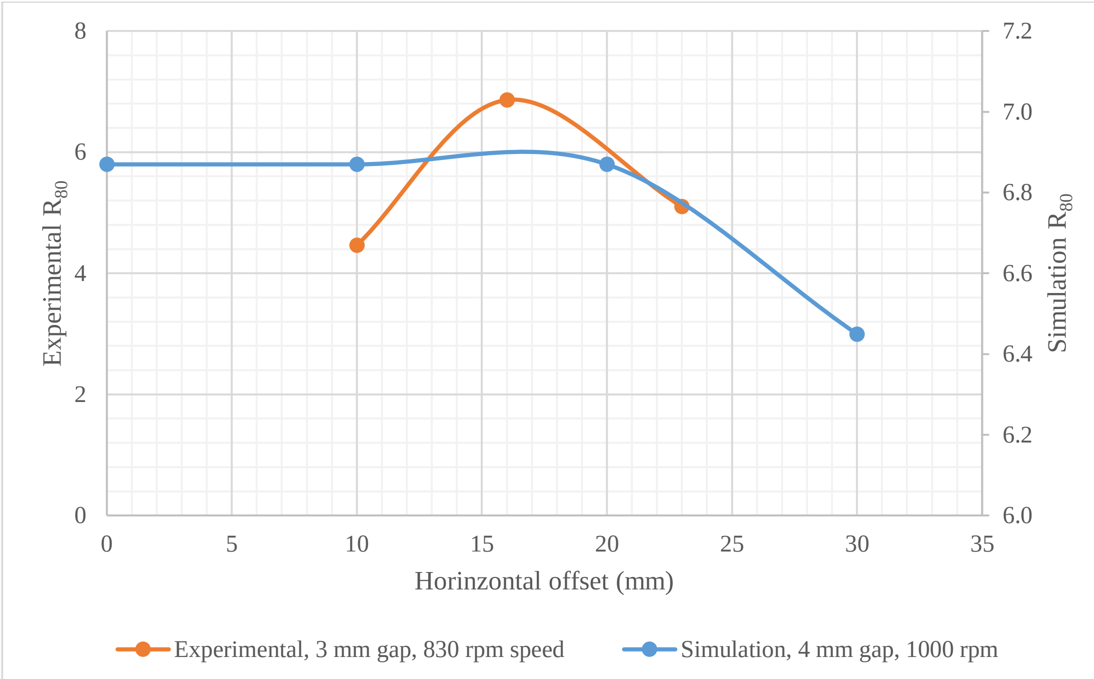

Figure 8. 5: Experimental and simulated reduction ratio versus top disc offset

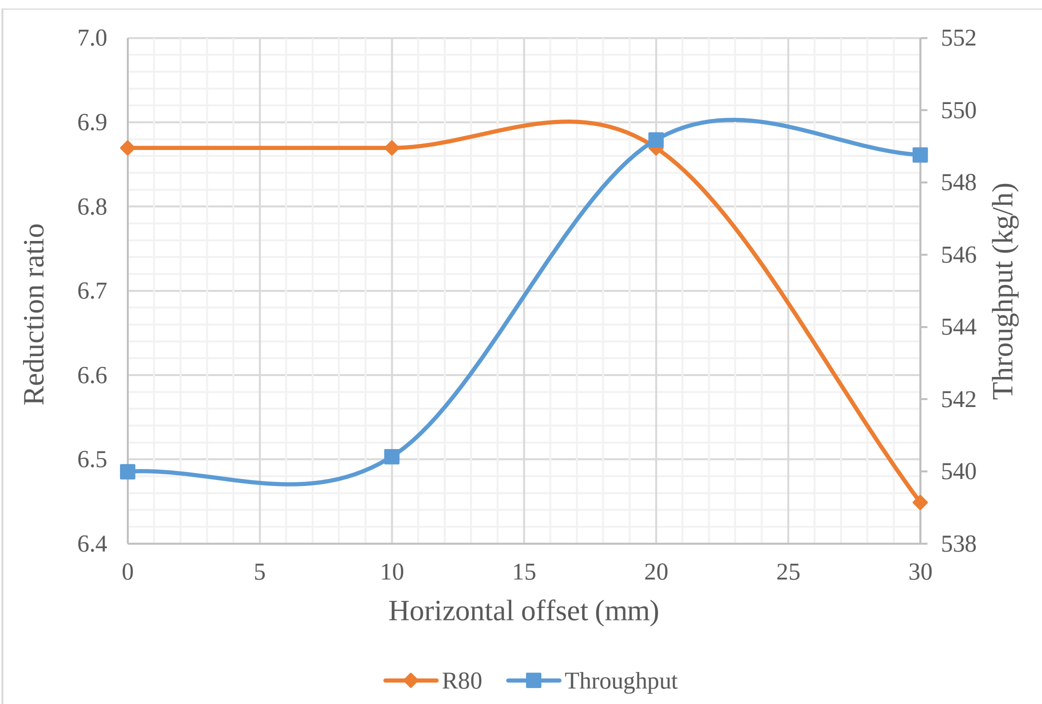

Figure 8. 6: Crusher throughput as a function of offset, based on simulation

8.3 Effect of rotational speed

DEM simulations were set-up to investigate the effect of the rotational speeds of the discs (ranging between 330 and 3000 rpm) while the feed rate, offset, exit gap were fixed at 1 tph, 10 mm and 4 mm respectively. The simulated speeds include the experimental values (330, 550, 830 and 1000 rpm rpm) whose results are discussed in section of 5.4 of Chapter 5 as well as the extrapolated ranges (above 1000 rpm).

8.3.1 Effect of rotational speed on impact and shear energies

The impact, shear, and dissipated energies due to particles-particles (P-P), particles-bottom disc (P-BD), and particles-top disc (P-TD) contacts for a variety of speeds are shown in Figures 8.7 and 8.8. It is clear from Figure 8.7 that the shear energies due to P-BD and P-TD increase with rotational speed while the impact energies decrease with the rotational speed until 1000 rpm, beyond which the speed does not affect the impact energies (compressive stress) that the particles experience. It can, therefore, be argued that particles in the ROC operating above 1000 rpm experience high shear stress, which is possibly only "polishing" the particles without a significant size reduction. To intensify the transmission of the compressive stress to the particles, speeds below 1000 rpm should be considered, but the crushing surfaces should also be modified to have some corrugations (the shape of the profile should be carefully optimized for a reduced wear rate). Another observation is that the low speeds are associated with more particle-particle impact events. The shear energy due to P-P interaction is about 4 J, and it seems to be insensitive to the change in speed. To leverage on the benefits of the inter-particle particle comminution mechanism in terms of energy utilization, as reported for high-pressure grinding rolls (HPGR) and vertical roller mills (VRM) (Altun et al., 2015; Daniel et al., 2010; Liu et al., 2018; Pareek & Sankhla, 2020; Reichert et al., 2015), it is critical that energies due to P-P contacts in the crushing zone of the ROC are further increased.

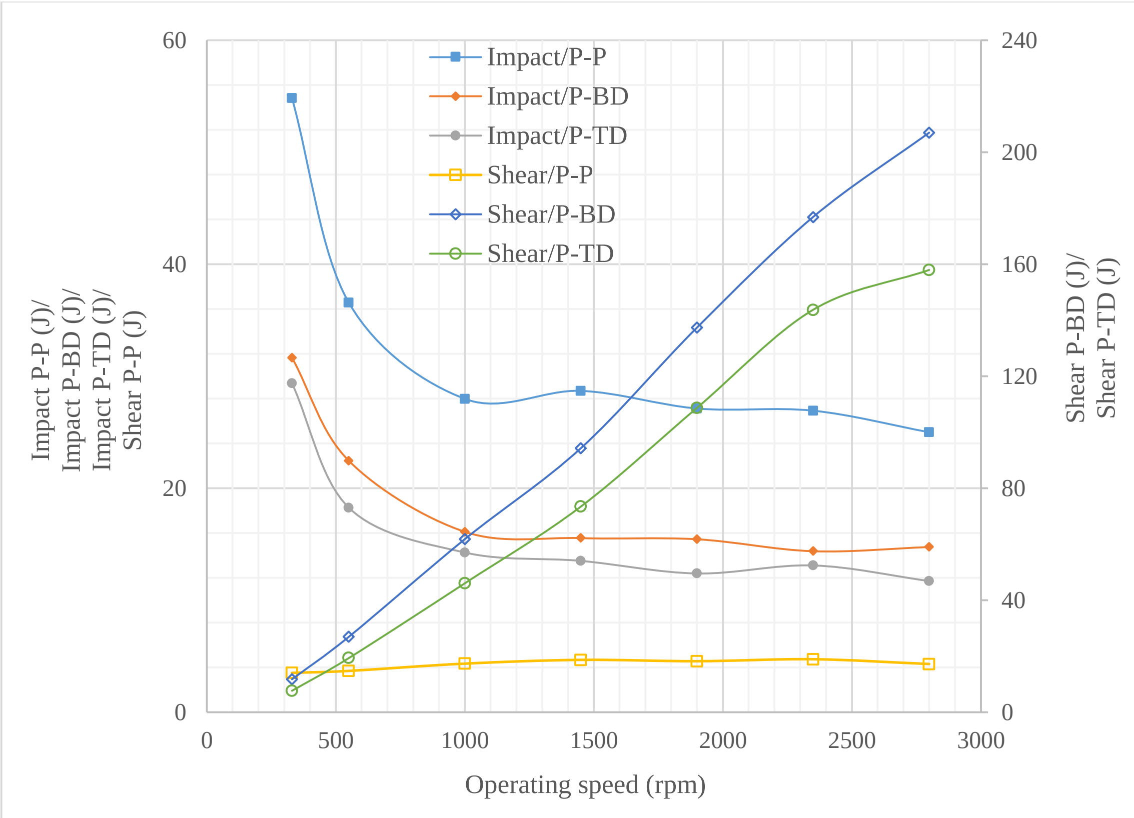

Figure 8. 7: Impact and shear energies as function of rotational speed

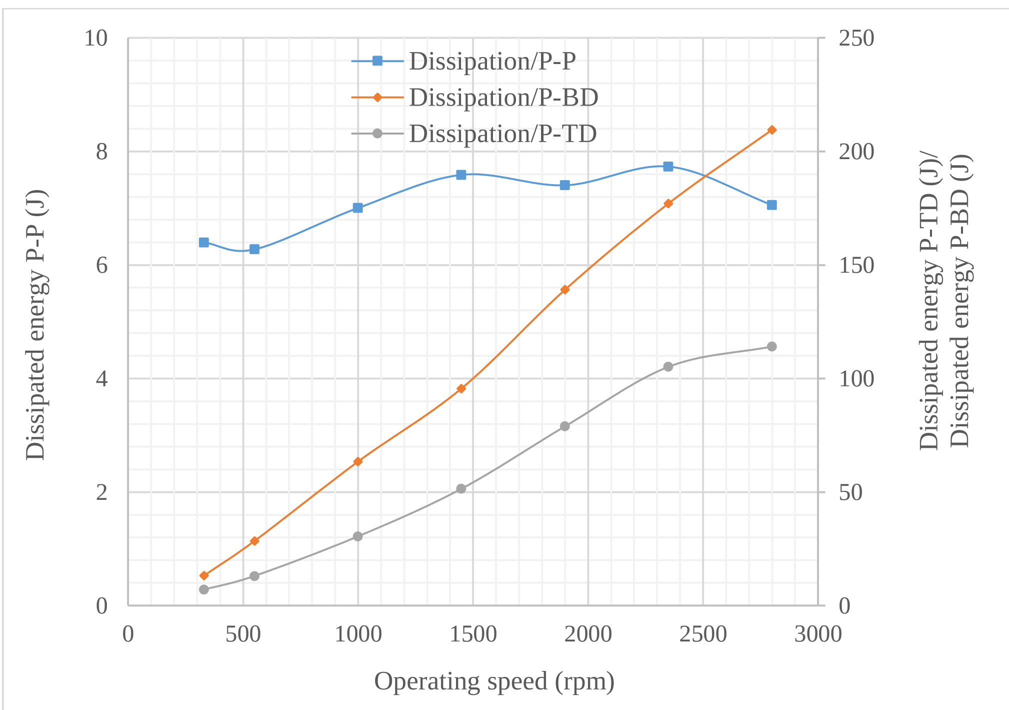

Figure 8. 8: Dissipated energies as function of rotational speed

The cumulative impact and shear energies due to P-BD interactions are presented in Figure 8.9. Only data for 330, 1000 and 2800 are plotted for clarity. The rest of the data are presented in Appendix J. It is observed that for any number of P-BD contact events, the impact energy is highest at 330 rpm. This suggests that the ROC should be operated at low speeds to maximize compressive stress. It is acknowledged that speeds smaller than 330 rpm were not simulated or experimentally tested to deduce a clear trend and help estimate the critical speed of the crusher. It is recommended that low speeds (e.g., 100 and 220 rpm) be investigated to determine the critical speed of the crusher.

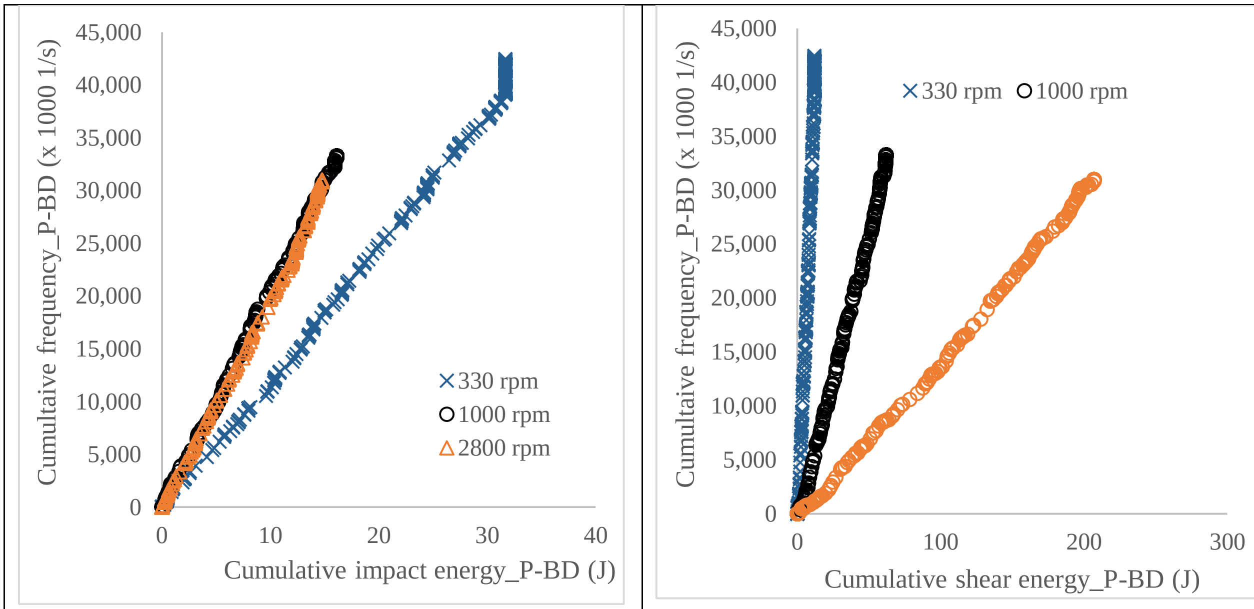

(a) Impact energies

(b) Shear energies

Figure 8. 9: Cumulative impact and shear energies due to discs-particles interactions for a variety of speeds

8.3.2 Crushing efficiency and throughput

Comminution energy, total specific energy, energy utilization, and the ratio of impact and shear energies are summarized in Table 8.2. The product size distributions for various speeds are shown in Figure 8.10. Reduction ratios, in terms of 80% passing size, are presented in Figure 8.11. The size distributions are not very different, except for the 1450 rpm, which is relatively coarser. It is acknowledged that the increasing trend between reduction ratios and speed observed in the experiments could not be replicated in the simulations. Results, in terms of energy consumption, should be analysed qualitatively. A decrease in energy utilization with speed suggests that increasing speed is associated with energy waste. High speed implies high power draw, but since the product does not necessarily become finer, more energy is available but not efficiently utilized to effect breakage. It is noted that the results were for the 1 tph feed rate. If more particles are available in the crushing zone, it is speculated that more comminution events will take place and efficiently use the available energy. For optimization purposes, it is recommended that the discs can be operated at different speeds (e.g., the top disc is operated at a low speed to increase the compressive stress, while the bottom disc is operated at a relatively higher speed to still achieve high throughput). For easy control during operation, it is recommended that the two motors for the respective discs be incorporated into the design, rather than having the top disc freewheeling and driven by the friction generated by the particles in the crushing zone. The power draw and reduction in the wear rate can be optimized through speed adjustments.

Table 8. 2: Summary of energy utilization for effect of offset

Speed (rpm)	**Comminution energy**		**Total energy (kWh/t)**
	J	kWh/t	
330	139.0	0.138	0.164
550	127.4	0.126	0.174
1000	170.7	0.169	0.270
1450	230.3	0.228	0.382
1900	305.7	0.303	0.527
2350	379.8	0.377	0.664
2800	420.8	0.417	0.745

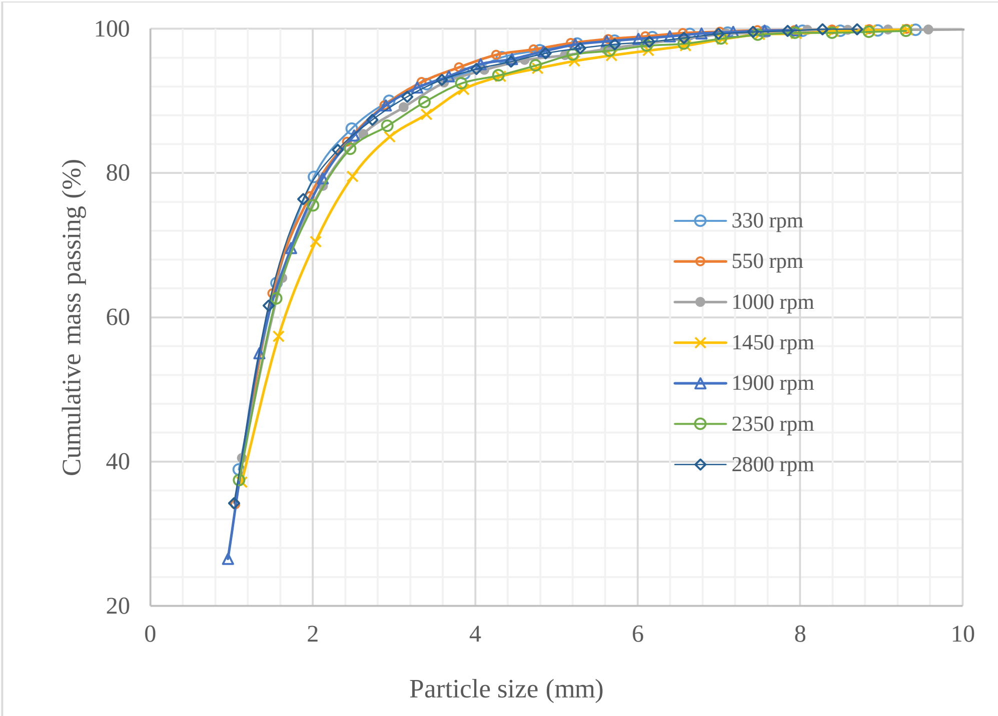

Figure 8. 10: Product size distributions for different speed

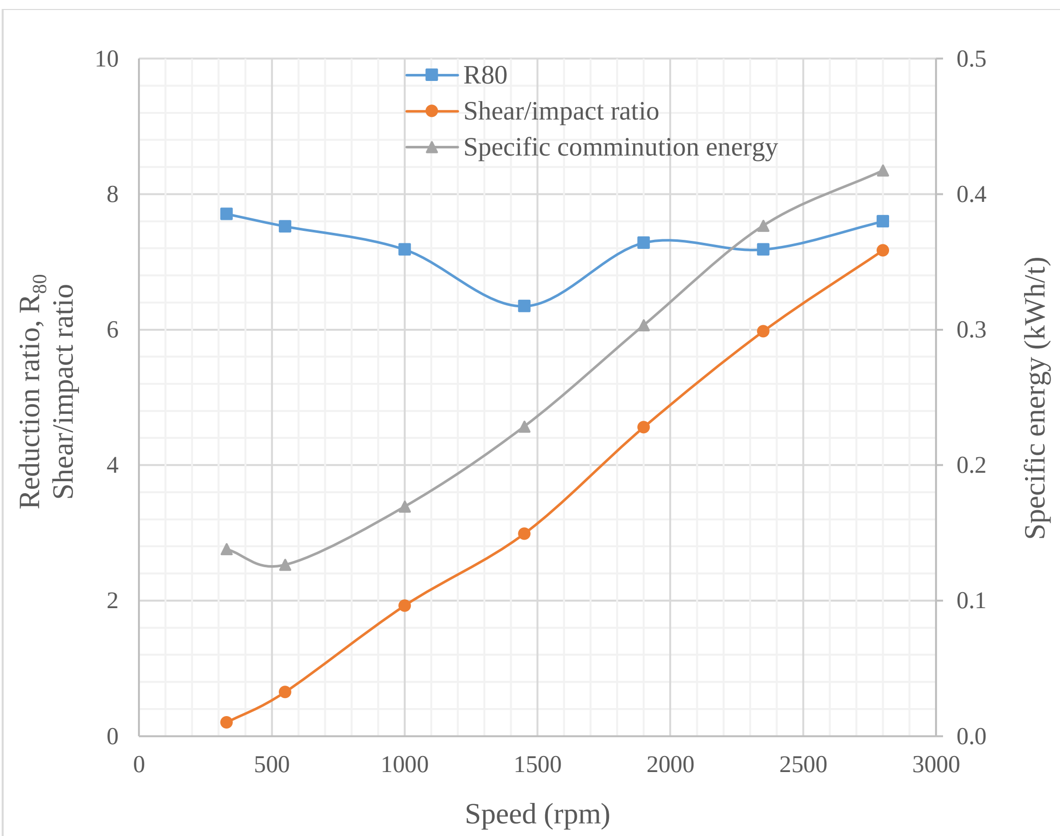

Figure 8. 11: Reduction ratio, shear/impact ratio and specific energy versus operating speed

The shear/impact ratio is plotted against energy utilization in Figure 8.12. Energy efficiency decreases with the ratio of shear to impact energy. Energy utilization can be related to the ratio of shear and impact energies using the following equation.

$$E_u = 69.005 {R_{S/I}}^{-0.116} \tag{8.2}$$

Since $R_{I/S}$ is linearly related to the speed (for speeds in the range of 330 and 3000 rpm), Eq. (8.2) can be modified into the following general equation.

$$E_u = p \times (k_1 N)^{-m} \tag{8.3}$$

Where p (=69.005) and m (=0.116) are model constants and k_1 is the slope of the straight line relating the speed to the ratio of shear and impact.

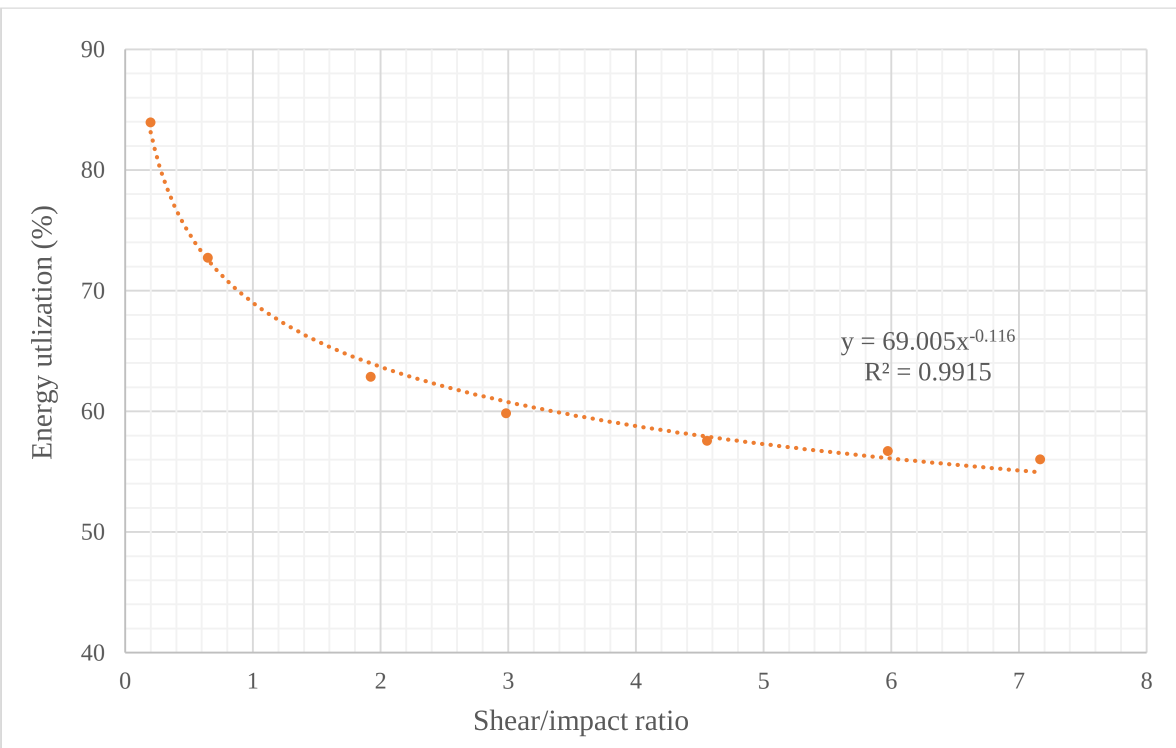

Figure 8. 12: Energy utilization versus shear/impact ratio

Crusher throughput is plotted against the speed in Figure 8.13. The throughput is constant for speeds below 1450 rpm, beyond which it slightly increases with the operating speed until 1900 rpm. Between 1900 and 2350 rpm, it is again constant. Beyond 2350 rpm, the throughput decreases with the operating speed. The throughput is highest around 2000 rpm for the simulated conditions and current design of the ROC.

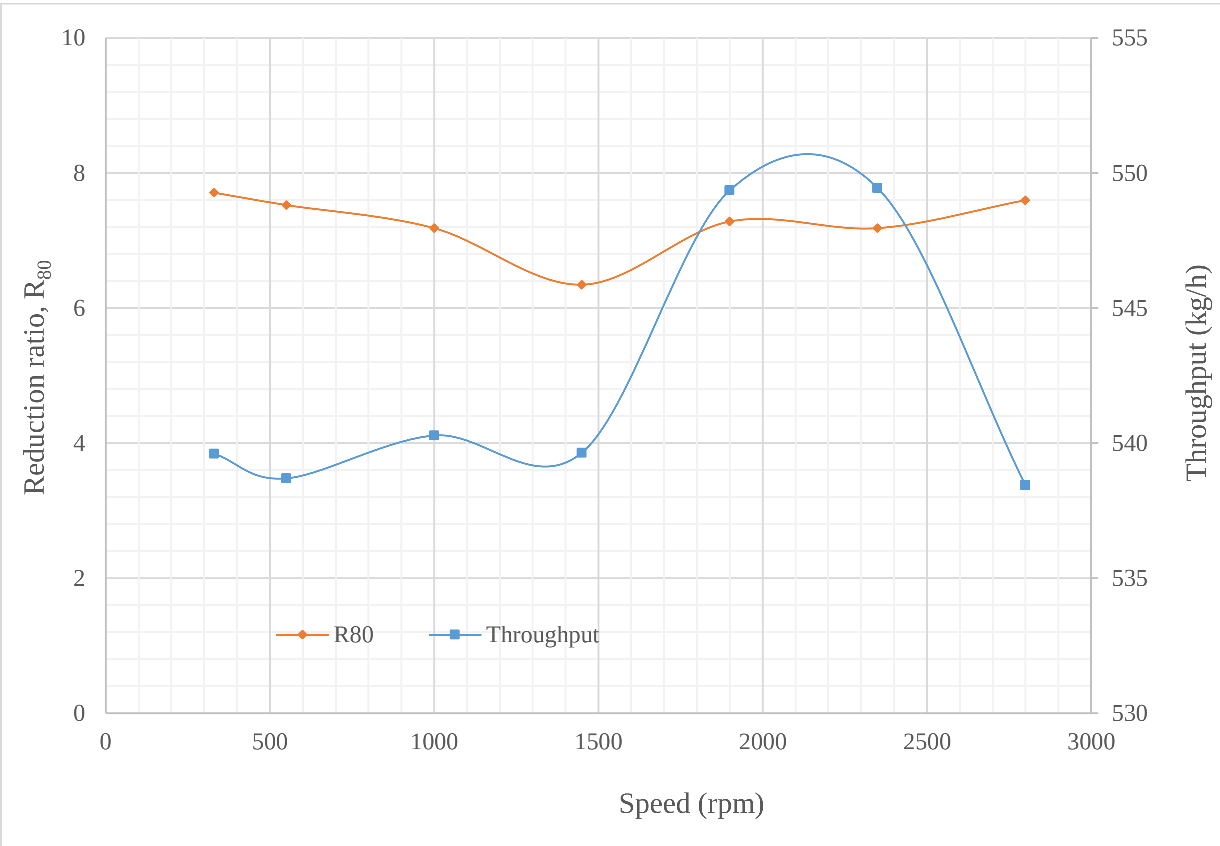

Figure 8. 13: Simulated ROC throughput and reduction ratio versus speed

8.4 Effect of counter-current operation on energy consumption and throughput

The ROC was simulated at 330 and 2350 rpm, but with the bottom disc rotating in the clockwise direction and the upper disc rotating in the anticlockwise direction. Both discs were rotating with the same speeds while the feed rate, offset and exit gap were 1 tph, 10 mm and 4 mm respectively. Table 8.3 compares the impact, shear and dissipated energies for counter-current and co-current operation. It is observed that the shear energy due to the discs-particles contacts increases when the discs are not rotating in the same direction. The same can also be observed for impact energy due to P-TD contacts. This suggests a high wear rate when the crusher is operated with discs rotating in opposite directions.

Table 8. 3: Summary of energies due to contacts for counter-current and co-current rotations

Speed (rpm)	Dissipated energy (J)			Impact energy (J)			Shear energy (J)		
	P-P	P-BD	P-TD	P-P	P-BD	P-TD	P-P	P-BD	P-TD
Counter-current rotation									
330	6.96	83.54	177.98	30.69	18.66	269.18	3.83	79.41	154.62
2350	7.56	1163.55	997.34	28.46	30.15	190.07	4.27	1158.05	1725.94
Co-current rotation									
330	6.40	13.23	7.00	54.83	31.67	29.37	3.52	11.87	7.75
2350	7.73	177.18	105.17	26.93	14.40	13.12	4.73	176.87	143.74

The size distributions for the two speeds are shown in Figure 8.14. It can be observed that the product size distributions are comparable to the co-current operation size distributions (see Figure 8.10).

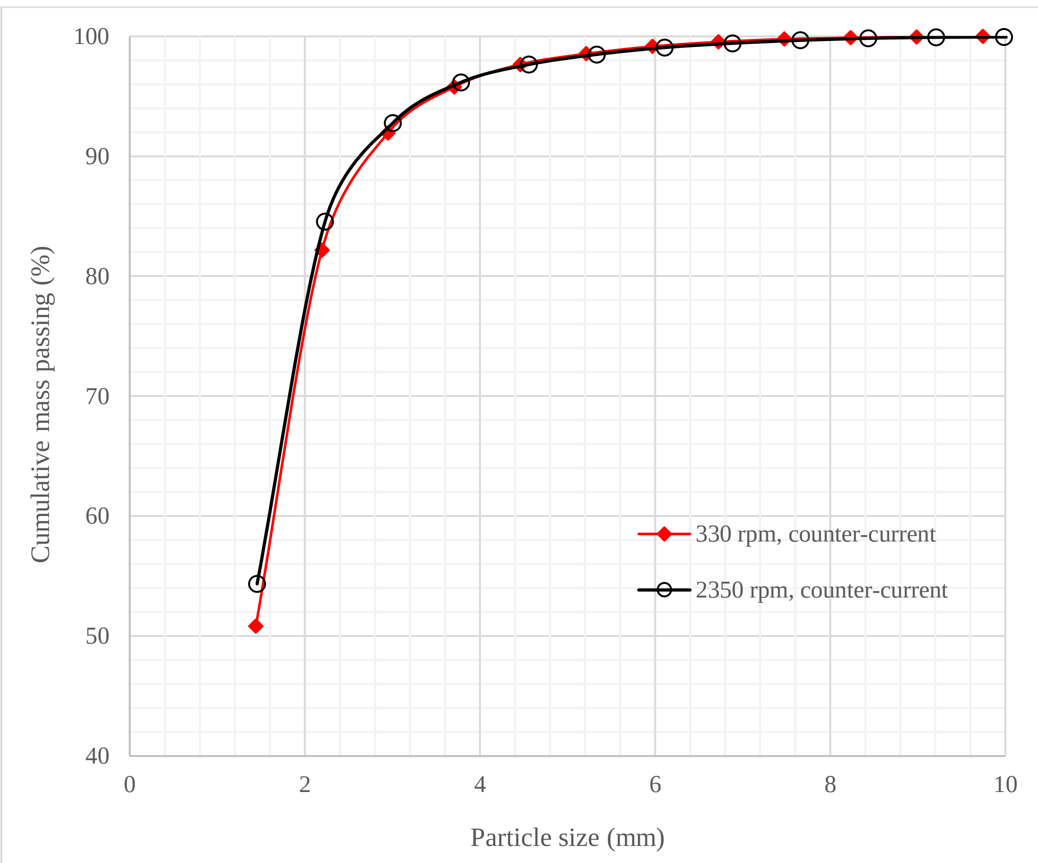

Figure 8. 14: Product size distributions for simulated ROC with counter-discs rotation

Reduction ratios, specific energies, energy utilization, shear/impact ratio and throughput are presented in Table 8.4. Energy utilization at 330 rpm decreased when the discs are rotated in the opposite directions, but E_u is the same for the type of rotation at the higher speed (2350 rpm). Higher specific energy associated with counter-current rotation could be attributed to Mode III (tearing). Reduction ratios are comparable for two types of operation. Since counter-current operation negatively affects both power draw and throughput, it is not recommended to operate the ROC with this arrangement. The results are attributed to the cancellation effect of the centrifugal force. Optimization of the ROC should be performed with the co-current rotation and only improve the design to intensify compression breakage while maximizing the throughput.

Table 8. 4: Summary of energy utilization for counter-current and co-current rotations

Speed (rpm)	**Comminution energy**		**Total energy (kWh/t)**	**Energy utilization (%)**	**Shear to Impact ratio**	**Q (kg/h)**	**R_{80} (mm)**
	J	kWh/t					
Counter-current operation							
330	556.4	0.55	0.82	67.5	0.75	214.8	7.60
2350	3137.0	3.11	5.26	59.1	11.61	239.5	7.45
Co-current operation							
330	139.0	0.14	0.16	83.9	0.20	539.6	7.71
2350	379.8	0.38	0.66	56.7	5.98	549.4	7.18

8.5 Effect of speed differential on energy utilization and shear/impact ratio

The ROC was simulated with the 330 rpm (highest compressive energy for the simulated speeds, see Figure 8.7), but varying the top disc speed such that there is 0, 5, 10 and 20% differences between the speed of the bottom disc and that of the top disc. The bottom disc was accelerated faster than the upper disc in all cases. Product size distributions are shown in Figure 8.15. It is evident that the size distributions are not very different. Energies are presented in Figure 8.16. Impact energies tend to be indifferent for all speed differentials. Shear energy is indifferent for 0, 5 and 10% differences in speeds. However, at 15% difference, shear energy increases significantly. This could suggest an increased dominance of Mode III (shear, twisting) which can facilitate breakage for rocks with cleavage planes.

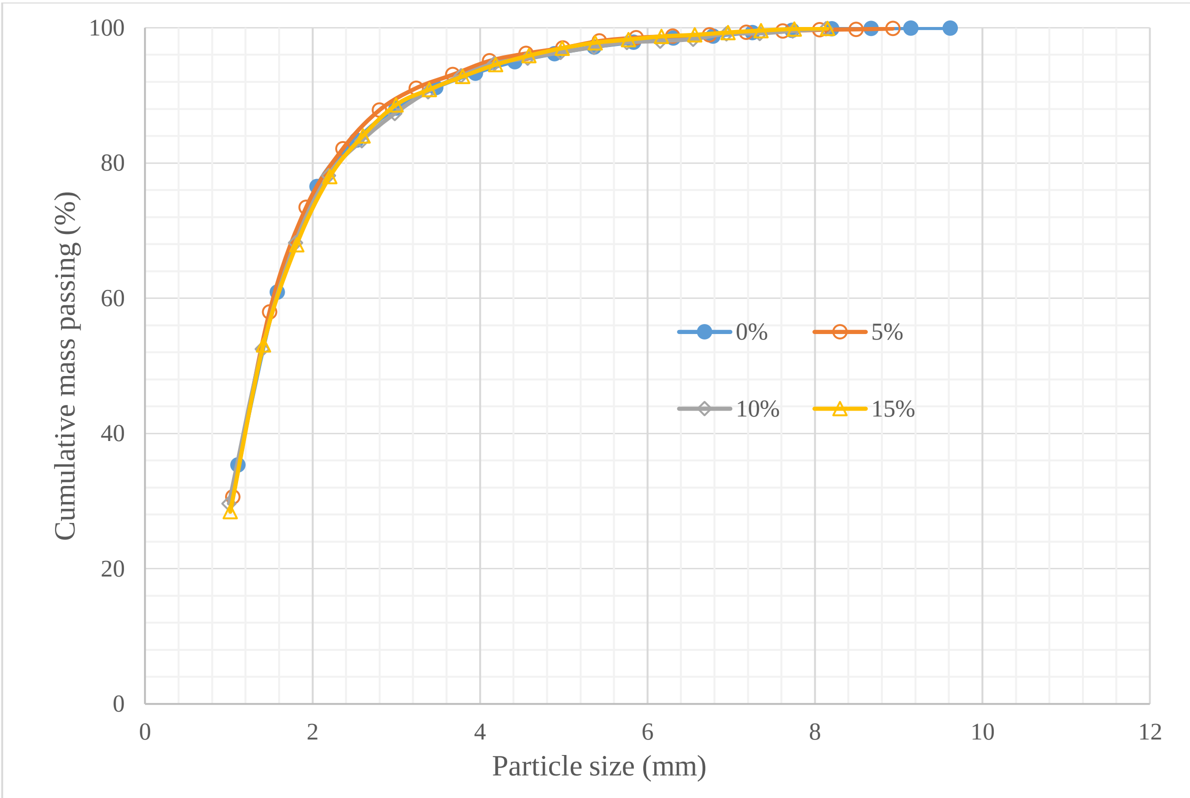

Figure 8. 15: Product size distributions of simulated ROC with speed differential

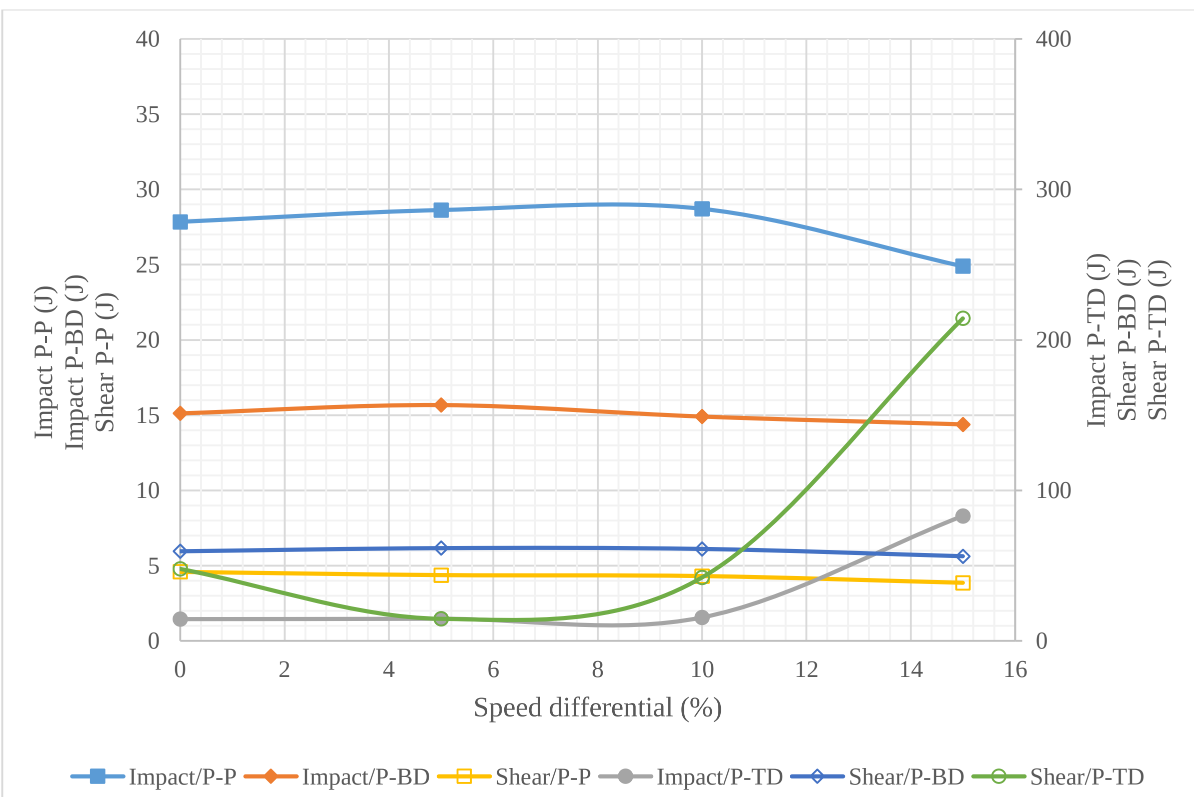

Figure 8. 16: Impact and shear energies against speed differential

Reduction ratios, specific energies, energy utilization, shear/impact ratio and throughput are presented in Table 8.5. Energy utilization at 0 and 10% speed difference are highest (~63%). With a 15% difference, energy utilization is lowest (33%). The 15% difference is associated with the highest ratio of shear/impact energies and specific energy, which could mean increased Mode III (twisting) as already mentioned. From Figure 8.17, it is observed that a higher reduction ratio of 7.02 was achieved with the 0 and 5% differences in speeds. A smaller reduction ratio (6.76) was recorded for 10 and 15% Throughput tends to slightly increase with speed differential. It is recommended that the crusher should be operated with the speed differential of at most 10% in the quest to optimize crushing efficiency and throughput.

Table 8. 5: Summary of energy utilization for various speed differentials

Speed difference (%)	**Comminution energy**		**Total energy (kWh/t)**	**Energy utilization (%)**	**Shear to Impact ratio**
	J	kWh/t			
0	169.6	0.168	0.267	63.0	1.95
5	139.9	0.139	0.241	57.6	1.37
10	166.9	0.166	0.264	62.8	1.82
15	396.7	0.393	1.180	33.4	2.24

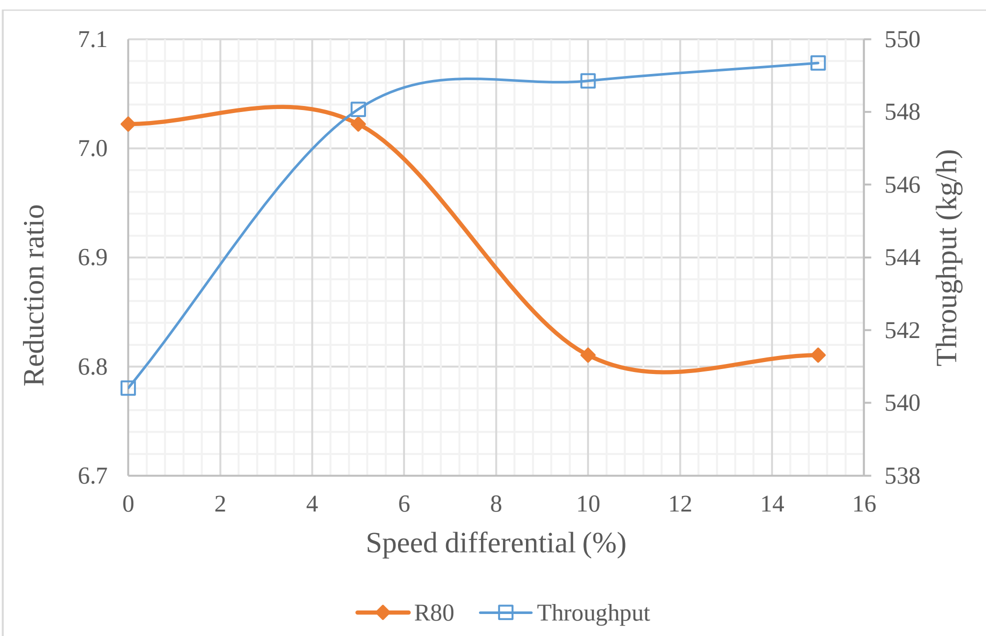

Figure 8. 17: Reduction ratio and throughput versus speed differential

8.6 Effect of increasing feed rate on energy utilization and shear/impact ratio

It is acknowledged that fast delivery of the particles to the crushing zone may not necessarily result in high throughput since the discharge rate of the ROC will also depend on the crushing kinetics which, in turn, depends on the following factors.

- Process material characteristics (particle size distribution, shape, and mechanical properties)
- Crushing surface characteristics (can affect the efficiency of transmission of the available forces to the particles)
- Operating variables (especially the rotational speed which affects the degree of dominance of the breakage mechanisms).

The crusher was simulated with a feed rate of 10 tph, with distinct feed particle size distributions (feed 1 had mono-sized feed with particles of diameter 15.8 mm and feed 2 has wide size distribution of -19+4.75 mm) to investigate the effect of speed on energy utilization, throughput and size distribution. The simulated ROC with -19+4.75 mm feed (polyhedral particles) is shown in Figure 8.18.

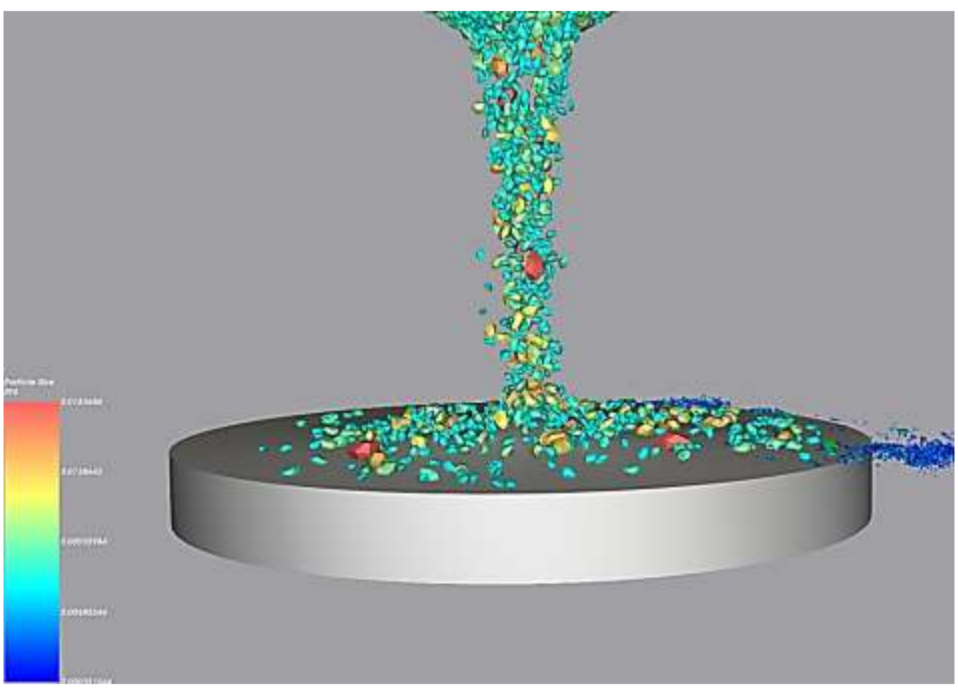

Figure 8. 18: Simulated feed wide size distribution (top disc and hopper hidden from the image for clear illustration)

8.6.1 Effect of feed size distribution on impact and shear energies

The impact and shear energies as well as dissipated energies of the particles due to discs-particles and particles-particles contacts are plotted against the operating speed in Figures 8.19 and 8.20. Compared to the results for 1 tph (in Figure 8.7), it is obviously evident that increased feed rate is accompanied by high power draw due to many particles in the crushing zone and thus increased comminution events (P-P, P-BD and P-TD). Beyond 1000 rpm, the impact energy is not changing with the speed. This was already observed in Figure 8.8 which also has data points between 1000 and 2350 rpm. The shear and dissipated energies are steadily increasing with rotational speed. It can be observed that generally more energy is utilized when a mono-size feed (with 15.8 mm diameter) is used. As discussed in section 8.6.2, the high-power draw also translated into a finer product.

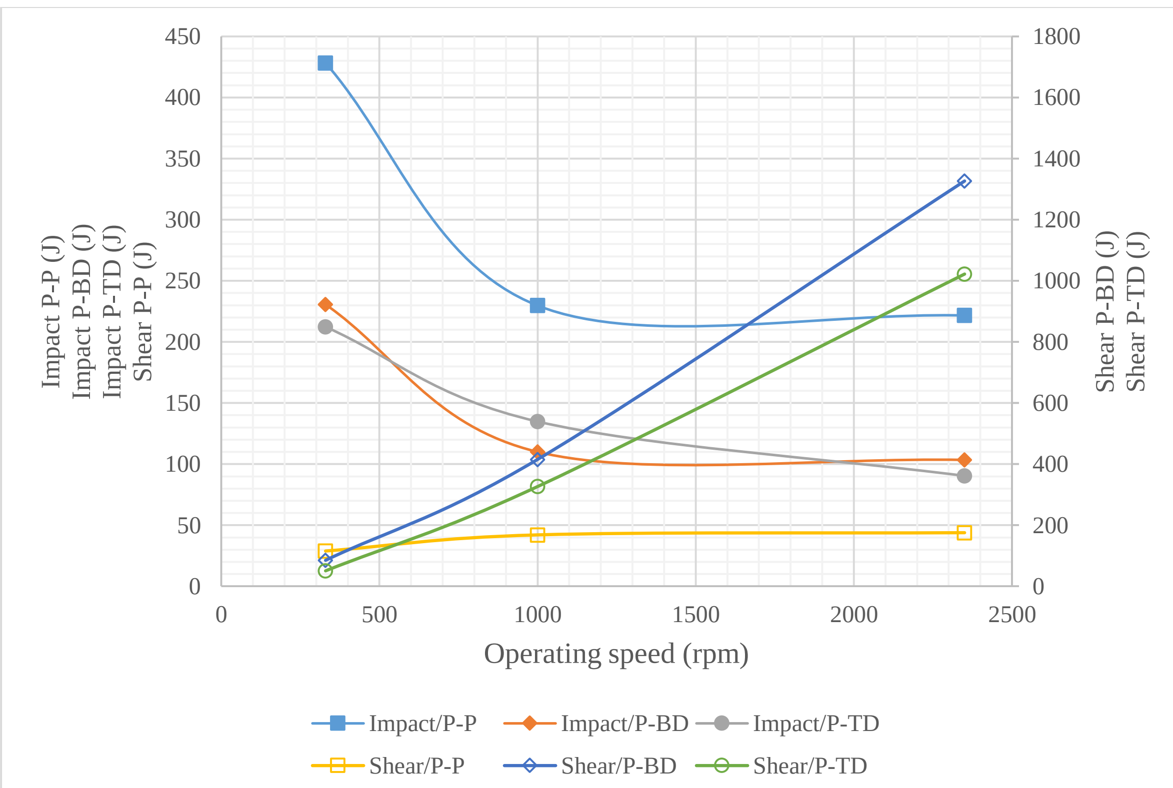

Figure 8. 1910: Impact and shear energies as function of rotational speed when ROC has feed rate of 10 tph (mono-size feed)

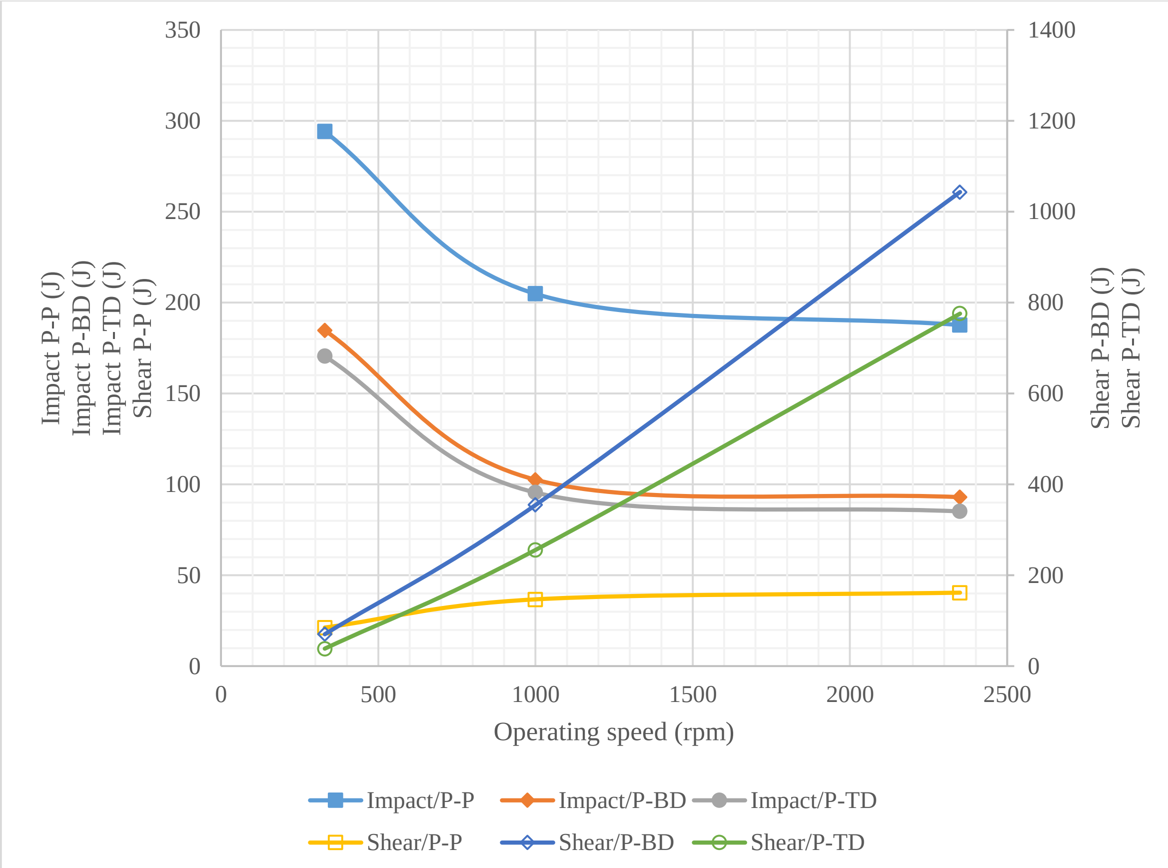

Figure 8. 20: Impact and shear energies as function of rotational speed when ROC has feed rate of 10 tph (wide size feed)

8.6.2 Crushing efficiency and throughput

Product size distributions are shown in Figure 8.21 and 8.22 for the feeds with mono-size and wide size distribution respectively. The experimental PSD for the feed with a wide size distribution (discussed in Chapter 5) was also included on Figure 8.22. With a mono-sized feed, it is clear that the product fineness decreases with the speed. The same trend was not replicated for the simulated feed with a wide size distribution. The speed of 330 rpm yielded a finer product, followed by 2350 rpm, and then 1000 rpm yielded the coarser product. It is recommended that simulations with higher feed rate should be performed in the quest to optimize the ROC and establish sustained trends.

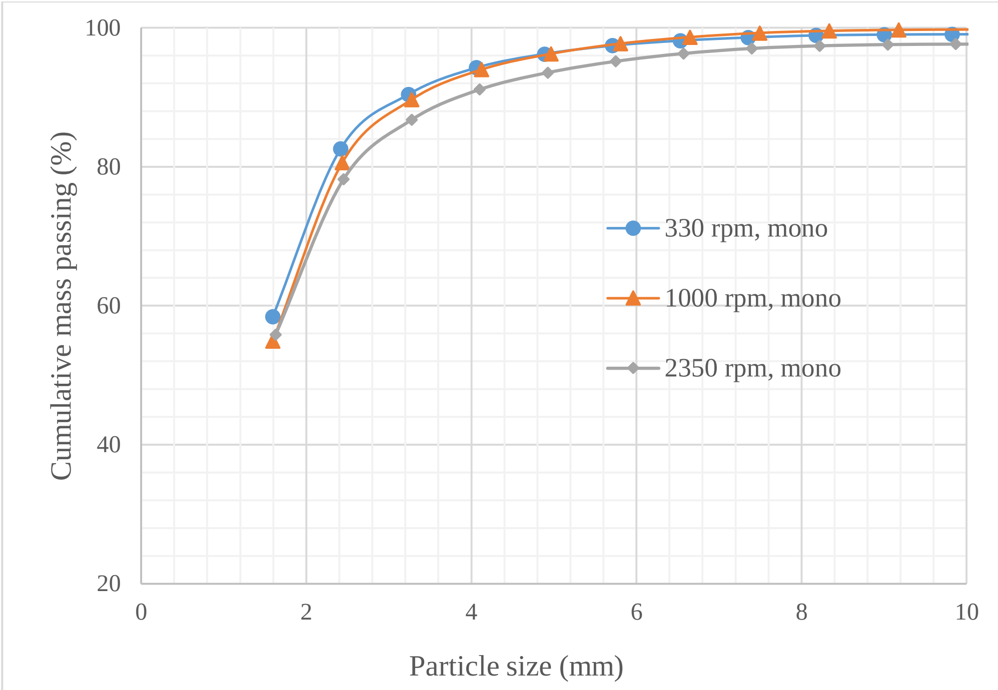

Figure 8. 21: Product size distribution when the crusher is operated at 10 tph (feed with a mono-size feed)

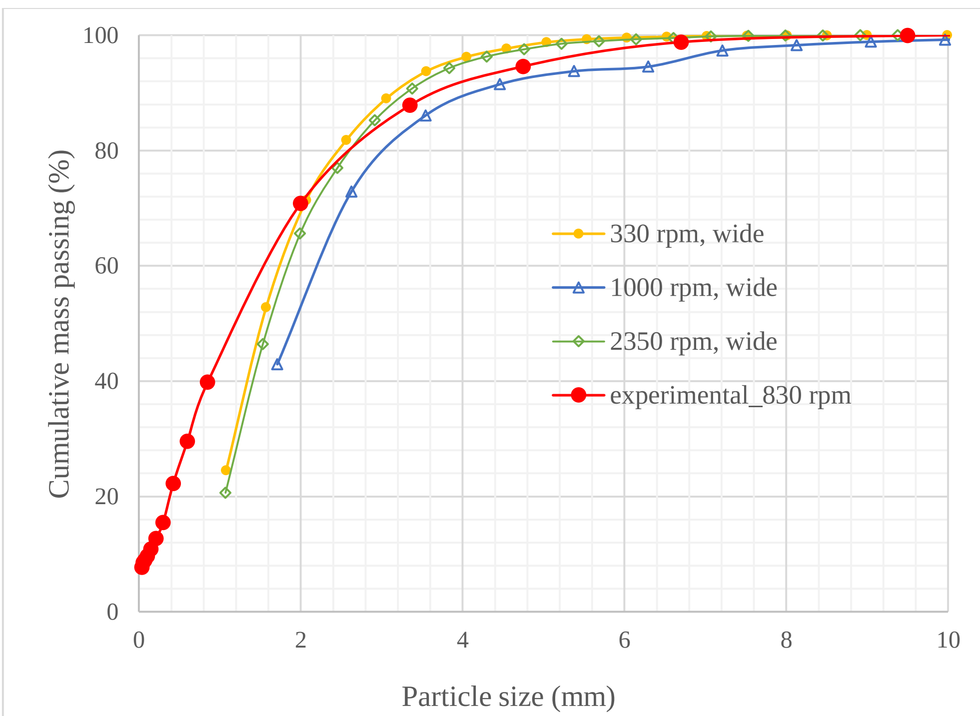

Figure 8. 22: Product size distribution when the crusher is operated at 10 tph (feed with a wide size distribution)

The ratio of shear energy to impact energy and specific comminution energy are plotted against speed in Figure 8.23 and 8.24. Shear/impact ratios are also relatively similar for the three feeds. A feed size distribution (also with near-vertical exit gap particles) should be considered in future studies with modified design to assess opportunities which promotes rock-on-rock comminution. Specific comminution energy increase with the rotational speed in Figure 8.24. The power consumption is higher for the simulated ROC with a mono-size feed (translated into finer products as shown in Figure 8.25).

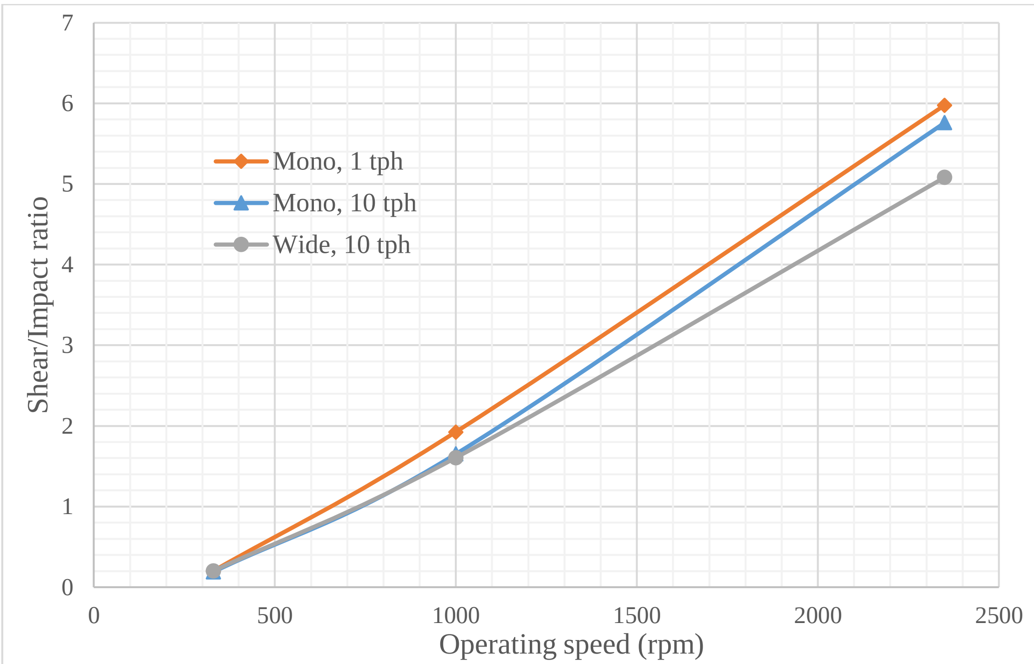

Figure 8. 23: Shear/impact ratio for crusher with feed rates of 10 tph and 1 tph

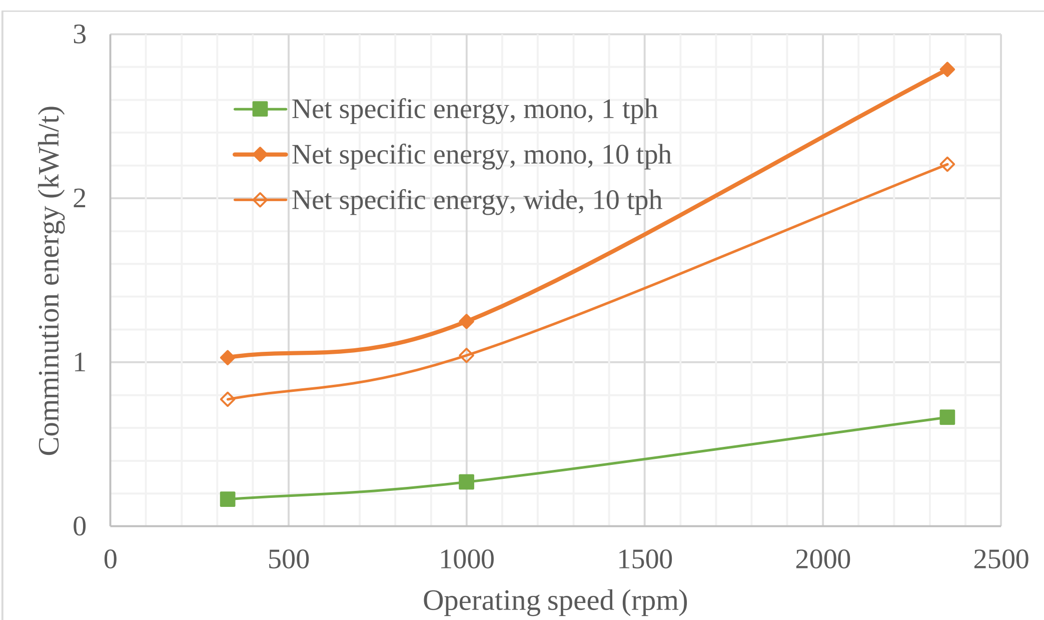

Figure 8. 24: Comminution energy and shear/impact ratio for crusher with a feed rate of 10 tph

Crusher throughputs and reduction ratios are shown in Figure 8.25. An increased feed rate produces coarse products (comparing the R_{80} values for 1 and 10 tph). Comparing the R_{80} values for the 10 tph, it is evident that the mono-size feed has higher reduction ratios than the feed with a wide size distribution. The crusher throughputs for the mono-size feeds (both 1 and 10 tph) are not very sensitive to the operating speed of the crusher. This is contrary to the feed with a wide size distribution, which shows that a 1000 rpm speed yields a maximum throughput. Below 1000 rpm, the throughput is increasing with the speed. Above 1000 rpm, the throughput decreases with the speed. However, since both feeds did not give a consistent trend, it cannot be generalized for all the feeds that 1000 rpm is a critical speed. Simulations after careful calibration of the contact parameters are recommended in order to assess the performance potential of the ROC.

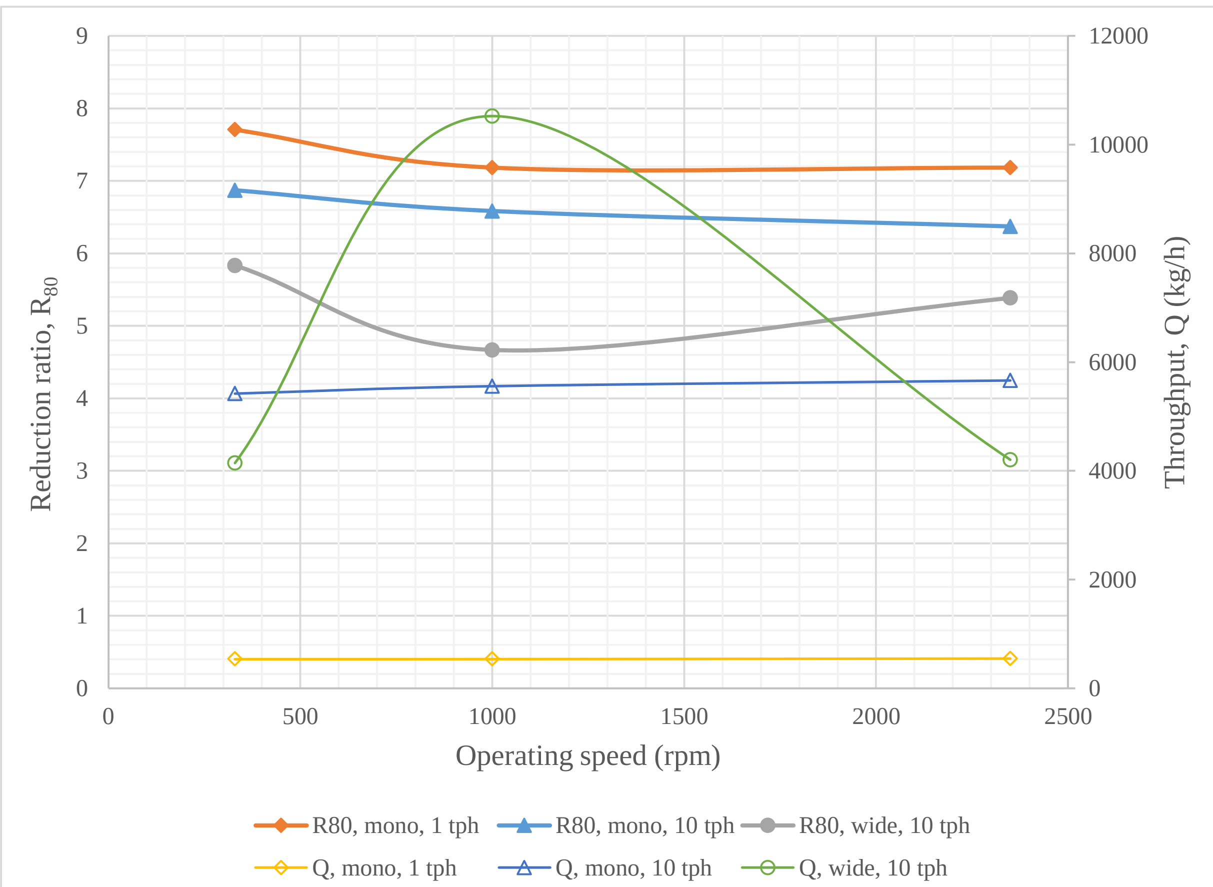

Figure 8. 25: Reduction ratios and throughput for crusher with a feed rate of 10 tph

8.7 Conclusions

From the DEM simulation, the reduction ratio is not very sensitive to offset between 10 mm and 30 mm. Mode III (tearing) seems to be prevalent at the 30 mm offset. Operating the crusher with no offset is undesirable because it is characterized by high power draw which does not translate into a finer product. The degree of dominance for the breakage mechanism (compressive or shear) is highly dependent on the speed of the discs. Shear energy steadily increases with rotational speed. This is contrary to the impact (compressive stress) energy which decreases with the speed until 1000 rpm, beyond which it is no longer sensitive to the change in the rotational speed. Operating the crusher with the discs rotating in opposite directions is associated with higher energy consumption and low throughput, and therefore not recommended. The crusher should be optimized for the discs rotating the same directions. The speed differential of the discs is one important parameter which can be considered when optimizing the ROC performance. Higher feed rates and feeds with wide size distributions are recommended for the simulation focusing on assessing the performance potential of the crusher in terms of throughput.

CHAPTER 9: CONCLUSIONS AND RECOMMENDATIONS

9.1 Summary of findings

A combination of physical experiment with the laboratory prototype and numerical modelling (using the discrete element method) was used to develop deeper insights of the processes underpinning the performance of the crusher. The main findings of the study are enumerated below.

- The horizontal offset between the vertical axes of the discs has less pronounced effect on the product size distribution and throughput. A slight increase of throughput with the offset was observed from both experimental and simulation data. However, operating the ROC without an offset is undesirable because that operation is characterized by high power draw. A 10 mm (representing 2% of the disc diameter) was found to be optimal for the provision of the necessary flexibility in the system. There appears to be a slightly higher impact due to P-P interactions (evidence of inter-particle comminution) for this offset. A higher value of the ratio of shear energy to impact energy for the 30 mm offset and high-power draw infer the increase in the failure Mode III (twisting) with the offset between the vertical axes of the discs.
- Speed of the discs is a key operating variable affecting the degree of dominance for the breakage mechanisms. Shear energy steadily increases with the operating speeds of the discs. Impact energy (inferring compression breakage mechanism) decreases with the operating speed until 1000 rpm, beyond which it stays constant. Overall, shear energy is higher than the compression energy for speeds above 550 rpm, which suggests that the dominant mechanism in the ROC is shear. Since shear energy increases steadily with the speed, it is not recommended to operate the crusher at high speeds because this can be associated with high operating costs (energy and wear) while the size reduction and throughput are not significantly maximized.
- Operating the crusher with the counter-current rotation of the discs is characterized by higher power draw which is attributed to failure Mode III (tearing. Furthermore, counter-current operation negatively affects the throughput. The results are attributed to the

cancelling effect of the centrifugal force. Optimization of the ROC should be done with the discs rotating in the same direction.

- Speed differential offers optimization opportunities in terms of degree of dominance of the breakage mechanism and energy consumption. The DEM simulations were conducted with the bottom disc rotating at 330 rpm while the top disc was slowed down such that there are 5, 10 and 15% differences in the speeds of the discs. Energy utilization at 0 and 10% speed difference are highest (~63%). With a 15% difference, energy utilization is lowest (33%). The 15% difference is associated with the highest ratio of shear/impact energies and specific energy, which could infer an increased Mode III (twisting). A higher reduction ratio of 7.02 was achieved with the 0 and 5% differences in speeds. It is recommended that the crusher should be operated with the speed differential of at most 10% in the quest to optimize crushing efficiency and throughput.
- Elimination of slab particles has to be tackled using multiple solutions including (1) choke feeding the crusher with a feed with a wider size distribution to promote rock-on-rock crushing, (2) imposition of vibratory motion to intensify the delivery of the impact forces to the particles (comparable to the nutating motion in cone crushers, and (3) corrugating the crushing surface to ensure compound crushing by tension, compression and shear.
- There was no definite trend between mass throughput and rotational speed. There exist speed regimes where transportation tends to be faster and other regimes where crusher throughput is inversely proportional to the speed. Overall, the following equation gives the factors which are driving material transport in the ROC.

$$Q = f\left(F, N_{dif}, x_{offset}, y_{gap}, X_f, S_p, C_{discs}\right) \qquad (8.1)$$

Where F is the feed rate, X_f is the feed particle size, S_p is the process material strength, N_{diff} is the speed difference between the discs, X_{offset} is the horizontal offset between the discs, Y_{gap} is the exit vertical gap and C_{discs} is the type of profile on the crushing surfaces.

9.2 Recommendations

It is acknowledged that the ROC currently has smooth profiles and a flat surface on the bottom disc. Modification of the crushing surface to have some profiles which can also intensify the crushing by a combination of compression, tension and shear should be considered in the future studies. Various profiles can be simulated in the DEM to generate the performance data (wear rate, reduction ratio, power draw, and throughput) which can guide the selection of the best design which can be manufactured and fitted on the laboratory prototype for experimentation.

It is also recommended that the volume of the crushing zone is increased by increasing the opening/gape of the comminution cavity from 20 mm by a factor of 2 or more so that the bed of particles is promoted. Furthermore, it is important that the feed rate is optimized to ensure maximum delivery of particles to the crushing zone. Material transport in the feeding zone of the crusher can potentially be a bottleneck to enhancing crusher throughput.

The imposition of the vertical (vibration) motion on the top disc to increase the compression (impact) breakage can also be considered. The DEM is the best tool that can be used to explore the benefits of vibration on size reduction, power draw and throughput. For the physical system, research into the possibility of having an ultrasonic motor to drive the top disc (or any other vibration-generating equipment/system) and generate the required vibration could be considered. Furthermore, a hydraulic system to reinforce mechanical rigidity is recommended for the ROC so that the vertical exit gap is well controlled and the available compressive forces are efficiently delivered towards comminution.

The difference between the speeds of the discs is one key variable that can also be manipulated to optimize the degree of dominance of the breakage mechanism, power draw and throughput. The crusher can be operated with various speed differentials (e.g., low speed of top disc to increase the compressive stress while the bottom disc is operated at a relatively higher speed to still achieve high throughput). However, for easy control during operation, it is recommended that the two motors for the respective discs should be incorporated in the design, rather than having the top disc freewheeling and driven by the friction generated by the particles in the crushing zone. It is also recommended that the performance of the crusher at low speeds (e.g., 100 and 220 rpm) should be investigated to establish its critical speed.

Once the full potential of the ROC has been established, it should be benchmarked against the existing crushers such as the cone crusher, high-pressure grinding rolls (HPGR) and vertical roller mills (VRM). It is acknowledged that the implementation of the ROC will depend on the demonstration of performance advantages in terms of throughput and energy consumption. The characteristics, such as shape and size distributions, of the crusher product would also influence the adoption of this technology in the minerals industry.

REFERENCES

Aadnøy, B. S., & Looyeh, R. (2019). *Petroleum rock mechanics* (Second). Gulf Professional Publishing. https://doi.org/doi.org/10.1016/B978-0-12-815903-3.00017-0

Agha, A., Gupta, S., & Joseph, T. (2015). Particle sliding on a turntable in the presence of friction. *American Journal of Physics*, *83*(2), 126–132. https://doi.org/10.1119/1.4896664

Åkerstedt, H. O. (2019). Transport and deposition of large aspect ratio prolate and oblate spheroidal nanoparticles in cross flow. *Processes*, *7*(12). https://doi.org/10.3390/PR7120886

Al-shayea, N. A. (2005). *Crack propagation trajectories for rocks under mixed mode I – II fracture*. *81*, 84–97. https://doi.org/10.1016/j.enggeo.2005.07.013

Alneasan, M., Behnia, M., & Bagherpour, R. (2018). Frictional crack initiation and propagation in rocks under compressive loading. *Theoretical and Applied Fracture Mechanics*, *97*(May), 189–203. https://doi.org/10.1016/j.tafmec.2018.08.011

Alneasan, M., Behnia, M., & Bagherpour, R. (2019). Analytical and numerical investigations of dynamic crack propagation in brittle rocks under mixed mode loading. *Construction and Building Materials*, *222*, 544–555. https://doi.org/10.1016/j.conbuildmat.2019.06.163

Altun, D., Gerold, C., Benzer, H., Altun, O., & Aydogan, N. (2015). Copper ore grinding in a mobile vertical roller mill pilot plant. *International Journal of Mineral Processing*, *136*, 32–36. https://doi.org/10.1016/j.minpro.2014.10.002

Altun, O., Benzer, H., Dundar, H., & Aydogan, N. A. (2011). Comparison of open and closed circuit HPGR application on dry grinding circuit performance. *Minerals Engineering*, *24*(3–4), 267–275. https://doi.org/10.1016/j.mineng.2010.08.024

André, D., Girardot, J., & Hubert, C. (2019). A novel DEM approach for modeling brittle elastic media based on distinct lattice spring model. *Computer Methods in Applied Mechanics and Engineering*, *350*, 100–122. https://doi.org/10.1016/j.cma.2019.03.013

André, F. P., & Tavares, L. M. (2020). Simulating a laboratory-scale cone crusher in DEM using polyhedral particles. *Powder Technology*, *372*, 362–371. https://doi.org/10.1016/j.powtec.2020.06.016

Askaripour, M., Saeidi, A., Mercier-Langevin, P., & Rouleau, A. (2022). A Review of Relationship between Texture Characteristic and Mechanical Properties of Rock.

Geotechnics, *2*(1), 262–296. https://doi.org/10.3390/geotechnics2010012

Austin, L. G., Klimpel, R. R., & Luckie, P. T. (1984). *Process Engineering of Size Reduction: Ball mills*. Society of Mining Engineers/American Institute of Mining, Metallurgical, and Petroleum Engineers.

Bhambhani, T. (2019). *The effects of particle size and shape on transport through confined channels in three-phase froths* (Vol. 1, Issue 1) [Columbia University]. http://www.ghbook.ir/index.php?name=فرهنگ و رسانه های نوین&option=com_dbook&task=readonline&book_id=13650&page=73&chkhashk=ED9C9491B4&Itemid=218&lang=fa&tmpl=component%0Ahttp://www.albayan.ae%0Ahttps://scholar.google.co.id/scholar?hl=en&q=APLIKASI+PENGENA

Bharadwaj, R. (2014). *What is discrete element method?* Bulk Power Solids. https://www.powderbulksolids.com/industries/what-is-discrete-element-method-

Bhattacharyya, S., & Bock, F. C. (1978). Abrasive wear of engineering materials by mineral and industrial wastes. *Wear*, *46*(1), 1–18. https://doi.org/https://doi.org/10.1016/0043-1648(78)90108-4

Bobet, A., & Einstein, H. H. (1998). Fracture coalescence in rock-type materials under uniaxial and biaxial compression. *International Journal of Rock Mechanics and Mining Sciences*, *35*(7), 863–888. https://doi.org///doi.org/10.1016/S0148-9062(98)00005-9

Boikov, A. V, Savelev, R. V, & Payor, V. A. (2018). DEM Calibration Approach : design of experiment. *Journal of Physics: Conference Series*, *1015*, 1–7. https://doi.org/10.1088/1742-6596/1015/3/032017

Bond, F. C. (1947). Bond, F.C., 1947, Crushing tests by pressure and impact. *Trans. AIME*, *169*, 58–66.

Brosh, T., Kalman, H., Levy, A., Peyron, I., & Ricard, F. (2014). DEM-CFD simulation of particle comminution in jet-mill. *Powder Technology*, *257*, 104–112. https://doi.org/10.1016/j.powtec.2014.02.043

Bruchmüller, J., van Wachem, B. G. M., Gu, S., & Luo, K. H. (2011). Modelling discrete fragmentation of brittle particles. *Powder Technology*, *208*(3), 731–739. https://doi.org/10.1016/j.powtec.2011.01.017

Burat, F., Dinç, N. İ., Dursun, H. N., & Ulusoy, U. (2023). The Role of Particle Size and Shape on the Recovery of Copper from Different Electrical and Electronic Equipment Waste.

Minerals, *13*(7). https://doi.org/10.3390/min13070847

Burns, J. A. (1981). Ball rolling on a turntable : Analog for charged particle dynamics. *American Journal of Physics*, *49*, 56–58. https://doi.org/10.1119/1.12610

Bwalya, M. M., & Chimwani, N. (2020). Development of a more descriptive particle breakage probability model. *Minerals*, *10*(8), 1–14. https://doi.org/10.3390/min10080710

Camalan, M. (2020). Correlating common breakage modes with impact breakage and ball milling of cement clinker and chromite. *International Journal of Mining Science and Technology*, *30*, 901–908. https://doi.org/10.1016/j.ijmst.2020.03.017

Campos, T. M., Bueno, G., & Tavares, L. M. (2020). Confined bed breakage of fine iron ore concentrates. *Minerals*, *10*(8), 1–15. https://doi.org/10.3390/min10080666

Charikinya, E., Bradshaw, S., & Becker, M. (2015). Characterising and quantifying microwave induced damage in coarse sphalerite ore particles. *Minerals Engineering*, *82*, 14–24. https://doi.org/10.1016/j.mineng.2015.07.020

Chen, W., Ye, F., Wheeler, C., Chen, B., Hu, J., Chen, K., & Chen, W. (2018). Calibration and verification of DEM parameters for dynamic particle flow conditions using a backpropagation neural network Calibration and verification of DEM parameters for dynamic particle flow conditions using a backpropagation neural network. *Advanced Powder Technology*, *March 2019*. https://doi.org/10.1016/j.apt.2018.11.005

Chikerema, P. (2011). *Effects of partcile sizem shape and density on the performance of an air fluidized bed in dry coal beneficiation*. University of the Witwatersrand.

Chimwani, N. (2024). Optimization of mechanical comminution - the crushing stage. In E. Flsso-Kankeu, B. B. Mamba, & A. F. Mulaba-Batabiandi (Eds.), *Recovery of values from low-grade and complex minerals: Development of sustainable processes*. John Wiley & Sons.

Cho, N. Ã., Martin, C. D., & Sego, D. C. (2007). *A clumped particle model for rock*. *44*, 997–1010. https://doi.org/10.1016/j.ijrmms.2007.02.002

Cil, M. B., Alshibli, K. A., Mcdowell, G. R., & Li, H. (2013). Discussion: 3D assessment of fracture of sand particles using discrete element method. *Géotechnique Letters*, *3*(1), 13–15. https://doi.org/10.1680/geolett.13.00004

Cleary, P. (2001). Modelling comminution devices using DEM. *International Journal for Numerical and Analytical Methods in Geomechanics*, *25*(1), 83–105.

https://doi.org/10.1002/1096-9853(200101)25:1<83::AID-NAG120>3.0.CO;2-K

Cleary, P. W., & Morrison, R. D. (2011). Understanding fine ore breakage in a laboratory scale ball mill using DEM. *Minerals Engineering*, *24*(3–4), 352–366. https://doi.org/10.1016/j.mineng.2010.12.013

Cleary, P. W., & Morrison, R. D. (2016). Comminution mechanisms, particle shape evolution and collision energy partitioning in tumbling mills. *Minerals Engineering*, *86*, 75–95. https://doi.org/10.1016/j.mineng.2015.12.006

Cleary, P. W., & Sinnott, M. D. (2015). Simulation of particle flows and breakage in crushers using DEM: Part 1 - Compression crushers. *Minerals Engineering*, *74*, 178–197. https://doi.org/10.1016/j.mineng.2014.10.021

Coetzee, C. J. (2016). Calibration of the discrete element method and the effect of particle shape. *Powder Technology*, *297*, 50–70. https://doi.org/10.1016/j.powtec.2016.04.003

Copyright. (2007). iv. https://doi.org/10.1016/S0165-1250(07)85019-X

Cundall, P. A., & Strack, O. D. L. (1979). A discrete numerical model for granular assemblies. *Geotechnique*, *29*(1), 47–65.

Daniel, M., Lane, G., & McLean, E. (2010). Efficiency, economics, energy and emissions-emerging criteria for comminution circuitdecision making. *XXV International Mineral Processing Congress 2010, IMPC 2010*, *5*(March 2019), 3523–3531.

Dehghani, F., Rahimi, M., & Rezai, B. (2013). Influence of particle shape on the flotation performance. *Journal of Southern Africa Institute of Mining and Metallurgy*, *113*(December), 905–911.

Desriviers Lehyt, P., Quintero, A., & Primeau, P. (2019). Effects of the mineralogical composition and particle size distribution on the rheology of gold and copper tailings. *Proceedings of the 22nd International Conference on Paste, Thickened and Filtered Tailings*, 504–514. https://doi.org/10.36487/acg_rep/1910_38_desriviers

Djordjevic, N. (2010). Improvement of energy efficiency of rock comminution through reduction of thermal losses. *Minerals Engineering*, *23*(15), 1237–1244. https://doi.org/10.1016/j.mineng.2010.08.019

Djordjevic, N., Shi, F. N., & Morrison, R. D. (2003). Applying discrete element modelling to vertical and horizontal shaft impact crushers. *Minerals Engineering*, *16*(10), 983–991. https://doi.org/10.1016/j.mineng.2003.08.007

Donzé, F. V, & Richefeu, V. (n.d.). *Advances in Discrete Element Method Applied to Soil, Rock and Concrete Mechanics*.

Dundar, H., Benzer, H., & Aydogan, N. (2013). Application of population balance model to HPGR crushing. *Minerals Engineering*, *50–51*, 114–120. https://doi.org/10.1016/j.mineng.2013.07.005

Ehrlich, R., & Tuszynski, J. (1995). Ball on a rotating turntable : Comparison of theory and experiment. *American Journal of Physics*, *63*, 351–358. https://doi.org/10.1119/1.17920

Eliáš, J. (2014). Simulation of railway ballast using crushable polyhedral particles. *Powder Technology*, *264*, 458–465. https://doi.org/10.1016/j.powtec.2014.05.052

ESSS. (2020). *Rocky DEM Technical Manual: version 4.3*.

Estay, D. A., & Chiang, L. E. (2013). Discrete crack model for simulating rock comminution processes with the Discrete Element Method. *International Journal of Rock Mechanics and Mining Sciences*, *60*, 125–133. https://doi.org/10.1016/j.ijrmms.2012.12.041

Evertsson, C. M. (1998). Output prediction of cone crushers. *Minerals & Metallurgical Processing*, *I*(3), 215–231.

Evertsson, C. M. (1999). Modelling of flow in cone crushers. *Minerals Engineering*, *12*(12), 1479–1499.

Evertsson, C. M., & Bearman, R. A. (1997). Investigation of interparticle breakage as applied to cone crushing. *Minerals Engineering*, *10*(2), 199–214.

Farzanegan, A., Sepahvand, E., & Mirzaei, Z. S. (2016). Optimization of HPGR-based clinker grinding circuit at Abyek cement plant using steady-state process simulations. *Journal of the Polish Mineral Engineering Society*, *17*(1), 255–260. https://doi.org/10.29227/IM-2016-02-29

Fuerstenau, D. W., 2, P. C. K., Schoenert, K., & Marktscheffel, M. (1990). Comparison of energy consumption in the breakage of singles in a rigidly mounted roll mill with ball mill grinding. *International Journal of Mineral Processing*, *28*(1–2), 109–125. https://doi.org/https://doi.org/10.1016/0301-7516(90)90030-3

Genç, Ö., Ergün, L., & Benzer, H. (2004). Single Particle Impact Breakage Characterization of Materials By Drop Weight Testing. *Fizykochemiczne Problemy Mineralurgii*, *38*(38), 241–255. http://www.minproc.pwr.wroc.pl/journal/pdf/2004/241-255.pdf

Ghorbani, Y., Becker, M., Petersen, J., Morar, S. H., Mainza, A., & Franzidis, J. P. (2011). Use of X-ray computed tomography to investigate crack distribution and mineral dissemination in sphalerite ore particles. *Minerals Engineering*, *24*(12), 1249–1257. https://doi.org/10.1016/j.mineng.2011.04.008

Ghorbani, Y., Mainza, A. N., Petersen, J., Becker, M., Franzidis, J. P., & Kalala, J. T. (2013). Investigation of particles with high crack density produced by HPGR and its effect on the redistribution of the particle size fraction in heaps. *Minerals Engineering*, *43–44*, 44–51. https://doi.org/10.1016/j.mineng.2012.08.010

Govender, N., Rajamani, R., Wilke, D. N., Wu, C. Y., Khinast, J., & Glasser, B. J. (2018). Effect of particle shape in grinding mills using a GPU based DEM code. *Minerals Engineering*, *129*(August), 71–84. https://doi.org/10.1016/j.mineng.2018.09.019

Griffith, A. A. (1920). *The Phenomena o f Rupture and Flow in Solid*. https://royalsocietypublishing.org/doi/pdf/10.1098/rsta.1921.0006

Gröndahl, A., Asbjörnsson, G., Hulthén, E., & Evertsson, M. (2018). Diagnostics of cone crusher feed segregation using power draw measurements. *Minerals Engineering*, *127*(August), 15–21. https://doi.org/10.1016/j.mineng.2018.07.008

Guo, J., Wang, G., Sun, G., Wang, S., Guan, W., & Chen, Z. (2024). DEM simulation and optimization of crushing chamber shape of gyratory crusher based on Ab - t 10 model. *Minerals Engineering*, *209*(September 2023), 108606. https://doi.org/10.1016/j.mineng.2024.108606

Gupta, A., & Yan, D. S. (2016). *Mineral Process Design and Operations: An Introduction* (1st ed.). Elsevier Science.

Gutierrez, A., & Guichou, J. (2014). Computational simulation of fracture of materials in comminution devices. *Minerals Engineering*, *61*, 73–81. https://doi.org/10.1016/j.mineng.2014.03.010

Guven, O. (2022). The effect of shape and roughness on flotation and aggregation of quartz particles. *Physicochemical Problems of Mineral Processing*, *58*(6). https://doi.org/10.37190/PPMP/154021

Hafez, A., Liu, Q., Finkbeiner, T., Alouhali, R. A., Moellendick, T. E., & Santamarina, J. C. (2021). The effect of particle shape on discharge and clogging. *Scientific Reports*, *11*(1), 1–11. https://doi.org/10.1038/s41598-021-82744-w

Heckel, R. W. (1961). Density–pressure relationships in powder compaction. *Trans. Metall. Soc.*

AIME 221, 671–675.

Herbst, J., Potapov, A., Hambidge, G., & Rademan, J. (2008). Modeling of diamond liberation and damage for Debswana kimberlitic ores. *Minerals Engineering*, *21*(11), 766–769. https://doi.org/10.1016/j.mineng.2008.06.006

Horabik, J., & Molenda, M. (2016). Parameters and contact models for DEM simulations of agricultural granular materials: A review. *Biosystems Engineering*, *147*, 206–225. https://doi.org/10.1016/j.biosystemseng.2016.02.017

Javed, A., Khan, K. F., & Quasim, M. A. (2023). Petrography of the Bajocian Sandstone of Joyan Member, Jaisalmer Basin, Western Rajasthan: Implications for Provenance and Basin Evolution. *Journal of the Geological Society of India*, *99*(1), 73–87. https://doi.org/10.1007/s12594-023-2269-1

Jeswiet, J., & Szekeres, A. (2016). Energy Consumption in Mining Comminution. *Procedia CIRP*, *48*, 140–145. https://doi.org/10.1016/j.procir.2016.03.250

Jiang, J. J., Xie, Y., Qian, W., & Hall, R. (2018). Important factors a ff ecting the gouging abrasion resistance of materials. *Minerals Engineering*, *128*(August), 238–246. https://doi.org/10.1016/j.mineng.2018.09.001

Jiang, S., Ye, Y., Li, X., Liu, S., Liu, J., Yang, D., & Tan, Y. (2019). DEM modeling of crack coalescence between two parallel flaws in SiC ceramics. *Ceramics International*, *January*. https://doi.org/10.1016/j.ceramint.2019.04.237

Jiménez-Herrera, N., Barrios, G. K. P. P., & Tavares, L. M. (2018). Comparison of breakage models in DEM in simulating impact on particle beds. *Advanced Powder Technology*, *29*(3), 692–706. https://doi.org/10.1016/j.apt.2017.12.006

Johansson, M., Bengtsson, M., Evertsson, M., & Hulthén, E. (2017). A fundamental model of an industrial-scale jaw crusher. *Minerals Engineering*, *105*, 69–78. https://doi.org/10.1016/j.mineng.2017.01.012

Johansson, M., Quist, J., Evertsson, M., & Hulthén, E. (2017). Cone crusher performance evaluation using DEM simulations and laboratory experiments for model validation. *Minerals Engineering*, *103–104*, 93–101. https://doi.org/10.1016/j.mineng.2016.09.015

Kelly, E. G., & Spottiswood, D. . (1990). The breakage function; What is it really? *Minerals Engineering*, *3*(5), 405–414. https://doi.org/10.1016/0892-6875(90)90034-9

Khanal, M., & Morrison, R. (2008). Discrete element method study of abrasion. *Minerals*

Engineering, *21*(11), 751–760. https://doi.org/10.1016/j.mineng.2008.06.008

Khazeni, A., & Mansourpour, Z. (2018). Influence of non-spherical shape approximation on DEM simulation accuracy by multi-sphere method. *Powder Technology*, *332*, 265–278. https://doi.org/10.1016/j.powtec.2018.03.030

Kime, M. B. (2016). Using the discrete-element method to investigate ball milling power draw, load behaviour, and impact energy profile. *CIM Journal*, *8*(1). https://doi.org/10.15834/cimj.2017.3

King, R. P. (2012). Modeling and Simulation of Mineral Processing Systems. In *Modeling and Simulation of Mineral Processing Systems* (1st ed.). Butterworth-Heinemann. https://books.google.com/books?hl=es&lr=&id=ztiwywayyH4C&pgis=1

Klichowicz, M., Reichert, M., Lieberwirth, H., & Mütze, T. (2014). Self-similarity and energy-size relationship of coarse particles comminuted in single particle mode. *IMPC 2014 - 27th International Mineral Processing Congress, June 2016*.

Knecht, J., & Patzelt, N. (2004). High pressure grinding rolls — applications for the platinum industry. *International Platinium Conference*, 83–88. hpgr

Kojovic, T., & Shi, F. (2008). Update on the JKRBT (JKMRC Rotary Breakage Tester). *Centre for Sustainable Resource Processing*, 43–46.

Koyama, T., & Jing, L. (2007). *Effects of model scale and particle size on micro-mechanical properties and failure processes of rocks — A particle mechanics approach*. *31*, 458–472. https://doi.org/10.1016/j.enganabound.2006.11.009

Latham, J. P., Munjiza, A., Garcia, X., Xiang, J., & Guises, R. (2008). Three-dimensional particle shape acquisition and use of shape library for DEM and FEM/DEM simulation. *Minerals Engineering*, *21*(11), 797–805. https://doi.org/10.1016/j.mineng.2008.05.015

Lee, H., Cho, H., & Kwon, J. (2010). Using the discrete element method to analyze the breakage rate in a centrifugal/vibration mill. *Powder Technology*, *198*(3), 364–372. https://doi.org/10.1016/j.powtec.2009.12.001

Legendre, D., & Zevenhoven, R. (2014). Assessing the energy efficiency of a jaw crusher. *Energy*, *74*(C), 119–130. https://doi.org/10.1016/j.energy.2014.04.036

Leon, L. G., Hogmalm, K. J., & Bengtsson, M. (2020). Understanding mineral liberation during crushing using grade-by-size analysis—a case study of the penuota sn-ta mineralization, spain. *Minerals*, *10*(2). https://doi.org/10.3390/min10020164

Li, H. (2013). *Discrete element method (DEM) modelling of rock flow and breakage within a cone crusher.* University of Nottingham.

Li, H., McDowell, G. R., & Lowndes, I. S. (2012). A laboratory investigation and discrete element modeling of rock flow in a chute. *Powder Technology*, *229*, 199–205. https://doi.org/10.1016/j.powtec.2012.06.032

Lichter, J., Lim, K., Potapov, A., & Kaja, D. (2009). New developments in cone crusher performance optimization. *Minerals Engineering*, *22*(7–8), 613–617. https://doi.org/10.1016/j.mineng.2009.04.003

Lisjak, A., & Grasselli, G. (2014). Journal of Rock Mechanics and Geotechnical Engineering A review of discrete modeling techniques for fracturing processes in discontinuous rock masses. *Journal of Rock Mechanics and Geotechnical Engineering*, *6*(4), 301–314. https://doi.org/10.1016/j.jrmge.2013.12.007

Liu, L., Tan, Q., Liu, L., & Cao, J. (2018). Comparison of different comminution flowsheets in terms of minerals liberation and separation properties. *Minerals Engineering*, *125*(December 2017), 26–33. https://doi.org/10.1016/j.mineng.2018.05.023

Liu, L. X., & Powell, M. (2016). New approach on confined particle bed breakage as applied to multicomponent ore. *Minerals Engineering*, *85*, 80–91. https://doi.org/10.1016/j.mineng.2015.10.016

Lu, M., & McDowell, G. R. (2007). The importance of modelling ballast particle shape in the discrete element method. *Granular Matter*, *9*(1–2), 69–80. https://doi.org/10.1007/s10035-006-0021-3

Luding, S. (2008). Introduction to discete element methods: {{Basics}} of contact force models and how to perform the micro-marco transition to continuum theory. *Euro. J. of Enviro. Civ. Eng.*, *12*(7–8), 785–826.

Maeno, N. (2014). Dynamics and curl ratio of a curling stone. *Sports Engineering*, *17*, 33–41. https://doi.org/10.1007/s12283-013-0129-8

Makgoale, D. M. (2019). *Effects of mill rotational speed on the batch grinding kinetics of a UG2 platinum ore* (Issue November). University of South Africa.

Mateo-Ortiz, D., & Méndez, R. (2016). Microdynamic analysis of particle flow in a confined space using DEM: The feed frame case. *Advanced Powder Technology*, *27*(4), 1597–1606. https://doi.org/10.1016/j.apt.2016.05.023

Moncada, M., Betancourt, F., Rodríguez, C. G., & Toledo, P. (2022). Effect of Particle Shape on Parameter Calibration for a Discrete Element Model for Mining Applications. *Minerals*, *13*(1), 40. https://doi.org/10.3390/min13010040

Morrison, R. D., Cleary, P. W., & Sinnott, M. D. (2009). Using DEM to compare the energy efficiency of pilot scale ball and tower mills. *Minerals Engineering*, *22*(7–8), 665–672. https://doi.org/10.1016/j.mineng.2009.01.016

Naik, S., Malla, R., Shaw, M., & Chaudhuri, B. (2013). Investigation of comminution in a Wiley Mill: Experiments and DEM Simulations. *Powder Technology*, *237*, 338–354. https://doi.org/10.1016/j.powtec.2012.12.019

Napier-Munn, T. J., Morrell, S., Morrison, R. D., & Kojovic, T. (2005). *Mineral comminution circuits: Their operation and optimisation* (3rd ed.). Julius Kruttschnitt Mineral Reseach Centre, The University of Queensland.

Narayanan, S. S., Lean, P. J., & Baker, D. C. (1987). Relationship between breakage parameters and process variables in ball milling - An industrial case study. In *International Journal of Mineral Processing* (Vol. 20, Issues 3–4, pp. 241–251). https://doi.org/10.1016/0301-7516(87)90069-X

Nematollahi, E., Zare, S., Maleki-moghaddam, M., Ghasemi, A., Ghorbani, F., & Banisi, S. (2021). DEM-based design of feed chute to improve performance of cone crushers. *Minerals Engineering*, *168*(April), 106927. https://doi.org/10.1016/j.mineng.2021.106927

Nghipulile, T. (2019). *Modelling studies of a rotary offset crusher*. MSc Thesis. School of Chemical and Metallurgical Engineering. The University of Witwatersrand.

Nghipulile, T., Nkwanyana, S., & Lameck, N. (2023). The Effect of HPGR and Conventional Crushing on the Extent of Micro-Cracks, Milling Energy Requirements and the Degree of Liberation: A Case Study of UG2 Platinum Ore. *Minerals*, *13*(10). https://doi.org/10.3390/min13101309

Nikolov, S. (2002). A performance model for impact crushers. *Minerals Engineering*, *15*(10), 715–721. https://doi.org/10.1016/S0892-6875(02)00174-7

Nikolov, S. (2004). Modelling and simulation of particle breakage in impact crushers. *International Journal of Mineral Processing*, *74*(SUPPL.), 219–225. https://doi.org/10.1016/j.minpro.2004.07.03l

Nyberg, H., Alfredson, S., Hogmark, S., & Jacobson, S. (2013). The asymmetrical friction mechanism that puts the curl in the curling stone. *Wear*, *301*(1–2), 583–589. https://doi.org/10.1016/j.wear.2013.01.051

Nyberg, H., Alfredsson, S., & Hogmark, S. (2013). *The mechanism that puts the curl in the curling stone revealed*. *May*, 1–2. https://doi.org/10.1007/s11249-013-0135-9

Obermayr, M., Dressler, K., Vrettos, C., & Eberhard, P. (2011). Prediction of draft forces in cohesionless soil with the Discrete Element Method. *Journal of Terramechanics*, *48*(5), 347–358. https://doi.org/10.1016/j.jterra.2011.08.003

Ozcan, O., & Benzer, H. (2013). Comparison of different breakage mechanisms in terms of product particle size distribution and mineral liberation. *Minerals Engineering*, *49*, 103–108. https://doi.org/10.1016/j.mineng.2013.05.006

Ozkan, A., Yekeler, M., & Aydogan, S. (2003). Breakage parameters of some minerals and coals ground in a laboratory size ceramic mill. *Indian Journal of Engineering and Materials Sciences*, *10*(4), 269–276.

Pachón-morales, J., Do, H., Colin, J., Puel, F., Perré, P., & Schott, D. (2019). *DEM modelling for flow of cohesive lignocellulosic biomass powders : Model calibration using bulk tests*. *30*, 732–750. https://doi.org/10.1016/j.apt.2019.01.003

Padokhin, V. A., & Zueva, G. A. (2009). Stochastic models of the grinding of disperse materials. *Theoretical Foundations of Chemical Engineering*, *43*(5), 682–689. https://doi.org/10.1134/S0040579509050108

Pareek, P., & Sankhla, V. S. (2020). Review on vertical roller mill in cement industry & its performance parameters. *Materials Today: Proceedings*, *44*, 4621–4627. https://doi.org/10.1016/j.matpr.2020.10.916

Park, B., Min, K., Thompson, N., & Horsrud, P. (2018). Three-dimensional bonded-particle discrete element modeling of mechanical behavior of transversely isotropic rock. *International Journal of Rock Mechanics and Mining Sciences*, *110*(May 2017), 120–132. https://doi.org/10.1016/j.ijrmms.2018.07.018

Park, C. H., & Bobet, A. (2009). Crack coalescence in specimens with open and closed flaws : A comparison. *International Journal of Rock Mechanics and Mining Sciences*, *46*(5), 819–829. https://doi.org/10.1016/j.ijrmms.2009.02.006

Pedrayes, F., Norniella, J. G., Melero, M. G., Menéndez-Aguado, J. M., & del Coz-Díaz, J. J. (2018). Frequency domain characterization of torque in tumbling ball mills using DEM modelling: Application to filling level monitoring. *Powder Technology*, *323*, 433–444. https://doi.org/10.1016/j.powtec.2017.10.026

Penner, A. R. (2000). The physics of sliding cylinders and curling rocks. *American Journal of Physics*, *69*(3), 332–339. https://doi.org/10.1119/1.1309519

Penner, A. R. (2018). *The Motion of a Curling Rock Penner – The Motion of a Curling Rock The Motion of a Curling Rock Author : Address : A . Raymond Penner Department of Physics Vancouver Island University 900 Fifth Street Nanaimo , BC , Canada Email : PACS : February*.

Penner, A. R. (2019). *A Scratch-Guide Model for the Motion of a Curling Rock Penner – The Motion of a Curling Rock A scratch-guide model for the motion of a curling rock Author : Address : A . Raymond Penner Department of Physics Vancouver Island University 900 Fifth Street Na*. *April*, 0–28. https://doi.org/10.1007/s11249-019-1144-0

Petrakis, E., & Komnitsas, K. (2017). Improved Modeling of the Grinding Process through the Combined Use of Matrix and Population Balance Models. *Minerals*, *7*(5), 67. https://doi.org/10.3390/min7050067

Petrakis, E., Stamboliadis, E., & Komnitsas, K. (2017). Identification of optimal mill operating parameters during grinding of quartz with the use of population balance modeling. *KONA Powder and Particle Journal*, *2017*(34), 213–223. https://doi.org/10.14356/kona.2017007

Potyondy, D. O., & Cundall, P. A. (2004). *A bonded-particle model for rock*. *41*, 1329–1364. https://doi.org/10.1016/j.ijrmms.2004.09.011

Powell, M. S., & Morrison, R. D. (2007). *The future of comminution modelling*. *84*, 228–239. https://doi.org/10.1016/j.minpro.2006.08.003

Quist, J. C. E. (2017). *DEM Modelling and Simulation of Cone Crushers and High Pressure Grinding Rolls*. Chalmers University of Technology.

Quist, J., & Evertsson, C. (2010). Application of discrete element method for simulating feeding conditions and size reduction in cone crushers. *XXV International Mineral Processing Congress (IMPC) 2010 Proceedings / Brisbane*.

Quist, J., & Evertsson, C. M. (2016a). Cone crusher modelling and simulation using DEM. *Minerals Engineering*, *85*, 92–105. https://doi.org/10.1016/j.mineng.2015.11.004

Quist, J., & Evertsson, C. M. (2016b). Cone crusher modelling and simulation using DEM Cone crusher modelling and simulation using DEM. *Minerals Engineering*, *85*(May 2018), 92–

105. https://doi.org/10.1016/j.mineng.2015.11.004

Radziszewski, P. (2013). Energy recovery potential in comminution processes. *Minerals Engineering*, *46–47*, 83–88. https://doi.org/10.1016/j.mineng.2012.12.002

Rajamani, R. K., Rashidi, S., & Dhawan, N. (2014). Advances in discrete element method application to grinding mills. *Mineral Processing and Extractive Metallurgy*, *100*(Morell 1992), 117–128.

Reichert, M., Gerold, C., Fredriksson, A., Adolfsson, G., & Lieberwirth, H. (2015). Research of iron ore grinding in a vertical-roller-mill. *Minerals Engineering*, *73*, 109–115. https://doi.org/10.1016/j.mineng.2014.07.021

Richter, C., Rößler, T., Kunze, G., Katterfeld, A., & Will, F. (2020). Development of a standard calibration procedure for the DEM parameters of cohesionless bulk materials – Part II : Ef fi cient optimization-based calibration. *Polymer Journal*, *360*, 967–976. https://doi.org/10.1016/j.powtec.2019.10.052

Romer, R. H. (1981). Motion of a sphere on a tilted turntable. *American Journal of Physics*, *59*, 985–986. https://doi.org/10.1119/1.12598

Rong, G., Liu, G., Hou, D., & Zhou, C. B. (2013). Effect of particle shape on mechanical behaviors of rocks: A numerical study using clumped particle model. *The Scientific World Journal*, *2013*. https://doi.org/10.1155/2013/589215

Rosario, P., & Hall, R. (2010). A structured approach to the evaluation of the energy requirements of HPGR and SAG mill circuits in hard ore applications. *Journal of the Southern African Institute of Mining and Metallurgy*, *110*(3), 117–123.

Rosario, P., Hall, R., Grundy, M., & Klein, B. (2011). A preliminary investigation into the feasibility of a novel HPGR-based circuit for hard, weathered ores containing clayish material. *Minerals Engineering*, *24*(3–4), 290–302. https://doi.org/10.1016/j.mineng.2010.09.011

Rozenblat, Y., Portnikov, D., Levy, A., Kalman, H., Aman, S., & Tomas, J. (2011). Strength distribution of particles under compression. *Powder Technology*, *208*(1), 215–224. https://doi.org/10.1016/j.powtec.2010.12.023

Sadrai, S., Meech, J. A., Ghomshei, M., Sassani, F., & Tromans, D. (2006). Influence of impact velocity on fragmentation and the energy efficiency of comminution. *International Journal of Impact Engineering*, *33*(1–12), 723–734. https://doi.org/10.1016/j.ijimpeng.2006.09.063

Sadrai, S., Meech, J. A., Tromans, D., & Sassani, F. (2011). Energy efficient comminution under high velocity impact fragmentation. *Minerals Engineering*, *24*(10), 1053–1061. https://doi.org/10.1016/j.mineng.2011.05.006

Saramak, D. (2011). The influence of chosen ore properties on efficiency of HPGR-based grinding circuits. *Gospodarka Surowcami Mineralnymi / Mineral Resources Management*, *27*(4), 33–44.

Saramak, D., Wasilewski, S., & Saramak, A. (2017). Influence of copper ore comminution in HPGR on downstream minerallurgical processes. *Archives of Metallurgy and Materials*, *62*(3), 1689–1694. https://doi.org/10.1515/amm-2017-0258

Schönert, K. (1988). A first survey of grinding with high-compression roller mills. *International Journal of Mineral Processing*, *22*(1–4), 401–412. https://doi.org/10.1016/0301-7516(88)90075-0

Schönert, K. (1996). The influence of particle bed configurations and confinements on particle breakage. *International Journal of Mineral Processing*, *44–45*(SPEC. ISS.), 1–16. https://doi.org/10.1016/0301-7516(95)00017-8

Segura-Salazar, J., Barrios, G. P., Rodriguez, V., & Tavares, L. M. (2017). Mathematical modeling of a vertical shaft impact crusher using the Whiten model. *Minerals Engineering*, *111*(June), 222–228. https://doi.org/10.1016/j.mineng.2017.06.022

Semsari Parapari, P., Parian, M., & Rosenkranz, J. (2020). Breakage process of mineral processing comminution machines – An approach to liberation. *Advanced Powder Technology*, *31*(9), 3669–3685. https://doi.org/10.1016/j.apt.2020.08.005

Shegelski, M., & Lozowski, E. P. (2019). Null effect of scratches made by curling rocks. *Journal of Sports Engineering and Technology*, *January*, 1–5. https://doi.org/10.1177/1754337118821575

Shegelski, M. R. A., & Lozowski, E. (2016). Pivot – slide model of the motion of a curling rock. *Canadian Journal of Physics*, *September*, 1305–1309. https://doi.org/10.1139/cjp-2016-0466

Shi, F., & Kojovic, T. (2007). Validation of a model for impact breakage incorporating particle size effect. *International Journal of Minera*, *82*, 156–163. https://doi.org/10.1016/j.minpro.2006.09.006

Shimoska, A., Nousou, I., Shirakawa, Y., & Hidaka, J. (2013). Effect of particle shape on size segregation of particles. *Chemical Engineering Transactions*, *32*, 2143–2148. https://doi.org/10.3303/CET1332358

Sima, J., Jiang, M., & Zhou, C. (2014). Numerical simulation of desiccation cracking in a thin clay layer using 3D discrete element modeling. *Computers and Geotechnics*, *56*, 168–180. https://doi.org/10.1016/j.compgeo.2013.12.003

Sinnott, M. D., & Cleary, P. W. (2015). Simulation of particle flows and breakage in crushers using DEM: Part 2 - Impact crushers. *Minerals Engineering*, *74*, 163–177. https://doi.org/10.1016/j.mineng.2014.11.017

Solsvik, J., & Jakobsen, H. A. (2015). The Foundation of the Population Balance Equation: A Review. *Journal of Dispersion Science and Technology*, *36*(4), 510–520. https://doi.org/10.1080/01932691.2014.909318

Tan, Q.-M. (2011). *Dimensional Analysis with Case Studies in Mechanics*. Springer Berlin Heidelberg. https://doi.org/e-ISBN 978-3-642-19234-0

Tang, Y., Yin, W., Huang, S., Xue, J., & Zuo, W. (2020). Enhancement of gold agitation leaching by HPGR comminution via microstructural modification of gold ore particles. *Minerals Engineering*, *159*(April), 106639. https://doi.org/10.1016/j.mineng.2020.106639

Tang, Z., Yu, L., Wang, F., Li, N., Chang, L., & Cui, N. (2018). Effect of particle size and shape on separation in a hydrocyclone. *Water*, *11*(1), 1–19. https://doi.org/10.3390/w11010016

Tavares, L. ., & King, R. . (1998). Single-particle fracture under impact loading. *International Journal of Mineral Processing*, *54*(1), 1–28. https://doi.org/10.1016/s0301-7516(98)00005-2

Tavares, L. M. (2004). Optimum routes for particle breakage by impact. *Powder Technology*, *142*(2–3), 81–91. https://doi.org/10.1016/j.powtec.2004.03.014

Tavares, L. M. (2005). Particle weakening in high-pressure roll grinding. *Minerals Engineering*, *18*(7), 651–657. https://doi.org/10.1016/j.mineng.2004.10.012

Tavares, L. M. (2008). Comparison of measures of rock crushability. *Fine Particle Technology and Characterization*, *June*.

Tavares, M. L., André, F. P., Potapov, A., & Maliska Jr, C. (2020). Adapting a breakage model to discrete elements using polyhedral particles. *Powder Technology*, *362*, 208–220. https://doi.org/10.1016/j.powtec.2019.12.007

Thornton, C., Cummins, S. J., & Cleary, P. W. (2013). An investigation of the comparative behaviour of alternative contact force models during inelastic collisions. *Powder Technology*, *233*, 30–46. https://doi.org/10.1016/j.powtec.2012.08.012

Tiersten, M. (2015). *Perturbation analysis of rolling friction on a turntable*. *November*. https://doi.org/10.1119/1.18333

Ting, J. M., Corkum, B. T., Kauffman, C. R., & Greco, C. (1989). *Discrete numerical model for soil mechanics*. *115*(3), 379–398.

Ting, J. M., Khwaja, M., Meachum, L. R., & Rowell, J. D. (1993). An ellipse-based discrete element model for granular materials. *International Journal for Numerical and Analytical Methods in Geomechanics*, *17*(November 1992), 603–623.

Ündül, Ö., Amann, F., & Plötze, M. L. (2015). *Micro-textural effects on crack initiation and crack propagation of andesitic rocks*. *193*, 267–275. https://doi.org/10.1016/j.enggeo.2015.04.024

Vásárhelyi, B., & Bobet, A. (2000). Modeling of crack initiation, propagation and coalescence in uniaxial compression. *Rock Mechanics and Rock Engineering*, *33*(2), 119–139. https://doi.org/10.1007/s006030050038

Vogel, L., & Peukert, W. (2004). Determination of material properties relevant to grinding by practicable labscale milling tests. *International Journal of Mineral Processing*, *74S*, 329–338. https://doi.org/10.1016/j.minpro.2004.07.018

Wang, E. Z., & Shrive, N. G. (1995). Brittle fracture in compression: Mechanisms, models and criteria. In *Engineering Fracture Mechanics* (Vol. 52, Issue 6, pp. 1107–1126). https://doi.org/10.1016/0013-7944(95)00069-8

Wang, J. H., Chen, Q. R., Kuang, Y. L., Lynch, A. J., & Zhuo, J. W. (2009). Grinding process within vertical roller mills: experiment and simulation. *Mining Science and Technology*, *19*(1), 97–101. https://doi.org/10.1016/S1674-5264(09)60018-1

Wang, L., Wu, B., Wu, Z., Li, R., & Feng, X. (2018). Experimental determination of the coefficient of restitution of particle-particle collision for frozen maize grains. *Powder Technology*, *338*, 263–273. https://doi.org/10.1016/j.powtec.2018.07.005

Weckesser, W. (1997). A ball rolling on a freely spinning turntable. *American Journal of Physics*, *65*, 736–738. https://doi.org/10.1119/1.18643

Weerasekara, N. S., Liu, L. X., & Powell, M. S. (2016). Estimating energy in grinding using DEM modelling. *Minerals Engineering*, *85*, 23–33.

https://doi.org/10.1016/j.mineng.2015.10.013

Weerasekara, N. S., Powell, M. S., Cleary, P. W., Tavares, L. M., Evertsson, M., Morrison, R. D., Quist, J., & Carvalho, R. M. (2013). The contribution of DEM to the science of comminution. *Powder Technology*, *248*, 3–4. https://doi.org/10.1016/j.powtec.2013.05.032

Whiten, W. J. (1972). The simulation of crushing plants with models developed using multiple spline regression. *Journal of the South African Institute of Mining and Metallurgy*, *72*(10), 257–264. http://www.saimm.co.za/Journal/v072n10p257.pdf

Wills, B. ., & Napier-Munn, T. . (2006). *Wills' Mineral Processing Technology* (7th ed.). Elsverier; Butterworth-Heinemann.

Wills, B. A., & Finch, J. (2016). *Wills' mineral processing technology: An introdution to prcatical aspects of ore treatment and mineral recovery* (8th ed.). Elsverier; Butterworth-Heinemann.

X., L., & T.-T., N. (1997). A three-dimensional discrete element model using arrays of ellipsoids. *Geotechnique*, *47*(2), 319--329.

Xu, J., & Li, Z. (2017). Damage evolution and crack propagation in rocks. *Acta Mechanica Solida Sinica*, *30*(6), 573–582. https://doi.org/10.1016/j.camss.2017.11.001

Yang, J., Guo, Y., Buettner, K. E., & Curtis, J. S. (2019). DEM investigation of shear flows of binary mixtures of non-spherical particles. *Chemical Engineering Science*, *202*, 383–391. https://doi.org/10.1016/j.ces.2019.03.027

Ye, F., Wheeler, C., Chen, B., Hu, J., Chen, K., & Chen, W. (2019). Calibration and verification of DEM parameters for dynamic particle flow conditions using a backpropagation neural network. *Advanced Powder Technology*, *30*(2), 292–301. https://doi.org/10.1016/j.apt.2018.11.005

You, M. (2015). Strength criterion for rocks under compressive-tensile stresses and its application. *Journal of Rock Mechanics and Geotechnical Engineering*, *7*(4), 434–439. https://doi.org/10.1016/j.jrmge.2015.05.002

Yunteng, W., Xiaoping, Z., & Yundong, S. (2017). *The modeling of crack propagation and coalescence in rocks under uniaxial compression using the novel conjugated bond-based peridynamics*. *129*, 614–643. https://doi.org/10.1016/j.ijmecsci.2017.05.019

Zhao, J., & Zhang, D. (2020). Dynamic microscale crack propagation in shale. *Engineering Fracture Mechanics*, *228*(February), 106906.

https://doi.org/10.1016/j.engfracmech.2020.106906

Zhao, Y., Zhang, L., Wang, W., Pu, C., Wan, W., & Tang, J. (2016). Cracking and Stress–Strain Behavior of Rock-Like Material Containing Two Flaws Under Uniaxial Compression. *Rock Mechanics and Rock Engineering*, *49*(7), 2665–2687. https://doi.org/10.1007/s00603-016-0932-1

Zhou, S., Zhuang, X., Zhu, H., & Rabczuk, T. (2018). Phase fi eld modelling of crack propagation , branching and coalescence in rocks. *Theoretical and Applied Fracture Mechanics*, *96*(May), 174–192. https://doi.org/10.1016/j.tafmec.2018.04.011

Zhou, X., Gu, X., & Wang, Y. (2015). Numerical simulations of propagation , bifurcation and coalescence of cracks in rocks. *International Journal of Rock Mechanics and Mining Sciences*, *80*, 241–254. https://doi.org/10.1016/j.ijrmms.2015.09.006

Zuo, W., & Shi, F. (2016). Ore impact breakage characterisation using mixed particles in wide size range. *Minerals Engineering*, *86*, 96–103. https://doi.org/10.1016/j.mineng.2015.12.007

Zuo, W., Shi, F., Van Der Wielen, K. P., & Weh, A. (2015). Ore particle breakage behaviour in a pilot scale high voltage pulse machine. *Minerals Engineering*, *84*, 64–73. https://doi.org/10.1016/j.mineng.2015.09.025

APPENDICES

Appendix A: DEM models and relevant equations

Table A 1: Spring stiffness constants and damping coefficients (Jiménez-Herrera, Barrios, & Tavares, 2018; Weerasekara et al., 2013)

	Normal direction (*n*)	**Tangential direction (*t*)**
Spring stiffness constant(K)	$K_n = \frac{4}{3}E^*\sqrt{R^*\delta_n}$	$K_t = 8G^*\sqrt{R^*\delta_t}$
Damping coefficient (C)	$C_n = 2\sqrt{\frac{5}{6}}\beta\sqrt{S_n m^*}$	$C_n = 2\sqrt{\frac{5}{6}}\beta\sqrt{K_t m^*}$
$S_n = 2E^*\sqrt{R^*\delta_n}$, $\beta = \frac{\ln\varepsilon}{\sqrt{\ln^2\varepsilon + \pi^2}}$ *E** is the effective Young modulus *G** is the effective shear modulus *m** is the effective mass		

Table A 2: Some contact models in ROCKY DEM software (source: ROCKY DEM technical manual)

Normal Direction Contact Models	**Tangential Direction Contact Models**
Hysteretic linear spring model $F_n^t = \begin{cases} \min(K_{nl}s_n^t, F_n^{t-\Delta t} + K_{nu}\Delta s_n)\ if\ \Delta s_n \ge 0 \\ \max(F_n^{t-\Delta t} + K_{nu}\Delta s_n, \lambda K_{nl}s_n^t)\ if\ \Delta s_n < 0 \end{cases}$ (A1) $\Delta s_n = s_n^t - s_n^{t-\Delta t}$ (A2) Where: F_n^t and $F_n^{t-\Delta t}$ are the normal elastic-plastic contact forces at the current time t and at the previous time $t - \Delta t$, respectively, where Δt is the time step. Δs_n is the change in the contact normal overlap during the current time. It is assumed to be positive as particles approach each other and negative when they separate. s_n^t and $s_n^{t-\Delta t}$ are the normal overlap values at the current and at the previous time, respectively. K_{nl} and K_{nu} are the values of loading and unloading contact stiffnesses, respectively. λ is a dimensionless small constant. I	Linear spring Coulomb limit model $F_\tau^t = \min\left(\lvert F_{\tau,e}^t\rvert, \mu F_n^t\right)\frac{F_t}{\lvert F_{\tau,e}^t\rvert}$ (A3) where: • F_n^t is the contact normal force at time t. • μ is the friction coefficient, defined as: $\mu = \begin{cases} \mu_s \text{ if no sliding takes place at the contact} \\ \mu_d \text{ if sliding does take place at the contact} \end{cases}$ (A4) in which μ_s and μ_d are, respectively, the static and the dynamic friction coefficients.
Linear spring-dashpot model $F_n = k_{nl}s_n + C_s\dot{s}_n$ (A5) Where: • K_{nl} is the normal contact stiffness • C_n is the normal damping coefficient. • s_n is the contact normal overlap. • $\dot{s}_n$ is the time derivative of the contact normal overlap.	Coulomb limit model This is the simplest tangential force model implemented in Rocky. The tangential force according to this model is given by: $F_\tau = -\mu F_n \frac{\dot{s}_\tau}{\lvert\dot{s}_\tau\rvert}$ (A6) where: • μ is the friction coefficient. • F_n is the normal force at the contact. • $\dot{s}_\tau$ is the tangential component of the relative velocity vector
Hertzian spring-dashpot model This model is similar to the linear spring-dashpot model, the main difference being that both the elastic and the damping components of the normal force are nonlinear functions of the overlap in the Hertzian model. The form of the Hertzian spring-dashpot model implemented in Rocky can be written as: $F_n = \hat{K}_H S_n^{\frac{3}{2}} + \hat{C}_H s_n^{\frac{1}{4}}\hat{s}_n$ (A7) in which the stiffness coefficient $\hat{K}_H$ is defined as $\hat{K}_H = \frac{4}{3}E^*\sqrt{R^*}$ (A8)	Mindlin-Deresiewicz model The tangential force in this model is given by the expressions: $F_\tau = -\mu F_n\left(1 - \varsigma^{\frac{3}{2}}\right)\frac{s_\tau}{\lvert s_\tau\rvert} + \eta_\tau\sqrt{\frac{6\mu m^* F_n}{s_{\tau,max}}}\varsigma^{\frac{1}{4}}\dot{s}_\tau$ (A9) $\varsigma = 1 - \frac{\min(\lvert s_\tau\rvert, s_{\tau,max})}{s_{\tau,max}}$ (A10) where: • μ is the friction coefficient • F_n is the normal force. • s_τ is the tangential relative displacement at the contact. • $\dot{s}_\tau$ is the tangential component of the relative velocity at the contact. • $s_{\tau,max}$ is the maximum relative tangential displacement at which particles begin to slide. • m_* is the effective mass. • η_τ is the tangential damping ratio

Appendix B: Derivation of Pi theorem

In deriving the Pi theorem, we consider the physical phenomenon to have *n* independent variables a_1, a_2, ..., a_n and one dependent variable a, i.e. a is a function of a_1, a_2, ..., a_n as represented mathematically below.

$$a = f(a_1, a_2, \ldots, a_k, a_{k+1}, a_{k+2}, \ldots, a_n) \tag{B1}$$

If the number of fundamental quantities is *k*, it is possible without losing generality to select *k* independent variables a_1, a_2,… a_k with mutually independent dimensions as a group of fundamental quantities having dimensions A_1, A_2, …, A_k respectively.

The remaining *n-k* independent variables a_{k+1}, a_{k+2}, …, a_n are derived quantities.

$$[a_{k+1}] = A_1^{P_1} A_2^{P_2} \ldots A_k^{P_k}$$

$$[a_{k+2}] = A_1^{q_1} A_2^{q_2} \ldots A_k^{q_k}$$

.

.

.

$$[a_n] = A_1^{r_1} A_2^{r_2} \ldots A_k^{r_k}$$

Where P_1, …, P_k, q_1, …, q_k, r_1, …, r_k are relevant power values.

Dependent variable a is derived quantity with a dimension given by the following equation:

$$[a] = A_1^{m_1} A_2^{m_2} \ldots A_k^{m_k} \tag{B2}$$

Where m_1, …, m_k are relevant power values.

The fundamental quantities (a_1, a_2, ..., a_k) can be taken as a unit system to measure all variables in Eq. (B2). Using Eq. (B2), the magnitudes of all the variables become dimensionless pure numbers as shown by Eq. (47).

$$\frac{a}{a_1^{m_1} a_2^{m_2} \ldots a_k^{m_k}} = f\left(1, 1, \ldots, 1;\ \frac{a_{k+1}}{a_1^{P_1} a_2^{P_2} \ldots a_k^{P_k}}, \frac{a_{k+2}}{a_1^{q_1} a_2^{q_2} \ldots a_k^{q_k}}, \ldots, \frac{a_n}{a_1^{r_1} a_2^{r_2} \ldots a_k^{r_k}}\right) \tag{B3}$$

The left hand side (LHS of Eq. (B3) is a dimensionless dependent variable which is denoted by π. On the right hand side (RHS), the magnitude of first k independent variables equal unity (i.e. 1) and thus they do not affect π. The magnitudes of the remaining n-k independent variables are denoted as π_1, π_2, ..., π_{n-k} (see below expressions) and they are the ones determining magnitude of dependent variable π as shown in Eq. (B4)

$$\pi = f(\pi_1, \pi_2, \ldots, \pi_{n-k}) \qquad \text{(B4)}$$

Where $\pi_1, \pi_2, \ldots, \pi_{n-k}$ are mutually independent variables. These dimensionally independent variables are given by the following equations:

$$\pi_1 = \frac{a_{k+1}}{a_1^{P_1} a_2^{P_2} \ldots a_k^{P_k}}$$

$$\pi_2 = \frac{a_{k+2}}{a_1^{q_1} a_2^{q_2} \ldots a_k^{q_k}}$$

$$\pi_{n-k} = \frac{a_n}{a_1^{r_1} a_2^{r_2} \ldots a_k^{r_k}}$$

Using implicit function, the Pi theorem can be formulated. If N variables a_1, a_2, ...a_N relate to a physical problem and include one dependent variable and N-1 independent variables, an implicit function can express the physical law of the problem.

$$f(a_1, a_2, \ldots, a_N) = 0 \qquad \text{(B5a)}$$

Without losing generality, k quantities a_1, a_2, ..., a_k can be selected as fundamental quantities and the rest N-k quantities can be selected as derived quantities , k fundamental quantities can be a unit system and Eq. (49a) can reduce to dimensionless relation:

$$f(1, 1, \ldots, 1; \pi_1, \pi_2, \ldots, \pi_{N-k}) = 0 \qquad \text{(B5b)}$$

Where $\pi_1, \pi_2, \ldots, \pi_{n-k}$ are magnitudes of a_{k+1}, a_{k+2}, …, a_N and magnitudes of the first k variables, a_1, ..., a_k = 1 and do not affect function f. Because only N-k dimensionless variables $\pi_1, \pi_2, \ldots, \pi_{n-k}$ are significant, Eq. (50b) can be

$$f(\pi_1, \pi_2, \ldots, \pi_{n-k}) = 0 \qquad \text{(B6)}$$

In summary, the Pi theorem states that "*If a physical problem has N variables that include one dependent variable and N-1 independent variables, k fundamental quantities and N-k derived quantities, then N-k dimensionless variables can form a definite relationship that reflect the substance of the problem*" (Tan, 2011).

Appendix C: Crushability work index results

Table C 1: Bond crushability data of silica sample

Specimen no.	Measured Rock Thickness (mm)	Initial mass (g)	Angle of breakage (º)	Mass of biggest particle (g)	Target mass of largest particle smaller than (g)
1	70	625.500	55	369.0	412.830
2	65	371.500	35	168.0	245.190
3	55	312.000	25	160.0	205.920
4	55	442.500	40	220.0	292.050
5	55	401.000	35	199.0	264.660
6	50	278.500	35	177.0	183.810
7	55	458.000	40	206.5	302.280
8	60	587.000	50	195.0	387.420
9	60	577.000	50	308.5	380.820
10	55	284.000	40	114.0	187.440
11	50	480.500	35	281.0	317.130
12	50	356.500	40	194.5	235.290
13	50	228.000	40	89.5	150.480
14	65	529.000	55	324.0	349.140
15	60	391.500	50	207.0	258.390
16	50	426.000	30	145.5	281.160
17	60	663.500	35	405.0	437.910
18	60	260.500	50	84.5	171.930
19	50	506.500	45	210.5	334.290
20	50	204.000	25	105.0	134.640
21	45	255.000	30	103.0	168.300
22	55	539.000	40	277.5	355.740
23	60	559.500	45	240.5	369.270
24	50	204.500	30	76.5	134.970
25	60	275.000	30	177.0	181.500
26	60	331.500	50	143.0	218.790
27	55	230.000	35	80.5	151.800
28	40	223.500	25	94.5	147.510
29	60	211.500	35	98.5	139.590
30	60	282.000	45	139.0	186.120

Table C 2: Bond crushability data of UG2 ore sample

Specimen no.	Measured Rock Thickness (mm)	Initial mass (g)	Angle of breakage (º)	Mass of biggest particle (g)	Target mass of largest particle smaller than (g)
1	65	525.000	50	208.5	346.500
2	65	657.000	35	266.0	433.620
3	65	698.000	30	375.5	460.680
4	65	941.000	55	468.0	621.060
5	65	640.500	35	359.5	422.730
6	65	531.500	65	250.0	350.790
7	65	753.500	55	179.0	497.310
8	65	695.000	25	235.0	458.700
9	65	883.500	20	248.5	583.110
10	70	529.000	40	236.5	349.140
11	55	447.000	40	144.5	295.020
12	60	536.000	45	217.0	353.760
13	65	571.000	75	251.5	376.860
14	65	842.500	25	432.0	556.050
15	60	478.000	35	227.5	315.480
16	55	743.000	30	411.5	490.380
17	55	589.500	30	351.0	389.070
18	55	261.000	20	160.5	172.260
19	60	522.000	55	306.5	344.520
20	55	288.500	20	85.5	190.410
21	60	352.000	40	87.5	232.320
22	50	675.500	15	404.0	445.830
23	50	662.000	40	159.5	436.920
24	60	393.000	45	232.5	259.380
25	55	229.500	35	101.5	151.470
26	55	408.000	20	197.0	269.280
27	50	242.500	45	99.5	160.050
28	45	203.500	15	101.5	134.310
29	60	394.500	35	250.5	260.370
30	60	361.000	35	167.0	238.260

Table C 3: Bond crushability final results of silica sample

Rock Specimen Number	Rock impact thickness (mm)	Impact angle (°)	Impact Energy E_B (J)	Impact Strength C_B (J/mm)	Work Index C_{WI} (kWh/tonne)
1	70	55	49.892	0.713	14.28
2	65	35	21.159	0.326	6.52
3	55	25	10.962	0.199	3.99
4	55	40	27.373	0.498	9.97
5	55	40	27.373	0.498	9.97
6	55	35	21.159	0.385	7.71
7	50	35	21.159	0.423	8.48
8	55	40	27.373	0.498	9.97
9	60	50	41.794	0.697	13.95
10	60	50	41.794	0.697	13.95
11	55	40	27.373	0.498	9.97
12	50	35	21.159	0.423	8.48
13	50	40	27.373	0.547	10.97
14	50	40	27.373	0.547	10.97
15	65	55	49.892	0.768	15.38
16	60	50	41.794	0.697	13.95
17	50	30	15.675	0.314	6.28
18	60	35	21.159	0.353	7.06
19	60	50	41.794	0.697	13.95
20	50	45	34.269	0.685	13.73
21	50	25	10.962	0.219	4.39
22	45	30	15.675	0.348	6.98
23	55	40	27.373	0.498	9.97
24	60	45	34.269	0.571	11.44
25	50	30	15.675	0.314	6.28
26	60	30	15.675	0.261	5.23
27	60	50	41.794	0.697	13.95
28	55	35	21.159	0.385	7.71
29	40	25	10.962	0.274	5.49
30	60	35	21.159	0.353	7.06

	Rock SG:		**Work Index:**		
	2.67	t/m^3	Minimum	4.0	kWh/tonne
			Maximum	15.4	kWh/tonne
			Average	9.6	kWh/tonne
			75th Percentile	13.8	kWh/tonne

Table C 4: Bond crushability final results of UG2 ore sample

Rock Specimen Number	Rock impact thickness (mm)	Impact angle (°)	Impact Energy E_B (J)	Impact Strength C_B (J/mm)	Work Index C_{WI} (kWh/tonne)
1	65	50	41.794	0.643	10.22
2	65	35	21.159	0.326	5.17
3	65	30	15.675	0.241	3.83
4	65	55	49.892	0.768	12.20
5	65	55	49.892	0.768	12.20
6	65	35	21.159	0.326	5.17
7	65	65	67.554	1.039	16.52
8	65	55	49.892	0.768	12.20
9	65	25	10.962	0.169	2.68
10	65	20	7.056	0.109	1.73
11	70	40	27.373	0.391	6.21
12	55	40	27.373	0.498	7.91
13	60	45	34.269	0.571	9.08
14	65	75	86.718	1.334	21.20
15	65	25	10.962	0.169	2.68
16	60	35	21.159	0.353	5.60
17	55	30	15.675	0.285	4.53
18	55	30	15.675	0.285	4.53
19	55	20	7.056	0.128	2.04
20	60	55	49.892	0.832	13.21
21	55	20	7.056	0.128	2.04
22	60	40	27.373	0.456	7.25
23	50	15	3.987	0.080	1.27
24	50	40	27.373	0.547	8.70
25	60	45	34.269	0.571	9.08
26	55	35	21.159	0.385	6.11
27	55	20	7.056	0.128	2.04
28	50	45	34.269	0.685	10.89
29	45	15	3.987	0.089	1.41
30	60	35	21.159	0.353	5.60

	Rock SG:		**Work Index:**		
	3.37	t/m^3	Minimum	1.3	kWh/tonne
			Maximum	21.2	kWh/tonne
			Average	7.1	kWh/tonne
			75th Percentile	10.4	kWh/tonne

Appendix D: Product size distributions of the breakage characteristics tests

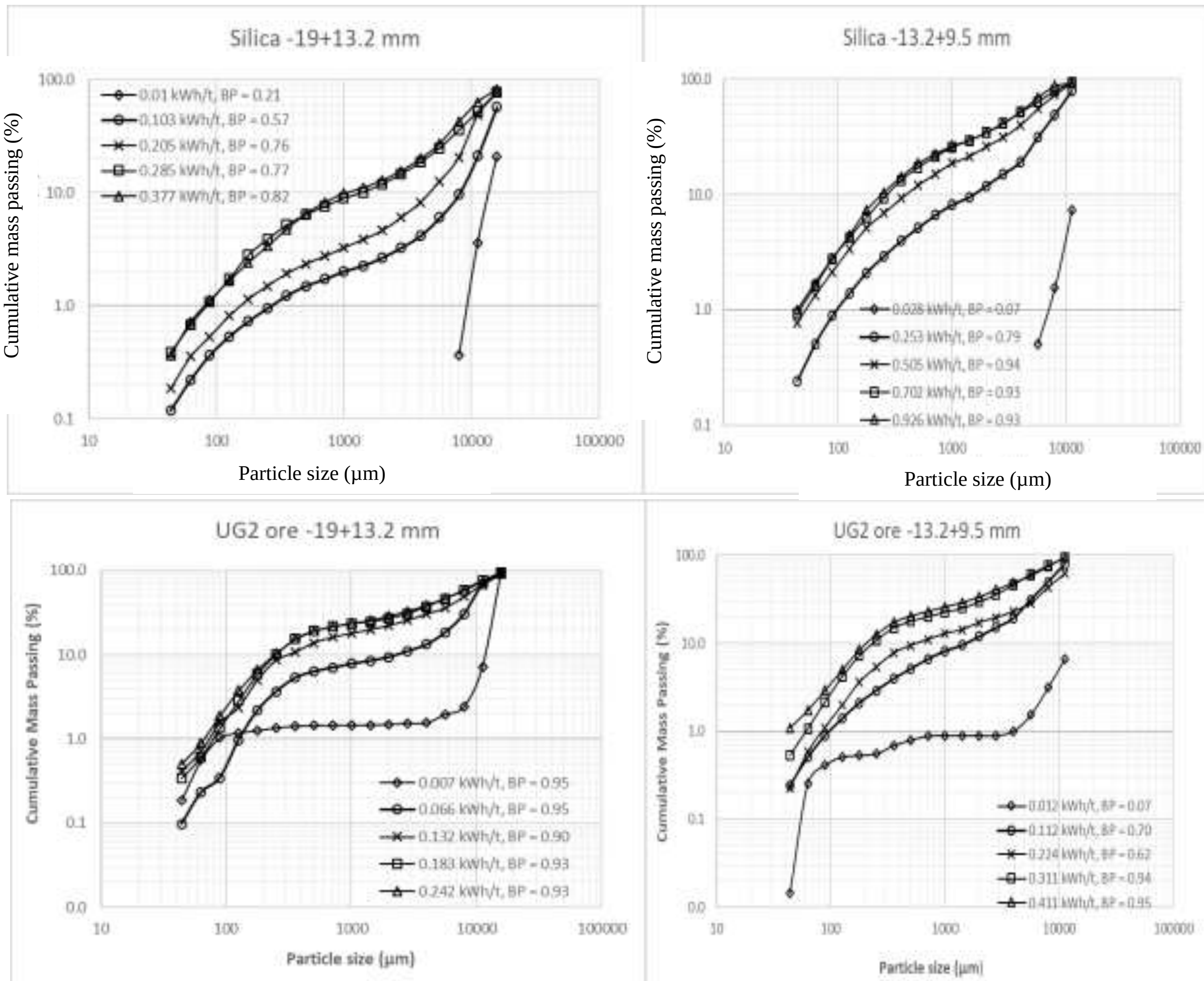

Figure D 1: DWT product size distributions of silica and UG2 ore

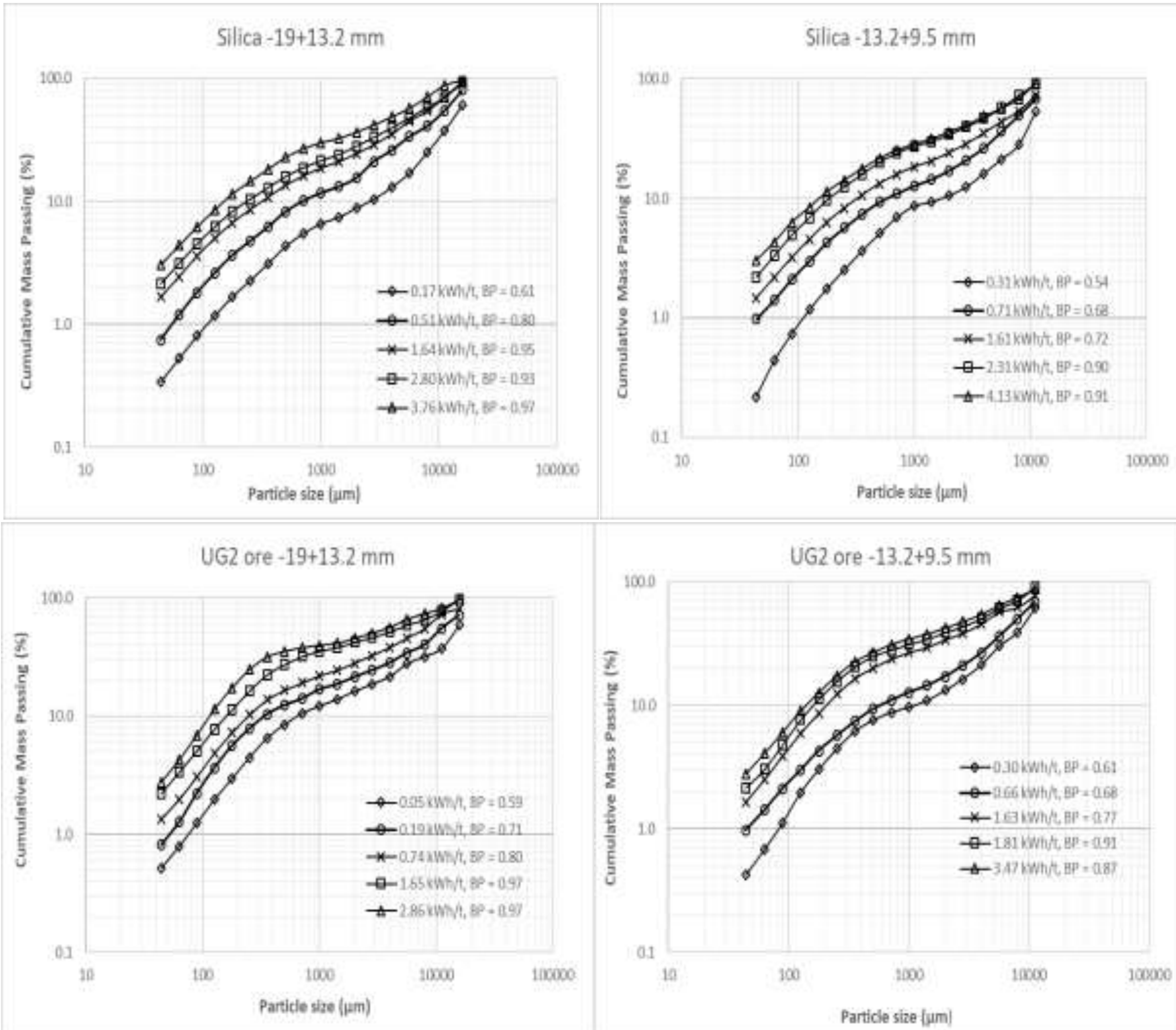

Figure D 2: Compression product size distributions of silica and UG2 ore

Appendix E: Dimensional analysis

Dimensionless analysis was done considering the five key variables (*n*) listed below.

$$\begin{cases} [f] = \frac{kg}{s} = \left[\frac{M}{T}\right] \\ [\omega] = s^{-1} = \left[\frac{1}{T}\right] \\ [d] = m = [L] \\ \left[z_{gap}\right] = m = [L] \end{cases} \qquad \text{(E1)}$$

The reference dimensions (denoted as *r*) used to express the key variables affecting particle transportation are M, L and T.

The number of dimensionless numbers (Π-groups) can be calculated using the following equation.

$$\pi - groups = n - r \qquad \text{(E2)}$$

From Eq. (E2), the total number of Π-groups is 1. These can be represented as *Π*.

The repeating variables, a set of variables which by themselves cannot form a dimensionless group, were identified among the five variables. Using that criteria, the feed rate, angular velocity and exit gap are repeating variables and the remainder particle size is non-repeating variable.

$$\pi = df^e \omega^f z^g \qquad \text{(E3)}$$

The magnitude of Π can be expressed as follows.

$$[\pi] = [d][f]^e[\omega]^f[z]^g \qquad \text{(E4)}$$

Replacing the variables with their dimensions results in the following equations.

$$[\pi] = [L]\left[\frac{M}{T}\right]^e \left[\frac{1}{T}\right]^f [L]^g \qquad \text{(E5)}$$

From Eq. (E5), when *Π* has no dimension in M, the following equation can be written.

$$e = 0 \qquad \text{(E6)}$$

For *Π* having no dimension in L, the following equation can be written.

$$1 + g = 0 \qquad \text{(E7)}$$

For Π having no dimension in T, the following equation can be written.

$$-e - f = 0 \tag{E8}$$

Solving the three equations yields the following solution.

$$e = 0\,,\ f = 0\ and\ g = -1 \tag{E9}$$

The non-dimensionless number, written as follows, is a reduction ratio of the crusher. The effect of various operating variables were related to the reduction ratio.

$$\pi = \frac{d}{z} \tag{E10}$$

Appendix F: ROC product size distributions

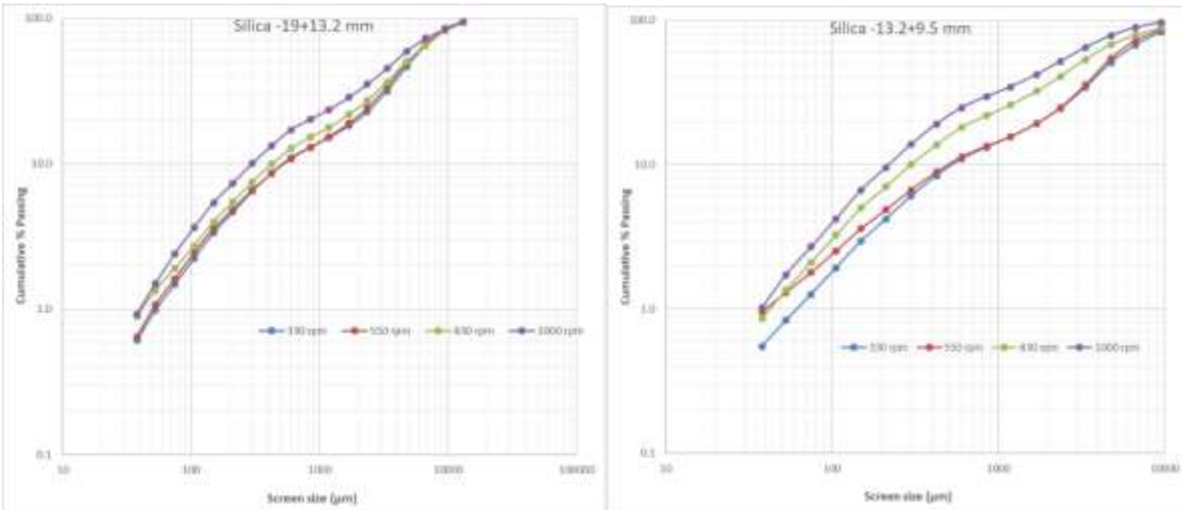

Figure F 1: Product size distributions of silica when processed in ROC at various speeds, feed rate was 1 tph

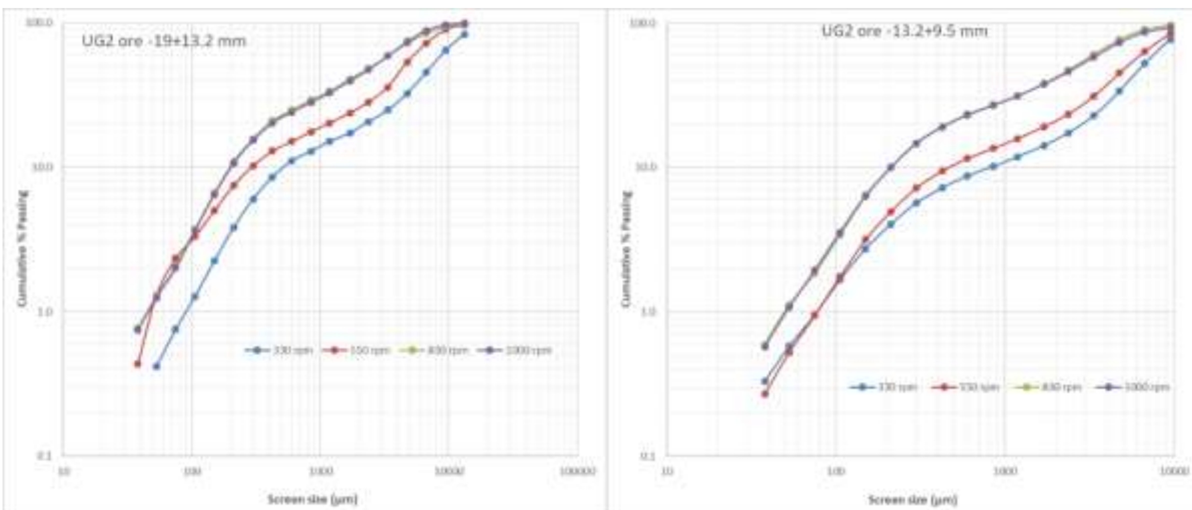

Figure F 2: Product size distributions of UG2 ore when processed in ROC at various speeds, feed rate was 1 tph

Appendix G: Common profiles used for jaw crushers

Table G 1: Some profiles in jaw crushers

(Accessed from: https://www.911metallurgist.com/blog/jaw-crusher-liner-plate-design-profile-shapes)

Types	Applications and benefits
Anti-slab (uneven tooth height) 	Less slabby product
Quarry thick 	• Good in abrasive and/or blasted rock. • Flat tooth profile maximise lifetime (more surface area to crush with). • More wearable Manganese steel than in standard jaws. • Higher stress and power requirements. • Less Space for fines to pass through. • Increase in slabby product.
Super grip 	• Good in gravel and non-abrasive rock. • Tooth spacing ideal for fines removal. • Power requirement and crushing stresses are in balance. • Less slabby product. • Reduced lifetime in abrasive application
Quarry and Supper grip 	• Sharp tooth profile (good grip on rocks). • Power requirement and crushing stresses are in balance. • Less slabby product.
Wavy like 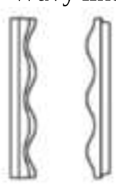	• Suitable for asphalt crushing. • Wide grooves (material flows easily through the cavity)

Appendix H: Correlations between Bond abrasion indices and metal wear rate

A high abrasion index, for example > 0.6 would suggest a preference for a single stage crusher-SAG mill circuit to avoid multiple stages of crushing and high operating costs due to liner replacement (Gupta & Yan, 2016). For Ai values > 0.15 non-autogenous impact crushers are considered uneconomic while for Ai values > 0.7 double toggle jaw crushers are preferred to single toggle crushers (Gupta & Yan, 2016).

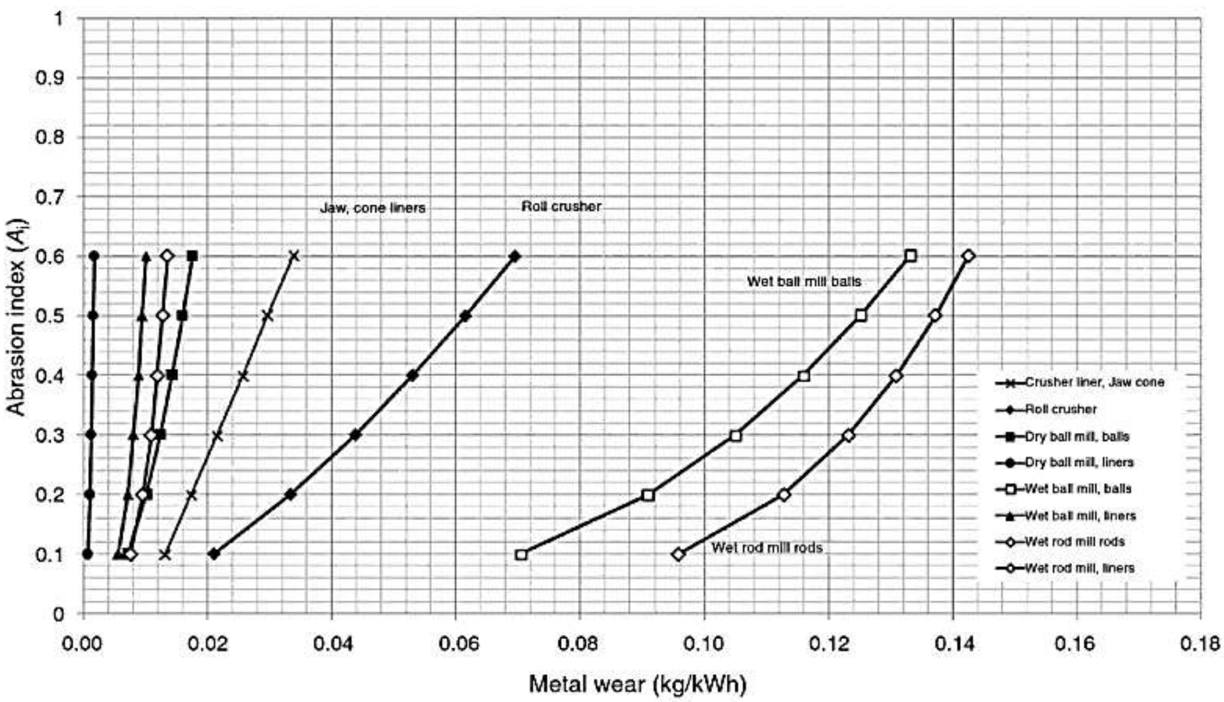

Figure H 1: Relationship between abrasion index and metal wear rate (Gupta & Yan, 2016)

Appendix I: Effect of offset

0.5 s

1.0 s

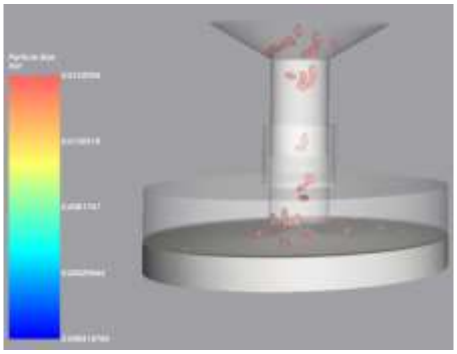

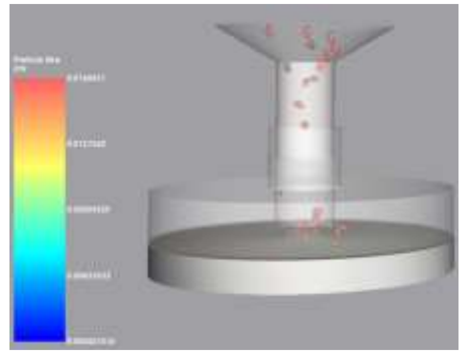

0 mm

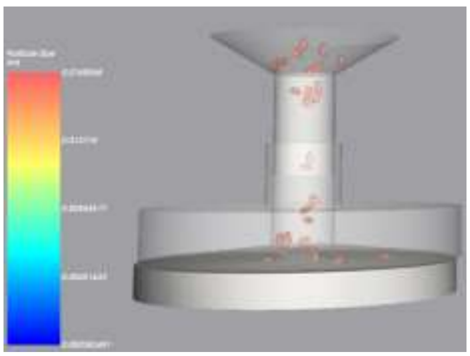

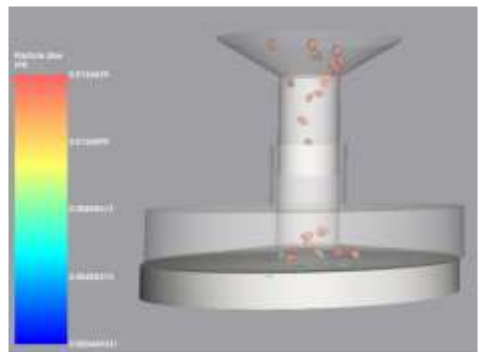

10 mm

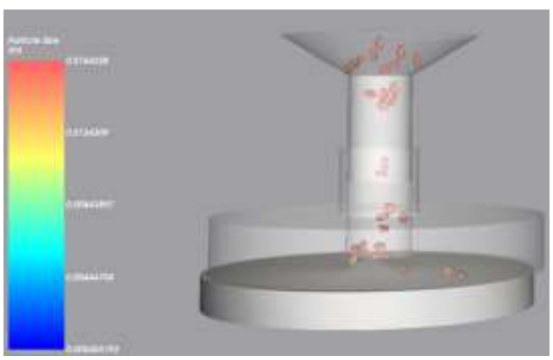

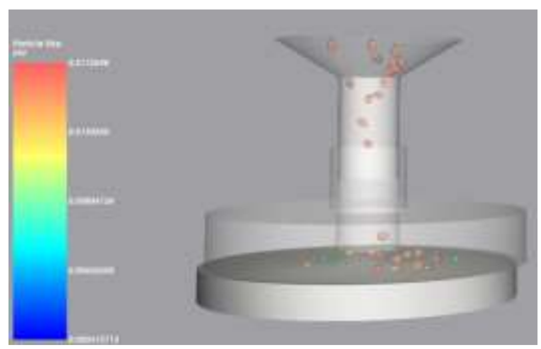

20 mm

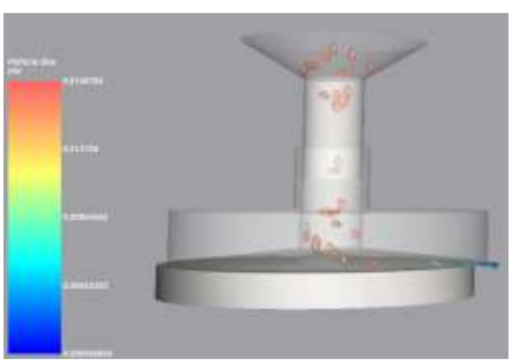

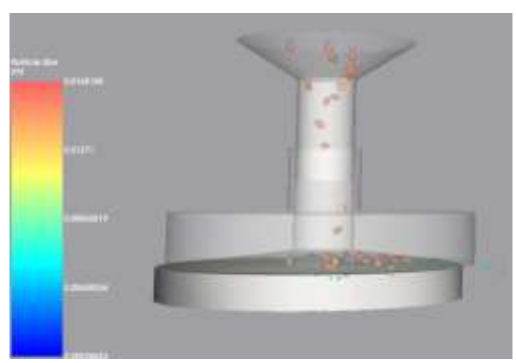

30 mm

Figure I 1: : Particle breakage in the ROC for various offset

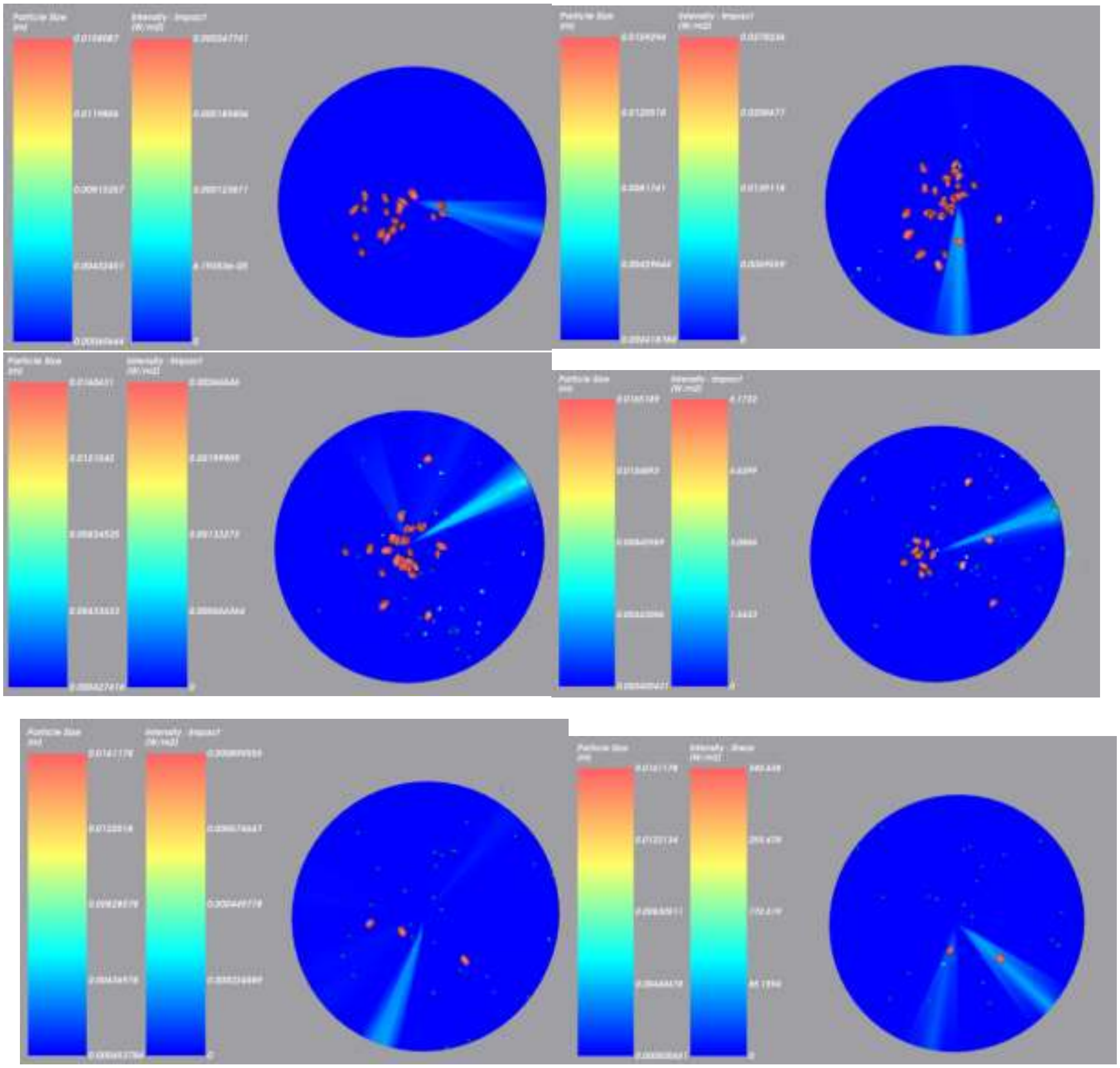

Figure I 2: Impact energies snap shots for 0 mm offset (a) 0.3 s, (b) 0.5 s, (c) 1 s, (d) 1.2 s, (e) 1.5 s and (f) 1.7 s

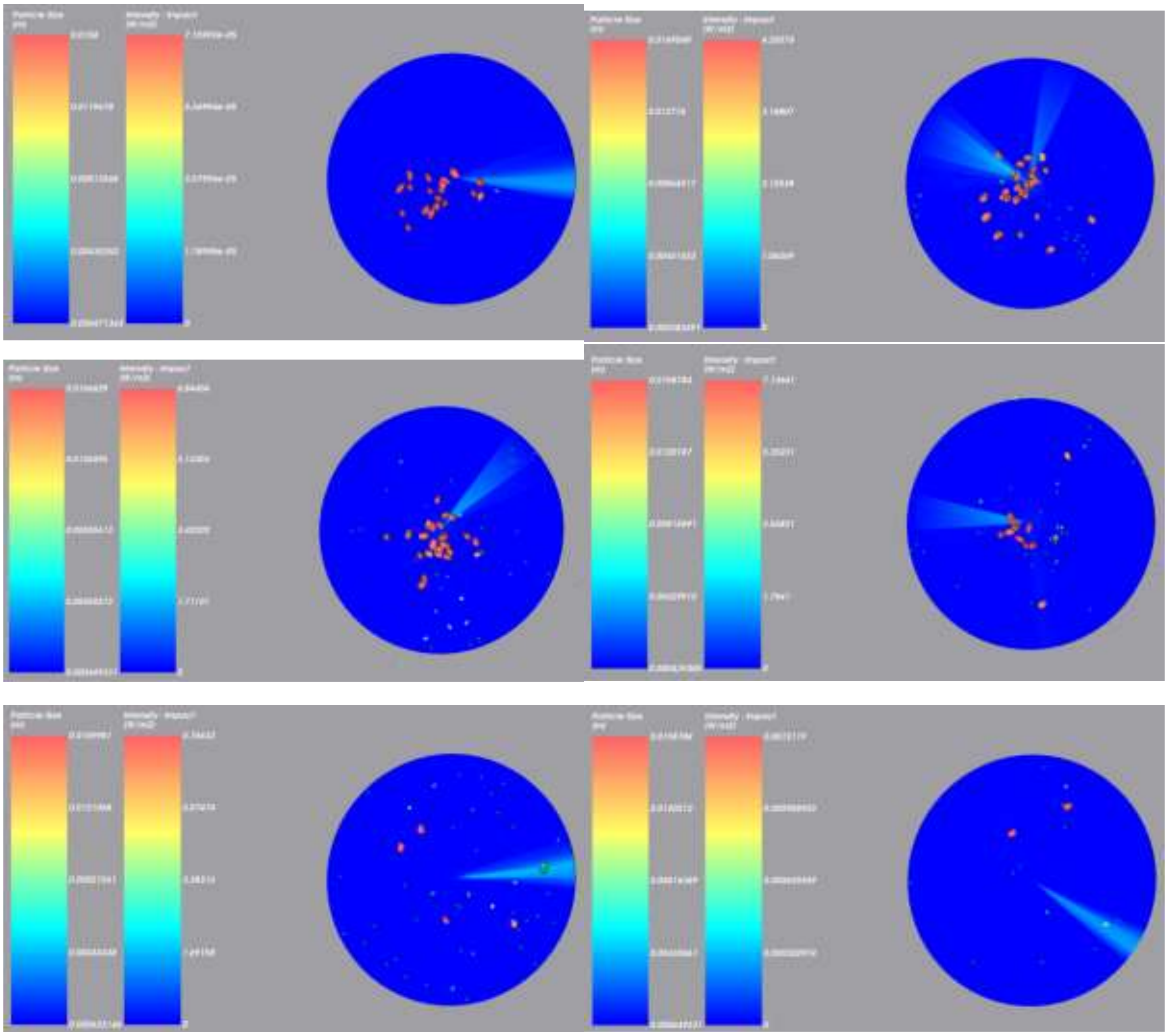

Figure I 3: Impact energies snap shots for 10 mm offset (a) 0.3 s, (b) 0.5 s, (c) 1 s, (d) 1.2 s, (e) 1.5 s and (f) 1.7 s

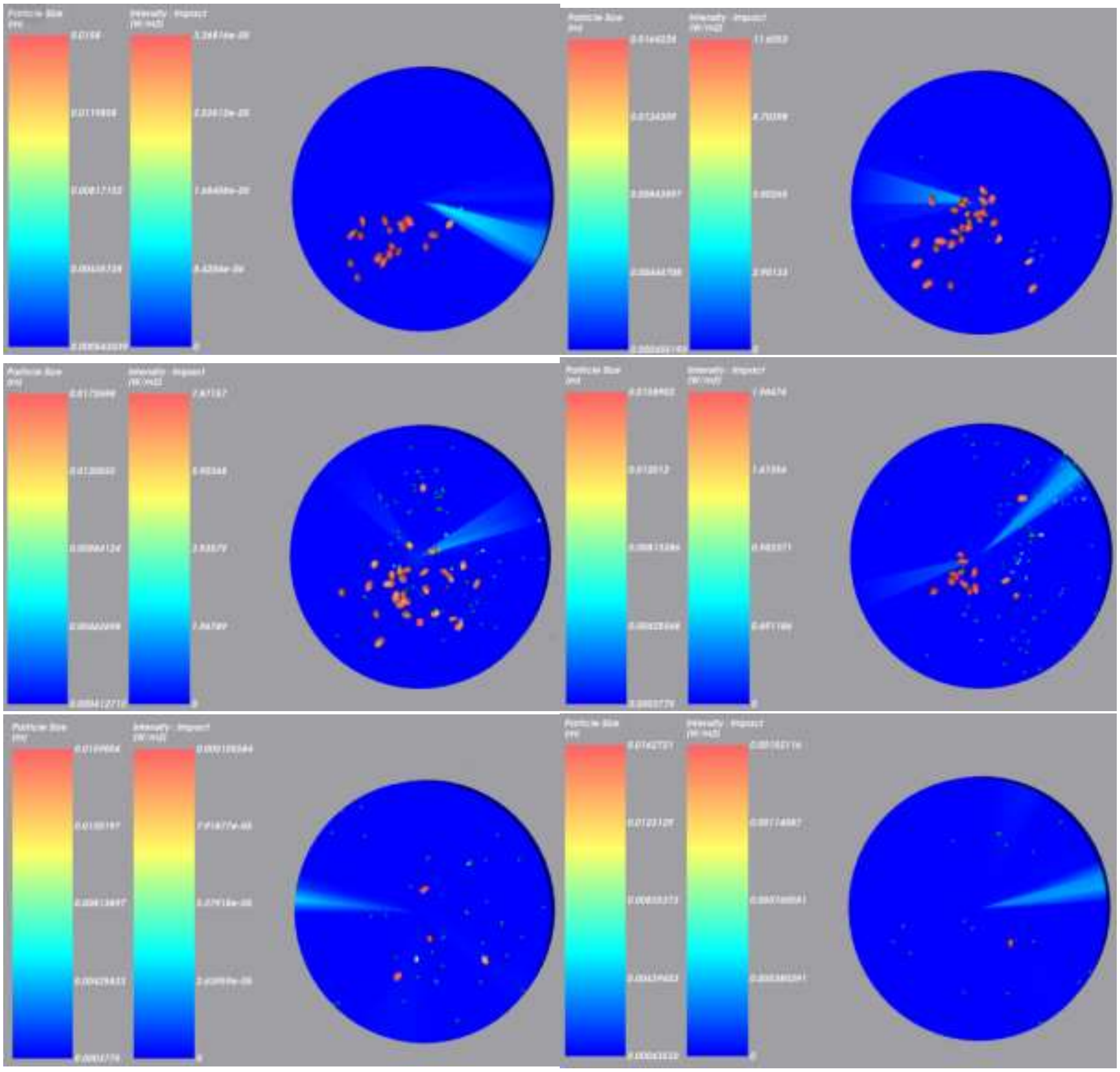

Figure I 4: Impact energies snap shots for 20 mm offset (a) 0.3 s, (b) 0.5 s, (c) 1 s, (d) 1.2 s, (e) 1.5 s and (f) 1.7 s

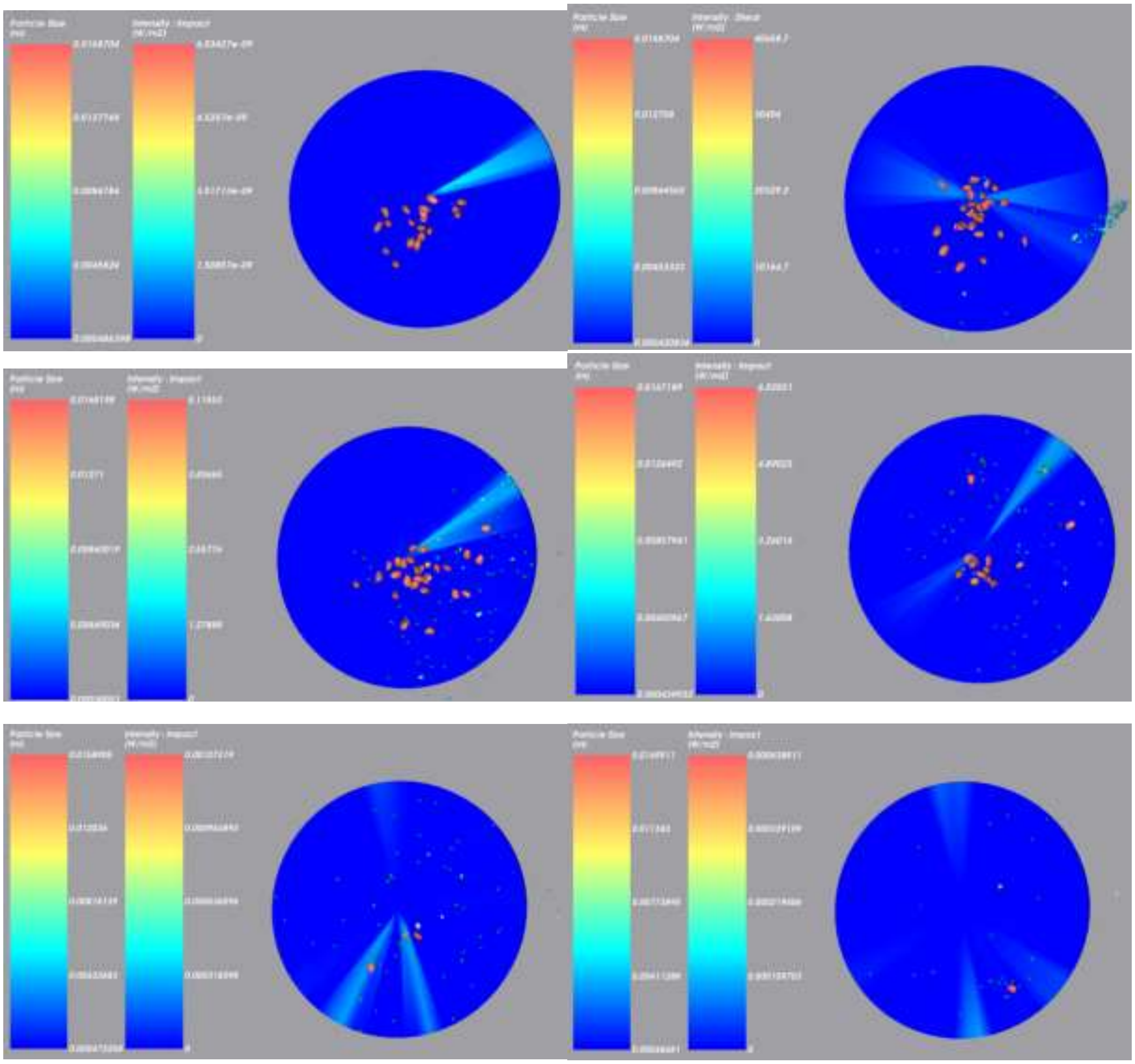

Figure I 5: Impact energies snap shots for 30 mm offset (a) 0.3 s, (b) 0.5 s, (c) 1 s, (d) 1.2 s, (e) 1.5 s and (f) 1.7 s

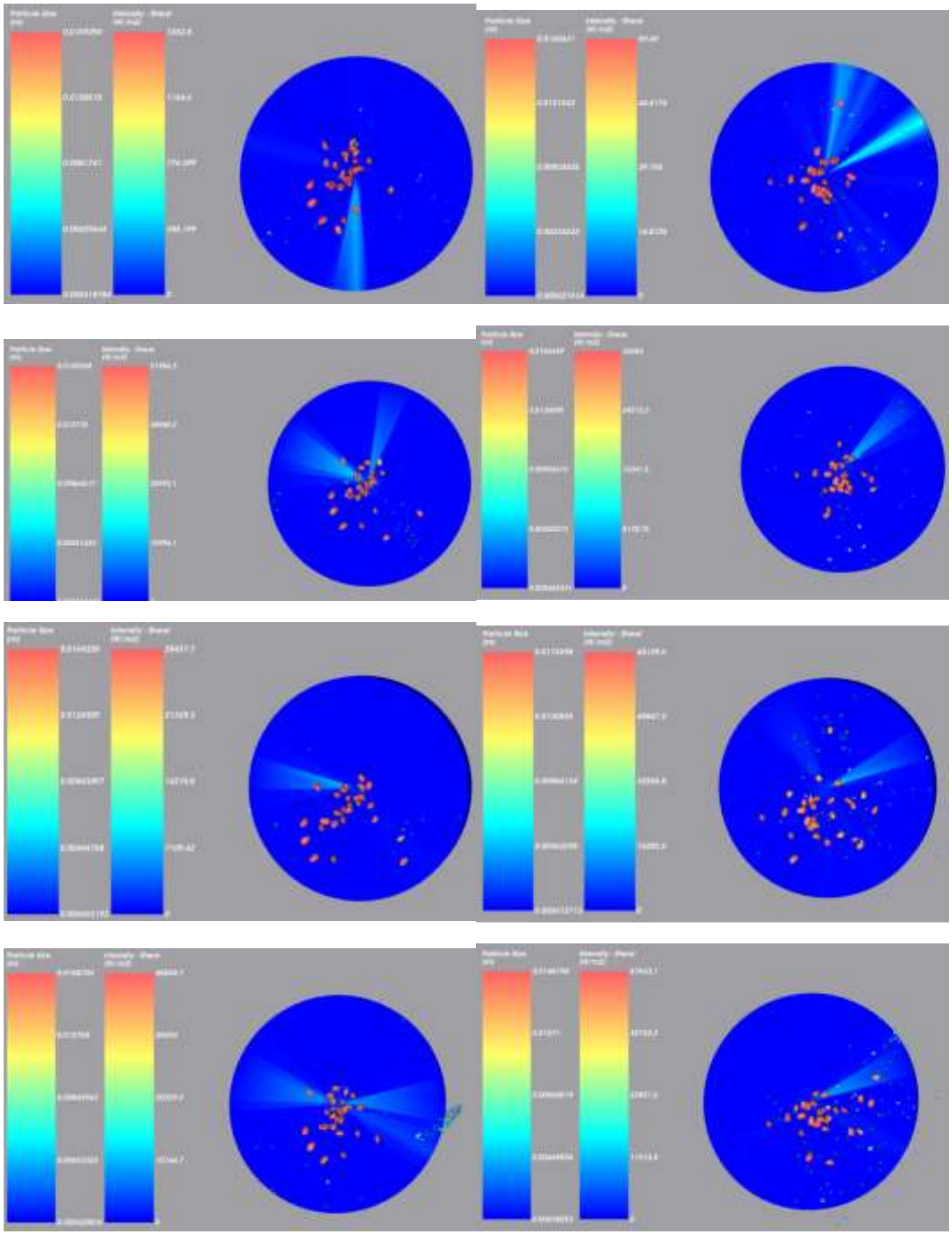

Figure I 6: Shear energy snap shots for 0.5 and 1.0 s (a) 0 mm offset, (b) 10 mm offset, (c) 20 mm offset, and (d) 30 mm offset

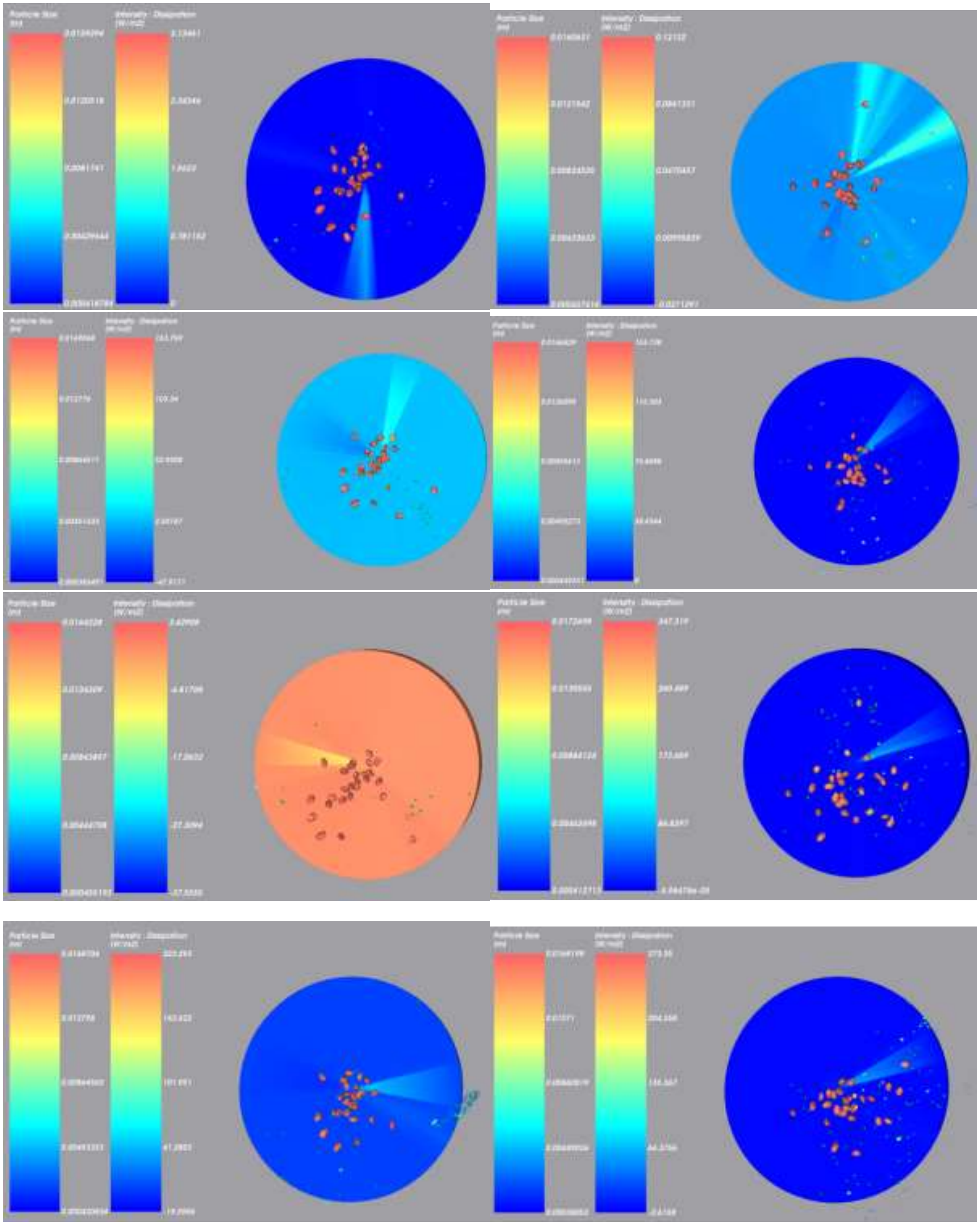

Figure I 7: Dissipated energy snap shots for 0.5 and 1.0 s (a) 0 mm offset, (b) 10 mm offset, (c) 20 mm offset, and (d) 30 mm offset

Appendix J: Additional results to Section 8.3 in Chapter 8

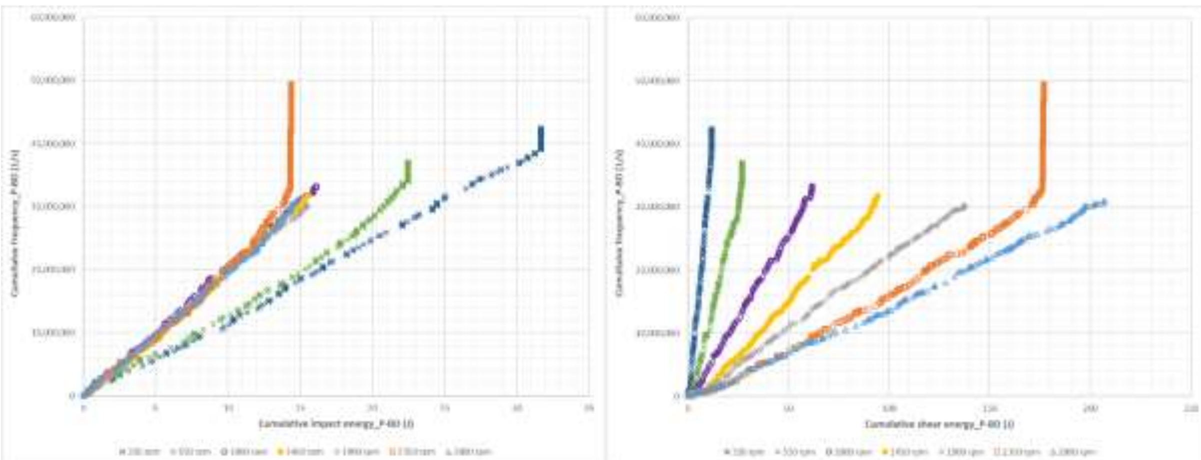

Figure J 1: Impact and shear energies as function of rotational speed

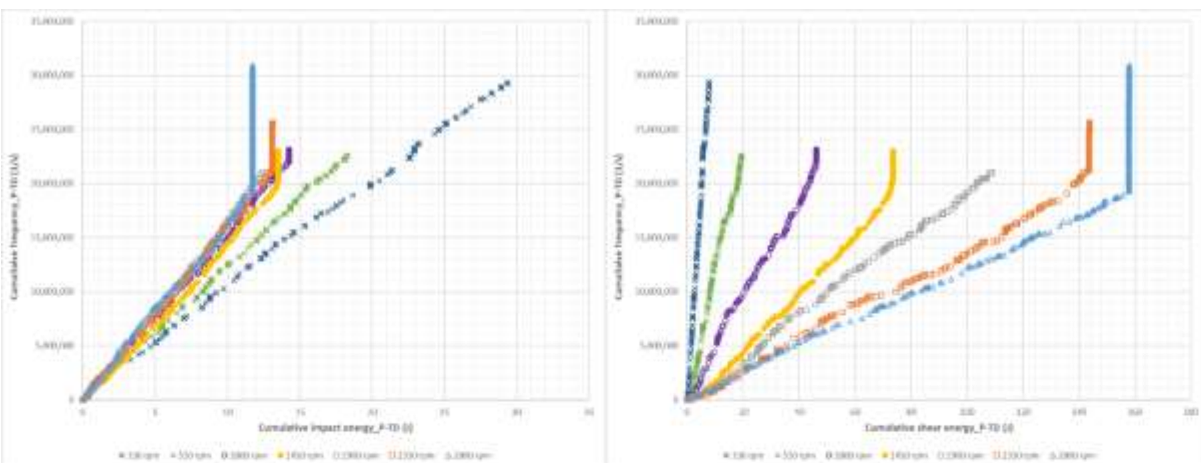

Figure J 2: Impact and shear energies as function of rotational speed

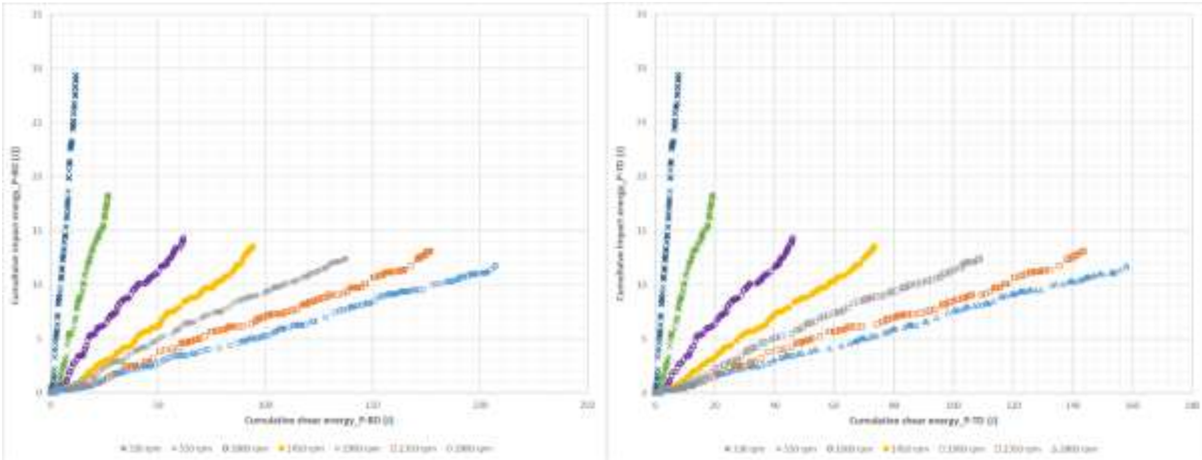

Figure J 3: Impact and shear energies as function of rotational speed